

RELIABLE PREDICTIONS OF THE PROPERTIES OF ACTINIDE COMPLEXES

by

VIRGIL EDWARD JACKSON

DAVID A. DIXON, COMMITTEE CHAIR

SHANE C. STREET

GREGORY SZULCZEWSKI

LOWELL D. KISPERT

TONYA M. KLEIN

A DISSERTATION

Submitted in partial fulfillment of the requirements
for the degree of Doctor of Philosophy
in the Department of Chemistry
in the Graduate School of
The University of Alabama

TUSCALOOSA, ALABAMA

2013

Copyright Virgil Edward Jackson 2013
ALL RIGHTS RESERVED

ABSTRACT

A study of reactions of laser-ablated thorium atoms and O_2 using matrix isolation infrared spectroscopy has been conducted using electronic structure calculations to interpret the infrared spectra of three new thorium oxide species, ThO_2^- , Th_2O_2 , and Th_2O_4 obtained in argon and neon matrixes.

The potential energy surface for the reaction of matrix isolated ThO with CH_4 to give the $CH_3Th(O)H$ intermediate has been calculated at the CCSD(T) level, it reveals that the $CH_3Th(O)H$ molecule possesses a pyramidal structure with a closed shell singlet ground state. Formation of the $CH_3Th(O)H$ molecule from the reaction of ThO and methane has an energy barrier of 30 kcal/mol, which is consistent with the appearance of the $^1CH_3Th(O)H$ absorptions under broad band mercury arc UV irradiation. The $^3Th + ^1CH_3OH$ asymptote is predicted to be 119 kcal/mol above the reactant asymptote, $^1ThO + CH_4$, utilizing the spin orbit correction to the 3Th atom which is in excellent agreement with the value of 118.7 ± 3.8 kcal/mol.

The first reliable predictions of the frequencies of the isolated uranyl ion have been made to develop new techniques to determine how this important form of uranium is being complexed in the environment. A comprehensive computational study of UO_2^{2+} complexed with the phosphate anions $H_2PO_4^-$, HPO_4^{2-} , and PO_4^{3-} and water ligands has been performed at the density functional theory (DFT) and correlated molecular orbital theory levels in the gas phase and in aqueous solution. This study was done to aid the effort in developing solutions to the *in situ* remediation challenge posed by the nuclear waste stored in the tanks at the Hanford and

Savannah River nuclear weapons production sites. This information can be used to provide a better understanding of the speciation of such species and to better our understanding of mobility issues of tank waste as well as stability concerns for waste matrices.

DEDICATION

To my mom, Virginia Jackson, and my dad, Edward Jackson, for their love and support; without which my success would not have been possible.

LIST OF ABBREVIATIONS AND SYMBOLS

ADE	Adiabatic electron affinity
ADF	Amsterdam Density Functional software
aug-cc-pVnZ	Augmented, correlation consistent, polarized valence n zeta basis sets, where n = double (D), triple (T) or quadruple (Q)
ANO-L	Large atomic natural orbital basis sets
ANO-S	Small atomic natural orbital basis sets
aug-cc-pVnZ-PP	aug-cc-pVnZ basis sets with pseudopotentials for heavy atoms
aug-cc-pwCVnZ	Augmented, correlation consistent, polarized weighted core valence n (D, T, Q or 5) zeta basis sets
aug-cc-pwCVTZ-PP	aug-cc-pwCVTZ basis set with pseudopotentials for heavy atoms
AVDZ	$E(n) = E_{\text{CBS}} + A \exp[-(n-1)] + B \exp[-(n-1)^2]$ n = 2 (aug-cc-pVDZ-PP)
AVTZ	$E(n) = E_{\text{CBS}} + A \exp[-(n-1)] + B \exp[-(n-1)^2]$ n = 3 (aug-cc-pVDZ-PP)
AVQZ	$E(n) = E_{\text{CBS}} + A \exp[-(n-1)] + B \exp[-(n-1)^2]$ n = 4 (aug-cc-pVDZ-PP)
awCVTZ	aug-cc-pwCVTZ basis sets
B3LYP	Becke 93 (exchange), Lee-Yang-Parr (correlation) DFT functional
BLYP	Becke 88 (exchange), Lee-Yang-Parr (correlation) DFT functional
BDE	Bond dissociation energy
BP86	Becke 88 (exchange), Perdew 86 (correlation) DFT functional

CAS	Complete active space
CASPT2	Complete active space second-order perturbation theory
CBS	Complete basis set
CCSD(T)	Coupled cluster singles, doubles, and disconnected triples
CCSD	Coupled cluster singles, doubles
COSMO	Conductor-like screening model
CI	Configuration interaction
CISD	Configuration interaction singles and doubles
CV	Core valence
DFT	Density functional theory
DHF	Dirac–Hartree–Fock
DZVP	DFT optimized double zeta valence basis set with polarization functions (except H)
DZVP2	DFT optimized double zeta valence basis set with polarization functions
ΣD_0 ($\Sigma D_{0,0K}$)	Total atomization energy
G3MP2	Gaussian 3 theory calculation using 2 nd order Møller Plesset perturbation theory (MP2)
ΔE_{CBS}	Complete basis set energy change
ΔE_{CV}	Core valence energy change
$\Delta E_{\text{PP,corr}}$	Pseudopotential error correction energy exchange: $\Delta E_{\text{PP,corr}} = \Delta E_{\text{awCVTZ-DK}} - (\Delta E_{\text{awCVTZ-PP}} + \Delta E_{\text{SR}})$.
ΔE_{Rel}	Scalar relativistic energy change: $\Delta E_{\text{Rel}} = \Delta E_{\text{SR}} + \Delta E_{\text{PP,corr}} = \Delta E_{\text{awCVTZ-DK}} - \Delta E_{\text{awCVTZ-PP}}$
ΔE_{SO}	Spin orbit energy change
ΔE_{SR}	Scalar relativistic correction calculated as the MVD expectation values

ΔE_{ZPE}	Zero point energy change
$\Delta E_{0\text{K}}/\Delta E_{298\text{K}}$	BDE at 0 K/298 K
ECP	Effective core potential
EA	Electron affinity
FA	Fluoride affinity
FCF	Franck-Condon factors
(FT-ICR-MS)	Fourier transform ioncyclotron resonance mass spectrometry
FTIR	Fourier transform infrared spectroscopy
FWAM	Full widths at half maximum
ΔG_{aq}	Aqueous deprotonation Gibbs free energy (solution free energy)
ΔG_{gas}	Gas phase free energy
$\Delta \Delta G_{\text{solv}}$	Aqueous solvation free energy
$\Delta G_{298\text{K}}$	Gas phase Gibbs acidity
GIAO	Gauge independent atomic orbital approximation
$\Delta H_{298\text{K}}$	Gas phase enthalpy acidity
HA	Hydride affinity
HF	Hartee-Fock
$\Delta H_{\text{f},0\text{K}}$	Heat of formation at 0K
$\Delta H_{\text{f},298\text{K}}$	Heat of formation at 298K
ΔH_{rxn}	Reaction enthalpy change
I	Intensities
IR	Infrared spectrscopy
K	Kelvin

MO	Molecular orbital
MP2	2 nd order Møller Plesset perturbation theory
MVD	Mass-velocity and Darwin operators
NIST-JANAF	National Institute of Standards and Technology - Joint Army-Navy-Air Force
NMR	Nuclear magnetic resonance
PA	Proton affinity
PBE	Perdew-Burke-Ernzerhof (exchange), Perdew-Burke-Ernzerhof (correlation) DFT functional
PES	Potential energy surface
pK _a	Negative logarithm of the acid dissociation constant
PP	Pseudopotential
PW91	Perdew-Wang 91 (exchange), Perdew-Wang 91 (correlation) DFT functional
R	Restricted method for the starting Hartree-Fock wavefunction
R	Gas constant
ROHF	Open-shell HF
R/UCCSD(T)	Open-shell CCSD(T)
SCF	Self consistent field
SCRf	Self consistent reaction field
SO	Spin orbit
SP	Square pyramidal
SR	Scalar relativistic
T	Temperature

TAE	Total atomization energy
TZ2P	Triple zeta basis set with 2 polarization functions
UV	Ultraviolet
VTZP	Valence high triple zeta basis set with polarized function
ZORA	Zeroth order regular approximation to the Dirac equation
ZPE	Zero point energy
>	Greater than
<	Less than
=	Equal to
Å	Angstrom
°	Degrees
±	Plus or minus

ACKNOWLEDGMENTS

I am pleased to have this opportunity to thank my research advisor Prof. David A. Dixon for his support, continuous guidance, and endless patience; his demand for excellence in all my efforts has made me a better researched and writer. I am very fortunate to have had the opportunity to work with him, to learn from him and to be a member of his research group.

I would like to thank my committee members, Prof. Shane C. Streets, Prof Gregory J. Szculczewski, Prof Lowell D. Kispert and Prof Tonya M. Klein for their supportive contributions throughout my work at the University of Alabama. I also thank Prof. Carl P. Johnson for his encouragement to further my education.

I would like to thank Prof. Kirk A. Peterson from Washington State University, Prof. Lester Andrews from the University of Virginia, and Prof. Karl O. Christe from the Loker Research Institute and the University of Southern California for the opportunity that I have had to work with them and for their contributors to this work.

I would like to thank my colleagues, all the past and present members of the Dixon group, who have become brothers and sisters to me. I give a special thanks to Prof. Shenggang Li for the tremendous help he provided not only to me but to every member of the Dixon group.

I would like to thank the University of Alabama and the Department of Chemistry for the financial support that has made my study possible.

Finally, I would like to thank my family for their love, support and understanding throughout the years I have spent at the University of Alabama completing my education.

CONTENTS

ABSTRACT.....	ii
DEDICATION.....	iv
LIST OF ABBREVIATIONS AND SYMBOLS.....	v
ACKNOWLEDGMENTS.....	x
LIST OF TABLES.....	xv
LIST OF FIGURES.....	xviii
CHAPTER 1 INTRODUCTION.....	1
1.1 Computational Methods.....	4
1.2 Prediction of the Vibrational Frequencies of UO_2^{2+} at the CCSD(T) Level.....	9
1.3 Matrix Infrared Spectra and Theoretical Studies of Thorium Oxide Species: ThO_x and Th_2O_y	9
1.4 Methane to Methanol Conversion Induced by Thorium Oxide through the $\text{CH}_3\text{Th}(\text{O})\text{H}$ Intermediate in Solid Argon.....	10
1.5 Density Functional Theory Study of the Complexation of the Uranyl Dication with Anionic Phosphate Ligands with and without Water Molecules.....	10
1.6 Thermochemical Properties of Selenium Fluorides, Oxides, and Oxofluorides.....	11
References.....	13
CHAPTER 2 PREDICTION OF THE VIBRATIONAL FREQUENCIES OF UO_2^{2+} AT THE CCSD(T) LEVEL.....	15

2.1	Introduction.....	15
2.2	Calculations.....	17
2.3	Results and Discussion	18
	References	30
CHAPTER 3. THE REACTION OF THORIUM OXIDE PLUS METHANE IN SOLID ARGON: A CH ₃ Th(O)H INTERMEDIATE PRECEDES FORMATION OF METHANOL PLUS THORIUM.....		
3.1	Introduction.....	34
3.2	Experimental and Theoretical Methods	36
3.3	Results and Discussion	37
3.4	Conclusion	43
	References.....	44
CHAPTER 4. MATRIX INFRARED SPECTRA AND THEORETICAL STUDIES OF THORIUM OXIDE SPECIES: ThO _x AND Th ₂ O _y		
4.1	Introduction.....	54
4.2	Experimental and Theoretical Methods	55
4.3	Results and Discussion	57
	4.3.1 Infrared spectral observations.....	57
	4.3.2 Th ₂ O ₄	59
	4.3.3 Th ₂ O ₂	62
	4.3.4 ThO ₂ ⁻	63
	4.3.5 Reactions in the matrix	64
	4.3.6 Additional Thorium Oxide Calculations.....	68
4.4	Conclusions.....	69
	References.....	71

CHAPTER 5. DENSITY FUNCTIONAL THEORY STUDY OF THE COMPLEXATION OF THE URANYL DICATION WITH ANIONIC PHOSPHATE LIGANDS WITH AND WITHOUT WATER MOLECULES	90
5.1 Introduction.....	90
5.2 Computational Methods	93
5.3 Results and Discussion	94
5.3.1 UO ₂ ²⁺ and the Ligands	94
5.3.2 Mono- and Di-ligand Anhydrous Uranyl Phosphate Complexes	96
5.3.3 Tri- and Tetra-ligand Anhydrous Uranyl Phosphate Complexes	99
5.3.4 Hydrated Phosphate Complexes	101
5.3.5 Comparison to experiment.....	108
5.3.6 Gas-Phase Uranyl Phosphate Reaction Energies	109
5.3.7 Solution Phase Reaction Energies: Phosphoric Acid.....	110
5.3.8 Solution Phase Reaction Energies: Uranyl Phosphates	112
5.4 Conclusions.....	118
References	122
CHAPTER 6 THERMOCHEMICAL PROPERTIES OF SELENIUM FLUORIDES, OXIDES AND OXOFLUORIDES	156
6.1 Introduction.....	156
6.2 Computational Methods.....	157
6.3 Results and Discussion	159
6.3.1 Geometries	159
6.3.2 Vibrational Frequencies	160
6.3.3 NMR Chemical Shifts.....	161
6.3.4 Calculated Heats of Formation	162

6.3.5	Bond Dissociation Energies	163
6.3.6	Fluoride Affinities	167
6.3.7	Fluorocation Affinities	168
6.3.8	Electron Affinities and Ionization Potentials	168
6.3.9	BDEs in the Cations and Anions	168
6.4	Conclusions	170
	References	172
CHAPTER 7.	CONCLUSIONS	207
	References	220

LIST OF TABLES

2.1.	Calculated Bond Distances (Å) and Harmonic Frequencies (cm ⁻¹).....	26
2.2.	Calculated Anharmonic Fundamental Frequencies (cm ⁻¹) for UO ₂ ²⁺	27
2.3.	UO ₂ ²⁺ Vibrational Anharmonicity Constants	28
2.4.	ThO ₂ Harmonic and Anharmonic Fundamental Vibrational Frequencies in cm ⁻¹	29
3.1.	Observed and Calculated (in Bold) Infrared Absorptions (cm ⁻¹) of the CH ₃ Th(O)H Molecule in Solid Argon.....	53
4.1.	Experimental Infrared Absorptions (cm ⁻¹) of New Products from the Reactions of Thorium and Isotopically Substituted O ₂ in Solid Ar and Ne Matrices	75
4.2.	Calculated Geometry Parameters (Bond Angles in Degrees) for Thorium Oxide Species	76
4.3.	Calculated B3LYP Vibrational Frequencies for Th ₂ O ₃ and Th ₂ O ₄	78
4.4.	Calculated CCSD(T) and B3LYP Vibrational Frequencies for the ThO, ThO ₂ , Th ₂ O, and Th ₂ O ₂ Neutral and Charged Species	80
5.1.	Calculated Ligand and Uranyl Bond Distances (Å) and Vibrational Frequencies (ν in cm ⁻¹).....	140
5.2.	Average NPA Charges per Atom on Ligands and Uranyl	141
5.3.	Selected Bond Lengths (Å), Angles (degrees), and UO ₂ ²⁺ Vibrational Frequencies (ν, cm ⁻¹) for Anhydrous Uranyl Phosphates.....	142
5.4.	Average NPA Charges (in electrons) for Anhydrous Uranyl Monophosphates.....	143
5.5.	Selected Bond Lengths (Å), Angles (degrees), and UO ₂ ²⁺ Vibrational Frequencies (ν, cm ⁻¹) for Hydrated Uranyl Monophosphates	144

5.6.	Selected Bond Lengths (Å), Angles (degrees), and UO_2^{2+} Vibrational Frequencies (ν , cm^{-1}) for Hydrated Uranyl Diphosphates.....	146
5.7.	Calculated Reaction Energetics for Binding of Phosphate Ligands to Form Anhydrous Uranyl Phosphate Complexes (kcal/mol)	149
5.8.	Calculated Gas Phase Reaction Energetics for the Reactions $\text{UO}_2(\text{H}_2\text{PO}_4)_2 + n\text{H}_2\text{O} \rightarrow [\text{UO}_2(\text{H}_2\text{O})_n(\text{H}_2\text{PO}_4)_2]$ and $[\text{UO}_2(\text{HPO}_4)_2]^{2-} + n\text{H}_2\text{O} \rightarrow [\text{UO}_2(\text{H}_2\text{O})_n(\text{HPO}_4)_2]^{2-}$ in kcal/mol.....	150
5.9.	Phosphoric Acid pK_{as} for the 1 st , 2 nd , and 3 rd Deprotonation	151
5.10.	MP2/aug-cc-pVTZ Reaction Free Energies in Aqueous Solution ($\Delta G_{298\text{Soln}}$) of Solvated Phosphates/ H_2O Complexes in kcal/mol	152
5.11.	MP2 Calculated Free Energies in Aqueous Solution ($\Delta G_{298\text{Soln}}$) of UO_2^{2+} /Solvated Phosphates/ H_2O Complexes in kcal/mol	153
5.12.	MP2 Reaction Free Energies in Aqueous Solution ($\Delta G_{298\text{Soln}}$) of UO_2^{2+} /Solvated Phosphates/ H_2O Complexes Using the IPCM Approach in kcal/mol	154
5.13.	Calculated Reaction Free Energies in Aqueous Solution ($\Delta G_{298\text{Soln}}$, kcal/mol) for the Successive Binding of a 1 st , 2 nd , 3 ^d , and 4 th Water Ligand to $\text{UO}_2(\text{H}_2\text{O})_n(\text{H}_2\text{PO}_4)_2$ to Form Hydrated Uranyl Phosphate Complexes	155
6.1.	Optimized Bond Lengths (Å) and Angles (degrees) for SeF_xO_y Geometries.....	178
6.2.	Calculated CCSD(T)/aug-cc-pVDZ (-PP on Se) Vibrational Frequencies, for SeF_2 , SeF_2^+ , SeF_6 and SeO_2^-	181
6.3.	Calculated CCSD(T)/aug-cc-pVDZ-PP Se-F and Se-O Vibrational Stretching Frequencies	182
6.4.	Calculated $\delta(^{19}\text{F})/\text{ppm}^{\text{a}}$ and $\delta(^{77}\text{Se})/\text{ppm}^{\text{b}}$ NMR chemical shifts.....	185
6.5.	Components for Calculating the Atomization Energies in kcal/mol	187
6.6.	Calculated CCSD(T)/CBS Heats of Formation (kcal/mol) at 0 and 298 K.....	190
6.7.	Calculated CCSD(T)/CBS Adiabatic and Diabatic BDEs in kcal/mol.....	192
6.8.	CCSD(T)/CBS Fluoride Affinities in kcal/mol at 298 K.....	293
6.9.	CCSD(T)/CBS Fluorocation Affinities (FCA) in kcal/mol at 298 K.....	194
6.10.	CCSD(T)/CBS Electron Affinities at 0 K in eV.....	195
6.11.	CCSD(T)/CBS Ionization energies at 0 K in eV	196

6.12.	CCSD(T)/CBS Adiabatic Anion BDEs in kcal/mol at 0 and 298 K	197
6.13.	CCSD(T)/CBS Adiabatic Cation BDEs in kcal/mol at 0 and 298 K.....	198
6.14.	CCSD(T)/CBS Adiabatic Heterolytic Se-F BDEs in kcal/mol at 0 and 298 K to Form a Cation and F ⁻	199

LIST OF FIGURES

3.1.	Infrared spectra of laser-ablated ThO, Th, and O and CH ₄ reaction products in solid argon: (a) ThO + 0.5% CH ₄ deposition for 60 min; (b) after annealing to 20 K; (c) after $\lambda > 290$ nm irradiation; (d) after $\lambda > 220$ nm irradiation; (e) annealing to 30 K; (f) after annealing to 35 K.....	48
3.2.	Infrared spectra of laser-ablated ThO, Th, and O and isotopically substituted CH ₄ reaction products in solid argon (all spectra taken after $\lambda > 220$ nm irradiation followed by annealing to 30 K): (a) ThO + 0.5% CH ₄ ; (b) ThO + 0.5% ¹³ CH ₄ ; (c) ThO + 0.5% CD ₄ ; (d) Infrared spectra of laser-ablated Th atoms and isotopically substituted CH ₃ OH reaction products in solid argon; (d) Th + 1.0% CH ₃ OH, after annealing to 35 K; (e) Th + 0.5% CH ₃ ¹⁸ OH, after annealing to 40 K.....	49
3.3.	Structure of the ¹ A ground state of the CH ₃ Th(O)H molecule calculated at the B3LYP level of theory. Bond lengths in Å. Top numbers using the 6-311++G(d,p) + SDD basis set. Bond lengths and angles with the aug-cc-pVTZ + ECP basis set in parentheses: \angle OThH: 104.6° (104.8°), \angle CThH: 96.8° (96.8°), \angle CThO: 103.1° (103.2°), \angle sum = 304.5° (304.8°). Th is blue, O is red, C is grey and H atoms are white	50
3.4.	Calculated potential energy Surface for the ¹ ThO + CH ₄ → ³ Th + CH ₃ OH reaction at the CCSD(T)/aug-cc-pVTZ(ECP)//B3LYP/ aug-cc-pVTZ(ECP') (see text for basis set details) level of theory in kcal/mol. The imaginary frequencies for the transition states are: 1315 <i>i</i> (¹ TS1), 688 <i>i</i> (³ TS1), 670 <i>i</i> (¹ TS2'), 1091 <i>i</i> (³ TS2'), 1439 <i>i</i> (¹ TS2''), 466 <i>i</i> (³ TS2''), 498 <i>i</i> (³ TS3'), and 834 <i>i</i> (³ TS3''). The spin-orbit corrected values for the ³ Th + ¹ CH ₃ OH asymptote is parentheses, and that for the ³ Th···CH ₃ OH complex is 81 kcal/mol.....	51
4.1.	Infrared spectra of laser-ablated Th atoms and O ₂ reaction products in solid argon: (a) Th + 0.1% O ₂ deposition for 60 min; (b) after annealing to 25 K; (c) after $\lambda > 380$ nm irradiation; (d) after $\lambda > 220$ nm irradiation; (e) after annealing to 35 K; (f) after annealing to 40 K.....	82
4.2.	Infrared spectra of laser-ablated Th atoms and isotopically substituted O ₂ reaction products in solid argon at 10 K after sample deposition for 60min: (a) Th + 0.1% ¹⁶ O ₂ ; (b) Th + 0.2% ¹⁸ O ₂ ; (c) Th + 0.2% ¹⁶ O ₂ + 0.2% ¹⁸ O ₂ ; (d) Th + 0.125% ¹⁶ O ₂ + 0.25% ¹⁶ O ¹⁸ O + 0.125% ¹⁸ O ₂	83
4.3.	Infrared spectra of laser-ablated Th atoms and isotopically substituted O ₂ molecule reaction products in solid argon in two spectral regions after annealing to 35 K and	

	recooling to 10 K. (a) Th + 0.2% $^{18}\text{O}_2$; (b) Th + 0.1% $^{16}\text{O}_2$; (c) Th + 0.2% $^{16}\text{O}_2$ + 0.2% $^{18}\text{O}_2$; (d) Th + 0.125% $^{16}\text{O}_2$ + 0.25% $^{16}\text{O}^{18}\text{O}$ + 0.125% $^{18}\text{O}_2$	84
4.4.	Infrared spectra of laser-ablated Th atoms and O_2 reaction products in solid neon at 4 K: (a) Th + 0.5 % O_2 deposition for 30 min; (b) after annealing to 8 K; (c) after $\lambda > 220$ nm irradiation; (d) after annealing to 10 K	86
4.5.	Infrared spectra of laser-ablated Th atoms and $^{18}\text{O}_2$ reaction products in solid neon at 4 K: (a) Th + 0.5 % $^{18}\text{O}_2$ deposition for 30 min; (b) after $\lambda > 220$ nm irradiation; (c) after annealing to 8 K; (d) after annealing to 10 K	87
4.6.	Computed structures (B3LYP) for the two major new products of the Th and O_2 reaction following ThO and ThO_2 . Bond lengths in Å and bond angles in degrees.....	88
4.7.	Simulated anion photoelectron spectra of ThO_2^- ($\text{ThO}_2/{}^1\text{A}_1 \leftarrow \text{ThO}_2/{}^2\text{A}_1$) at the CCSD(T)/aug-cc-pVTZ level at 300 K with full width at half maximum of 5 cm^{-1} (blue) and 400 cm^{-1} (red). The transition energy is shown in eV relative to that of the 0-0 transition	89
5.1.	Optimized structures of $[\text{UO}_2(\text{H}_2\text{PO}_4)_n(\text{H}_2\text{O})_m]^{z\pm}$	132
5.2.	Optimized structures of $[\text{UO}_2(\text{HPO}_4)_n(\text{H}_2\text{O})_m]^{z-}$	134
5.3.	Optimized structures of $[\text{UO}_2(\text{PO}_4)_n(\text{H}_2\text{O})_m]^{z-}$	136
5.4.	Optimized structures of $[\text{H}_n\text{PO}_4(\text{H}_2\text{O})_4]^{z-}$	138
5.5.	Phosphoric acid $\text{pK}_{\text{a,s}}$ for the 1 st , 2 nd , and 3 rd ($n = 1, 2, 3$) deprotonations of H_3PO_4 geometries optimized at the B3LYP/DZVP2, with single point energies at the MP2/Aug-cc-pVnZ ($n = \text{D, T, and Q}$) levels. pK_{a} 's calculated from the gas phase values at each level plus single point B3LYP/DZVP2 CPCM with COSMO-RS radii SCRf calculations. Experimental data from reference 107	139
6.1.	Lewis dot structures for the selenium fluorides, oxides and oxofluorides of SeF_n ($n=2-6$) $^{+,0,-}$, SeOF_n ($n=0-4$) $^{+,0,-}$, and SeO_2F_n ($n=0-2$) $^{+,0,-}$ molecules.....	200
6.2.	Heats of formation and the reaction enthalpies for the addition of F^+ , F , and F^- at 298 K as well as ionization potentials ($-e^-$) and electron affinities ($+e^-$) of SeOF_n . All values in kcal/mol. Heats of formation are given below each species <i>in italics</i> . Vertical arrows correspond to the addition of F to SeOF_n to form SeOF_{n+1} for the cation, neutral, and anion. Horizontal arrows to the left correspond to fluoride anion affinities. Horizontal arrows to the left correspond to the fluorocation affinities. Horizontal arrows to the right correspond to fluoride anion affinities. Diagonal arrows to the left correspond to the ionization potential ($-e^-$). Diagonal arrows to the right correspond to the electron affinity ($+e^-$). The heat of formation of F^- at 298 K is -59.5 kcal/mol using the electron affinity of F . ⁴⁹	203

- 6.3. Heats of formation and the reaction enthalpies for the addition of F^+ , F , and F^- at 298 K as well as ionization potentials ($-e^-$) and electron affinities ($+e^-$) of SeO_2F_n . All values in kcal/mol. Heats of formation are indicated below each species *in italics*. Vertical arrows correspond to the addition of F to SeO_2F_n to form SeO_2F_{n+1} in terms of the cation, neutral, and anion. Horizontal arrows to the left correspond to the fluorocation affinities. Horizontal arrows to the right correspond to fluoride anion affinities. Diagonal arrows to the left correspond to the ionization potential ($-e^-$). Diagonal arrows to the right correspond to the electron affinity ($+e^-$).....204
- 6.4. Heats of formation and the reaction enthalpies for the addition of F^+ , F , and F^- at 298 K as well as ionization potentials ($-e^-$) and electron affinities ($+e^-$) of SeF_n . All values in kcal/mol. Heats of formation are indicated below each species *in italics*. Vertical arrows correspond to the addition of F to SeF_n to form SeF_{n+1} in terms of the cation, neutral, and anion. Horizontal arrows to the left correspond to fluoride anion affinities. Horizontal arrows to the left correspond to the fluorocation affinities. Horizontal arrows to the right correspond to fluoride anion affinities. Diagonal arrows to the left correspond to the ionization potential ($-e^-$). Diagonal arrows to the right correspond to the electron affinity ($+e^-$).....205
- 6.5. Heats of formation and reaction enthalpies for the addition of an F to SeF_n to form SeF_{n+1} , O to SeF_n to form $SeOF_n$, F to $SeOF_n$ to form $SeOF_{n+1}$ and O to SeO_2F_n to form SeO_3F_n at 298 K in kcal/mol. Heats of formation are indicated below each molecule *in italics*. Vertical arrows correspond to the addition of F to SeF_n or $SeOF_n$ to form SeF_{n+1} or $SeOF_{n+1}$. Horizontal arrows to the right correspond to the addition of O to SeF_n , $SeOF_n$ or SeO_2F_n to form $SeOF_n$, SeO_2F_n and SeO_3F_n respectively.....206

CHAPTER 1

INTRODUCTION

The actinide series consist of the heavy elements with atomic numbers 90 to 103 with chemistry dominated by the role of the $5f$ orbitals. All of the actinides have radioactive isotopes, in many cases with short lifetimes making experimental work difficult. Only thorium, protactinium and uranium are naturally occurring and prior to 1940 were the only known actinides. The remaining actinide elements have been synthesized in nuclear reactors. The actinides have a wide range of oxidation numbers which makes their chemistry interesting and complex.^{1,2}

The actinides play a key role in alternative energy scenarios as they are the fuel for nuclear reactors to produce electricity. Optimal fuel designs and the management of the waste from the nuclear plants require an improved understanding of their chemistry. The usual fuel for a fission based nuclear reactor is uranium and its chemistry has been extensively studied. Thorium oxides have been considered as potential nuclear fuels for the nuclear power industry, although their applications in this area are quite limited compared with the more widely used uranium and uranium-plutonium oxide materials. The use of thorium oxides in the nuclear fuel cycle has attracted attention, especially in India and Canada due to their mineral resources of thorium and the different non-proliferation issues of the spent fuel from thorium reactors.

Besides their use as nuclear reactor fuels, the actinides form the core of nuclear weapons. The United States and the Soviet Union produced thousands of nuclear warheads during the Cold War arms race. During this time the United States developed a large nuclear complex for the research, manufacture, and testing of nuclear materials and bombs. Sixteen major facilities grew out of this complex and were scattered across the United States with large facilities in Washington, Nevada, Tennessee, South Carolina, New Mexico, and Idaho.³ Approximately 120 tons of plutonium were used to manufacture over 20,000 warheads. The uranium fuel was exposed to neutrons in a reactor and reprocessed in chemical plants at the Hanford Site in Washington, and the Savannah River Site near Aiken, South Carolina. Weapons production was more important than waste management during the Cold War leading to the creation of substantial amounts of highly radioactive waste.³ This radioactive waste is stored in underground tanks: 177 at the Hanford site (WA), 51 at the Savannah River site (SC), 34 at Oak Ridge (TN), 11 at the Idaho National Engineering and Environmental Laboratory (ID), and 2 tanks at West Valley (NY). These operations created large volumes of waste that were piped to structures such as storage tanks, repackaged, or released into the environment, often in the presence of other chemicals.³

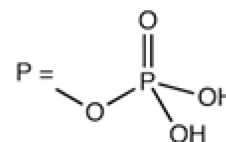
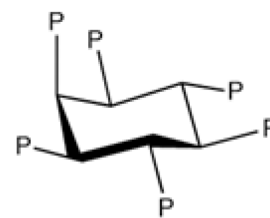
Today, these sites are the focus of the world's largest environmental cleanup effort managed by the U.S. Department of Energy (DOE), with many challenges to be resolved in the face of overlapping technical, political, regulatory, and cultural (especially Native American) interests. The cleanup effort at the Hanford Site, for example, is focused on restoring the Columbia River corridor for other uses, and converting the central plateau to long-term waste treatment and storage.⁴ In recent years, the federal government has spent about \$2 billion

annually on the Hanford project,⁵ and about 11,000 workers are on site to consolidate, clean up, and mitigate waste, contaminated buildings, and contaminated soil.⁶

Phosphates and their derivatives ((RO)₃PO), R = H, alkyl, phenyl) form one of the most important classes of ligands in actinide chemistry. Historically, phosphates played a crucial role in the efforts of the United States to separate various actinide species from irradiated fuels during the Manhattan Project. For example, the first large-scale process used to separate plutonium from uranium and fission products was the bismuth phosphate (BiPO₄) process. The BiPO₄ process was ultimately replaced by a process involving another phosphate, tri(*n*-butyl)phosphate (TBP), which is considered to be the most important reagent in all of actinide separations. TBP is the main ingredient in the PUREX (Plutonium and Uranium Recovery by EXtraction) process, normally as a 30% solution in a paraffinic hydrocarbon. The TBP-PUREX process is the primary tool for nuclear fuel reprocessing in the U.S. and around the world today. Many other tailored phosphorus-based (mainly organophosphorus) ligands and extractant

molecules exist and have been studied for their selective extraction abilities. The neutralization of wastes from the BiPO₄ process in the Hanford tanks led to the formation of actinide phosphate solids such as NaUO₂PO₄, which have low to negligible solubility under aqueous conditions, are resistant to intense radiation fields and radiolysis, and are very stable. *In situ* phosphate barriers for the immobilization of actinides

have been proposed. For example, a water-soluble organophosphate compound such as phytic acid is introduced into the soil. The acid ligand forms a complex with actinide ions and then hydrolyzes to form actinide phosphate minerals. Biological organisms can accumulate and precipitate a wide variety of metal ions from the environment, including uranyl ions. It was



Phytic acid

determined that uranium binding primarily occurs at the phosphoryl residues on the cell walls of Gram-positive residues from *Bacillus cereus* and *Bacillus sphaericus* cells and spores. It was suggested that lipopolysacharides and phospholipids within the bacterial cell wall can also provide phosphoryl groups for metal ion binding.

There is significant interest in the thermochemical properties including bond dissociation energies (BDEs) of compounds of the main group elements of the second- and higher-rows. The Dixon group has previously performed extensive computational studies on sulfur oxyfluorides, iodofluorides, and rare gas halides as well halogen oxides. Selenium is found in a number of minerals and plays a role in a number of technologies. Se is in the active site of the enzymes glutathione peroxidase and thioredoxin reductase and most animals require trace amount of Se. Compounds containing selenium are pollutants and are used in chemical vapor deposition (CVD) for the synthesis and doping of semiconductor materials.

1.1 Computational methods

In 1926, Erwin Schrödinger provided a mathematical foundation of quantum mechanics in the form of an eigenvalue problem leading to the Schrödinger equation. The time dependent Schrödinger equation (1),

$$i\hbar \frac{\partial}{\partial t} \Psi = \hat{H} \Psi \quad (1)$$

where \hbar is Planck's constant divided by 2π , Ψ is the wave function (eigenfunction), and \hat{H} , the Hamiltonian operator which corresponds to the total energy of the system, is a partial differential equation which describes how the quantum state of a physical system evolves with time. The time-independent, non-relativistic Schrödinger equation (2),

$$\hat{H} \Psi = E \Psi \quad (2)$$

where the eigenvalues of the Hamiltonian are represented by E , the system's total energy, is used to solve for stationary states of the particles. The electronic Hamiltonian can be written in atomic units as (3)

$$\hat{H} = -\frac{1}{2}\sum_i \nabla_i^2 - \sum_{iA} \frac{Z_A}{|R_A - r_i|} + \sum_{i < j} \frac{1}{|r_i - r_j|} \quad (3)$$

where the first term represents the kinetic energy, the second term is the nuclear-electron attraction energy, and the third term denotes the electron-electron repulsion energy. ∇^2 is the Laplace operator, a second order differential operator of the coordinates, Z is the atomic number, R and r are the respective coordinates for the nuclei and electrons, the subscript A designates different nuclei, and the subscripts i and j represent different electrons. The Schrödinger equation for electronic motion can be solved analytically for a chemical system that contains one electron and one nucleus, H or He^+ for example. Approximations must be applied to solve for the stationary states of atoms and molecules with more than the one electron. Using the time independent Schrödinger equation to solve for the energy and the wavefunction of a molecule is a challenging task. The first approximation is the Born–Oppenheimer (BO) approximation which separates the wavefunction of a molecule into its nuclear (rotational, vibrational) and electronic degrees of freedom. This approximation can be made because the electron is 1836^7 times less massive than the proton, so the electrons can be treated as moving about a set of fixed nuclei.

The Schrödinger equation can be approximately solved using the self-consistent field (SCF) Hartree-Fock (HF) method,^{8,9,10} which has several approximations that include: (a) the neglect of relativistic effects, (b) the use of a finite basis set, (c) the total wave functions are the products of one-electron wave functions, and (d) the energy of an electron is solved for in the average field of the remaining $n-1$ electrons. The classical repulsion between two individual electrons leads to a cusp so the correlations between electrons is neglected in the last

approximation. In the HF theory, the n -electron wavefunction (Φ_0) is constructed as the product of n one-electron molecular orbitals where the proper Fermi-Dirac statistics (antisymmetry for an electron) are accounted for by the use of a Slater determinant (4).

$$|\Phi_0\rangle = |\phi_1(1)\phi_2(2)\dots\phi_n(n)\rangle \quad (4)$$

Here the molecular orbitals are constructed as linear combinations of a finite number of atom-centered basis functions (X_α), generally in the form of Gaussian functions (GTFs)⁷ or contracted GTFs. Gaussian functions are used because the two electron integrals can be solved for analytically.

$$\phi_i = \sum_{\alpha} c_{i\alpha} X_{\alpha} \quad (5)$$

The HF equations are transformed into the form of the Roothan-Hall equation^{11,12} for closed shell systems and the coefficients, $c_{i\alpha}$, are treated as variational parameters. These equations are solved using a self-consistent field (SCF) field approach to give the energy and wavefunction for a molecule.

The HF approach is a mean field method and is missing the correlation energy. The correlation energy (E_{corr}) is defined as the difference between the HF energy (E_{HF}) and the exact energy (E_{exact}). Even though the E_{corr} is usually a small percentage, approximately 1%, it is crucial for the accurate evaluation of the energetic properties of molecules and reactions. Approximations for the correlation energy considerably increase the computational cost. Examples of such correlation corrections to Hartree-Fock energies are Møller-Plesset (MP) perturbation theory, coupled cluster (CC) theory, configuration interaction, and multi-reference methods.

The simplest post-HF method is Møller-Plesset (MP) perturbation theory,^{13,14} abbreviated MP_n , where n is the highest order term used in the perturbative expansion. In MP_n

theory, the Hamiltonian (\hat{H}) is split into an unperturbed term (\hat{H}_0) and a perturbation term (\hat{V}) as in equation (6)

$$\hat{H} = \hat{H}_0 + \lambda \hat{V} \quad (6)$$

where λ is a dimensionless perturbation coefficient. The second order Möller-Plesset perturbation theory, or MP2, is the simplest treatment of electron correlation. The second order energy can be written as equation (7)

$$\sum_{\substack{i < j \\ a < b}} E_0^2 = \sum_{\substack{i < j \\ a < b}} \frac{\left| \left\langle \Phi_0 \left| \sum_{i < j} r_{ij}^{-1} \right| \Phi_{ij}^{ab} \right\rangle \right|^2}{\varepsilon_i + \varepsilon_j - \varepsilon_a - \varepsilon_b} \quad (7)$$

where the subscripts i and j correspond to the occupied MOs, a and b correspond to the virtual MOs, and ε are the respective orbital energies. MP2 scales as N^5 , where N is the number of basis functions due to the need to transform the two electron integrals in the atomic orbital basis to the molecular orbitals and recovers $\sim 80\%$ of E_{corr} . This form of perturbation does not converge quickly and the results can oscillate at higher orders.

Coupled-cluster (CC) methods^{15,16,17,18} generate the correlated wavefunction using an exponential operator, as shown in equation (8)

$$|\Phi_{\text{CC}}\rangle = e^T |\Phi_0\rangle \quad (8)$$

where T is the cluster operator and Φ_0 is the reference wavefunction, usually the HF wavefunction. The cluster operator \hat{T} takes the form of equation (9)

$$\hat{T} \equiv \hat{T}_1 + \hat{T}_2 + \hat{T}_3 + \dots + \hat{T}_n \quad (9)$$

where n describes a specific degree of excitation, i.e., Singles ($n = 1$), Doubles ($n = 2$), Triples ($n = 3$), etc. The CC equations are solved projectively, rather than variationally, due to their complexity, and when truncated, they are completely size consistent/extensive. A full treatment

of triple excitation in CC calculations (CCSDT) scales as an iterative N^8 for N basis functions. The triples correction is usually evaluated perturbatively, giving the CCSD(T) method, which scales as N^7 . The truncated coupled-cluster approach is superior to a truncated configuration interaction (CI) approach that is solved variationally.^{19,20,21} The CI operators are identical to the cluster operators giving the same result in the limit of all excitations, a full configuration interaction calculation. Within the CI framework, however excitations enter in a linear fashion, rather than exponentially, and as a result upon truncation, result in energies which are not size consistent/extensive with the exception of full CI.

An alternative to molecular orbital theory is density functional theory (DFT). The DFT method, as outlined in seminal papers by Hohenberg and Kohn²² and Kohn and Sham,²³ naturally incorporates electron correlation into its equations. DFT proposes that the electron density (ρ), rather than the complex $3n$ dimensional wavefunction, can be used to determine the ground state energy of a system. The energy is a functional of the electron density and within the Kohn-Sham scheme, is written as equation (10)

$$E[\rho] = T_s[\rho] + V_{\text{ext}}[\rho] + V_H[\rho] + E_{xc}[\rho] \quad (10)$$

where T_s is the kinetic energy, E_{ext} is the electronic-nuclear external potential energy, E_H is the Hartree (Coulomb) interaction energy, and E_{xc} is the exchange-correlation energy. The resulting equations are similar to the HF equations and must be solved by the SCF method. Unlike the HF theory, DFT is an exact theory, provided E_{xc} as a function of ρ is explicitly known. However, this functional is not known and the theory behind it is still being developed. There are a variety of functionals, including local which depend only on the electron density, and non-local which depend on the electron density and its gradient, explicitly, the generalized gradient approximation (GGA) functionals). One of the popular functionals, B3LYP,^{24,25} which will be

used widely throughout this work, is a hybrid functional and contains a component of HF exchange.

1.2 Prediction of the Vibrational Frequencies of UO_2^{2+} at the CCSD(T) Level

There is substantial interest in the behavior of the uranyl dication due to the role that it plays in many different technological regimes from energy production to waste storage. Vibrational spectroscopy of uranyl is being used to determine the types of ligands bonded to uranyl as well as the effect of the ligand on the uranyl frequencies. One issue is that there are no direct measurements of the vibrational spectra of the isolated ion. Electronic structure calculations at the coupled cluster (CCSD(T)) and density functional theory levels with relativistic effective core potentials and large basis sets have been used to predict the isolated uranyl ion frequencies to provide a benchmark for other computational methods and so that experimentalists have a value for the isolated ion against which to gauge substituent effects. The effects of anharmonicity and spin-orbit corrections on the harmonic frequencies were included. Because, ThO_2 can be synthesized and has been observed in a rare gas matrix, the anharmonic vibrational frequencies of the isoelectronic ThO_2 molecule were calculated and compared to experiment in order to calibrate the UO_2^{2+} results. The ThO_2 calculations were performed before the experimental results for ThO_2 were available.

1.3 Matrix Infrared Spectra and Theoretical Studies of Thorium Oxide Species: ThO_x and Th_2O_y

The properties of bulk thorium oxides are well-known because of their roles in reactor technologies, but the properties of small thorium oxide molecular clusters are not well-understood. In order to remedy this situation, a study of reactions of laser-ablated thorium atoms and O_2 using matrix isolation infrared spectroscopy was undertaken at the University of Virginia

in the group of Prof. L. Andrews jointly with our computational study of small thorium oxide clusters. The results of high level correlated molecular orbital theory and DFT calculations were used to assign the vibrational spectra, provide molecular structures, and predict reaction energies. The Th₂O₄ and Th₂O₂ molecules were studied as they can be regarded as potential basic building blocks for the synthesis and construction of bulk thorium oxides.

1.4 Methane to Methanol Conversion Induced by Thorium Oxide through the CH₃Th(O)H Intermediate in Solid Argon

Methane activation is of broad interest due its availability in natural gas and the difficulty in activating the C-H bond. Although reactions of neutral transition metal oxide molecules and methane have been systematically studied under matrix isolation conditions, no investigation has been carried out on the reactivity of neutral actinide oxide species, even though the role of actinide elements in catalytic reactions is of interest. Reactions of ThO molecules and CH₄ have been investigated in solid argon near 4 K at the University of Virginia in the group of Prof. L. Andrews. In conjunction with the experimental effort, we used high level correlated molecular orbital theory and DFT calculations to map out the potential energy surface for the reaction of ThO + CH₄ → Th + CH₃OH. This aided in the identification of the novel intermediate CH₃Th(O)H. This work is the first high level CCSD(T) mapping of a potential energy surface for the reaction of actinides that we are aware of.

1.5 Density Functional Theory Study of the Complexation of the Uranyl Dication with Anionic Phosphate Ligands with and without Water Molecules

Details about the binding modes and energetics of phosphate-uranyl complexes are important for developing thermodynamic and kinetic models that can be used to understand mobility versus immobilization in tank wastes and the environment, as well as stability concerns

for waste matrices and their role in bioremediation and bio-transport. For this reason, a detailed computational study of the structures and energetics of anhydrous and hydrated complexes of UO_2^{2+} with the phosphate anions H_2PO_4^- , HPO_4^{2-} , and PO_4^{3-} at the density functional theory (DFT) and MP2 molecular orbital theory levels as isolated gas phase species and in aqueous solution by using self-consistent reaction field (SCRF) calculations with different solvation models was undertaken. The geometries, and vibrational frequencies of the major binding modes for these complexes are compared to experiment where possible. The SCRF calculations with the CPCM, IEF-PCM and IPCM models/parameterizations have been used to predict the behavior of these complexes in solution to investigate the thermodynamics of binding, and the equilibrium constants for the reactions of UO_2^{2+} with phosphate and water ligands. A set of benchmark calculations on the acidities of phosphoric acid and of uranyl/phosphate complexation was done to study the type of SCRF approach to use and types of reactions to be used.

1.6 Thermochemical Properties of Selenium Fluorides, Oxides, and Oxofluorides

To extend our knowledge of the properties of Se compounds and to further our knowledge of the bonding in main group compounds, the heats of formation, bond dissociation energies (BDEs), fluoride and fluorocation affinities, and electron affinities of SeF_n ($n=1-6$), SeOF_n ($n=0-4$), and SeO_2F_n ($n=0-2$) have been predicted with coupled cluster CCSD(T) theory extrapolated to the complete basis set limit. To achieve near chemical accuracy, additional corrections were added to the complete basis set binding energies based on frozen core coupled cluster theory energies. These included corrections for core-valence effects, scalar relativistic effects, for first-order atomic spin-orbit effects, and vibrational zero point energies. The adiabatic and diabatic BDEs were calculated to compare them. For thermochemical calculations, the adiabatic values must be used, whereas for bond strength and kinetic considerations, the diabatic

values should be used when only small displacements of the atoms without change of the geometry of the molecule are involved. The basic science interest in these molecules arises from the fact that many of them possess both a Se free valence electron pair and a free unpaired valence electron, raising the questions of their preferred location and their influence on the Se-F and Se=O bond strengths.

References

- ¹ Konigs, R. J. M.; Morss, L. R.; Fuger, J. *The Chemistry of the Actinide and Transactinide Elements*, 3rd Ed.; Springer: Dordrecht, the Netherlands, 2006; Vol. 4, Chapter 19, pp 2113–2224.
- ² Cotton, S. *Lanthanide and Actinide Chemistry*. Chichester, England; Hoboken, NJ: Wiley, 2006.
- ³ Gephart, R. E.; Lundgren, R. E. *Hanford Tank Cleanup: A Guide to Understanding the Technical Issues*. Battelle Press: Columbus, 1998.
- ⁴ *Hanford Site Tour Script*. United States Department of Energy. October 2007. Archived from the original on February 27, 2008. Retrieved January 29, 2007.
- ⁵ Stiffler, L. (March 20, 2008). "Troubled Hanford cleanup has state mulling lawsuit". Seattle Post-Intelligencer. Retrieved May 8, 2008.
- ⁶ *Hanford Quick Facts*. Washington Department of Ecology. Archived from the original on June 24, 2008. Retrieved January 19, 2010.
- ⁷ Levie, I. N. *Physical Chemistry*, 4th ed.; McGraw-Hill: New York, 1995.
- ⁸ Hartree, D. R. The Wave Mechanics of an Atom with a Non-Coulomb Central Field. Part I - Theory and Methods. *Proc. Camb. Phill. Soc.* **1928**, 24, 89-110.
- ⁹ Hartree, D. R. The Wave Mechanics of an Atom with a Non-Coulomb Central Field. Part II - Results and Discussion *Proc. Camb. Phill. Soc.* **1928**, 24, 111-132.
- ¹⁰ Fock, V. Self-Consistent Field with Exchange for Sodium. *Zeitschrift fuer Physik* **1930**, 62, 795-805.
- ¹¹ Roothan, C. C. New Developments in Molecular Orbital Theory. *J. Rev. Mod. Phys.* **1951**, 23, 69-89.
- ¹² Hall, G. G. The Molecular Orbital Theory of Chemical Valency. VIII. A Method of Calculating Ionization Potentials. *Proc. R. Soc. Lond. A* **1951**, 205, 541-552.
- ¹³ Möller, C.; Plesset, M. S. Note on an Approximation Treatment for Many-Electron Systems. *Phys. Rev.* **1934**, 46, 618-622.
- ¹⁴ Pople J. A., Binkley J. S. and Seeger R. Theoretical Models Incorporating Electron Correlation. *Int. J. Quantum Chem. Symp.* **1976**, 10, 1–19.
- ¹⁵ Purvis, G. D. III; Bartlett, R. J. A Full Coupled-Cluster Singles and Doubles Model: The Inclusion of Disconnected Triples. *J. Chem. Phys.* **1982**, 76, 1910-1918.

-
- ¹⁶ Raghavachari, K.; Trucks, G. W.; Pople, J. A.; Head-Gordon, M. A Fifth-Order Perturbation Comparison of Electron Correlation Theories. *Chem. Phys. Lett.* **1989**, *157*, 479-483.
- ¹⁷ Watts, J. D.; Gauss, J.; Bartlett, R. J. Coupled-Cluster Methods with Noniterative Triple Excitations for Restricted Open-Shell Hartree-Fock and other General Single Determinant Reference Functions. Energies and Analytical Gradient. *J. Chem. Phys.* **1993**, *98*, 8718-8733.
- ¹⁸ Bartlett, R. J.; Musial, M. Coupled-Cluster Theory in Quantum Chemistry. *Rev. Mod. Phys.* **2007**, *79*, 291-352.
- ¹⁹ Löwdin, P.-O. Quantum Theory of Many-Particle Systems. I. Physical Interpretations by Means of Density Matrices, Natural Spin-Orbitals, and Convergence Problems in the Method of Configurational Interaction *Phys. Rev.* **1955**, *97*, 1474-1489.
- ²⁰ Krishnan, R.; Schlegel, H. B.; Pople, J. A. Derivative Studies in Configuration-Interaction Theory. *J. Phys. Chem.* **1980**, *72*, 4654-4655.
- ²¹ Pople, J. A.; Seeger, R.; Krishnan, R. Variational Configuration Interaction Methods and Comparison with Perturbation Theory. *Int. J. Quantum Chem. Symp.* **1977**, *S11*, 149-163.
- ²² Hohenberg, P.; Kohn, W. Inhomogeneous Electron Gas. *Phys. Rev. B* **1964**, *136*, 864-871.
- ²³ Kohn, W.; Sham, L. Self-Consistent Equations Including Exchange and Correlation Effects. *J. Phys. Rev. A* **1965**, *140*, 1133-1138.
- ²⁴ Becke, A. D. Density-Functional Thermochemistry. III. The Role of Exact Exchange. *J. Chem. Phys.* **1993**, *98*, 5648-5652.
- ²⁵ Lee, C.; Yang, W.; Parr, R. G. Development of the Colle-Salvetti Correlation-Energy Formula into a Functional of the Electron Density. *Phys. Rev. B* **1988**, *37*, 785-789.

CHAPTER 2

PREDICTION OF THE VIBRATIONAL FREQUENCIES OF UO_2^{2+} AT THE CCSD(T) LEVEL

From Jackson, V. E.; Craciun, R.; Dixon, D. A.; Peterson, K. A.; de Jong, W. A. *J. Phys. Chem. A* **2008**, *112*, 4095-4099.

2.1 Introduction

There is substantial interest in the behavior of the uranyl dication due to the role that it plays in many different technological regimes from energy production to waste storage. Vibrational spectroscopy of uranyl has been used to determine the types of ligands bonded to uranyl as well as the effect of the ligand on the uranyl frequencies. One issue is that there are no direct measurements of the vibrational spectra of the isolated ion. There have been many measurements, however, of the spectra of the ion in solution when complexed to different ligands.^{1,2,3,4,5,6,7,8,9,10,11} More recently, the spectra of complexes of uranyl with different ligands were observed in the gas phase through a combination of electrospray ionization, Fourier transform ion cyclotron resonance mass spectrometry (FT-ICR-MS), and infrared multiphoton dissociation using the FELIX free electron laser. The combination of these techniques has enabled the spectra of uranyl complexed to acetone and acetonitrile as well as other ligands to be measured.¹²

At the same time as the advances in experimental techniques, there was a comparable advance in electronic structure methods for the treatment of actinides. Until recently, computational studies of heavy elements, particularly actinides, were

challenging because of the large number of electrons and the importance of relativistic effects. However, with the development of density functional methods and relativistic effective core potentials, the treatment of actinide-containing complexes has become more routine and the results more reliable.^{13,14,15,16,17} There have been numerous studies of uranyl complexation with ubiquitous ligands such as H₂O, NO₃⁻, CO₃²⁻, and the halides.^{13,14,15,16,18,19}

An important issue for understanding as to how ligands affect the vibrational spectrum of the ion is the value of each of the three vibrational frequencies that describe isolated uranyl. The critical frequencies for comparison with experiment are the symmetric and asymmetric stretches, and improved values are needed for the harmonic value and the fundamental including the role of anharmonicity. Although a number of computational studies previously were performed, we focus on three studies with the results summarized in Table 1. de Jong and coworkers²⁰ performed benchmark calculations on UO₂²⁺ at a variety of levels. The largest calculations were performed at the Dirac-Hartree-Fock plus coupled cluster single and double excitations plus a perturbative correction for triples (CCSD(T)) level^{21,22,23,24} with the U(6s, 6p, 6d, 5f) electrons correlated as well as the O(2s, 2p) electrons. In addition, these workers studied the use of density functional theory (DFT) with the local and B3LYP exchange-correlation functionals in combination with different effective core potentials (ECP) and basis sets. Gagliardi and Roos²⁵ performed complete active space plus second-order perturbation theory (CASPT2) calculations on the frequencies of UO₂²⁺. The CAS was a (12/12) calculation. They used the Stuttgart ECP and basis set for U without g functions^{26,27} and the ANO-s (4s3p2d)²⁸ and ANO-L (4s3p2d1f) basis functions on O.²⁹

They also reported results for the B3LYP functional with the 6-311G** basis set on O. Clavaguéra-Sarrio et. al.³⁰ studied the use of different exchange-correlation functionals in combination with the small core Stuttgart pseudo-potential for uranium and a polarized double- ζ plus diffuse function basis set for oxygen with the 1s electrons treated by a pseudo-potential.³¹ Of interest to our study is the fact that they predicted the anharmonic contributions to UO_2^{2+} with the B3LYP functional.

The vibrational spectrum of the isoelectronic neutral ThO_2 molecule was observed in both Ar^{32,33} and Ne³⁴ matrices, and two stretches were observed, confirming that the molecule was bent. Thus, ThO_2 can serve as an additional benchmark of the computational approach.

2.2 *Calculations*

The current CCSD(T) calculations were performed with the program system MOLPRO 2006.1³⁵ on the University of Alabama Opteron-based Parallel Quantum Solutions Linux cluster computer. As in the previous calculations by de Jong et al., we correlated 24 valence electrons in the CCSD(T) calculations. We used the small core RECP and spin-orbit potential from the Stuttgart group with the associated basis set on U augmented by 2 g functions [8s, 7p, 6d, 4f, 2g]^{14,19,26,36} (g exponents = 0.42 and 1.18) and the aug-cc-pVTZ [5s, 4p, 3d, 2f] on O.³⁷ We label this basis set as aVTZ(1). We calculated the CCSD(T) energies (30 symmetry-unique points) on a three-dimensional grid in terms of the bond lengths and bond angles. These energies were fit to polynomials in displacement coordinates, and the resulting full quartic force field (with selected quintic contributions) was used in the program SURFIT³⁸ to calculate the harmonic frequencies and anharmonic corrections from the usual second-order perturbation theory

expressions.³⁹ Additional CCSD(T) calculations on this same three-dimensional grid also were carried out with the newer segmented basis set for U of the form (14s,13p,10d,8f,6g)/[10s,9p,5d,4f,3g] and the aVTZ basis on O.^{26,27} We label this basis set as aVTZ(2). Two additional grids were calculated by adding a set of two optimized *h* functions (exponents = 1.7696, 0.7134) and a set of *i* functions (exponent = 1.2525) to the U basis set (optimized for the ⁵I 5f⁴ state of U in averaged coupled pair functional calculations), both for our original [8s, 7p, 6d, 4f, 2g] set and the newer [10s,9p,5d,4f,3g] basis set, with the aVQZ basis set on O. These basis sets were labeled as aVQZ(1) and aVQZ(2) respectively. To calibrate the uranyl ion calculations, analogous calculations on ThO₂ also were carried out at the CCSD(T) level with the aVTZ(2) basis set. These latter calculations involved a grid with a total of 47 symmetry-unique geometries.

DFT calculations also were carried out with the previous basis set with the B3LYP exchange-correlation functional^{40,41} with the programs Gaussian03⁴² and NWChem.^{43,44} Two-component spin-orbit relativistic ECP DFT calculations,⁴⁵ with the appropriate Stuttgart one-electron spin-orbit potentials included variationally, were performed with NWChem.

2.3 *Results and Discussion*

The calculated harmonic frequencies are given in Table 1, and the anharmonic fundamentals are shown in Table 2. The anharmonicity constants are explicitly shown in Table 3.

The harmonic frequencies exhibit interesting behavior. Our calculated asymmetric stretch is predicted to be 1108 cm⁻¹ at the CCSD(T)/aVTZ(1) level. This can be compared to the value of 1121 cm⁻¹ calculated at the DHF + CCSD(T) level of theory. The

difference of 13 cm^{-1} is within the differences expected due to the use of different basis sets and the different treatment of the relativity. What is of interest is that the bond distance does not correlate exactly with the harmonic frequency. The longer bond distance obtained at the DHF + CCSD(T) level has a higher asymmetric stretching frequency than the calculation with the shorter bond distance at the CCSD(T)/aVTZ(1) level. The symmetric stretch is, however, smaller in the former case. A similar result was found by Gagliardi and Roos²⁵ who added f functions to the O atom and obtained a shorter bond distance by 0.009 \AA and a surprising decrease in the asymmetric stretch frequency of 87 cm^{-1} . The effect of the (T) correction is essentially the same for the DHF-CCSD(T) and ECP-CCSD(T) calculations, a lowering of 65 cm^{-1} in the former and of 67 cm^{-1} in the latter.

The behavior of the symmetric stretching frequency, which lies below the asymmetric stretch, shows a larger variation on the electronic structure method than does the asymmetric stretch. In particular, the difference between the symmetric and asymmetric stretch varies depending on the method. At the CASPT2 level, the difference is $\sim 110\text{ cm}^{-1}$ and is not strongly dependent on the basis set, even though the individual frequencies are very sensitive. At the DHF level, the difference is $\sim 145\text{ cm}^{-1}$ at the CCSD and CCSD(T) levels. With the aVTZ(1) basis set, we find a difference of 83 cm^{-1} at the CCSD level and 89 cm^{-1} at the CCSD(T) level. The different B3LYP values range from 90 to 100 cm^{-1} . Thus, all of the differences obtained with an ECP-based approach fall in the range of 80 to 110 cm^{-1} . Within a given approach, the symmetric stretch does depend on the U=O bond distance but different methods can give quite different symmetric stretches at the same bond distance. For example, the CASPT2/ANO-s calculation

predicts a bond distance of 1.714 Å and a symmetric stretch of 1043 cm⁻¹ as compared to the DHF-CCSD(T) value of 974 cm⁻¹ at a bond distance of 1.715 Å. Similarly, the CASPT2/ANO-L calculation predicts a bond distance of 1.705 Å and a frequency of 959 cm⁻¹, whereas the B3LYP value of the frequency at the same bond distance is 1041 cm⁻¹.

The bending frequency ranges from 160 to 200 cm⁻¹, and all of the methods where the bends are reported predict a linear structure. We note that the CCSD(T)/aVTZ(1) results predict a bending frequency that is 13 cm⁻¹ higher than the DHF + CCSD(T) value.

We next estimated the spin-orbit correction for the harmonic frequency at the spin-orbit DFT level. The calculations were performed with the B3LYP exchange-correlation functional and the same basis set and ECP as used for the CCSD(T)/aVTZ(1) calculations. The bending frequency was very sensitive to both the geometry and energy convergence in these calculations since it was calculated numerically. Hence, very tight convergence thresholds were required for all of the computational parameters including the integrals. The effect of the spin-orbit was to increase the asymmetric stretch by 1.6 cm⁻¹ and to increase the symmetric stretch by more than double this amount, 3.5 cm⁻¹. The effect of the spin-orbit on the bend was to decrease the frequency by just 2.9 cm⁻¹. Thus, spin-orbit effects on the harmonic frequencies are small. Rösch and co-workers⁴⁶ reported that the spin-orbit correction at the DFT level⁴⁷ with gradient corrected functionals is small, -3 cm⁻¹, and opposite to the direction we found.

The calculated fundamental frequencies (i.e., including anharmonic effects) are shown in Table 2, and the associated anharmonicity constants X_{ij} are given in Table 3. The latter are all relatively small and negative, indicating only small overall effects due to

vibrational anharmonicity. The asymmetric stretch was calculated to decrease by just 7.8 cm^{-1} on incorporation of anharmonic effects at the CCSD(T)/aVTZ(1) level. The symmetric stretch has a slightly smaller change of 6.6 cm^{-1} at the same level of theory. The bend is predicted to decrease by only 0.9 cm^{-1} at the CCSD(T)/aVTZ(1) level. Essentially the same changes are predicted at the CCSD/aVTZ(1) level of theory, and these small effects are borne out by the small calculated anharmonicity constants. The anharmonic effects at the B3LYP level³⁰ for the two stretches are comparable to the CCSD(T)/aVTZ(1) and CCSD/aVTZ(1) values. The B3LYP functional³⁰ surprisingly predicts the bend to increase by 8-9 cm^{-1} upon inclusion of anharmonic effects. This could, perhaps, be due to the sensitivity of the bending frequency to the computational convergence parameters in the DFT calculations. Overall, the anharmonic effects on the two UO_2^{2+} stretching modes are less than 10 cm^{-1} , so comparison of calculated harmonic values to experimental fundamentals would be expected to produce agreement to within about 10 cm^{-1} if the harmonic values are exactly predicted.

We next improved the quality of the basis set to aVTZ(2). The asymmetric stretching fundamental increased by $\sim 11 \text{ cm}^{-1}$, and the symmetric stretching fundamental increased by $\sim 8 \text{ cm}^{-1}$, both consistent with the bond distance slightly decreasing. The fundamental bend also was predicted to increase. The addition of the *2h* and *i* functions to aVTZ(1) led to a shortening of the U-O bond distance as expected and an increase in the fundamental stretching frequencies by 14.7 cm^{-1} for the asymmetric stretch and 11.1 cm^{-1} for the symmetric stretch. The bend only increased slightly. Addition of the *2h* and *i* basis functions to the aVTZ(2) basis set to give the AVQZ(2) basis set led to no change in the asymmetric stretch, an increase of 7.6 cm^{-1} in the symmetric stretch, and a decrease of 5.8

cm^{-1} in the bend. As a consequence the difference in the symmetric and asymmetric stretch was reduced to 81.4 cm^{-1} from 91.1 cm^{-1} with the aVTZ(2) basis set. Our best estimated values for the fundamental frequencies were at the CCSD(T)/SO/aVQZ(2) level, where the spin-orbit correction was taken from the SO-DFT calculations and are given in Table 2. The effects of anharmonicity are small: 8.6 cm^{-1} for the asymmetric stretch, 7.2 cm^{-1} for the symmetric stretch, and 1 cm^{-1} for the bend. The spin-orbit correction is even smaller and in the opposite direction, leading to an increase for the stretches.

To test our approach, we also calculated the fundamental frequencies for ThO_2 . ThO_2 was predicted to be bent with a bond distance of 1.9054 \AA and a bond angle of 116.47° at the CCSD(T)/aVTZ(2) level. This is in agreement with the experimental observation of two stretching fundamentals in an infrared study of matrix-isolated ThO_2 .^{32,33,34} The calculated frequencies at the CCSD(T)/aVTZ(2) level are given in Table 4 and compared to the experimental values from Ar^{32,33} and Ne³⁴ matrices. The anharmonic correction is even smaller for ThO_2 than for UO_2^{2+} with the asymmetric stretch reduced by 4.8 cm^{-1} , the symmetric stretch by 3.8 cm^{-1} , and the bend by 1 cm^{-1} as compared to the respective harmonic values. The spin-orbit DFT corrections are small and in the opposite direction to the anharmonic corrections, increasing the asymmetric stretch by 2.6 cm^{-1} , the symmetric stretch by 4.4 cm^{-1} , and the bend by 1.2 cm^{-1} . As in UO_2^{2+} , the spin-orbit correction for the asymmetric stretch is smaller than for the symmetric stretch. The agreement with the Ne matrix values³⁴ is excellent, with the two stretching frequencies predicted to within 1 cm^{-1} of the experimental values. The addition of higher angular momentum basis functions probably would raise the symmetric stretch

by a few cm^{-1} on the basis of the UO_2^{2+} results. The comparison of our results with the Ne matrix values indicate that there is likely to be only a small matrix effect due to Ne and an Ar matrix effect of about 20 cm^{-1} , reducing the stretching frequencies. The results for ThO_2 support the quality of the UO_2^{2+} results and demonstrate that our results at the CCSD(T)/SO/aVQZ(2) level for UO_2^{2+} should be good to $\pm 5 \text{ cm}^{-1}$.

From the above results, it is clear that the harmonic stretching frequencies for UO_2^{2+} are sensitive to the correlation treatment, the basis set, and the treatment of relativistic effects. Comparison of the results at the CCSD(T)/aVTZ(1) level shows that the CCSD method overestimates the values by a substantial amount. The CCSD(T) values for the asymmetric stretch are in the range of $1100\text{-}1120 \text{ cm}^{-1}$ and do not show much dependence on whether an ECP is used or if the relativistic effects are included at the DHF level. Once a reasonable size basis set is reached (aVTZ(1)), the frequencies are not strongly dependent on the quality of the basis set. The CASPT2 values show that there can be a substantial underlying basis set dependence for the asymmetric stretch. Although it is difficult to draw a definitive conclusion due to the use of different basis sets, it appears that the CASPT2 method underestimates the harmonic stretching frequencies. The DFT B3LYP values, however, show little dependence on the basis set for this stretch and are about 20 cm^{-1} above the CCSD(T)/aVQZ(2) value. The difference between the asymmetric and symmetric stretch is very dependent on the method. Essentially, all of the calculations with an ECP predicted a separation of 80 to 100 cm^{-1} . The CASPT2 calculations predicted a value of around 110 cm^{-1} , whereas the DHF+CCSD(T) results predicted a separation of close to 150 cm^{-1} . This latter value seems to be too high and may be due to the somewhat smaller basis set that was used in

that case. Experimental results for mono-, di-, and triacetate binding to uranyl in solution and the solid state showed a decrease in the band origin separation from 93 to 87 to 75-78 cm^{-1} as the charge changes from +1 to 0 to -1.^{6,8,9,10,48} The splitting for UO_2^{2+} in aqueous solution with four to five bound H_2O molecules was $\sim 90\text{-}95 \text{ cm}^{-1}$.⁴⁹ Calculations at the B3LYP/ECP level¹⁹ on UO_2^{2+} embedded in up to 15 H_2O molecules predicted a value of $\sim 95 \text{ cm}^{-1}$, consistent with the experimental results. Our best results (CCSD(T)/SO/aVQZ(2)) predicted a splitting of 81.4 cm^{-1} . Thus, we suggest that the splitting for the symmetric and asymmetric stretches in the bare ion UO_2^{2+} should be $80\text{-}85 \text{ cm}^{-1}$. We also note that the bending frequency is sensitive to the method and to the actual criteria used in the calculations. We found that the accuracy criteria can cause variations in the bending frequency by up to 30 cm^{-1} in DFT calculations. This can present issues when one is looking at the deviation of uranyl from linearity in the presence of different ligands, so one should be careful in such calculations to ensure that there are no artifacts being introduced by the grid or the convergence criteria.

Acknowledgments. We thank Prof. L. Andrews (University of Virginia) for sharing results on the vibrational frequencies for ThO_2 in a Ne matrix. This work was supported in part by the Chemical Sciences, Geosciences and Biosciences Division, Office of Basic Energy Sciences, U.S. Department of Energy (DOE) under the Geosciences program. D.A.D. also thanks the Robert Ramsay Chair Fund of The University of Alabama for support. Part of this work was performed using the Molecular Science Computing Facility at the W. R. Wiley Environmental Molecular Sciences Laboratory, a national scientific user facility sponsored by DOE's Office of Biological and Environmental

Research and located at Pacific Northwest National Laboratory, operated for the DOE by Battelle.

Table 2.1. Calculated Bond Distances (Å) and Harmonic Frequencies (cm⁻¹).

Method	R_e	Asym stretch	Sym stretch	Δ(A-S)^a	Bend	Ref.
CASPT2/ANO-s	1.714	1153	1043	110		25
CASPT2/ANO-L	1.705	1066	959	107		25
DHF + CCSD/VTZ + cc-pVTZ	1.697	1186	1041	145	180	20
DHF + CCSD(T)/VTZ + cc-pVTZ	1.715	1121	974	147	164	20
CCSD/aVTZ(1)	1.6800	1175.7	1093.3	83	198.7	This work
CCSD(T)/aVTZ(1)	1.6984	1108.5	1019.4	89	176.7	This work
CCSD(T)/aVTZ(2)	1.6941	1119.9	1027.6	92	184.4	This work
CCSD(T)/aVQZ(1)	1.6924	1123.6	1030.8	93	180.9	This work
CCSD(T)/aVQZ(2)	1.6898	1120.0	1035.3	85	178.4	This work
B3LYP/ECP + DZP + diff	1.705	1140	1041	99	161	30
B3LYP/ECP + TZVP	1.696	1142	1049	93	163	20
B3LYP/aVTZ(1)	1.6935	1137.3	1046.2	91	165.6	This work
B3LYP/ SO/aVTZ(1)	1.6950	1138.9	1049.7	89	162.7	This work

^a Difference between asymmetric and symmetric stretching frequencies in cm⁻¹.

Table 2.2. Calculated Anharmonic Fundamental Frequencies (cm⁻¹) for UO₂²⁺.

Mode	Asym stretch	Sym stretch	$\Delta(A-S)^a$	Bend
CCSD/aVTZ(1)	1168.8	1087.2	81.6	197.9
CCSD(T)/aVTZ(1)	1100.7	1012.8	87.9	175.8
CCSD(T)/aVTZ(2)	1111.6	1020.5	91.1	183.2
CCSD(T)/aVQZ(1)	1115.4	1023.9	91.5	179.7
CCSD(T)/aVQZ(2)	1111.4	1028.1	83.3	177.4
CCSD(T)/SO/aVQZ(2) ^b	1113.0	1031.6	81.4	174.5
B3LYP/SO(Ref. 30)	1132.7	1033.9	98.8	169.5

^a Difference between asymmetric and symmetric stretching frequencies in cm⁻¹.

^b Obtained by adding correction from spin-orbit DFT calculation to CCSD(T)/aVQZ(2) anharmonic frequencies.

Table 2.3. UO_2^{2+} Vibrational Anharmonicity Constants^a.

Method	X_{11}	X_{22}	X_{33}	X_{12}	X_{13}	X_{23}
CCSD/aVTZ(1)	-1.35	-0.12	-1.58	-0.63	-5.59	-0.94
CCSD(T)/aVTZ(1)	-1.35	-0.11	-1.83	-0.73	-6.23	-1.11
CCSD(T)/aVTZ(2)	-1.45	-0.15	-1.93	-0.89	-6.52	-1.19
CCSD(T)/aVQZ(1)	-1.43	-0.18	-1.90	-0.82	-6.43	-1.22
CCSD(T)/aVQZ(2)	-1.54	-0.02	-1.89	-0.85	-6.66	-1.51

^a X_{ij} : (1 is symmetric stretch, 2 is bend, 3 is asymmetric stretch) in cm^{-1} . For definition of X_{ij} , see ref 50.

Table 2.4. ThO₂ Harmonic and Anharmonic Fundamental Vibrational Frequencies in cm⁻¹.

Method	R _e ^a	θ _e ^b	Asymm stretch	Symm stretch	Bend
CCSD(T)/aVTZ(2) harmonic	1.9054	116.47	809.9	755.4	165.1
CCSD(T)/aVTZ(2) anharmonic			805.1	751.6	164.1
CCSD(T)/SO/aVTZ(2) ^c			807.7	756.0	165.3
B3LYP/SO/aVTZ(2)	1.8992	119.23	822.5	770.4	156.1
Experiment ^{d,e} (Ar)		122.5 ± 2 ^c	787.4	735.3	
Experiment ^f (Ne)			808.3	756.8	

^a Bond distance in angstroms. ^b Bond angle in degrees. ^c Obtained by adding correction from spin-orbit DFT calculation to CCSD(T)/aVTZ(2) anharmonic frequencies. ^d Ref. 32. ^e Ref. 33. ^f Ref. 34.

References

- ¹ Allen, P. G.; Bucher, J. J.; Clark, D. L.; Edelstein, N. M.; Ekberg, S. A.; Gohdes, J. W.; Hudson, E. A.; Kaltsoyannis, N.; Lukens, W. W.; Neu, M. P.; Palmer, P. D.; Reich, T.; Shuh, D. K.; Tait, C. D.; Zwick, B. D. *Inorg. Chem.* **1995**, *34*, 4797.
- ² Docrat, T. I.; Mosselmans, J. F. W.; Charnock, J. M.; Whiteley, M. W.; Collison, D.; Livens, F. R.; Jones, C.; Edmiston, M. J. *Inorg. Chem.* **1999**, *38*, 1879.
- ³ Amayri, S.; Arnold, T.; Reich, T.; Foerstendorf, H.; Geipel, G.; Bernard, G.; Massanek, A. *Environ. Sci. Technol.* **2004**, *38*, 6032; Amayria, S.; Reicha, T.; Arnoldb, T.; Geipelb, G.; Bernhard, G. *J. Solid State Chem.* **2005**, *178*, 567.
- ⁴ Frost, R. L.; Erickson, K. L.; Weier, M. L.; Carmody, O.; Cejka, J. *J. Mol. Struct.* **2005**, *737*, 173.
- ⁵ Brooker, M. H.; Huang, C.-H.; Sylwestrowicz, J. *J. Inorg. Nucl. Chem.* **1980**, *42*, 1431.
- ⁶ Nguyen-Trung, C.; Begun, G. M.; Palmer, D. A. *Inorg. Chem.* **1992**, *31*, 5280.
- ⁷ Jones, L. H. *Spectrochim. Acta* **1959**, *14*, 409. Jones, L. H. *J. Chem. Phys.* **1955**, *23*, 2105. Jones, L. H.; Penneman, R. A. *J. Chem. Phys.* **1953**, *21*, 542.
- ⁸ Quilès, F.; Burneau, A. *Vib. Spectrosc.* **1998**, *18*, 61.
- ⁹ Gál, M.; Goggin, P. L.; Mink, J. *Spectrochim Acta* **1992**, *48A*, 121.
- ¹⁰ McGlynn, S. P.; Smith, J. K.; Neely, W. C. *J. Chem. Phys.* **1961**, *35*, 105.
- ¹¹ Clark, D. L.; Conradson, S. D.; Donohoe, R. J.; Keogh, D. W.; Morris, D. E.; Palmer, P.; Rogers, R. D.; Tait, C. D. *Inorg. Chem.* **1999**, *38*, 1456
- ¹² Groenewold, G. S.; Gianotto, A. K.; Cossel, K. C.; Van Stipdonk, M. J.; Moore, D. T.; Polfer, N.; Oomens, J.; de Jong, W. A.; Visscher, L. *J. Am. Chem. Soc.* **2006**, *107*, 4802.
- ¹³ Kaltsoyannis, N. *Chem. Soc. Rev.* **2003**, *32*, 9.
- ¹⁴ de Jong, W. A.; Aprà, E.; Windus, T. L.; Nichols, J. A.; Harrison, R. J.; Gutowski, K. E.; Dixon, D. A. *J. Phys. Chem. A.* **2005**, *109*, 11568.
- ¹⁵ Schreckenbach, G.; Hay, P. J.; Martin, R. L. *J. Comput. Chem.* **1999**, *20*, 70.
- ¹⁶ Hay, P. J.; Martin, R. L. *Los Alamos Sci.* **2000**, *26*, 382.
- ¹⁷ Hay, P. J.; Martin, R. L.; Schreckenbach, G. *J. Phys. Chem. A* **2000**, *104*, 6259.

-
- ¹⁸ Vallet, V.; Macak, P.; Wahlgren, U.; Grenthe, I. *Theor. Chem. Acta* **2006**, *115*, 145.
- ¹⁹ Gutowski, K. E.; Dixon, D. A. *J. Phys. Chem. A* **2006**, *110*, 8840.
- ²⁰ de Jong, W. A.; Harrison, R. J.; Nichols, J. A.; Dixon, D. A. *Theor. Chim. Acc.* **2001**, *107*, 22; 318 (correction).
- ²¹ Purvis, G. D. III; Bartlett, R. J. *J. Chem. Phys.* **1982**, *76*, 1910.
- ²² Raghavachari, K.; Trucks, G. W.; Pople, J. A.; Head-Gordon, M. *Chem. Phys. Lett.* **1989**, *157*, 479.
- ²³ Watts, J. D.; Gauss, J.; Bartlett, R. J. *J. Chem. Phys.* **1993**, *98*, 8718.
- ²⁴ Bartlett, R. J.; Musial, M. *Rev. Mod. Phys.* **2007**, *79*, 291.
- ²⁵ Gagliardi, L.; Roos, B. O. *Chem. Phys. Lett.*, **2000**, *31*, 229.
- ²⁶ Institut für Theoretische Chemie Universität Stuttgart; <http://www.theochem.uni-stuttgart.de/>. The original basis set is no longer available at the website and has been updated, see Ref. 27.
- ²⁷ Cao, X.; Dolg, M.; Stoll, H. *J. Chem. Phys.* **2003**, *118*, 487. Cao, X.; Dolg, M. *J. Mol. Struct.* **2004**, *673*, 203.
- ²⁸ Pierloot, K.; Dumez, B.; Widmark, P.-O.; Roos, B. O. *Theor. Chim. Acta* **1995**, *90*, 87.
- ²⁹ Widmark, P.-O.; Malmqvist, P.-Å; Roos, B. O. *Theor. Chim. Acta* **1990**, *77* 291.
- ³⁰ Clavaguéra-Sarrio, C.; Ismail, N.; Marsden, C. J.; Bégué, D.; Pouchan, C. *Chem. Phys.* **2004**, *302*, 1.
- ³¹ Bouteiller, Y.; Mijoule, C.; Nizam, M.; Barthelat, J.-C.; Daudey, J.-P.; Pelissier, M.; Silvi, B. *Mol. Phys.* **1988**, *65*, 295. Ismail, N.; Heully, J.-L.; Saue, T.; Daudey, J.-P.; Marsden, C. J. *Chem. Phys. Lett.* **1999**, *300*, 296. Zhou, M.; Andrews, L.; Ismail, N.; Marsden, C. J. *J. Phys. Chem. A* **2000**, *104*, 5495.
- ³² Gabelnick, S. D.; Reedy, G. T.; Chasanov, M. G. *J. Chem. Phys.* **1974**, *60*, 1167.
- ³³ Souter, P. F.; Kushto, G. P.; Andrews, L.; Neurock, M. *J. Phys. Chem. A* **1997**, *101*, 1287.
- ³⁴ Andrews, L. private communication, Dec. 2007.

³⁵ Werner, H.-J.; Knowles, P. J.; Lindh, R.; Manby, F. R.; Schütz, M.; Celani, P.; Korona, T.; Rauhut, G.; Amos, R. D.; Bernhardsson, A.; Berning, A.; Cooper, D. L.; Deegan, M. J. O.; Dobbyn, A. J.; Eckert, F.; Hampel, C.; Hetzer, G.; Lloyd, A. W.; McNicholas, S. J.; Meyer, W.; Mura, M. E.; Nicklass, A.; Palmieri, P.; Pitzer, R.; Schumann, U.; Stoll, H.; Stone, A. J.; Tarroni, R.; Thorsteinsson, T. *MOLPRO, version 2006.1, A Package of Ab Initio Programs*; see <http://www.molpro.net>.

³⁶ The older U basis set and ECP can be obtained from the Extensible Computational Chemistry Environment Basis Set Database, Version 02/02/06, as developed and distributed by the Molecular Science Computing Facility, Environmental and Molecular Sciences Laboratory, which is part of the Pacific Northwest Laboratory, P.O. Box 999, Richland, Washington 99352, and funded by the U.S. Department of Energy, Office of Biological and Environmental Research. <http://www.emsl.pnl.gov/forms/basisform.html>.

³⁷ Kendall, R. A.; Dunning, T. H. Jr. Harrison, R. J. *J. Chem. Phys.* **1994**, *96*, 6796.

³⁸ Senekowitsch, J. *Spektroskopische Eigenschaften aus elektronischen Wellenfunktionen*. PhD. Thesis, Johann Wolfgang Goethe Universität, Frankfurt am Main, Germany, 1988.

³⁹ Mills, I. M. *Vibration-Rotation Structure in Asymmetric and Symmetric Top Molecules*. In *Molecular Spectroscopy: Modern Research*; Rao, K. N., Mathews, C. W., Eds.; Academic: New York, 1972; Vol. 1. Chapter 3.2, pp 115–140.

⁴⁰ Becke, A. D. *J. Chem. Phys.* **1993**, *98*, 5648.

⁴¹ Lee, C.; Yang, W.; Parr, R. G. *Phys. Rev. B: Condens. Matter Mater. Phys.* **1988**, *37*, 785.

⁴² Frisch, M. J.; Trucks, G. W.; Schlegel, H. B.; Scuseria, G. E.; Robb, M. A.; Cheeseman, J. R.; Montgomery, J. A. Jr.; Vreven, T.; Kudin, K. N.; Burant, J. C.; Millam, J. M.; Iyengar, S. S.; Tomasi, J.; Barone, V.; Mennucci, B.; Cossi, M.; Scalmani, G.; Rega, N.; Petersson, G. A.; Nakatsuji, H.; Hada, M.; Ehara, M.; Toyota, K.; Fukuda, R.; Hasegawa, J.; Ishida, M.; Nakajima, T.; Honda, Y.; Kitao, O.; Nakai, H.; Klene, M.; Li, X.; Knox, J. E.; Hratchian, H. P.; Cross, J. B.; Bakken, V.; Adamo, C.; Jaramillo, J.; Gomperts, R.; Stratmann, R. E.; Yazyev, O.; Austin, A. J.; Cammi, R.; Pomelli, C.; Ochterski, J. W.; Ayala, P. Y.; Morokuma, K.; Voth, G. A.; Salvador, P.; Dannenberg, J. J.; Zakrzewski, V. G.; Dapprich, S.; Daniels, A. D.; Strain, M. C.; Farkas, O.; Malick, D. K.; Rabuck, A. D.; Raghavachari, K.; Foresman, J. B.; Ortiz, J. V.; Cui, Q.; Baboul, A. G.; Clifford, S.; Cioslowski, J.; Stefanov, B. B.; Liu, G.; Liashenko, A.; Piskorz, P.; Komaromi, I.; Martin, R. L.; Fox, D. J.; Keith, T.; Al-Laham, M. A.; Peng, C. Y.; Nanayakkara, A.; Challacombe, M.; Gill, P. M. W.; Johnson, B.; Chen, W.; Wong, M. W.; Gonzalez, C.; and Pople, J. A.; *Gaussian 03*, revision D.02; Gaussian, Inc.: Pittsburgh, PA, 2004.

-
- ⁴³ Bylaska, E. J.; de Jong, W. A.; Kowalski, K.; Straatsma, T. P.; Valiev, M.; Wang, D.; Aprà, E.; Windus, T. L.; Hirata, S.; Hackler, M. T.; Zhao, Y.; Fan, P.-D.; Harrison, R. J.; Dupuis, M.; Smith, D. M. A.; Nieplocha, J.; Tipparaju, V.; Krishnan, M.; Auer, A. A.; Nooijen, M.; Brown, E.; Cisneros, G.; Fann, G. I.; Früchtl, H.; Garza, J.; Hirao, K.; Kendall, R.; Nichols, J. A.; Tsemekhman, K.; Wolinski, K.; Anchell, J.; Bernholdt, D.; Borowski, P.; Clark, T.; Clerc, D.; Dachsel, H.; Deegan, M.; Dylla, K.; Elwood, D.; Glendening, E.; Gutowski, M.; Hess, A.; Jaffe, J.; Johnson, B.; Ju, J.; Kobayashi, R.; Kutteh, R.; Lin, Z.; Littlefield, R.; Long, X.; Meng, B.; Nakajima, T.; Niu, S.; Pollack, L.; Rosing, M.; Sandrone, G.; Stave, M.; Taylor, H.; Thomas, G.; van Lenthe, J.; Wong, A.; Zhang, Z. *NWChem, A Computational Chemistry Package for Parallel Computers, Version 5.0* (2006), Pacific Northwest National Laboratory, Richland, WA, 2006.
- ⁴⁴ Kendall, R. A.; Aprà, E.; Bernholdt, D. E.; Bylaska, E. J.; Dupuis, M.; Fann, G. I.; Harrison, R. J.; Ju, J.; Nichols, J. A.; Nieplocha, J.; Straatsma, T. P.; Windus, T. L.; Wong, A. T. *Comput. Phys. Commun.* **2000**, *128*, 260.
- ⁴⁵ Hay, P. J.; Wadt, W. R.; Kahn, L. R.; Raffanetti, R. C.; Philips, D. H. *J. Chem. Phys.* **1979**, *71*, 1767. Lee, Y. S.; Ermler, W. C.; Pitzer, K. S. *J. Chem. Phys.* **1980**, *73*, 360.
- ⁴⁶ Garcia-Hernandez, M.; Lauterbach, C.; Kruger, S.; Matveev, A.; Rosch, N. J. *Comput. Chem.* **2002**, *23*, 834.
- ⁴⁷ Mayer, M.; Kruger, S. Rosch, N. J. *Chem. Phys.* **2001**, *115*, 4411.
- ⁴⁸ Kline, R. J.; Kershner, C. J. *Inorg. Chem.* **1966**, *5*, 932.
- ⁴⁹ Toth, L. M.; Begun, G. M. *J. Phys. Chem.* **1981**, *85*, 547. Basile, L. J.; Sullivan, J. C.; Ferraro J. R.; LaBonville, P. *Appl. Spectrosc.* **1974**, *28*, 142. Jones, L. H.; Penneman, R. A. *J. Chem. Phys.* **1952**, *21*, 542-544. Quilès, F.; Burneau, A. *Vib. Spectrosc.* **2000**, *23*, 231.
- ⁵⁰ Herzberg, G. *Molecular Spectra and Molecular Structure. II. Infrared and Raman Spectra of Polyatomic Molecules*; Van Nostrand Reinhold Co.: New York, 1945.

CHAPTER 3

THE REACTION OF THORIUM OXIDE PLUS METHANE IN SOLID ARGON: A $\text{CH}_3\text{Th}(\text{O})\text{H}$ INTERMEDIATE PRECEDES FORMATION OF METHANOL PLUS THORIUM

From Gong, Y.; Andrews, L.; Jackson, V. E.; Dixon, D. A. *Inorg. Chem.* **2012**, *51*, 11055–11060.

3.1 Introduction

The conversion from methane to methanol has attracted numerous studies since methanol can be widely used as a fuel as well as the starting material for producing other useful chemicals.¹ The successful partial oxidation of methane requires effective catalysts to break the inert C-H bond. A large number of studies have been performed on the preparation and optimization of homogeneous, heterogeneous and enzyme catalysts as well as probing the catalytic mechanisms.^{2,3,4,5} In addition to these studies in the condensed phase, systematic gas phase studies using mass spectrometric methods have also been carried out in a wide range on the reactions of size-selected transition metal oxide ions toward methane as well as other hydrocarbons, as summarized in a series of recent reviews.^{6,7,8} Although these studies were focused on simplified model molecular systems, valuable information on the mechanistic aspects can be obtained especially when combined with high level theoretical calculations.⁹ Apart from the numerous studies in the gas phase employing charged species, the reactions of neutral transition metal oxide molecules and methane have received less attention, and most results are from spectroscopic studies in noble gas matrixes.¹⁰ In particular, the cryogenic matrix environment makes it possible to relax and trap intermediates in the methane oxidation reaction, which are usually not accessible in the gas phase.¹⁰

Although reactions of neutral transition metal oxide molecules and methane have been systematically studied under matrix isolation conditions,^{10,11,12} no investigation has been carried out on the reactivity of neutral actinide oxide species, even though the role of actinide elements in catalytic reactions has been the subject of many recent studies.^{13,14} The most easily accessible actinide metals, uranium and thorium, have been shown to activate the C-H bonds of different hydrocarbons.^{14,15} Gas phase mass spectrometric studies have provided detailed information on the reactivity and thermodynamics of actinide containing cations.¹⁶ Recent experimental and theoretical studies on the reactions of thorium and uranium cations revealed that while thorium cations and dications reacted with CH₄ to form the ThCH₂⁺ and ThCH₂²⁺ products, no similar dehydrogenation reaction was observed for uranium cation owing to the endothermic character as well as the high energy barrier for the uranium reactions.^{17,18,19,20,21}

Our recent matrix isolation infrared spectroscopic studies have provided evidence for the activation of methane by neutral uranium and thorium atoms, as the methylenes complexes CH₂MH₂ (M = U, Th) were observed. The computed structure of the uranium product is more distorted due to stronger agostic interactions.^{22,23} For reactions involving uranium and thorium oxide cations in the gas phase, the oxide-arene adducts were the major products in most cases with H₂ and CH₄ elimination observed in a few cases depending on the reactant arenes.^{16,24} The overall reaction efficiency for the actinide oxide cations was much lower than that for bare metal cations as evidenced by a series of reactivity studies with different hydrocarbons, and almost no reaction was observed between actinide oxide cations and methane.¹⁸ In the current work, we report the reactions of laser-ablated neutral thorium oxide molecules and methane in solid argon at 4 K. Here, ThO molecules react with CH₄ when broad band UV irradiation is employed, which produces the CH₃Th(O)H intermediate trapped in a solid argon matrix. At the same time, evidence is also

provided for the formation of methanol, suggesting that the oxidation of methane proceeds in the presence of thorium oxide molecules.

3.2 *Experimental and Theoretical Methods*

The experimental apparatus and procedure for studying laser-ablated ThO and CH₄ reactions has been described previously.^{25,26} The Nd:YAG laser fundamental (1064 nm, 10 Hz repetition rate with 10 ns pulse width) was focused onto a thorium dioxide (thoria ceramic) target mounted on a rotating rod. Laser-ablated thorium oxide materials, (ThO, Th, and O) were co-deposited with 4 mmol of argon (Matheson, research grade) containing 0.5 % CH₄ (Matheson) onto a CsI cryogenic window at 4 K. Isotopic precursors CD₄ and ¹³CH₄ (Cambridge Isotope Laboratories 99% enrichment) were used without purification. Complementary Th and methanol experiments also employed CH₃¹⁸OH (Cambridge Isotope Laboratories, 95% enrichment). FTIR spectra were recorded at 0.5 cm⁻¹ resolution on a Nicolet 750 FTIR instrument with HgCdTe range B detector. Matrix samples were annealed at different temperatures and cooled back to 4 K for spectral acquisition. Selected samples were subjected to broadband photolysis by a medium-pressure mercury arc street lamp (Philips, 175W) with the outer globe removed to emit the entire quartz envelope output (220 < λ < 900 nm), which was also reduced using selected long wavelength pass optical glass filters.

Density functional theory (DFT)²⁷ with the B3LYP hybrid exchange-correlation functional²⁸ was used to optimize all of the structures. The initial calculations on ¹CH₃Th(O)H were done with the 6-311++G(d,p) basis set²⁹ on H, C, and O and the SDD effective core potential and basis set on Th.³⁰ (The preceding superscript in a formula corresponds to the usual spin state definition.) Subsequent calculations at the DFT/B3LYP level with the aug-cc-pVTZ³¹ basis set on H, C, and O and the small core relativistic effective core potential (ECP) from the

Stuttgart group^{30,32} with the corresponding segmented [8s,7p,6d,4f,2g] basis set on Th were used to map out the potential energy surface. The Gaussian 09 program system was used for the optimization and frequency calculations of the minima and for the final DFT energies.³³ We were able to optimize some of the transition states using the options available for such optimizations in the Gaussian code.³⁴ In cases where we could not determine the transition state, we used the STEPPER approach with specific mode following in NWChem.³⁵ The DFT geometries were used in single point CCSD(T) calculations³⁶ performed with the MOLPRO 2010.1 program system³⁷ and with open shell molecules treated at the R/UCCSD(T) level.³⁸ The same ECP for Th was used as given above, but a larger basis set of the form [10s,9p,5d,4f,3g] was used following our previous work on ThO₂³⁹ with the aug-cc-pVTZ basis set on H, C, and O. We correlated³⁹ 12 valence electrons on Th in the CCSD(T) calculations (nominally the 6s, 6p, 7s, and 6d) and 6 electrons on O, 4 electrons on C, and 1 electron on each H atom.

3.3 Results and Discussion

Infrared spectra from the reactions of laser-ablated thorium oxide materials (ThO, Th, and O) and methane in solid argon are shown in Figure 1. Strong absorption due to ThO, as well as weak ThO₂ bands were observed right after sample deposition (Figure 1, trace a), which result from laser ablation of the thorium oxide target. The yield of ThO in these experiments is much higher than that of ThO₂ relative to previous work with Th + O₂ reactions,⁴⁰ so we must conclude that either some ThO molecules survive ablation or that extensive recombination of the elements gives the high yield of ThO. In addition, the broad methyl radical absorption centered at 603 cm⁻¹ (not shown here) was observed.⁴¹ which is common in all of our reactions of laser-ablated metal atoms and methane, where the laser ablation plume photodissociates methane.²⁶ Trace absorptions were observed for two matrix trapping sites of CH₃OH at 1033.7 and 1027.0 cm⁻¹ on

sample deposition: these likely arise from reaction of laser-ablated O atoms with methane. Also weak bands at 1435.7, 1397.1, and 670.8 cm^{-1} due to the CH_2ThH_2 methyldene complex result from the reactions of thorium atoms and methane.²² Subsequent sample annealing to 20 K increased the ThO_2 absorptions as well as a band at 842.6 cm^{-1} (Figure 1, trace b), which was assigned previously to the HThO molecule.⁴² The CH_2ThH_2 bands increased and a new band pair was produced at 1370 and 817 cm^{-1} on exposure to pyrex filtered ($\lambda > 290 \text{ nm}$) irradiation. When the sample was next exposed to full arc ($\lambda > 220 \text{ nm}$) irradiation, the CH_2ThH_2 bands and the new pair at 1370 and 817 cm^{-1} increased along with the 1027.0 cm^{-1} matrix site band of the C–O stretching mode for CH_3OH . Together with the absorptions due to CH_2ThH_2 , the 1370 and 817 cm^{-1} absorptions sharpened and shifted to 1375.5 and 816.7 cm^{-1} during sample annealing to 30 K but decreased slightly upon sample annealing to 35 K. After the absorption due to methanol increased at 1027.0 cm^{-1} upon UV irradiation, conversions between the two 1027.0 and 1033.7 cm^{-1} matrix site absorptions occurred during sample annealing (see Figure 1, traces d and e). Clearly, the increase of CH_3OH on full arc ($\lambda > 220 \text{ nm}$) irradiation accompanies a further increase of the new pair of bands to be identified here.

Complementary studies of the reaction of thorium and methanol were also performed, and these showed similarities with the thorium oxide and methane reaction (Figure 2, trace d). The new band at 816.7 cm^{-1} appeared as well when the sample was annealed after sample deposition. However, the 1375.5 cm^{-1} band in the thorium and methanol experiment was not well resolved because of overlap with the methanol precursor absorptions.

A new product molecule resulting from the reaction of thorium oxide and methane must be considered since the 1375.5 and 816.7 cm^{-1} absorptions were not observed in reactions of thorium and methane. The 816.7 cm^{-1} band should be due to a terminal $\text{Th}=\text{O}$ stretching mode due to the

band position as well as the characteristic $^{16}\text{O}/^{18}\text{O}$ ratio of 1.0560 obtained from the Th and $\text{CH}_3^{18}\text{OH}$ reaction (Figure 2). Experiments with $^{13}\text{CH}_4$ revealed no ^{13}C shift for the 816.7 cm^{-1} band, and the reaction of thorium oxide and CD_4 resulted in a very small red shift of 1.8 cm^{-1} , which is comparable with the 2.1 cm^{-1} red shift of the HThO molecule (Figure 2).⁴² These observations suggest that this new terminal $\text{Th}=\text{O}$ stretching mode is slightly perturbed by vibrational motions involving hydrogen. For the other band at 1375.5 cm^{-1} , an experiment with $^{13}\text{CH}_4$ gave no isotopic shift, indicating that carbon in the new molecule is not involved in this higher frequency vibrational mode. When CD_4 was used as the reactant, no band was observed between 1370 and 1450 cm^{-1} . This follows since absorptions in this region have been assigned to Th-H stretching modes of the CH_2ThH_2 molecule.²² Hence it is also reasonable to assign the 1375.5 cm^{-1} band to the Th-H stretching mode of the new molecule. If the H/D isotopic ratio for the 1375.5 cm^{-1} band is similar to that of other Th-H containing species (1.39-1.40),⁴² the deuterium counterpart would be observed in the region of 980 - 990 cm^{-1} ; this is on the red side of the strong CD_4 absorption, which broadens upon sample annealing. On the basis of the two experimental frequencies, the new product molecule is identified as $\text{CH}_3\text{Th}(\text{O})\text{H}$ with terminal $\text{Th}=\text{O}$ and Th-H moieties.

Our assignment of this new molecule is strongly supported by calculations at the DFT/B3LYP level (Table 1). The $\text{CH}_3\text{Th}(\text{O})\text{H}$ molecule is predicted to have a closed shell singlet ground state with a pyramidal geometry (Figure 3), similar to the recently characterized $\text{CH}_3\text{U}(\text{O})\text{H}$ molecule.⁴³ The $\text{Th}=\text{O}$ bond length and the corresponding stretching frequency for $\text{CH}_3\text{Th}(\text{O})\text{H}$ are also close to those of the two previously characterized the H_2ThO and $(\text{CH}_3)_2\text{ThO}$ molecules with $\text{Th}(\text{IV})$ center.^{42,44} The calculations predict two bands at 1397.2 and 834.8 cm^{-1} that are much stronger than all of the other absorptions above 400 cm^{-1} . The Th-H harmonic

stretching band predicted at 1397.2 cm^{-1} is slightly higher than the observed anharmonic frequency at 1375.5 cm^{-1} . The deuterium counterpart is calculated to be 993.4 cm^{-1} with only half of the intensity of the 1397.2 cm^{-1} band, in the region where the CD_4 precursor molecule absorbs. The Th-D band for the $\text{CD}_3\text{Th}(\text{O})\text{D}$ molecule is probably covered by the strong CD_4 precursor band as noted above. For the calculated Th=O stretching mode at 834.8 cm^{-1} , the $^{16}\text{O}/^{18}\text{O}$ ratio is 1.0562. Both the band position and the isotopic frequency ratio agree well with the experimental results. We note that the calculated values are for the harmonic frequencies and the experimental values include anharmonic components as well as the influence of matrix atoms. These values reported to 0.1 cm^{-1} come from precise calculations and experiments, but one should not associate an error bar with the calculated frequencies to this accuracy.

In order to explore the reaction mechanism, the potential energy surface for the $^1\text{ThO} + \text{CH}_4 \rightarrow ^3\text{Th} + \text{CH}_3\text{OH}$ reaction was calculated at the CCSD(T)//B3LYP level of theory (Figure 4) with the CCSD(T) energies including the B3LYP zero point energy correction. All of the singlet and triplet species except for the $^1\text{ThO}(\text{CH}_4)$ complex discussed below are shown. Formation of the $^1\text{CH}_3\text{Th}(\text{O})\text{H}$ molecule from the reaction of ^1ThO and CH_4 is predicted to be exothermic ($\Delta H_{\text{rxn}} = -11\text{ kcal/mol}$), with an energy barrier ($^1\text{TS1}$) of 30 kcal/mol separating reactants and the product. This modest energy barrier is consistent with the appearance of the $^1\text{CH}_3\text{Th}(\text{O})\text{H}$ absorptions under broadband mercury arc UV irradiation. Geometry optimization of the $^1\text{ThO}(\text{CH}_4)$ complex resulted in separated ^1ThO and CH_4 at the DFT and MP2 levels, in agreement with the absence of the observation of this molecular complex in our experiments. $^3\text{CH}_3\text{Th}(\text{O})\text{H}$ is predicted to be 56 kcal/mol above $^1\text{CH}_3\text{Th}(\text{O})\text{H}$. Further decomposition of $^1\text{CH}_3\text{Th}(\text{O})\text{H}$ is prohibited by energy barriers of 47 and 77 kcal/mol separating it from $^1\text{CH}_3\text{ThOH}$ and $^1\text{CH}_3\text{OThH}$ with the former being 24 kcal/mol more stable than the latter. Both $^1\text{CH}_3\text{ThOH}$ and $^1\text{CH}_3\text{OThH}$ are predicted to be

less stable than the reactant asymptote of ThO + CH₄. As observed in other divalent thorium species,^{42,44,45} both the CH₃OThH and CH₃ThOH molecules have singlet ground states. ³CH₃ThOH is predicted to be 14 kcal/mol higher than ¹CH₃ThOH and ³CH₃OThH is predicted to be 12 kcal/mol above ¹CH₃OThH. The presence of relatively small singlet-triplet splittings for Th (a heavy element) should enable spin orbit coupling in this region and crossing from the singlet to the triplet thereby allowing access to the lowest energy ³Th + ¹CH₃OH product asymptote. The molecular singlet-triplet splitting is smaller than the ³F-¹D splitting of 20.8 kcal/mol in the thorium atom, which is consistent with this hypothesis.⁴⁶

The ³Th + ¹CH₃OH asymptote is predicted to be 128 kcal/mol above the reactant asymptote ¹ThO + CH₄. Application of a spin orbit correction to the ³Th atom ($\Delta E_{SO} = \sum_J[(2J+1)\Delta E(J)] / \sum_J[(2J+1)]$) using the experimental spin orbit splittings⁴⁶ for the Th atom ($\Delta E(J)$) gives a reaction energy of 119 kcal/mol in excellent agreement with the value of 118.7 ± 3.8 kcal/mol calculated from the experimental heats of formation.⁴⁷ A stable ³Th...CH₃OH complex is 38 kcal/mol lower in energy than the product asymptote. This complex is separated by a 22 kcal/mol barrier from ³CH₃OThH, which is the higher energy isomer. The moderate barrier is due to the ease of hydrogen transfer. A much higher barrier of 58 kcal/mol separates the ³Th...CH₃OH complex from the more stable isomer ³CH₃ThOH. The higher barrier is due to the difficulty in transferring the CH₃ group and actually lies above the ³Th + ¹CH₃OH product asymptote. Since thorium atoms react spontaneously with methanol, it is most likely for the reaction to proceed through the higher energy ³CH₃OThH isomer, which essentially requires no activation energy. A similar mechanism has been observed in the reactions of scandium and lanthanide atoms with methanol.⁴⁸ Our proposed pathway through the higher energy isomer with the lower barrier is also consistent with the fact that CH₃OH can be formed by broadband UV

irradiation (Figure 1, trace d), where the UV energies applied in the experiment have approximately zero intensity at 220 nm (130 kcal/mol) and considerable intensity at 240 nm (119 kcal/mol). The energy of the 240 nm photon is just enough to overcome the endothermicity of the reaction from the stable intermediate to $^3\text{Th} + \text{CH}_3\text{OH}$ and both photon energies are too low for the highest energy barrier to be accessed. This is consistent with the fact that lower energy >290 nm photolysis produces the $\text{CH}_3\text{Th}(\text{O})\text{H}$ intermediate but *not additional* CH_3OH . All of the molecules on the potential energy surface prefer singlet ground states except for the $^3\text{Th} + \text{CH}_3\text{OH}$ asymptote and the $^3\text{Th}(\text{CH}_3\text{OH})$ complex. This suggests that intersystem crossing occurs during the overall reaction, which is consistent with gas phase reactions involving transition metal oxide cations with high spin ground states.^{6d,49}

Previous studies on the reactions of transition metal oxide molecules and methane revealed that $\text{CH}_3\text{M}(\text{O})\text{H}$ intermediates were observed when laser-ablated TiO , NbO and TaO molecules reacted with methane whereas the reactions of MnO and FeO with CH_4 gave the CH_3MOH products without metal-oxygen multiple bonds.¹⁰ Formation of the $\text{CH}_3\text{Th}(\text{O})\text{H}$ molecule further supports the similarity of thorium with the group IV metals, both of which have a highest oxidation state of IV, as is also displayed by the corresponding dioxides.^{40,50} However, no $\text{ThO}(\text{CH}_4)$ complex was observed in the thorium oxide experiments, which differs from the titanium case. It should be noted that TiO possesses a triplet ground state whereas the closed shell singlet is the most stable for the ThO molecule.⁵¹ There is almost no reaction between ThO^+ cations and CH_4 from previous gas phase studies.¹⁸ This reaction profile should be different from that of the neutrals because the $\text{CH}_3\text{Th}(\text{O})\text{H}^+$ cation will have a weaker Th-O bond energy with only three electrons available for that interaction rather than the four electrons available for neutral $\text{CH}_3\text{Th}(\text{O})\text{H}$. Hence, the CH_3ThOH^+ cation with Th-C and Th-OH bonds or its decomposition

products are expected to be formed, as observed in gas phase studies on the reactions of transition metal oxide cations with methane.⁶

3.4 Conclusion

Matrix isolated ThO molecules react with CH₄ to give the CH₃Th(O)H product in solid argon at 4 K during UV irradiation. Infrared absorptions due to methanol also increased, along with the formation of CH₃Th(O)H using full arc ($\lambda > 220$ nm) irradiation, suggesting a methane to methanol conversion induced by thorium oxide going through the CH₃Th(O)H intermediate. Calculations at the B3LYP level reveal that the CH₃Th(O)H molecule possesses a pyramidal structure with a closed shell singlet ground state. From the calculated potential energy surface, formation of the CH₃Th(O)H molecule from the reaction of ThO and methane has an energy barrier of 30 kcal/mol and the CH₃Th(O)H product is 11 kcal/mol more stable than the asymptotic reactants. Decomposition of this intermediate to ³Th + CH₃OH is endothermic by 127 kcal/mol, and the formation of ³Th will require a spin crossing. On the other hand, no activation energy is required for the reaction of ³Th and methanol, which results in the spontaneous production of ¹CH₃Th(O)H, again with a surface crossing needed. The reactions of thorium oxide and methane studied here suggest that actinide oxides such as ThO might be used to oxidize methane to methanol under photochemical conditions, analogous to transition metal oxide molecules.^{10,11}

Acknowledgements. We gratefully acknowledge financial support from DOE Office of Science, Basic Energy Supported by DOE Grant DE-SC0001034 (L.A.) and the BES SISGR program in actinide sciences (D.A.D.).

References

- ¹ Holmen, A. *Catal. Today* **2009**, *142*, 2-8.
- ² Hashiguchi, B. G.; Hoevelmann, C. H.; Bischof, S. M.; Lokare, K. S.; Leung, C. H.; Periana, R. A. *In Methane to Methanol Conversion. Energy Production and Storage: Inorganic Chemical Strategies for a Warming World*; Crabtree, R. H., Ed.; Wiley: New York, 2010; p 101.
- ³ Gunay, A.; Theopold, K. H. *Chem. Rev.* **2010**, *110*, 1060–1081.
- ⁴ Vanelderen, P.; Hadt, R. G.; Smeets, P. J.; Solomon, E. I.; Schoonheydt, R. A.; Sels, B. F. *J. Catal.* **2011**, *284*, 157-164.
- ⁵ Himes, R. A.; Barnese, K.; Karlin, K. D. *Angew. Chem., Int. Ed.* **2010**, *49*, 6714-6716.
- ⁶ (a) Böhme, D. K.; Schwarz, H. *Angew. Chem. Int. Ed.* **2005**, *44*, 2336-2354. (b) Schröder, D.; Schwarz, H. *Proc. Natl. Acad. Sci. USA* **2008**, *105*, 18114-18119. (c) Schlangen, M.; Schwarz, H. *Dalton Trans.* **2009**, 10155-10165. (d) Schwarz, H. *Angew. Chem. Int. Ed.* **2011**, *50*, 10096-10115. (e) Dietl, N.; Schlangen, M.; Schwarz, H. *Angew. Chem. Int. Ed.* **2012**, *51*, 5544-5555.
- ⁷ (a) Johnson, G. E.; Tyo, E. C.; Castleman, A. W., Jr. *Proc. Natl. Acad. Sci. USA* **2008**, *105*, 18108-18113. (b) Johnson, G. E.; Mitrić, R.; Bonačić-Koutecký, V.; Castleman, A. W., Jr. *Chem. Phys. Lett.* **2009**, *475*, 1-9. (c) Irikura, K. K.; Beauchamp, J. L. *J. Am. Chem. Soc.* **1989**, *111*, 75–85.
- ⁸ (a) Yin, S.; Bernstein, E. R. *Int. J. Mass Spectrom.* **2012**, *321–322*, 49–65. (b) Zhao, Y. X.; Wu, X. N.; Ma, J. B.; He, S. G.; Ding, X. L. *Phys. Chem. Chem. Phys.* **2011**, *13*, 1925–1938. (c) Ding, X. L.; Wu, X. N.; Zhao, Y. X.; He, S. G. *Acc. Chem. Res.* **2012**, *45*, 382-390. (d) Operti, L.; Rabazzana, R. *Mass Spectrom. Rev.* **2006**, *25*, 483– 513.
- ⁹ Roithová, J.; Schröder, D. *Chem. Rev.* **2010**, *110*, 1170-1211.
- ¹⁰ Wang, G. J.; Zhou, M. F. *Int. Rev. Phys. Chem.* **2008**, *27*, 1-25.
- ¹¹ Wang, G. J.; Gong, Y.; Chen, M. H.; Zhou, M. F. *J. Am. Chem. Soc.* **2006**, *128*, 5974-5980.
- ¹² (a) Wang, G. J.; Chen, M. H.; Zhou, M. F. *J. Phys. Chem. A* **2004**, *108*, 11273-11278. (b) Wang, G. J.; Lai, S. X.; Chen, M. H.; Zhou, M. F. *J. Phys. Chem. A* **2005**, *109*, 9514-9520.
- ¹³ (a) Andrea, T.; Eisen, M. S. *Chem. Soc. Rev.* **2008**, *37*, 550-567. (b) Barnea, E.; Eisen, M. S. *Coord. Chem. Rev.* **2006**, *250*, 855-899.
- ¹⁴ Fox, A. R.; Bart, S. C.; Meyer, K.; Cummins, C. C. *Nature*, **2008**, *455*, 341-349.
- ¹⁵ Pool, J. A.; Scott, B. L.; Kiplinger, J. L. *J. Am. Chem. Soc.* **2005**, *127*, 1338-1339.

- ¹⁶ (a) Gibson, J. K. *Int. J. Mass Spectrom.* **2002**, *214*, 1-21. (b) Gibson, J. K.; Marcalo, J. *Coord. Chem. Rev.* **2006**, *250*, 776-783. (c) Gibson, J. K.; Haire, R. G.; Marcalo, J.; Santos, M.; Leal, J. P.; Pires de Matos, A.; Tyagi, R.; Mrozik, M. K.; Pitzer, R. M.; Bursten, B. E. *Eur. Phys. J. D* **2007**, *45*, 133-138.
- ¹⁷ Di Santo, E.; Santos, M.; Michelini, M. C.; Marcalo, J.; Russo, N.; Gibson, J. K. *J. Am. Chem. Soc.* **2011**, *133*, 1955-1970.
- ¹⁸ Gibson, J. K.; Haire, R. G.; Marcalo, J.; Santos, M.; Pires de Matos, A.; Mrozik, M. K.; Pitzer, R. M.; Bursten, B. E. *Organometallics* **2007**, *26*, 3947-3956.
- ¹⁹ (a) Heinemann, C.; Cornehl, H. H.; Schwarz, H. *J. Organomet. Chem.* **1995**, *501*, 201-209. (b) Armentrout, P. B.; Hodges, R. V.; Beauchamp, J. L. *J. Chem. Phys.* **1977**, *66*, 4683-4688.
- ²⁰ Marcalo, J.; Leal, J. P.; Pires de Matos, A. *Int. J. Mass Spectrom. Ion Processes* **1996**, *157/158*, 265-274.
- ²¹ (a) Di Santo, E.; Michelini, M. d. C.; Russo, N. *Organometallics* **2009**, *28*, 3716-3726. (b) de Almeida, K. J.; Duarte, H. A. *Organometallics* **2010**, *29*, 3735-3745. (c) de Almeida, K. J.; Duarte, H. A. *Organometallics* **2009**, *28*, 3203-3211. (d) de Almeida, K. J.; Cesar, A. *Organometallics* **2006**, *25*, 3407-3416.
- ²² Andrews, L.; Cho, H. G. *J. Phys. Chem. A* **2005**, *109*, 6796-6798.
- ²³ Lyon, J. T.; Andrews, L.; Malmqvist, P. Å.; Roos, B. O.; Yang, T.; Bursten, B. E. *Inorg. Chem.* **2007**, *46*, 4917-4925.
- ²⁴ Marcalo, J.; Leal, J. P.; Pires de Matos, A. *Organometallics* **1997**, *16*, 4581-4588.
- ²⁵ (a) Andrews, L.; Citra, A. *Chem. Rev.* **2002**, *102*, 885-911. (b) Andrews, L. *Chem. Soc. Rev.* **2004**, *33*, 123-132.
- ²⁶ (a) Andrews, L.; Cho, H. G. *Organometallics* **2006**, *25*, 4040-4053. (b) Cho, H. G.; Wang, X. F.; Andrews, L. *J. Am. Chem. Soc.* **2005**, *127*, 465-473.
- ²⁷ Parr, R. G.; Yang, W. *Density-functional theory of atoms and molecules*, Oxford Univ. Press, Oxford, 1989.
- ²⁸ (a) Becke, A. D. *J. Chem. Phys.* **1993**, *98*, 5648-5652. (b) Lee, C.; Yang, W.; Parr, R. G. *Phys. Rev. B* **1988**, *37*, 785-789.
- ²⁹ Frisch, M. J.; Pople, J. A.; Binkley, J. S. *J. Chem. Phys.* **1984**, *80*, 3265-3269.
- ³⁰ Kuechle, W.; Dolg, M.; Stoll, M. H.; Preuss, H. *J. Chem. Phys.* **1994**, *100*, 7535-7542.
- ³¹ Kendall, R. A.; Dunning, T. H., Jr.; Harrison, R. J. *J. Chem. Phys.* **1994**, *96*, 6796-6806.

© 2004 by the author(s). All rights reserved. No part of this publication may be reproduced, stored in a retrieval system, or transmitted, in any form or by any means, electronic, mechanical, photocopying, recording, or by any information storage or retrieval system, without the prior written permission of the author(s).

³² (a) Institut für Theoretische Chemie Universität Stuttgart, <http://www.theochem.unistuttgart.de/pseudopotentials/index.en.html>. (b) Cao, X.; Dolg, M.; Stoll, H. *J. Chem. Phys.* **2003**, *118*, 487-496. (c) Cao, X.; Dolg, M. *J. Mol. Struct. (Theochem)*, **2004**, *673*, 203-209.

³³ Frisch, M. J.; et al. *Gaussian 09*; Gaussian, Inc.: Wallingford, CT, 2009.

³⁴ (a) Peng, C.; Schlegel, H. B. *Israel J. Chem.*, **1993**, *33*, 449-454. (b) Peng, C.; Ayala, P. Y.; Schlegel, H. B.; Frisch, M. J. *J. Comput. Chem.* **1996**, *17*, 49-56.

³⁵ (a) Valiev, M. et al. *Comput. Phys. Commun.* **2010**, *181*, 1477-1489. (b) Kendall, R. A. et al. *Comput. Phys. Commun.* **2000**, *128*, 260-283.

³⁶ Bartlett, R. J.; Musial, M. *Rev. Mod. Phys.* **2007**, *79*, 291-352.

³⁷ Knowles, P. J.; Manby, F. R.; Schu

Morss, L. R.; Edelman, N. M.; Fuger, J., Eds.; Springer: Dordrecht, the Netherlands, 2006; Vol. 4, Chapter 19, pp 2113-2224. (c) Cox, J. D.; Wagman, D. D.; Medvedev, V. A. *CODATA Key Values for Thermodynamics*, Hemisphere, New York, 1989. (d) Chase, M. W., Jr. *NIST-JANAF Thermochemical Tables*, 4th ed.; Journal of Physical and Chemical Reference Data, Monograph 9; American Institute of Physics: Woodbury, NY, 1998; Suppl 1.

⁴⁸ (a) Gong, Y.; Andrews, L.; Chen, M. Y.; Dixon, D. A. *J. Phys. Chem. A* **2011**, *115*, 14581-14592. (b) Chen, M. H.; Huang, Z. G.; Zhou, M. F. *J. Phys. Chem. A* **2004**, *108*, 5950-5955.

⁴⁹ Schröder, D.; Shaik, S.; Schwarz, H. *Acc. Chem. Res.* **2000**, *33*, 139-145.

⁵⁰ Chertihin, G. V.; Andrews, L. *J. Phys. Chem.* **1995**, *99*, 6356-6366.

⁵¹ Gong, Y.; Zhou, M. F.; Andrews, L. *Chem. Rev.* **2009**, *109*, 6765-6808.

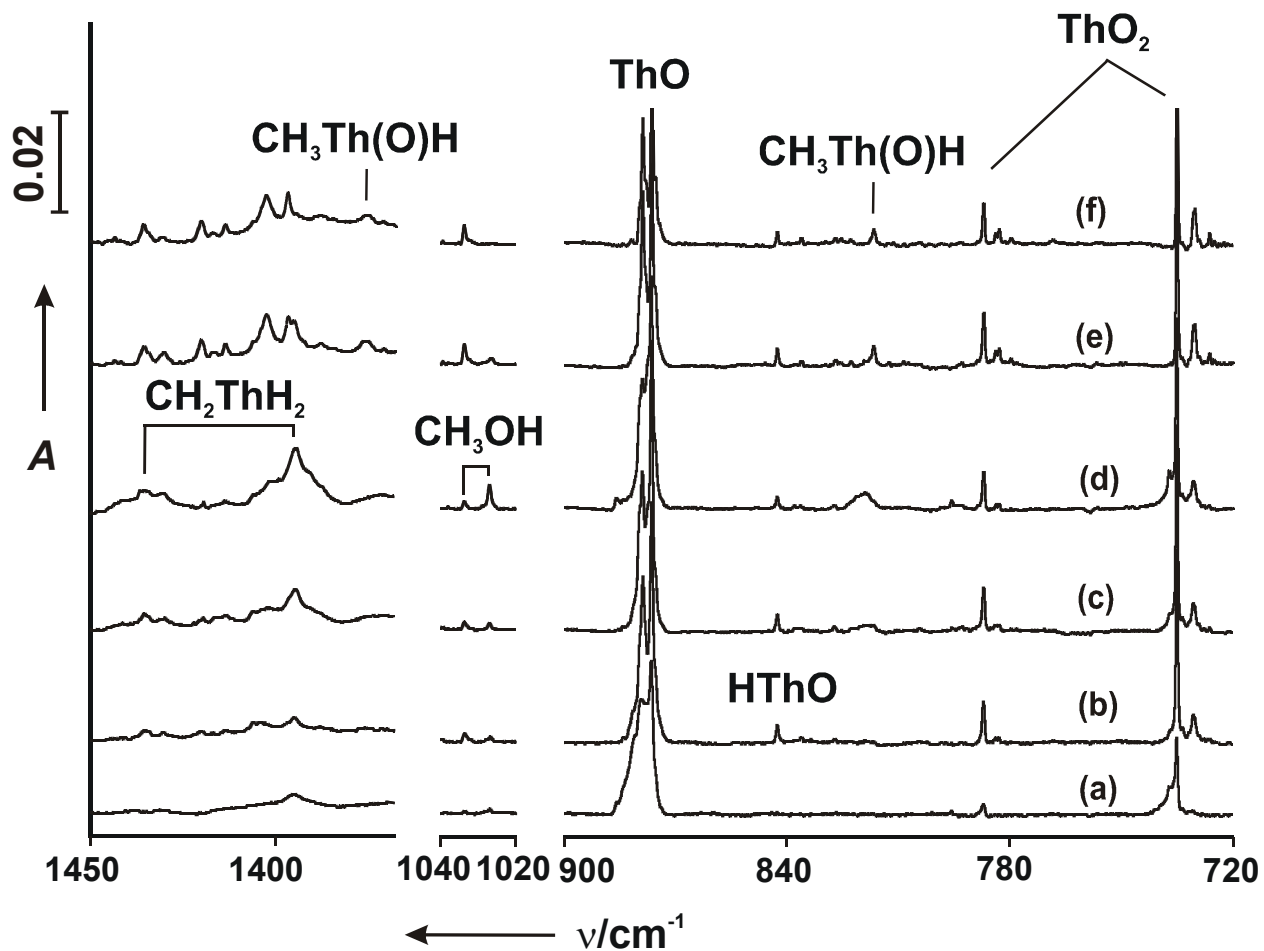


Figure 3.1. Infrared spectra of laser-ablated ThO, Th, and O and CH₄ reaction products in solid argon: (a) ThO + 0.5% CH₄ deposition for 60 min; (b) after annealing to 20 K; (c) after $\lambda > 290$ nm irradiation; (d) after $\lambda > 220$ nm irradiation; (e) annealing to 30 K; (f) after annealing to 35 K.

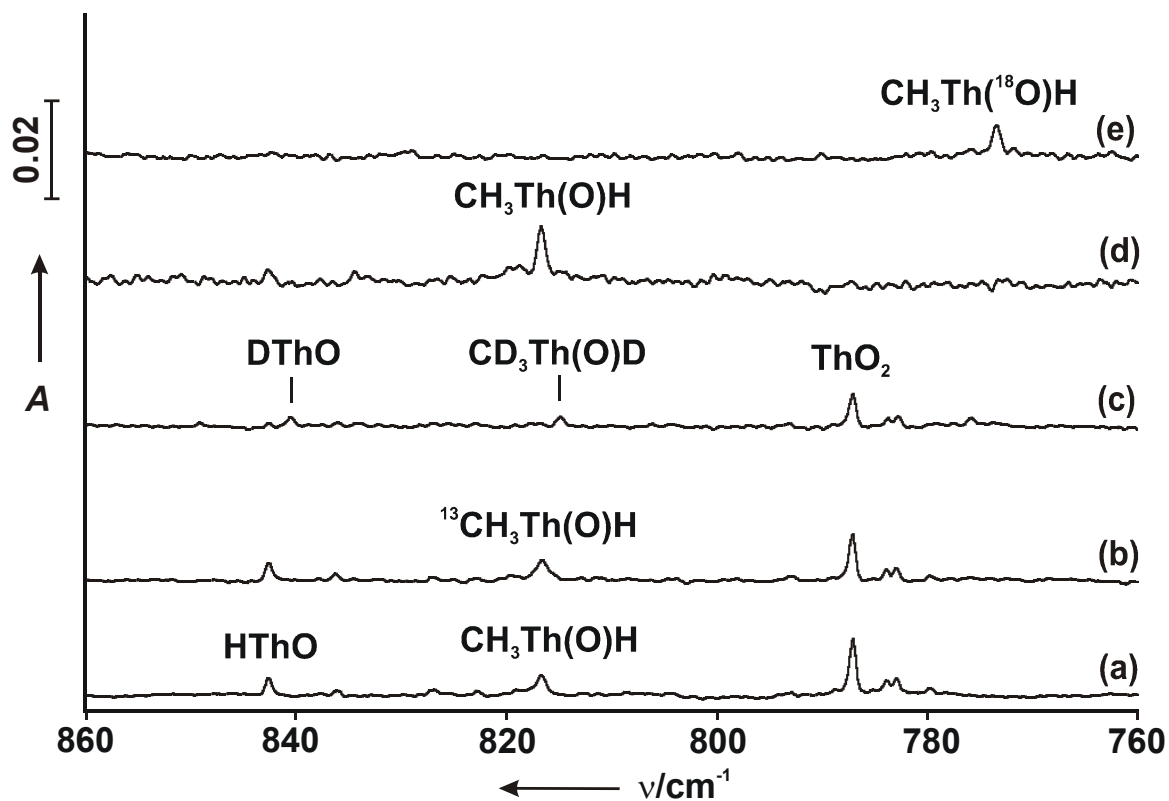


Figure 3.2. Infrared spectra of laser-ablated ThO, Th, and O and isotopically substituted CH₄ reaction products in solid argon (all spectra taken after $\lambda > 220$ nm irradiation followed by annealing to 30 K): (a) ThO + 0.5% CH₄; (b) ThO + 0.5% ¹³CH₄; (c) ThO + 0.5% CD₄; (d) Infrared spectra of laser-ablated Th atoms and isotopically substituted CH₃OH reaction products in solid argon; (d) Th + 1.0% CH₃OH, after annealing to 35 K; (e) Th + 0.5% CH₃¹⁸OH, after annealing to 40 K.

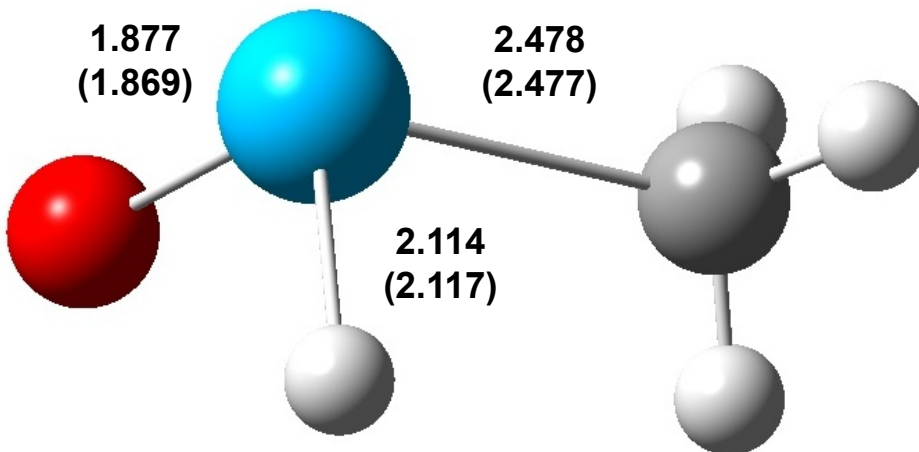


Figure 3.3. Structure of the 1A ground state of the $\text{CH}_3\text{Th}(\text{O})\text{H}$ molecule calculated at the B3LYP level of theory. Bond lengths in Å. Top numbers using the 6-311++G(d,p) + SDD basis set. Bond lengths and angles with the aug-cc-pVTZ + ECP basis set in parentheses: $\angle\text{OThH}$: 104.6° (104.8°), $\angle\text{CThH}$: 96.8° (96.8°), $\angle\text{CThO}$: 103.1° (103.2°), \angle sum = 304.5° (304.8°). Th is blue, O is red, C is grey and H atoms are white.

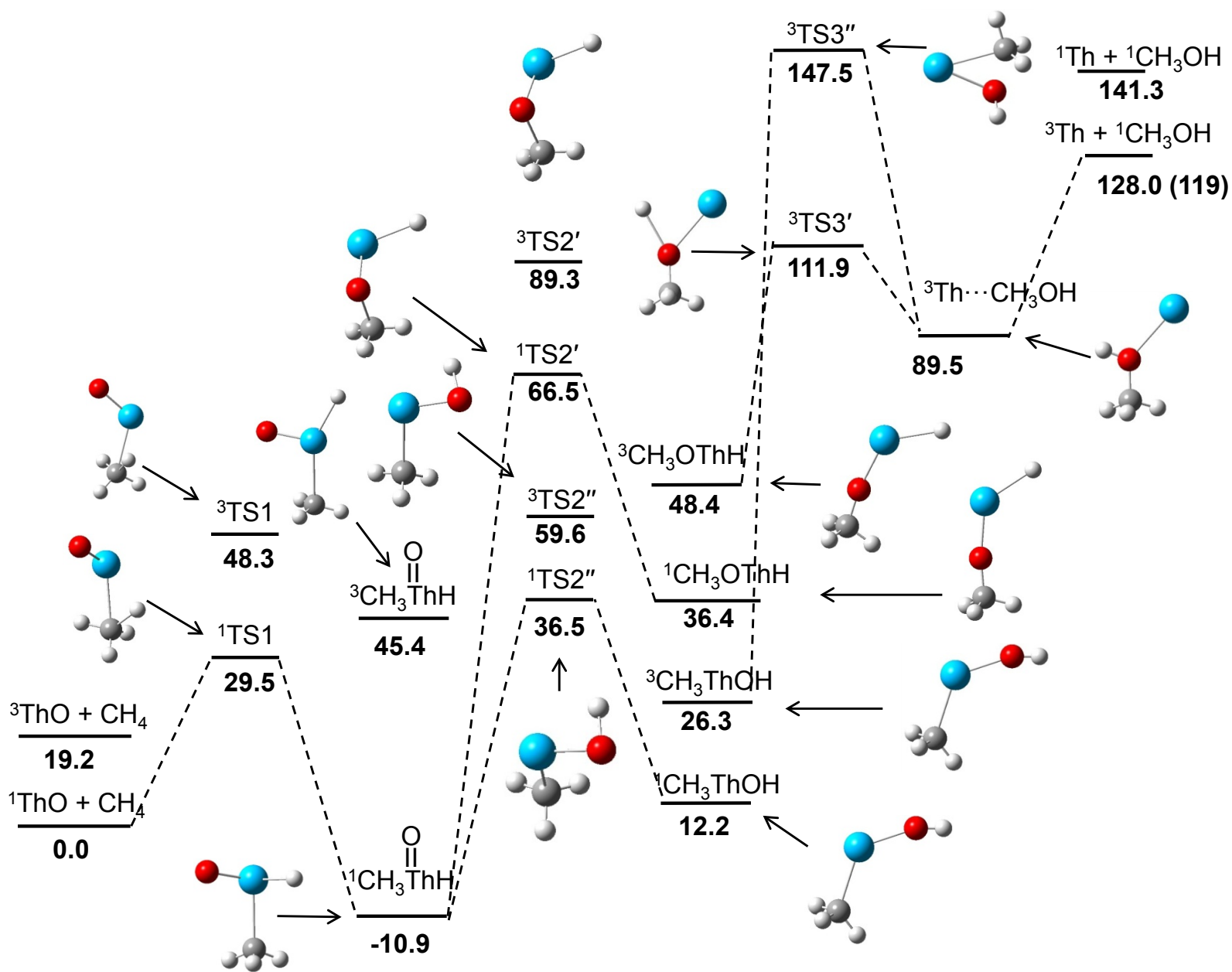


Figure 3.4. Calculated potential energy Surface for the $^1\text{ThO} + \text{CH}_4 \rightarrow ^3\text{Th} + \text{CH}_3\text{OH}$ reaction at the CCSD(T)/aug-cc-pVTZ(ECP)//B3LYP/ aug-cc-pVTZ(ECP') (see text for basis set details) level of theory in kcal/mol. The imaginary frequencies for the transition states are: $1315i$ ($^1\text{TS1}$), $688i$ ($^3\text{TS1}$), $670i$ ($^1\text{TS2}'$), $1091i$ ($^3\text{TS2}'$), $1439i$ ($^1\text{TS2}''$), $466i$ ($^3\text{TS2}''$), $498i$ ($^3\text{TS3}'$), and $834i$ ($^3\text{TS3}''$). The spin-orbit corrected values for the $^3\text{Th} + ^1\text{CH}_3\text{OH}$ asymptote is parentheses, and that for the $^3\text{Th}\cdots\text{CH}_3\text{OH}$ complex is 81 kcal/mol.

Table 3.1. Observed and Calculated (in Bold) Infrared Absorptions (cm⁻¹) of the CH₃Th(O)H Molecule in Solid Argon^a.

	CH ₄	¹³ CH ₄	CD ₄	CH ₃ ¹⁸ OH
Th-H str.	1375.5	1375.5	^b	1375.5
	1397.2 (479)^c	1397.2 (479)	993.4 (224)	1397.0 (480)
Th=O str.	816.7	816.7	814.9	773.4
	834.8 (255)^c	834.7 (255)	832.4 (263)	790.4 (230)

^a Numbers in Parentheses are Infrared Intensities in km/mol Calculated at B3LYP Level of Theory

^b Not observed due to band overlap. ^c Using the larger aug-cc-pVTZ(ECP) basis set at the B3LYP level, the Th-H frequency is 1394.4 (477) cm⁻¹ and the Th=O frequency is 845.2 (255) cm⁻¹.

CHAPTER 4

MATRIX INFRARED SPECTRA AND THEORETICAL STUDIES OF THORIUM OXIDE SPECIES: ThO_x AND Th₂O_y

From Andrews, L.; Gong, Y.; Binyong, L.; Jackson, V. E.; Flamerich, R.; Li, S.; Dixon, D. A. Matrix Infrared Spectra and Theoretical Studies of Thorium Oxide Species: ThO_x and Th₂O_y. *J. Phys. Chem. A* **2011**, *115*, 14407-14416.

4.1 Introduction

Thorium oxides have been considered as potential nuclear fuels for the nuclear power industry, although their applications in this area are quite limited compared with the more widely used uranium and uranium-plutonium oxide materials. However the use of thorium oxides in the nuclear fuel cycle still attracts much attention due to their unique benefits despite the challenges for utilizing this material.^{1,2,3,4} In contrast to the well-known properties of bulk thorium oxide species, which are used in a number of applications,⁵ the properties of small thorium oxide clusters are much less understood. Most experimental and theoretical studies on this subject are limited to the simplest thorium monoxide molecule. ThO has been characterized in both the gas phase and cryogenic matrixes, and the vibrational frequency, ionization energy, and molecular constants have been reported.^{6,7,8,9,10} High level correlated molecular orbital theory including spin orbit coupling and new basis sets have been used to predict the electronic structure and other properties of ThO.^{6,11,12,13,14} For thorium dioxide (ThO₂), the ionization energy was determined from gas phase measurements together with a multiconfiguration quantum chemical study,^{15,16} while spectroscopic information on this species is only from matrix isolation studies. Convincing infrared spectra of ThO₂ evaporated at 2300° C and trapped in solid argon at 15 K revealed

symmetric and antisymmetric stretching modes at 787.4 and 735.3 cm^{-1} ,⁹ and the oxygen isotopic frequency ratio for the antisymmetric stretching mode enabled a prediction of a $122.5 \pm 2^\circ$ for the $\angle\text{O-Th-O}$ angle, which has stood the test of time based on more recent observations^{17,18} and a number of theoretical calculations.^{10,18,19,20,21,22,23} The most detailed theoretical calculations to date²⁰ on ThO_2 were done at the CCSD(T) level with a large augmented correlation-consistent basis set on O and a large basis set with an effective core potential on Th. The calculated values are $r(\text{Th-O}) = 1.9054\text{ \AA}$, $\angle(\text{O-Th-O}) = 116.47^\circ$, $\nu_{\text{sym}} = 807.7$, $\nu_{\text{asym}} = 756.0$, and $\nu_{\text{bend}} = 165.3\text{ cm}^{-1}$. The calculations included anharmonic corrections in the frequencies and spin-orbit corrections.

The element thorium is also of interest for comparing the chemistry of thorium with that of group 4 transition metals.²⁴ Comparisons can be made with the group 4 metal dioxide^{25,26,27} and tetrahydride molecules,^{17,28,29} both of which have the metal in the formal +4 oxidation state. No experimental and theoretical studies have been reported on the structure and bonding of other small thorium oxides that we are aware of, except for the structure of the $\text{Th}_6\text{O}_8^{8+}$ cluster, which has recently been studied by x-ray crystallography and density functional theory (DFT) calculations.³⁰ In this paper, the infrared spectra of three new thorium oxide species in noble gas matrixes are reported. Electronic structure calculations at the correlated molecular orbital theory and DFT levels were performed on the Th_2O_4 and Th_2O_2 molecules, which can be regarded as potential basic building blocks for bulk thorium oxides. Evidence for the formation of the ThO_2^- anion is also presented, which is well supported by the electronic structure calculations. Additional small thorium oxide molecules have been studied computationally.

4.2 Experimental and Theoretical Methods

The experimental apparatus and procedure for Th reactions with O_2 have been described previously.³¹ The Nd:YAG laser fundamental (1064 nm , 10 Hz repetition rate with 10 ns pulse

width) was focused onto a freshly cleaned thorium (Oak Ridge National Laboratory, high purity) target mounted on a rotating rod. Laser-ablated thorium atoms were codeposited with 4-2 mmol of argon (Matheson, research) or neon containing 0.05-0.5% O₂ (Matheson) onto a CsI cryogenic window at 4 K. Isotopic ¹⁸O₂ (Yeda R & D) was used without further purification. A scrambled ¹⁶O₂ + ¹⁶O¹⁸O + ¹⁸O₂ (1:2:1) mixture was prepared via Tesla coil discharge of mixed ¹⁶O₂ + ¹⁸O₂ (1:1) sample. Complementary experiments were done ablating the back of a thorium dioxide crucible into condensing argon and neon. FTIR spectra were recorded at 0.5 cm⁻¹ resolution on Nicolet 550 and 750 FTIR instruments with a HgCdTe range B detector. Frequency measurements are reproduced within 0.2 cm⁻¹. Matrix samples were annealed at different temperatures and cooled back to 10 K (4 K for Nicolet 750) for spectral acquisition. Selected samples were subjected to broadband photolysis with different filters by a medium-pressure mercury arc street lamp (Philips, 175W) with the outer globe removed.

The initial DFT calculations³² were performed using the Gaussian 09 program system.³³ The geometries were optimized, and analytical second derivatives were calculated to predict the harmonic vibrational frequencies. These calculations were performed with the B3LYP hybrid exchange-correlation functional³⁴ with the aug-cc-pVTZ³⁵ basis set on O and the small core relativistic effective core potential (ECP) from the Stuttgart group with the corresponding segmented basis set on Th.^{12a,36} The contracted form of the Th basis set is [8s,7p,6d,4f,2g].

The CCSD(T) calculations³⁷ were done with the MOLPRO 2006.1 program system.³⁸ The same ECP for Th was used as for the DFT calculations, but a larger basis set of the form [10s,9p,5d,4f,3g] was used following our previous work on ThO₂.²⁰ The aug-cc-pVTZ basis set was used for O. As in our previous calculations,²⁰ we correlated 24 valence electrons in the CCSD(T) calculations (12 on the Th, nominally from the 6s, 6p, 7s, and 6d; and 6 electrons on

each O). The geometries and frequencies were calculated numerically at the CCSD(T) level. The calculations were done on our Opteron- and Xeon-based Penguin computing clusters.

4.3 *Results and Discussion*

4.3.1 *Infrared spectral observations.* A series of experiments with different O₂ concentrations were done in argon and neon matrixes. The infrared spectra from the reactions of laser-ablated thorium atoms and 0.1% O₂ in solid argon are shown in Figure 1. Metal independent absorptions due to O₃, O₄⁻ and O₄⁺ species were observed in the spectrum right after sample deposition.^{39,40} Thorium-dependent product absorptions were observed at 876.4, 787.1, 735.1, 653.2 and 616.0 cm⁻¹ in the Ar matrix. The first three bands have been previously assigned to the ThO molecule and the symmetric and antisymmetric O-Th-O stretching modes of ThO₂,⁹ but the last two absorptions were not reported in the earlier experiments. The ThO₂ absorptions increased 4-fold. The new band at 653.2 cm⁻¹ slightly increased when the sample was annealed to 25 K, while the 616.0 cm⁻¹ absorption decreased. All of the other absorptions remained unchanged upon sample annealing. At the same time, a new set of product bands at 775.7, 581.4 and 478.0 cm⁻¹ increased, which were also present in the spectrum after 1 h of sample deposition but with weak intensities. No change was found for all of the newly observed product bands when the sample was exposed to irradiation with a $\lambda > 380$ nm filter, and only the 653.2 cm⁻¹ absorption decreased during broad band irradiation ($\lambda > 220$ nm). Further sample annealing increased the 775.7, 581.4 and 478.0 cm⁻¹ absorptions markedly, but the intensity of the 653.2 cm⁻¹ band remained unchanged.

Similar experiments using ¹⁸O₂, ¹⁶O₂ + ¹⁸O₂ and ¹⁶O₂ + ¹⁶O¹⁸O + ¹⁸O₂ samples were also carried out to obtain the isotopic shifts of the new bands to aid the product identifications. The infrared spectra from the reactions of thorium and different isotopic samples are shown in

Figures 2 and 3, and the observed frequencies and isotopic ratios for the new products are listed in Table 1.

The reactions of thorium and O₂ were also studied in solid Ne to probe the influence of the matrix atoms. In addition to the O₃, O₄⁻ and O₄⁺ species,^{40,41} simple thorium oxide absorptions were observed at 887.1 (ThO), 808.7 and 756.9 cm⁻¹ (ThO₂) after codeposition with 0.5% O₂ sample at 4 K,¹⁸ and the dioxide absorptions showed multiple site splittings. New product bands were observed at 794.1, 666.8, 619.7, 600.7 and 487.7 cm⁻¹ (Figure 4). These bands decreased on sample annealing, while only the 666.8 cm⁻¹ absorption disappeared when broad band irradiation was used. In addition, the 666.8 cm⁻¹ absorption was not produced when high laser energy was used under conditions where the O₄⁻ band was barely observed. In particular, the 619.7 cm⁻¹ absorption was three times as strong, while the ThO band was one-fourth the intensity with 0.05% O₂ compared to 0.5% O₂. The Ne-to-Ar shifts for the new product bands are less than 3%, suggesting weak interactions between the guest molecules and matrix atoms.⁴² All of these absorptions in the Ne matrix exhibited ¹⁸O shifts that were similar to those observed in solid argon (Figure 5). The band positions are also listed in Table 1.

The frequencies for the ThO₂ species in the Ne matrix of 808.7 and 756.9 cm⁻¹ closely match the frequencies of 807.7 and 756.0 cm⁻¹ from the high accuracy CCSD(T) calculations²⁰ on the free molecule showing that there is an (21.6-21.8 cm⁻¹) argon matrix shift but very little shift in the neon matrix.

Complementary experiments were done ablating solid thorium dioxide into argon and neon condensing at 4 K. The infrared spectra are compared in Figures S1 and S2 with spectra from the Th + O₂ reaction (Supporting Information), and some important changes in product distribution are noted. First with argon, solid ThO₂ ablation gave an increased yield of ThO, a

much decreased yield of ozone, and ThO₂, as well as the new products at 653.2 , 581.4, and 478.0 cm⁻¹, while the weak new product at 616 cm⁻¹ was about the same intensity in both experiments. Second with neon, ThO₂ ablation again gave an increased yield of ThO and a much decreased yield of ozone, ThO₂, and the new products at 666.8 and 600.7 cm⁻¹ while the weak new product at 619.7 cm⁻¹ was increased 2-fold.

4.3.2 Th₂O₄. The argon matrix absorptions at 775.7, 581.4 and 478.0 cm⁻¹ exhibit identical behavior throughout the experiments, suggesting that they are different vibrational modes of the same molecule. The 581.4 and 478.0 cm⁻¹ absorptions shifted to 551.3 and 452.7 cm⁻¹ for the reaction with ¹⁸O₂, the isotopic ratios of which are slightly lower than that of the diatomic ThO molecule (1.0563). A triplet split was observed in both mixed ¹⁶O₂ + ¹⁸O₂ and ¹⁶O₂ + ¹⁶O¹⁸O + ¹⁸O₂ experiments (Figure 3, traces c and d), in line with the fact that two equivalent oxygen atoms are involved in these two modes. As these band positions are too low for terminal Th=O stretches, we assign these transitions to Th-O stretches in a rhombic (ThO)₂ ring. The band positions of the first and last absorptions in the ¹⁶O₂ + ¹⁸O₂ experiment are exactly the same as those observed in pure isotopic experiments, whereas slight shifts are found for both of them in the experiment with mixed ¹⁶O₂ + ¹⁶O¹⁸O + ¹⁸O₂ sample. As a result, the Th-O stretches in the rhombic Th₂O₂ ring should be coupled with other vibrational modes involving oxygen atoms. Consistent with this conclusion, a new band at 775.7 cm⁻¹ in the terminal Th=O stretching region was found to track the 581.4 and 551.3 cm⁻¹ absorptions, and its ¹⁸O shift (isotopic ¹⁶O/¹⁸O frequency ratio = 1.0541) is slightly lower than that of the diatomic ThO molecule (1.0563) . Note that two closely spaced bands at 776.9 and 775.7 cm⁻¹ were observed in the mixed ¹⁶O₂ + ¹⁸O₂ experiment, which implies the involvement of two terminal Th=O bonds in this mode, and the other Th=O mode is very close to the observed one. On the basis of the three experimental

infrared absorptions, a Th₂O₄ molecule with two terminal Th=O bonds and a rhombic Th₂O₂ core ring is proposed.

Calculations at the CCSD(T) and DFT/B3LYP levels of theory reveal that the lowest energy structure of the Th₂O₄ molecule has a nonplanar C_{2h} geometry with a closed shell singlet ground state (Figure 6 and Table 2). The frequency calculations (Table 3) predict only three vibrational modes to be infrared active above 400 cm⁻¹. The two rhombus IR active Th-O stretches are calculated to be 611.7 and 481.1 cm⁻¹ with respective ¹⁶O/¹⁸O isotopic ratios (DFT) of 1.0555 and 1.0562, which are close to the experimental frequencies of 581.4 and 478.0 cm⁻¹ as well as the experimental ¹⁶O/¹⁸O ratios of 1.0546 and 1.0559. The antisymmetric Th=O terminal stretching frequency is calculated to be 806.9 cm⁻¹, about 30 cm⁻¹ higher than the 775.7 cm⁻¹ band observed in the experiment. This is consistent with the type of matrix shift expected from the CCSD(T) calculations on ThO₂.²⁰ The infrared inactive symmetric stretching mode, 805.8 cm⁻¹, is predicted to be almost the same as the antisymmetric stretching mode, as suggested from the experiments. The inactive rhombus Th-O stretch is predicted to be 565.9 cm⁻¹.

To provide an estimate of the quality of the B3LYP calculations, we can compare the calculated harmonic frequencies for ThO₂ at the B3LYP level with those at the CCSD(T) level where the anharmonic frequencies are in good agreement with experiment.²⁰ There is 10 cm⁻¹ agreement between the B3LYP and CCSD(T) harmonic frequencies for ThO₂ (Table 4). The comparison of the B3LYP and CCSD(T) results for the molecular geometries shows overall agreement (Table 2) with most of the B3LYP bond distances within 0.02 Å and bond angles within 2° of the CCSD(T) values. The exceptions are the bond angle for the very floppy ThO₂⁺ and a Th-O bond distance in Th₂O₄ (C_{3v}). The B3LYP frequencies for the molecules where CCSD(T) calculations were also performed are also in quite good agreement with the CCSD(T)

values except in one case. Other than the antisymmetric stretch in ThO_2 (3B_1) where the CCSD(T) value is 130 cm^{-1} larger than the B3LYP value, the only difference between the B3LYP and CCSD(T) values more than 25 cm^{-1} is the ThO_2^+ bend. Thus, overall, the use of the B3LYP exchange-correlation functional with the basis set and ECP that were used give very good agreement with the CCSD(T) results for the frequencies and geometry parameters.

In addition to the structure with C_{2h} geometry, another Th_2O_4 isomer with two oxygen atoms on the same side of the rhombus ring with C_{2v} symmetry is predicted to be 4.1 kcal/mol higher in energy than the C_{2h} isomer (CCSD(T)) (Table 2). The C_{2v} isomer has two infrared active terminal Th=O stretching modes due to the change in molecular symmetry at 816.0 and 807.6 cm^{-1} . Three IR-active Th-O stretch rhombus modes are predicted at 604 , 563 , and 475 cm^{-1} with respective isotopic ratios of 1.0554 , 1.0591 , and 1.0560 .

The triplet C_{3v} structure of Th_2O_4 (Table 2) is 67.0 kcal/mol higher in energy than the C_{2h} ground state structure (CCSD(T)). This structure has a terminal Th=O stretch at 630.5 cm^{-1} , which is IR active, and Th-O ring modes at 563.7 , 538.4 (e), and 479.9 cm^{-1} . The higher energy C_{2v} and C_{3v} isomers were not observed based on the mismatch of their calculated vibrational frequencies with the experimental values.

The structure of the Th_2O_4 molecule is similar to that of group 4 metal dioxide dimers, which were also characterized to have non-planar C_{2h} symmetry and singlet ground states.^{27,43} Two different kinds of Th-O bonds are present in the Th_2O_4 molecule. The terminal Th=O bond length is calculated to be 1.902 \AA at the B3LYP level of theory, consistent with the values of other Th=O double bonds.^{20,44,45} A longer Th-O bond length of 2.175 \AA is calculated in the rhombus Th_2O_2 moiety, close to the value of a Th-O single bond.^{45,46} These results all show that the Th is in the formal +4 oxidation state, the same formal oxidation state found for the group 4

metal oxides.^{27,43} The Th-Th distance in the Th₂O₄ molecule is predicted to be 3.464 Å, comparable to the sum of covalent single bond length of thorium (3.5 Å),⁴⁷ suggesting a weak interaction between the two thorium centers.

Analysis of the orbitals reveals that only the 6d and 7s orbitals are involved in the bonding of Th₂O₄ while all the 5f orbitals remain unoccupied. Again, this is similar to the behavior of the group 4 metal oxides with the M₂O₄ composition. The relative infrared intensities of the rhombus (b_u) and terminal M-O stretching modes increase from Ti (0.9:1) to Zr (1.5:1) and Hf (1.9:1).⁴³ The ratio for the Th₂O₄ molecule is 2.4:1, which suggests a higher ionicity in Th₂O₄.

4.3.3 Th₂O₂. The broad infrared absorption centered at 616.0 cm⁻¹ shifted to 583.2 in the ¹⁸O₂ sample. The isotopic ratio of 1.0562 is very close to that of diatomic ThO, and the band position suggests a rhombic Th-O stretching mode. An isotopic doublet was observed in the mixed ¹⁶O₂ + ¹⁸O₂ experiment, whereas an intermediate absorption at 600.5 cm⁻¹ was produced when the scrambled ¹⁶O₂ + ¹⁶O¹⁸O + ¹⁸O₂ sample was used (Figure 2, traces c and d). On the basis of the experimental results, the 616.0 cm⁻¹ absorption can be assigned to a Th-O stretching mode of a Th₂O₂ molecule with two equivalent oxygen atoms. In the neon matrix Th + O₂ experiment, Th₂O₂ was observed at 619.7 cm⁻¹, which is a major product band with 0.05% O₂, and with ThO₂ ablation, the increased yield of ThO was accompanied by a 2-fold increase in the 619.7 cm⁻¹ absorption.

For comparison, the calculated values for the Th-O stretch in the ThO diatomic are $\omega_e = 895.5$ cm⁻¹ and $\omega_e x_e = 2.26$ at the CCSD(T) level ($\omega_e = 896.1$ cm⁻¹ at the B3LYP level) in comparison to the experimental gas phase values of $\omega_e = 895.77$ and $\omega_e x_e = 2.39$ cm⁻¹.⁴⁸ The calculated isotopic ratio is 1.0565.

The ground state of Th₂O₂ is predicted to have D_{2h} symmetry and is a singlet (Table 2 and Figure 6). At the B3LYP level of theory, the triplet is 22.3 kcal/mol higher in energy. The Th-O bond length of the Th₂O₂ molecule is about the same as that of the rhombic ring in the Th₂O₄ molecule, and the calculated Th-Th distance (3.358 Å) is slightly shorter than that in the Th₂O₄ molecule. Frequency calculations at the CCSD(T) level give two infrared active absorption modes above 400 cm⁻¹ (Table 4). The b_{1u} mode is calculated to be 621.4 cm⁻¹ with an ¹⁶O/¹⁸O ratio of 1.0565, both of which are in excellent agreement with the experimental values. For the IR-active b_{2u} mode at 520.3 cm⁻¹, the lower predicted infrared intensity compared with the b_{1u} mode probably makes it impossible for this mode to be observed in our experiment. In addition, the a_g mode at 630.4 cm⁻¹ is IR-inactive. Similarly, the recently characterized M₂O₂ (M=Zr, Hf) molecules also have D_{2h} symmetry, and only one rhombic M-O stretching mode was observed.⁴³

4.3.4 ThO₂⁻. The 653.2 cm⁻¹ absorption produced on sample deposition decreased during broad band irradiation and did not increase when the sample was further annealed. This suggests that the 653.2 cm⁻¹ band could be due to an anionic species, as it exhibits similar behavior to that of oxide anions identified in previous experiments.^{49,50,51,52} Experiments with ¹⁸O₂ sample reveal an isotopic shift of 33.6 cm⁻¹ with the ¹⁶O/¹⁸O ratio of 1.0542, the same as that of the antisymmetric mode of ThO₂ (1.0544). A doublet split at 653.2 and 619.6 cm⁻¹ and a triplet split at 653.2, 631.6 and 619.6 cm⁻¹ were observed in the experiments with mixed and scrambled isotopic samples (Figure 2, traces c and d), indicating the involvement of two equivalent oxygen atoms in this mode. Hence, we can assign the 653.2 cm⁻¹ absorption to the antisymmetric O-Th-O mode of the ThO₂⁻ anion. Note that the intermediate band in the scrambled experiment is closer to the pure ¹⁸O band, which implies the unobserved symmetric O-Th-O mode of the anion is higher than the antisymmetric one. The neon counterpart of the ThO₂⁻ anion was observed at 666.8 cm⁻¹ (Figure

4), which was produced upon sample deposition and almost disappeared during broad band irradiation. Experiment with $^{18}\text{O}_2$ sample resulted in a shift to 632.7 cm^{-1} (Figure 5), similar to the experimental shift from 653.2 cm^{-1} to 619.6 cm^{-1} observed in argon.

To support our assignment of the ThO_2^- anion, electronic structure calculations were performed. The anion is predicted to have a 2A_1 ground state with C_{2v} symmetry just as found for MO_2^- ($M = \text{Ti, Zr, and Hf}$). Compared with the structures of neutral ThO_2 , both the bond length and angles are only slightly different upon electron attachment (Table 2). The antisymmetric and symmetric Th-O stretches for the anion are predicted to be 692.9 and 756.4 cm^{-1} (CCSD(T)) with the relative intensities of approximately 2.2:1 (B3LYP). Experimentally, the 653.2 cm^{-1} absorption is in qualitative agreement with the frequency of the antisymmetric stretching mode of the free anion, and the observed isotopic ratio for this band (1.0542) is almost the same as the calculated value (1.0547). Furthermore, the antisymmetric Th-O stretch for the $^{16}\text{OTh}^{18}\text{O}^-$ isotopmer is calculated to be 12 cm^{-1} higher than that of the $\text{Th}^{18}\text{O}_2^-$ isotopmer, in good agreement with our experimental observations.

The infrared spectra for group 4 metal dioxide anions in solid argon have been reported, all of which were observed on the red side of the strong dioxide bands.³⁹ The shifts for the antisymmetric O-M-O stretch of the anions upon electron attachment are 38.7 cm^{-1} for Ti, 56.6 cm^{-1} for Zr and 66.1 cm^{-1} for Hf. The experimental 81.9 cm^{-1} shift for ThO_2 follows the trend of the group 4 dioxide anions. Our calculated shift for ω_e is a red shift of 63 cm^{-1} at the CCSD(T) level for the isolated anion as compared to the isolated neutral.

4.3.5 Reactions in the matrix. Our experimental observation of 4-fold increase in ThO_2 absorptions on annealing in solid argon (Figure 1) reveal that ground state thorium atoms react with O_2 spontaneously to form ThO_2 (Reaction 1). Further sample annealing allows thorium



dioxide molecules to diffuse and react to give the Th_2O_4 dimer molecule (Reaction 2), the



formation of which is also spontaneous without activation energy. Evidence for the dimerization of thorium dioxide on annealing can be found from the presence of an intermediate mixed oxygen isotopic absorption in the mixed $^{16}\text{O}_2 + ^{18}\text{O}_2$ experiment (Figure 3, trace c). Similar mechanisms have been proposed for the formation of other transition metal dioxide dimers.^{43,53,54} The enthalpy at 298 K of reaction 1 in the gas phase, -252.7 ± 3.8 kcal/mol, can be obtained from the heats of formation of gaseous Th and ThO_2 which are 143.9 ± 1.4 and -108.8 ± 2.4 kcal/mol, respectively.^{55,56} The enthalpy at 298 K of reaction 2 in the gas phase is -100.8 kcal/mol at the CCSD(T) level. In addition, the experimental heat of formation of ThO_2 together with the reaction enthalpy for (2) gives a value of -318.4 kcal/mol for the heat of formation of gaseous Th_2O_4 .⁵⁶

In addition to Th_2O_4 , the Th_2O_2 molecule is also produced in our experiments. Although the dimerization of ThO to form the Th_2O_2 molecule cannot be completely precluded (Reaction 3), most Th_2O_2 molecules are believed to be formed via the reaction of Th_2 and O_2 (Reaction 4), as evidenced by the doublet of bands in the



mixed $^{16}\text{O}_2 + ^{18}\text{O}_2$ experiment instead of a triplet found for the Th_2O_4 molecule (Figure 2, trace c) and the higher yield of Th_2O_2 in the 0.05% O_2 in neon experiment. The enthalpy at 298 K of reaction 3 is -60.2 kcal/mol at the CCSD(T) level. Use of the experimental heat of formation⁵⁶ of ThO of -5 ± 2.4 kcal/mol gives -70.2 kcal/mol for the heat of formation of Th_2O_2 at 298 K. We

can calculate the enthalpy at 298 K of reaction 4 from our calculated heat of formation of Th₂O₂ and the heat of formation of Th₂. Roos *et al.* predicted the ground state of Th₂ to be ³Δ_g with the ¹Σ_g⁺ state 400 cm⁻¹ higher in energy but noted that their CASPT2 calculations were not definitive in determining the ground state.⁵⁷ These authors suggested the presence of a quadruple bond in Th₂ with a Th-Th bond dissociation energy (BDE) of 75.4 kcal/mol. We can use this BDE together with the heat of formation of the Th atom to estimate the heat of formation of Th₂ to be 212 kcal/mol. This gives ΔH(Reaction 4) = -282 kcal/mol. A series of rhombic molecules with transition metal centers have been observed in solid matrixes, and transition metal dimers are believed to participate in the formation of the M₂O₂ molecules.^{43,58,59}

The ThO₂⁻ anion band is observed after sample deposition, which decreased only on broad band irradiation (Figures 1, 4, and 5). The intensity of this species did not increase during further sample annealing. The ThO₂⁻ anion band is not observed in the experiments with higher laser energy due to the photodetachment of the electron by the laser ablation plume from the metal target when the O₄⁻ anion band is also quite weak. All of these experimental observations suggest that the ThO₂⁻ anion is produced via electron attachment to the neutral thorium dioxide molecule upon sample deposition (reaction 5).



Our calculations at the CCSD(T) level of theory predict the adiabatic electron affinity (ADE) of ThO₂ to be 1.15 eV at 0 K. The adiabatic electron affinities of the group 4 metal dioxide molecules have been obtained via anion photoelectron spectroscopy extrapolations as well as high level CCSD(T) calculations extrapolated to the complete basis set (CBS) limit. The experimental values are: ADE(TiO₂) = 1.59 ± 0.03 eV, ADE(ZrO₂) = 1.64 ± 0.03 eV and ADE(HfO₂) = 2.14 ± 0.03 eV.²⁶ The corresponding CCSD(T)/CBS values are: ADE(TiO₂) = 1.66

eV, $\text{ADE}(\text{ZrO}_2) = 1.68 \text{ eV}$ and $\text{ADE}(\text{HfO}_2) = 2.10 \text{ eV}$.²⁷ The ADE of ThO_2 is clearly substantially lower than for the Group 4 MO_2 species.

To better understand the properties of ThO_2 and ThO_2^- , multidimensional Franck-Condon factors (FCFs) for the vibronic transitions from the ground state of ThO_2^- to that of ThO_2 were calculated within the harmonic approximation to simulate the photoelectron spectrum, which can be compared to the experimental anion photoelectron spectra when they become available. These FCFs were calculated⁶⁰ using the recursion relations derived by Doktorov *et al.*⁶¹ adapted from the work of Yang *et al.*⁶² The three-level binary tree algorithms of Ruhoff and Ratner,⁶³ originated from the binary tree algorithm of Gruner and Brumer,⁶⁴ have been implemented. In addition, the backtracking algorithm by Kemper *et al.*⁶⁵ has been implemented to generate all of the vibrational states to be calculated at a given level. The backtracking algorithm also allows for the efficient utilization of the calculated integrals. In simulating the spectra, the theoretical equilibrium geometries, harmonic frequencies, and normal coordinates were used. A Boltzmann distribution was used to account for the finite temperature effect with a Lorentzian line shape with an experimental line width.

The simulated anion photoelectron spectra of ThO_2^- are shown in Figure 7. The simulations were carried out using the CCSD(T) results with a vibrational temperature of 300 K and full widths at half maximum (fwhm) of 5 and 400 cm^{-1} . The latter fwhm is also used as it is typical for anion photoelectron spectra of transition metal oxide clusters. The simulated spectra of ThO_2^- display a fairly strong progression in the Th-O symmetric stretching mode, whose frequency is calculated to be $\sim 810 \text{ cm}^{-1}$ at the CCSD(T) level for the neutral molecule. At a resolution of $\sim 0.05 \text{ eV}$, this vibrational progression can be clearly resolved. A fairly strong progression for the M-O symmetric stretch was also predicted for the anion photoelectron spectra

of TiO_2^- and ZrO_2^- .²⁷ In contrast, stronger progressions for the O-Hf-O bending mode were predicted for HfO_2^- .²⁷

4.3.6 Additional Thorium Oxide Calculations. In addition to the experimentally observed species, calculations were also carried out on the structures of ThO^+ , ThO^- , ThO_2^+ , Th_2O , and Th_2O_3 (Table 2). Removal of an electron from ThO to form ThO^+ gives a decrease in the Th-O bond distance of 0.036 Å and an increase of 59 cm^{-1} in the vibrational frequency, which is close to the experimental results on the oxide cation.⁶⁶ The calculated ionization potential is 6.54 eV for ThO , which is in reasonable agreement with the experimental values.^{6,66} This calculated ionization energy is also in good agreement with the spin-orbit multiconfigurational second-order perturbation theory (SO-CASPT2) result of 6.56 eV.¹⁶ The attachment of an electron to ThO to form ThO^- leads to a decrease in the frequency of 91 cm^{-1} and an increase in the bond distance of 0.049 Å. The calculated electron affinity for ThO is 0.35 eV.

The ionization of ThO_2 to form the cation leads to a decrease in all of the frequencies compared to both the neutral and the anion. The cation ThO_2^+ is linear (CCSD(T)) with a bond angle of 180°. The symmetric stretch is 70 cm^{-1} lower; the asymmetric stretch is 148 cm^{-1} lower; and the bend is 148 cm^{-1} lower in the cation as compared to the neutral, all calculated at the CCSD(T) level. The computed adiabatic (0 K) ionization potential of ThO_2 is 8.59 eV in comparison to an experimental value of 8.9 ± 0.4 eV.¹⁵

Surprisingly, the ground state of Th_2O is the $^3\text{B}_1$ (C_{2v}), which is lower in energy than the $^1\text{A}_1$ (C_{2v}) state by 4.5 kcal/mol. The singlet and triplet have the same Th-O bond length at the CCSD(T) level of theory and the Th-O-Th bond angle of the triplet is 3.3° smaller than that of the singlet. The triplet has a symmetric Th-O stretch of 538.3 cm^{-1} , a asymmetric Th-O stretch of 522.9 cm^{-1} and a Th-O-Th bend of 107.8 cm^{-1} (Table 4). The corresponding singlet values are

produced from the reactions of Th₂ and O₂. Electron capture by neutral ThO₂ during sample deposition results in the formation of the ThO₂⁻ anion.

Calculations at the CCSD(T) and B3LYP level of theory reveal that the Th₂O₄ molecule has nonplanar C_{2h} symmetry and a closed-shell singlet ground state just as in the structures of M₂O₄ for the group 4 transition metals. For the Th₂O₂ molecule, a rhombus structure with D_{2h} symmetry and a singlet spin state is found to be most stable. The Th-Th distances in both the Th₂O₄ and Th₂O₂ molecules are predicted to be around 3.4 Å, indicating weak interactions between the two Th atoms. A doublet ground state is predicted for the ThO₂⁻ anion, and its geometric parameters are similar to those of the neutral dioxide molecule. All three new thorium oxide species characterized here are similar with the group IV analogs. The ground state structures for the unobserved Th₂O and Th₂O₃ molecules were studied theoretically. Th₂O₃ is also calculated to have a rhombic Th₂O₂ ring but with only one out-of-plane terminal oxygen atom connected to the thorium center.

Acknowledgments. We gratefully acknowledge financial support from DOE Office of Science, Basic Energy Sciences (BES) Grant No. DE-SC0001034 and NCSA computing Grant No. CHE07-0004N (University of Virginia), and from the BES SISGR program in actinide sciences. D.A.D. thanks the Robert Ramsay Fund at the University of Alabama for partial support.

Supporting Information Available: Figures S1 and S2 compare infrared spectra of products from the Th + O₂ reaction with those formed by ablating solid thorium dioxide into both condensing argon and neon, respectively. This material is available free of charge via the Internet at <http://pubs.acs.org>.

References

- ¹ Lung, M.; Gremm, O. *Nucl. Eng. Des.* **1998**, *180*, 133-146.
- ² Bae, K.-M.; Kim, M.-H. *Nucl. Eng. Tech.* **2005**, *37*, 91-97.
- ³ Lombardi, C.; Luzzi, L.; Padovani, E.; Vettrano, F. *Prog. Nucl. Energy* **2008**, *50*, 944-953.
- ⁴ *Thorium Fuel Cycle - Potential Benefits and Challenges*; International Atomic Energy Agency: Vienna, Austria, 2005.
- ⁵ (a) Greenwood, N. N.; Earnshaw, A. *Chemistry of the Elements*. 1984, Pergamon, Oxford, 1984; pp 1425-1456. (b) Emsley, J. *Nature's Building Blocks*; Oxford University Press, Oxford, 2001; p 441.
- ⁶ Heaven, M. C. *Phys. Chem. Chem. Phys.* **2006**, *8*, 4497-4509.
- ⁷ Wang, F.; Le, A.; Steimle, T. C.; Heaven, M. C. *J. Chem. Phys.* **2011**, *134*, 031102.
- ⁸ Dewberry, C. T.; Etchison, K. C.; Cooke, S. A. *Phys. Chem. Chem. Phys.* **2007**, *9*, 4895-4897.
- ⁹ (a) Gabelnick, S. D.; Reedy, G. T.; Chasanov, M. G. *J. Chem. Phys.* **1974**, *60*, 1167-1171. (b) Linevsky, M. J. *General Electric Report Nos. WADD-TR-60_646 (Pt. IV) and AD-611856*, 1963.
- ¹⁰ Gong, Y.; Zhou, M.; Andrews, L. *Chem. Rev.* **2009**, *109*, 6765-6808.
- ¹¹ (a) Marian, C. M.; Wahlgren, U.; Gropen, O.; Pyykkö, P. *THEOCHEM* **1988**, *46*, 339-354. (b) Watanabe, Y.; Matsuoka, O. *J. Chem. Phys.* **1997**, *107*, 3738-3739.
- ¹² (a) W. Kuechle, W.; Dolg, M.; Stoll, H.; Preuss, H. *J. Chem. Phys.* **1994**, *100*, 7535-7542. (b) Seijo, L.; Barandiaran, Z.; Harguindey, E. *J. Chem. Phys.* **2001**, *114*, 118-129.
- ¹³ Paulovič, J.; Nakajima, T.; Hirao, K.; Lindh, R.; Malmqvist, P. Å. *J. Chem. Phys.* **2003**, *119*, 798-805.
- ¹⁴ Buchachenko, A. A. *J. Chem. Phys.* **2010**, *133*, 041102.
- ¹⁵ Marçalo, J.; Gibson, J. K. *J. Phys. Chem. A* **2009**, *113*, 12599-12606.
- ¹⁶ Infante, I.; Kovacs, A.; La Macchia, G.; Shahi, A. R. M.; Gibson, J. K.; Gagliardi, L. *J. Phys. Chem. A* **2010**, *114*, 6007-6015.
- ¹⁷ (a) Souter, P. F.; Kushto, G. P.; Andrews, L.; Neurock, M. *J. Phys. Chem. A* **1997**, *101*, 1287-1291. (b) unpublished work from this laboratory.
- ¹⁸ Zhou, M. F.; Andrews, L. *J. Chem. Phys.* **1999**, *111*, 11044-11049.

- ¹⁹ Kovács, A.; Konings, R. J. M. *J. Phys. Chem. A* **2011**, *115*, 6646–6656.
- ²⁰ Jackson, V. E.; Craciun, R.; Dixon, D. A.; Peterson, K. A.; de Jong, W. A. *J. Phys. Chem. A* **2008**, *112*, 4095-4099.
- ²¹ Dyall, K. G. *Mol. Phys.* **1999**, *96*, 511-518.
- ²² Pyykkö, P.; Laakkonen, L. J.; Tatsumi, K. *Inorg. Chem.* **1989**, *28*, 1801-1805.
- ²³ Wadt, W. R. *J. Am. Chem. Soc.* **1981**, *103*, 6053-6057.
- ²⁴ (a) Pyykko, P. *Chem. Rev.* **1988**, *88*, 563-594. (b) Cotton, F. A.; Wilkinson, G.; Murillo, C. A.; Bochmann, M. *Advanced Inorganic Chemistry*, 6th ed., Wiley: New York, 1999.
- ²⁵ Chertihin, G. V.; Andrews, L. *J. Phys. Chem.* **1995**, *99*, 6356-6366.
- ²⁶ (a) Wu, H. B.; Wang, L. S. *J. Chem. Phys.* **1997**, *107*, 8221-8228. (b) Zheng, W.; Bowen, K. H., Jr.; Li, J.; Dąbkowska, I.; Gutowski, M. *J. Phys. Chem. A* **2005**, *109*, 11521-11525.
- ²⁷ Li, S.; Dixon, D. A. *J. Phys. Chem. A*, **2008**, *112*, 6646-6666; Li, S.; Dixon, D. A., *J. Phys. Chem. A*, **2010**, *114*, 2665-2683.
- ²⁸ (a) Chertihin, G. V.; Andrews, L. *J. Am. Chem. Soc.* **1994**, *116*, 8322-8327. (b) Chertihin, G. V.; Andrews, L. *J. Am. Chem. Soc.* **1995**, *117*, 6402-6403.
- ²⁹ Wang, X. F.; Andrews, L.; Gagliardi, L. *J. Phys. Chem. A* **2008**, *112*, 1754-1761.
- ³⁰ Knope, K. E.; Wilson, R. E.; Vasiliu, M.; Dixon, D. A.; Soderholm, L. *Inorg. Chem.* **2011**, *50*, 9696-9704.
- ³¹ (a) Andrews, L.; Citra, A. *Chem. Rev.* **2002**, *102*, 885-911. (b) Andrews, L. *Chem. Soc. Rev.* **2004**, *33*, 123-132. (c) Andrews, L.; Cho, H.-G. *Organometallics* **2006**, *25*, 4040-4053.
- ³² (a) Hohenberg, P.; Kohn, W. *Phys. Rev.* **1964**, *136*, B864-B871. (b) Kohn, W.; Sham, L. *J. Phys. Rev.* **1965**, *140*, A1133-A1138. (c) Parr, R. G.; Yang, W. *Density-functional theory of atoms and molecules*; Oxford Univ. Press, Oxford, 1989. (d) Salahub, D. R.; Zerner, M. C., Eds. *The Challenge of d and f Electrons*; ACS: Washington, D.C., 1989.
- ³³ Frisch, M. J.; Trucks, G. W.; Schlegel, H. B.; Scuseria, G. E.; Robb, M. A.; Cheeseman, J. R.; Scalmani, G.; Barone, V.; Mennucci, B.; Petersson, G. A.; Nakatsuji, H.; Caricato, M.; Li, X.; Hratchian, H. P.; Izmaylov, A. F.; Bloino, J.; Zheng, G.; Sonnenberg, J. L.; Hada, M.; Ehara, M.; Toyota, K.; Fukuda, R.; Hasegawa, J.; Ishida, M.; Nakajima, T.; Honda, Y.; Kitao, O.; Nakai, H.; Vreven, T.; Montgomery, Jr., J. A.; Peralta, J. E.; Ogliaro, F.; Bearpark, M.; Heyd, J. J.; Brothers, E.; Kudin, K. N.; Staroverov, V. N.; Kobayashi, R.; Normand, J.; Raghavachari, K.; Rendell, A.; Burant, J. C.; Iyengar, S. S.; Tomasi, J.; Cossi, M.; Rega, N.; Millam, N. J.; Klene, M.; Knox, J. E.; Cross, J. B.; Bakken, V.; Adamo, C.; Jaramillo, J.; Gomperts, R.; Stratmann, R. E.; Yazyev, O.; Austin, A. J.; Cammi, R.; Pomelli, C.; Ochterski, J. W.; Martin, R. L.; Morokuma, K.; Zakrzewski, V. G.; Voth, G. A.; Salvador, P.; Dannenberg, J. J.; Dapprich, S.; Daniels, A. D.;

Farkas, Ö.; Foresman, J. B.; Ortiz, J. V.; Cioslowski, J.; Fox, D. J. *Gaussian 09*, Revision B.01; Gaussian, Inc.: Wallingford, CT, 2010.

³⁴ (a) Becke, A. D. *J. Chem. Phys.* **1993**, *98*, 5648-5652. (b) Lee, C.; Yang, W.; Parr, R. G. *Phys. Rev. B* **1988**, *37*, 785-789.

³⁵ Kendall, R. A.; Dunning, T. H. Jr. Harrison, R. J. *J. Chem. Phys.* **1994**, *96*, 6796-6806.

³⁶ (a) Institut für Theoretische Chemie Universität Stuttgart, <http://www.theochem.uni-stuttgart.de/pseudopotentials/index.en.html>. Accessed May 16, 2011. (b) Cao, X.; Dolg, M.; Stoll, H. *J. Chem. Phys.* **2003**, *118*, 487-496; (c) Cao, X.; Dolg, M. *J. Molec. Struct. (Theochem)*, **2004**, *673*, 203-209.

³⁷ (a) Purvis, G. D., III; Barlett, R. J. *J. Chem. Phys.* **1982**, *76*, 1910-1918. (b) Raghavachari, K.; Trucks, G. W.; People, J. A.; Head - Gordon, M. *Chem. Phys. Lett.* **1989**, *157*, 479-483. (c) Watts, J. D.; Gauss, J.; Bartlett, R. J. *J. Chem. Phys.* **1993**, *98*, 8718-8733. (d) Barlett, R. J.; Musial, M. *Rev. Mod. Phys.* **2007**, *79*, 291-352.

³⁸ Werner, H.-J.; Knowles, P. J.; Lindh, R.; Manby, F. R.; Schütz, M.; Celani, P.; Korona, T.; Rauhut, G.; Amos, R. D.; Bernhardsson, A.; Berning, A.; Cooper, D. L.; Deegan, M. J. O.; Dobbyn, A. J.; Eckert, F.; Hampel, C.; Hetzer, G.; Lloyd, A. W.; McNicholas, S. J.; Meyer, W.; Mura, M. E.; Nicklass, A.; Palmieri, P.; Pitzer, R.; Schumann, U.; Stoll, H.; Stone, A. J.; Tarroni, R.; Thorsteinsson, T. *MOLPRO, version 2006.1, a package of ab initio programs*. See <http://www.molpro.net>. Accessed May 16, 2011.

³⁹ Chertihin, G. V.; Andrews, L. *J. Chem. Phys.* **1998**, *108*, 6404-6407.

⁴⁰ Zhou, M. F.; Hacıoğlu, J.; Andrews, L. *J. Chem. Phys.* **1999**, *110*, 9450-9456.

⁴¹ Thompson, W. E.; Jacox, M. E. *J. Chem. Phys.* **1989**, *91*, 3826-3837.

⁴² Jacox, M. E. *Chem. Phys.* **1994**, *189*, 149-170.

⁴³ Gong, Y.; Zhang, Q. Q.; Zhou, M. F. *J. Phys. Chem. A* **2007**, *111*, 3534-3539.

⁴⁴ Liang, B. Y.; Andrews, L.; Li, J.; Bursten, B. E. *J. Am. Chem. Soc.* **2002**, *124*, 6723-6733.

⁴⁵ Gong, Y.; Andrews, L. *Dalton Trans.* **2011**, *40*, 11106-11114.

⁴⁶ Wang, X. F.; Andrews, L. *Phys. Chem. Chem. Phys.* **2005**, *7*, 3834-3838.

⁴⁷ Pyykkö, P.; Atsumi, M. *Chem. Eur. J.* **2009**, *15*, 186-197.

⁴⁸ (a) Edvinsson, G.; Selvin, L. E.; Aslund, N. *Ark. Fys.* **1965**, *30*, 28. (b) Edvinsson, G.; Lagerqvist, A. *Phys. Scr.* **1984**, *30*, 309-320.

- ⁴⁹ Zhou, M. F.; Andrews, L. *J. Chem. Phys.* **1999**, *111*, 4230-4238.
- ⁵⁰ Gong, Y.; Zhou, M. F. *J. Phys. Chem. A* **2009**, *113*, 4990-4995.
- ⁵¹ Li, Z. H.; Gong, Y.; Fan, K. N.; Zhou, M. F. *J. Phys. Chem. A* **2008**, *112*, 13641-13649.
- ⁵² Gong, Y.; Zhou, M. F. *Chem. Phys. Lett.* **2010**, *489*, 181-186.
- ⁵³ (a) Chertihin, G. V.; Bare, W. D.; Andrews, L. *J. Chem. Phys.* **1997**, *107*, 2798-2806. (b) Zhang, Q. Q.; Zhao, Y. Y.; Gong, Y.; Zhou, M. F. *J. Phys. Chem. A* **2007**, *111*, 9775-9780.
- ⁵⁴ Ould Souvi, S.; Danset, D.; Alikhani, M. E.; Manceron, L. *J. Phys. Chem. A* **2010**, *114*, 11399-11407.
- ⁵⁵ (a) Cox, J. D.; Wagman, D. D.; Medvedev, V. A. *CODATA Key Values for Thermodynamics*, Hemisphere, New York, 1989. (b) Konigs, R. J. M.; Benes, O. J. *J. Phys. Chem. Ref. Data*, **2010**, *39*, 043102.
- ⁵⁶ Konigs, R. J. M.; Morss, L. R.; Fuger, J. *Thermodynamic Properties of Actinides and Actinide Compounds in The Chemistry of the Actinide and Transactinide Elements*, 3rd ed. Morss, L. R.; Edelstein, N. M.; Fuger, J. Springer Dordrecht, 2006, Chapter 19, Vol. 4. 2113-2224.
- ⁵⁷ Roos, B.O.; Malmqvist, P.; Gagliardi, L. *J. Am. Chem. Soc.* **2006**, *128*, 17000-17006.
- ⁵⁸ Danset, D.; Manceron, L. *Phys. Chem. Chem. Phys.* **2005**, *7*, 583-591.
- ⁵⁹ Allouti, F.; Manceron, L.; Alikhani, M. E. *Phys. Chem. Chem. Phys.* **2006**, *8*, 3715-3725.
- ⁶⁰ Li, S. Ph.D. Thesis, University of Kentucky, August, 2004.
- ⁶¹ Doktorov, E. V.; Malkin, I. A.; Man'ko, V. I. *J. Mol. Spectrosc.* **1977**, *64*, 302-326.
- ⁶² Yang, D.-S.; Zgierski, M. Z.; Rayner, D. M.; Hackett, P. A.; Mrtinex, A.; Salahub, D. R.; Roy, P. N.; Carrington, T. Jr. *J. Chem. Phys.* **1995**, *103*, 5335-5342.
- ⁶³ Ruhoff P. T.; Ratner, M. A. *Int. J. Quant. Chem.* **2000**, *77*, 383-392.
- ⁶⁴ Gruner D.; Brumer, P. *Chem. Phys. Lett.* **1987**, *138*, 310-314.
- ⁶⁵ Kemper, M. J. H.; van Dijk, J. M. F.; Buck, H. M. *Chem. Phys. Lett.* **1978**, *53*, 121-125.
- ⁶⁶ Goncharov, V.; Heaven, M. C. *J. Chem. Phys.* **2006**, *124*, 064312.

Table 4.1. Experimental Infrared Absorptions (cm⁻¹) of New Products from the Reactions of Thorium and Isotopically Substituted O₂ in Solid Ar and Ne Matrices^a.

Molecule	¹⁶ O ₂	¹⁸ O ₂	¹⁶ O/ ¹⁸ O	¹⁶ O ₂ + ¹⁸ O ₂	¹⁶ O ₂ + ¹⁶ O ¹⁸ O+ ¹⁸ O ₂
ThO ₂ ⁻	653.2	619.6	1.0542	653.2, 619.6	653.2, 631.6, 619.6
	666.8	632.7	1.0539		
Th ₂ O ₂	616.0	583.2	1.0562	616.6, 583.2	616.6, 600.5, ^b
	619.7	587.0	1.0557		
Th ₂ O ₄	775.7	735.9	1.0541	776.9, 775.7, ^b	^b
	794.1	752.8	1.0549		
	581.4 [579.6] ^c	551.3 [549.5]	1.0546	581.4, 567.0,	579.9, 566.9, 552.2
	600.7 [599.6]	569.6 [568.4]	1.0546	551.3	
	478.0	452.7	1.0559	478.0, 462.7,	^d , 462.8, ^d
	487.7	461.7	1.0563	452.7	

^a Numbers in bold are Ne frequencies. ^b Absorptions not observed due to band overlap ^c Numbers in bracket are matrix site splittings ^d Absorptions too weak to be observed.

Table 4.2. Calculated Geometry Parameters (Bond Angles in Degrees) for Thorium Oxide

Species.

Property	B3LYP	CCSD(T)	CCSD(T)- B3LYP
ThO $C_{\infty v}$			
r(Th-O) Å	1.835	1.845	0.010
ThO ⁻ $C_{\infty v}$			
r(Th-O) Å	1.884	1.894	0.010
ThO ⁺ $C_{\infty v}$			
r(Th-O) Å	1.802	1.809	0.007
ThO ₂ C_{2v}			
r(Th-O) Å	1.899	1.905	0.006
∠O-Th-O	118.4	116.5	-2.0
ThO ₂ ⁻ C_{2v}			
r(Th-O) Å	1.941	1.943	0.002
∠O-Th-O	115.4	113.6	-1.8
ThO ₂ ⁺ ^a C_{2v}			
r(Th-O) Å	1.847	1.874	0.027
∠O-Th-O	170.3	180.0	9.5
Th ₂ O C_{2v}			
r(Th-O) Å	2.082	2.090	0.008
∠Th-O-Th	106.1	105.2	-0.9
Th ₂ O ₂ D_{2h}			
r(Th-O) Å	2.102	2.110	0.008
∠ Th-O-Th	106.0	105.2	-0.8
∠O-Th-O	74.0	74.8	0.8
Th ₂ O ₃ D_{3h}			
r(Th-O) Å	2.140	2.146	0.006
∠ Th-O-Th	92.1	91.7	-0.4
Th ₂ O ₃ Cs			
r(Th-O) Å	2.045	2.070	0.025

r(Th=O) Å	1.880	1.891	0.011
∠Th-O-Th	104.8	103.8	-1.0
∠O-Th-O	71.2	72.5	1.3
Th ₂ O ₄ C _{2h}			
r(Th-O) Å	2.175	2.183	0.008
r(Th=O) Å	1.902	1.904	0.002
∠Th-O-Th	105.6	105.1	-0.5
∠O-Th-O	74.4	74.9	0.5
Th ₂ O ₄ C _{2v}			
r(Th-O) Å	2.182	2.197	0.015
r(Th=O) Å	1.895	1.907	0.012
∠Th-O-Th	105.6	104.5	-1.1
∠O-Th-O	74.0	75.2	1.2
Th ₂ O ₄ C _{3v}			
r(Th-O) Å	2.138	2.149	0.011
r(Th-O) Å	2.037	2.091	0.057
∠Th-O-Th	91.2	90.8	-0.4

^a CCSD(T) structure is linear, D_{∞h}.

Table 4.3. Calculated B3LYP Vibrational Frequencies for Th₂O₃ and Th₂O₄.

Freq	B3LYP cm ⁻¹	B3LYP I(km/mol)	Assignment
Th ₂ O ₃ ¹ A' (C _s)			
a'	825.7	354	Th=O stretch
a'	653.9	26	Th-O stretch
a''	539.1	99	Th-O stretch
a'	502.6	43	Th-O stretch
a''	327.3	3	Th-O stretch
a'	183.6	17	O-Th-O bend
a'	137.8	13	O-Th-O bend
a'	81.7	23	O-Th=O bend
a''	81.1	17	O-Th=O bend
Th ₂ O ₃ ¹ A ₁ ' (D _{3h})			
a ₁ '	649.7	0	Th-O sym stretch
e'	555.1	79	Th-O asym stretch
a ₂ ''	412.5	822	Th-O sym stretch
e'	327.9	22	O-Th-O bend
a ₁ '	238.5	0	O-Th-O stretch
e''	236.2	0	Th-O asym stretch
Th ₂ O ₄ ¹ A _g (C _{2h})			
b _u	806.9	373	Th=O asym stretch
a _g	805.8	0	Th=O sym stretch
b _u	611.7	908	Th-O sym stretch
a _g	565.9	0	Th-O sym stretch
a _u	481.1	208	Th-O asym stretch
b _g	363.6	0	Th-O asym stretch
b _u	249.2	38	O-Th-O bend
a _g	202.6	0	O-Th-O bend
b _g	176.2	0	O-Th-O bend
a _g	120.3	0	O-Th=O bend
a _u	101.0	48	O-Th=O bend
b _u	87.3	36	O-Th=O bend

Th₂O₄ ¹A₁ (C_{2v})

a ₁	816.0	332	Th=O sym stretch
b ₂	807.6	61	Th=O asym stretch
b ₂	604.4	833	Th-O sym stretch
a ₁	562.6	9	Th-O sym stretch
b ₁	475.1	213	Th-O asym stretch
a ₂	347.7	0	Th-O asym stretch
a ₁	239.8	33	O-Th-O bend
a ¹	192.1	2	O-Th-O bend
b ₁	161.5	13	O-Th-O bend
b ₂	111.3	39	O-Th=O bend
a ₁	93.5	0	O-Th=O bend
a ₂	87.5	0	O-Th=O bend

Th₂O₄ ³A₁ (C_{3v})

a ₁	630.5	105	Th-O sym stretch
a ₁	563.7	299	Th-O sym stretch
e	538.4	120	Th-O asym stretch
a ₁	479.9	68	Th-O stretch
e	326.5	70	Th-O Bend
a ₁	223.3	0.2	O-Th-O bend
e	200.6	0	O-Th-O bend
e	38.3	32	O-Th-O bend

Table 4.4. Calculated CCSD(T) and B3LYP Vibrational Frequencies for the ThO, ThO₂, Th₂O, and Th₂O₂ Neutral and Charged Species.

Freq	B3LYP cm ⁻¹	B3LYP I(km/mol)	CCSD(T) cm ⁻¹	CCSD(T)- B3LYP	assignment
ThO ¹ Σ (C _{∞v})					
σ	896.1	224	895.5	-0.6	Th-O stretch
ThO ⁺ ² Σ (C _{∞v})					
σ	963.4	189	954.4	-9.0	Th-O stretch
ThO ⁻ ² Σ (C _{∞v})					
σ	789.2	222	804.4	15.2	Th-O stretch
ThO ₂ ¹ A ₁ (C _{2v})					
a ₁	816.2	120	809.7	-6.5	O-Th-O sym stretch
b ₂	760.5	394	755.5	-5.0	O-Th-O asym stretch
a ₁	159.0	35	163.8	4.8	O-Th-O bend
ThO ₂ ⁺ ^a ² B ₂ (C _{2v})					
a ₁	742.7	1	739.2	-3.5	O-Th-O sym stretch
b ₂	614.2	4	607.2	-7.0	O-Th-O asym stretch
a ₁	64.1	44	16.0	-48.1	O-Th-O bend
ThO ₂ ⁻ ² A ₁ (C _{2v})					
a ₁	754.6	187	756.4	1.8	O-Th-O sym stretch
b ₂	695.1	413	692.9	-2.2	O-Th-O asym stretch
a ₁	175.7	29	182.3	6.6	O-Th-O bend
Th ₂ O ³ B ₁ (C _{2v})					
a ₁	562.3	18	538.3	-24.0	Th-O-Th sym stretch
b ₂	392.0	0.1	522.9	130.9	Th-O-Th asym stretch
a ₁	114.5	0.7	107.8	-6.7	bend
Th ₂ O ₂ ¹ A _g (D _{2h})					
a _g	646.2	0	630.4	-15.8	Th-O stretch
b _{1u}	617.5	323	621.4	3.9	Th-O stretch
b _{2u}	537.6	35	520.3	-17.3	Th-O stretch
b _{3g}	381.4	0	356.0	-25.4	Th-O stretch

a_g	199.7	0	198.3	-1.4	O-Th-O bend
b_{3u}	159.0	5	171.1	12.1	O-Th-O bend

^a CCSD(T) structure is linear, $D_{\infty h}$.

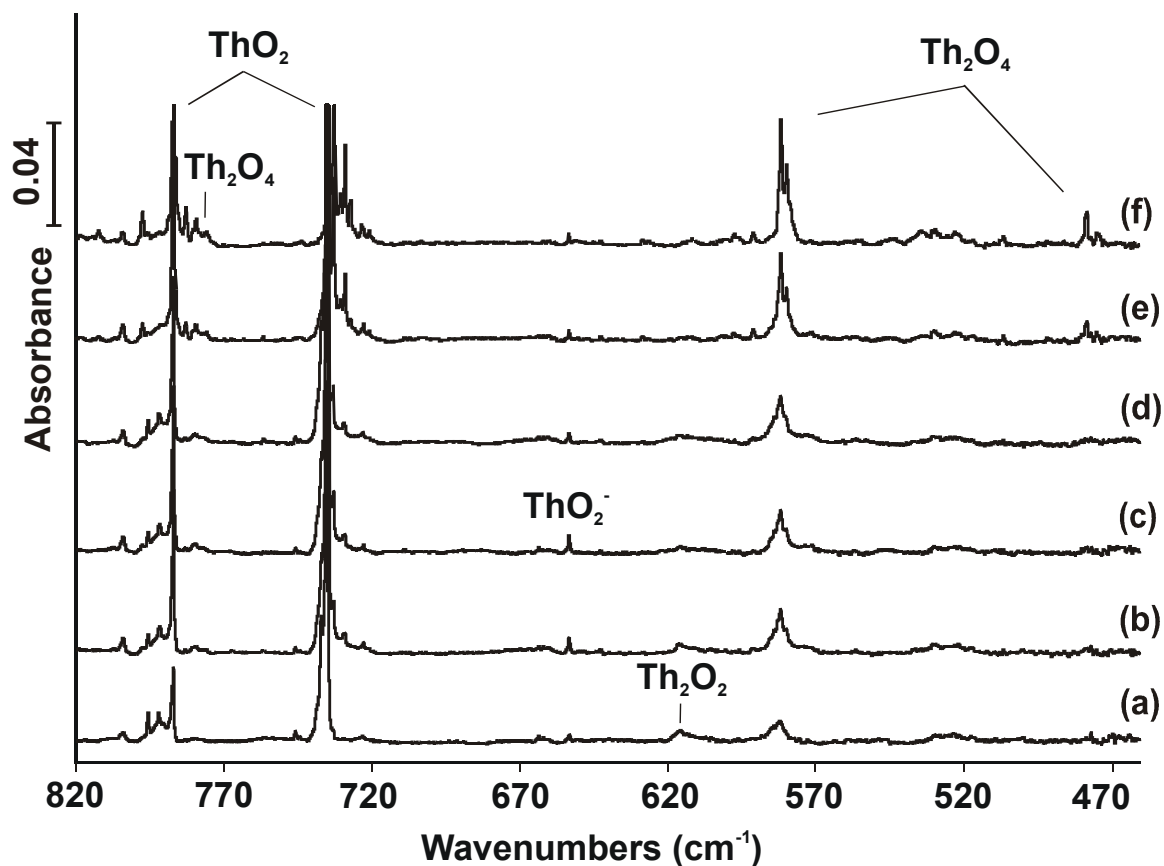


Figure 4.1. Infrared spectra of laser-ablated Th atoms and O₂ reaction products in solid argon: (a) Th + 0.1% O₂ deposition for 60 min; (b) after annealing to 25 K; (c) after $\lambda > 380$ nm irradiation; (d) after $\lambda > 220$ nm irradiation; (e) after annealing to 35 K; (f) after annealing to 40 K.

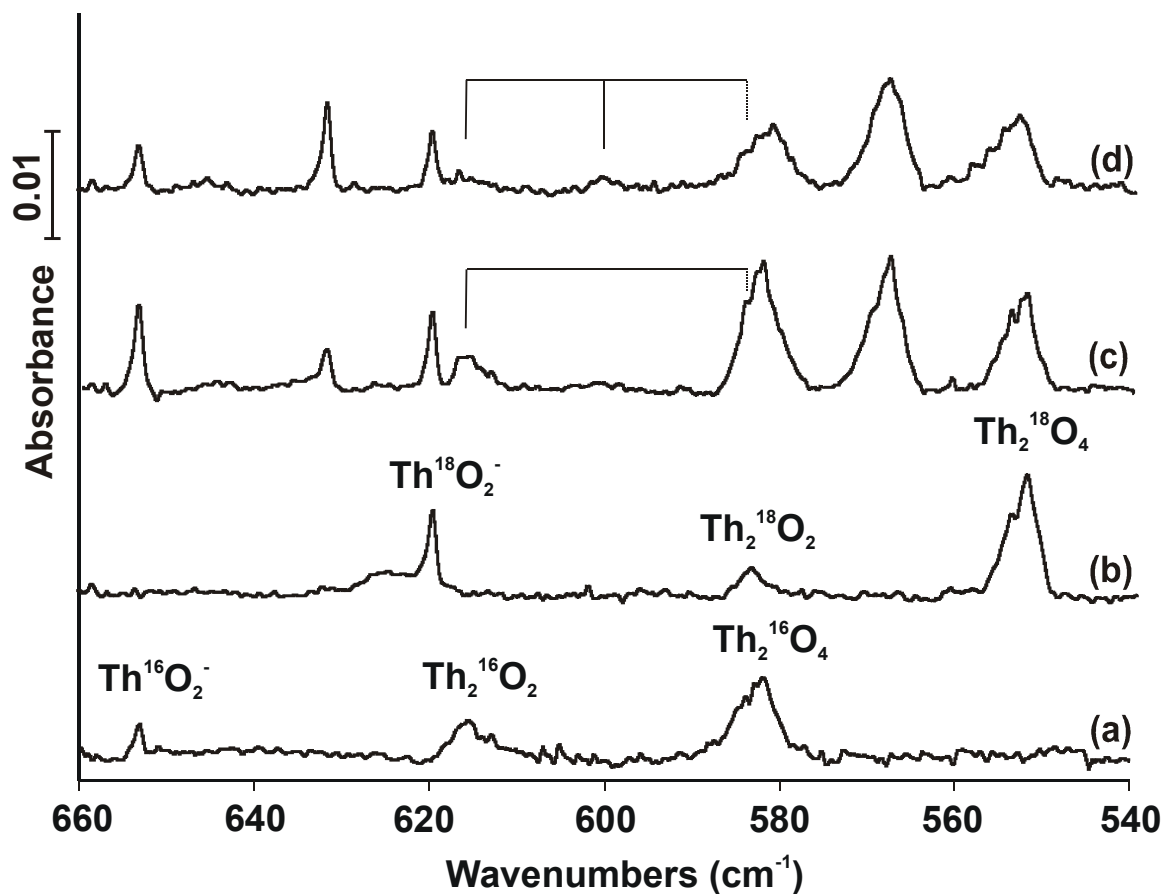
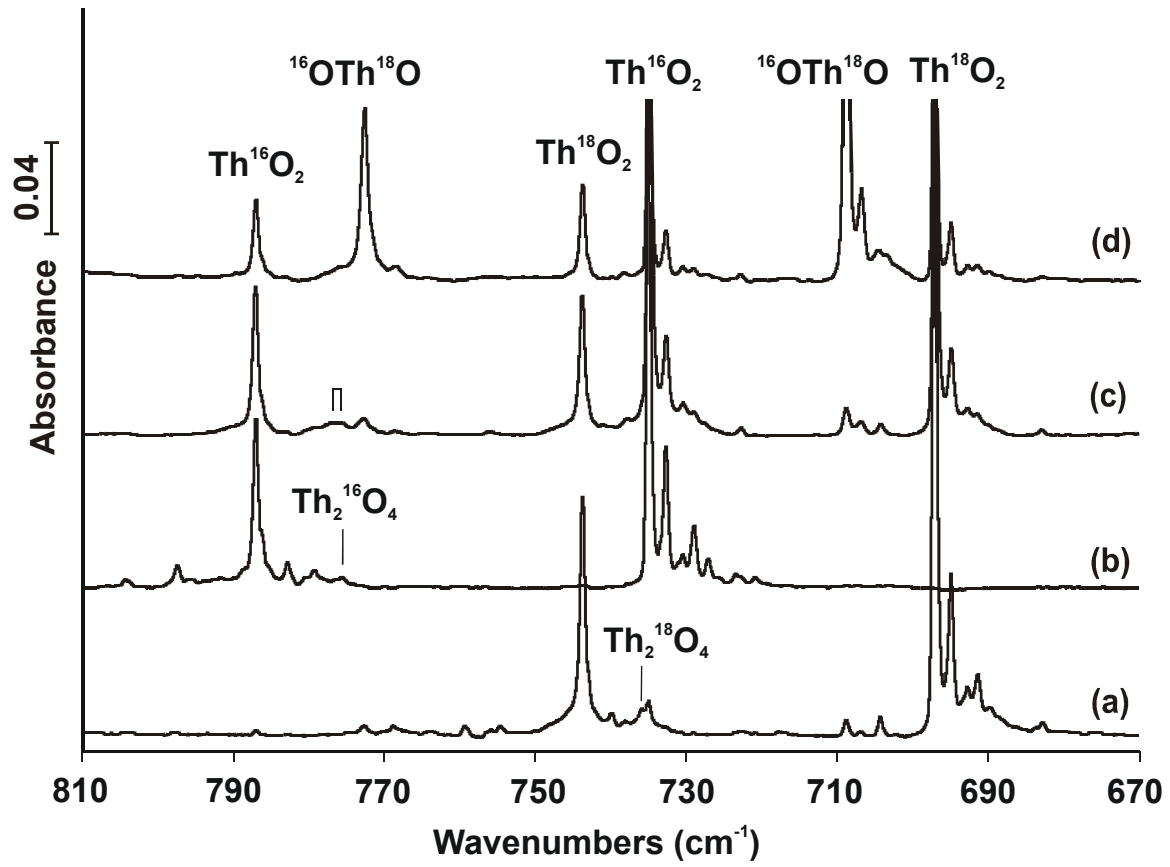


Figure 4.2. Infrared spectra of laser-ablated Th atoms and isotopically substituted O₂ reaction products in solid argon at 10 K after sample deposition for 60min: (a) Th + 0.1% ¹⁶O₂; (b) Th + 0.2% ¹⁸O₂; (c) Th + 0.2% ¹⁶O₂ + 0.2% ¹⁸O₂; (d) Th + 0.125% ¹⁶O₂ + 0.25% ¹⁶O¹⁸O + 0.125% ¹⁸O₂.

part A, Fig 3



Part B, Fig 3

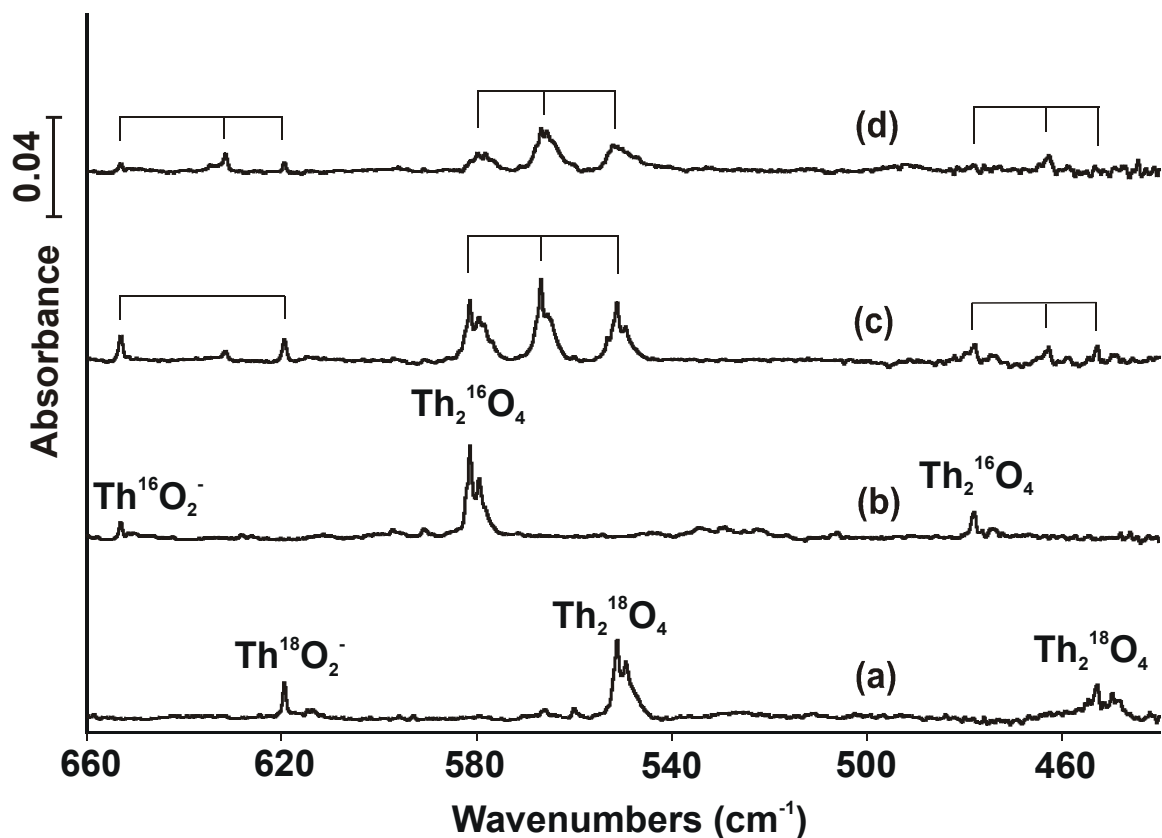


Figure 4.3. Infrared spectra of laser-ablated Th atoms and isotopically substituted O₂ molecule reaction products in solid argon in two spectral regions after annealing to 35 K and recoiling to 10 K. (a) Th + 0.2% ¹⁸O₂; (b) Th + 0.1% ¹⁶O₂; (c) Th + 0.2% ¹⁶O₂ + 0.2% ¹⁸O₂; (d) Th + 0.125% ¹⁶O₂ + 0.25% ¹⁶O¹⁸O + 0.125% ¹⁸O₂.

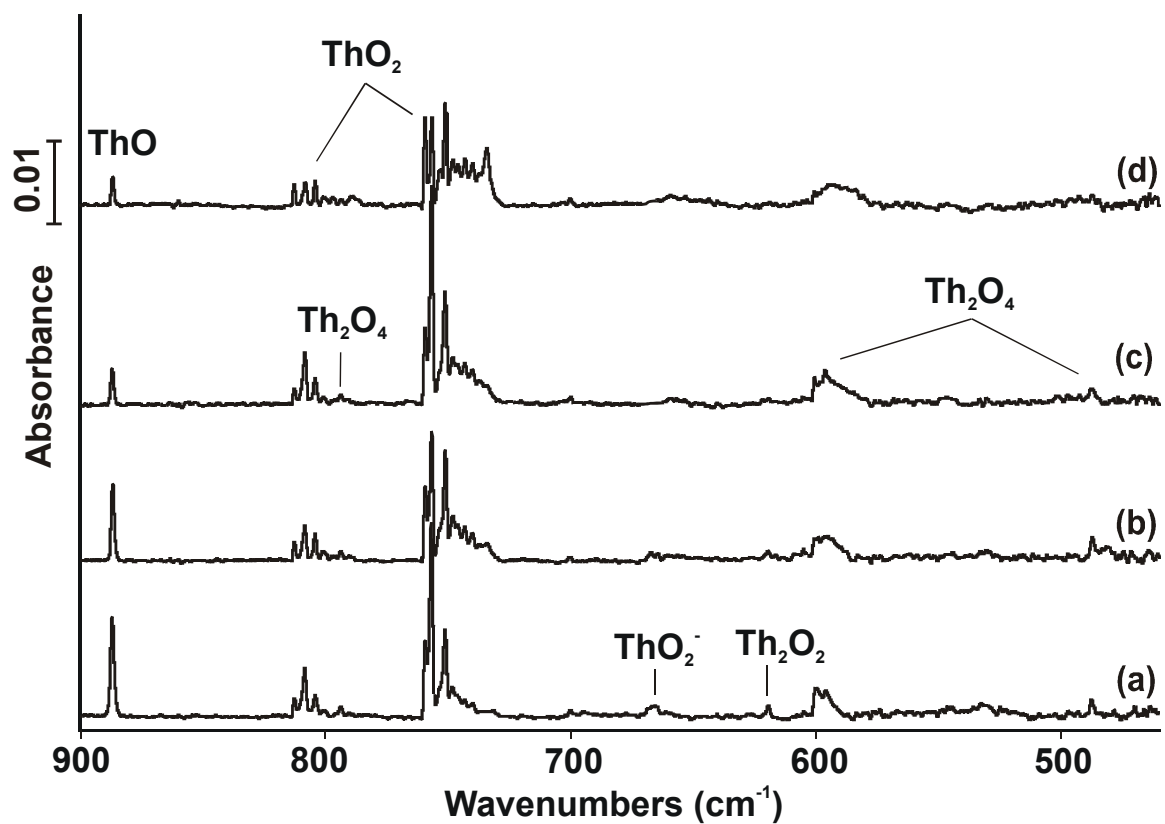


Figure 4. Infrared spectra of laser-ablated Th atoms and O₂ reaction products in solid neon at 4 K: (a) Th + 0.5 % O₂ deposition for 30 min; (b) after annealing to 8 K; (c) after $\lambda > 220$ nm irradiation; (d) after annealing to 10 K.

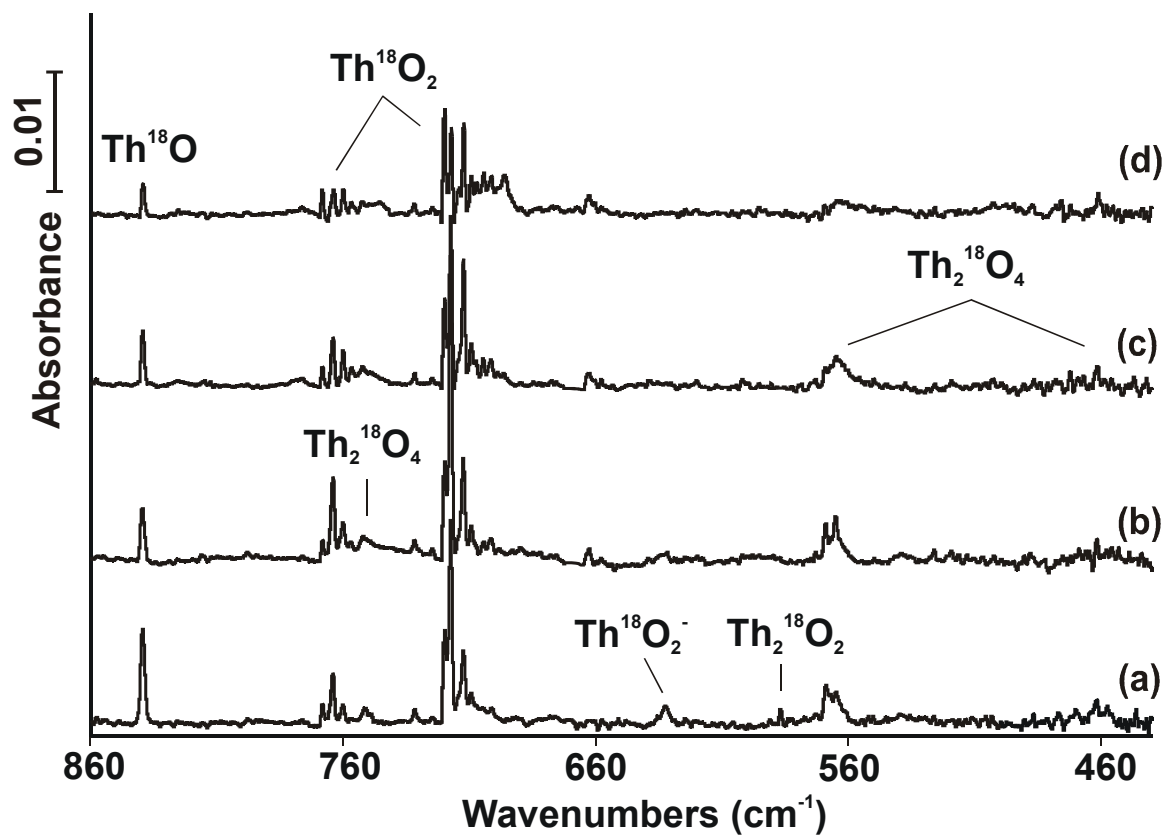
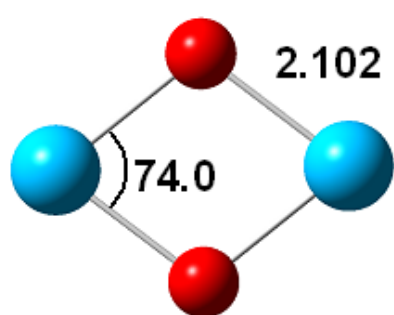
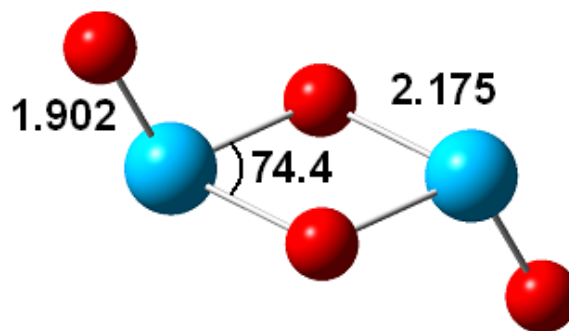


Figure 5. Infrared spectra of laser-ablated Th atoms and $^{18}\text{O}_2$ reaction products in solid neon at 4 K: (a) Th + 0.5 % $^{18}\text{O}_2$ deposition for 30 min; (b) after $\lambda > 220$ nm irradiation; (c) after annealing to 8 K; (d) after annealing to 10 K.



Th₂O₂ D_{2h} ¹A_g



Th₂O₄ C_{2h} ¹A_g

Figure 4.6. Computed structures (B3LYP) for the two major new products of the Th and O₂ reaction following ThO and ThO₂. Bond lengths in Å and bond angles in degrees.

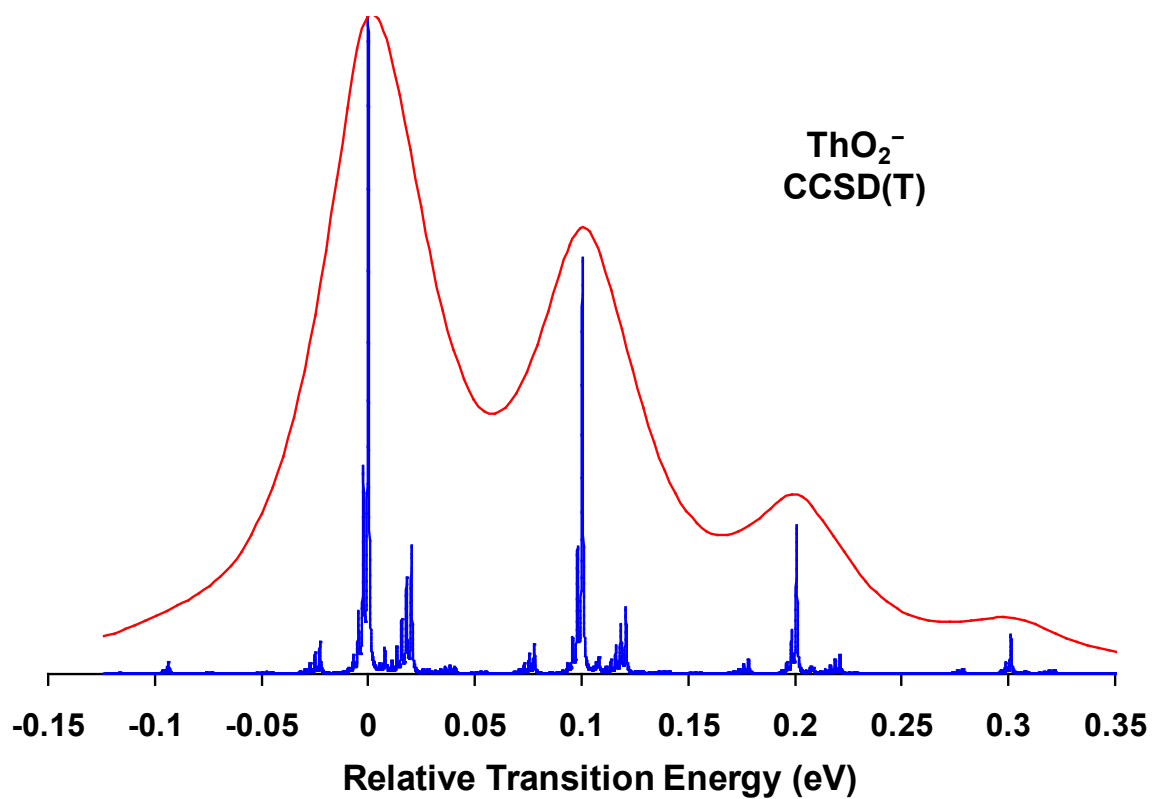


Figure 4.7. Simulated anion photoelectron spectra of ThO₂⁻ (ThO₂⁻/¹A₁ ← ThO₂⁻/²A₁) at the CCSD(T)/aug-cc-pVTZ level at 300 K with full width at half maximum of 5 cm⁻¹ (blue) and 400 cm⁻¹ (red). The transition energy is shown in eV relative to that of the 0-0 transition.

CHAPTER 5

DENSITY FUNCTIONAL THEORY STUDY OF THE COMPLEXATION OF THE URANYL ION WITH ANIONIC PHOSPHATE LIGANDS WITH AND WITHOUT WATER MOLECULES

5.1 Introduction

Phosphates and their derivatives ((RO)₃PO), R = H, alkyl, phenyl) form one of the most important classes of ligands in actinide chemistry. Historically, phosphates played a crucial role in the efforts of the United States to separate various actinide species from irradiated fuels beginning with the Manhattan Project and continuing today with the PUREX (Plutonium and Uranium Recovery by EXtraction) process.^{1,2} Closely related to the reprocessing and separation of actinides from spent fuel is their speciation in and separation from nuclear wastes. Nuclear wastes, primarily stored in large tanks at the Hanford and the Savannah River sites present a grand challenge for remediation and clean-up technologies.^{3,4,5,6} Due to the extremely basic nature of much of the waste at Hanford, actinides are mainly present as insoluble solids that have settled into the sludge and salt-cake layers in the tanks, making their recovery challenging. A consequence of the neutralization of wastes from the original separation process using BiPO₄ has been the formation of actinide phosphate solids such as NaUO₂PO₄. Such complexes are noted for their low to negligible solubility under aqueous conditions, their resistance to intense radiation fields and radiolysis, and their long-term stability to degradation and decomposition.^{7,8} Waste containing actinide and fission products that has leaked from many of the tanks poses a threat to the environment, both to the soil and water supply, thus requiring that they be recovered or immobilized to prevent transport,^{9,10,11} for example, the proposed use of *in situ* phosphate

barriers for the immobilization of actinides,^{12,13,14,15,16,17} Extended X-ray absorption fine structure (EXAFS) spectroscopy on surface media from various Department of Energy facilities including Oak Ridge and Savannah River has shown that uranyl phosphate complexes were present and constitute an appreciable fraction of the adsorbed uranyl species.^{18,19} Complexation of uranyl with phosphate ligands can result in a mineralization process and over 40 phosphate minerals are known from nature,²⁰ including autunite ($\text{Ca}(\text{UO}_2)_2(\text{PO}_4)_2$), parsonite ($\text{Pb}_2(\text{UO}_2)(\text{PO}_4)_2$), tobernite ($\text{Cu}(\text{UO}_2)_2(\text{PO}_4)_2$), and uranocircite ($\text{Ba}(\text{UO}_2)_2(\text{PO}_4)_2$), all with varying degrees of hydration. Monodentate phosphate binding, accompanied by extensive bridging, is commonly observed in experimental x-ray crystal structures of uranyl and other actinide phosphate complexes and minerals, resulting in great structural diversity and extended networks.^{21,22,23,24,25,26,27,28} Mineralization has been considered as an approach to produce actinide phosphates as matrices for long-term radioactive waste storage. Biological organisms can accumulate and precipitate uranyl ions from the environment.^{29,30,31,32} EXAFS measurements of the nature of the uranyl complexes formed at the surfaces of *Bacillus cereus* and *Bacillus sphaericus* cells and spores³³ showed that uranium binding primarily occurs at the phosphoryl residues on the cell walls of these Gram-positive residues, mainly in a monodentate fashion. It was suggested that lipopolysaccharides and phospholipids within the bacterial cell wall can also provide phosphoryl groups for metal ion binding.^{34,35,36,37,38}

Quantum chemical studies of the uranyl ion in both the gas phase and solution phase can provide insight into properties that are difficult to measure experimentally.^{39,40,41} Computational studies of compounds containing heavy elements, particularly actinides, are now possible with the development of density functional methods and relativistic effective core potentials (RECPs).^{41,42,43,44,45} Although there have been numerous studies of uranyl complexation with

ubiquitous ligands such as H_2O , NO_3^- , CO_3^{2-} , and the halides, there has been no systematic computational studies of uranyl complexation with the phosphate series of ligands, including H_2PO_4^- , HPO_4^{2-} , and PO_4^{3-} . Majumdar and Balasubramanian calculated the structure of $\text{UO}_2(\text{HPO}_4) \cdot 3\text{H}_2\text{O}$ at the DFT/B3LYP and MP2 levels with RECPs.⁴⁶ Kubicki et al⁴⁷ predicted the $\text{U}=\text{O}$ and $\text{U}-\text{OH}_2$ distances of the uranyl phosphates $\text{UO}_2(\text{H}_2\text{PO}_4) \cdot 30(\text{H}_2\text{O})$, $\text{UO}_2\text{HPO}_4 \cdot 33(\text{H}_2\text{O})$ and $\text{UO}_2\text{PO}_4 \cdot 30(\text{H}_2\text{O})$ from density functional theory calculations using the B3LYP exchange-correlation functional.

Because of the important role of actinide phosphates, it is important to have speciation information about such complexes including information about the binding of the uranyl to the phosphates in terms of structures and energetics. We present a detailed computational study at the density functional theory (DFT) level of a single UO_2^{2+} complexed with the phosphate anions H_2PO_4^- , HPO_4^{2-} , and PO_4^{3-} with energetics at the correlated second order Møller/Plesset (MP2)⁴⁸ molecular orbital theory level to better understand the structural diversity and the energetic so binding. Anhydrous (no water in first coordination sphere) and hydrated (water present in first coordination sphere) complexes are studied. The structures are chosen to give a broad spectrum of the types of binding at the uranyl in the presence of the phosphate ions and water molecules. The resulting structures can be compared to those in the solid state but represent a broader range of the types of structures that could be found in solution and in gas phase experiments^{49,50,51} used to characterize the binding at uranyl. In addition, self-consistent reaction field calculations⁵² (SCRf) using a number of different solvation models^{53,54,55,56,57,58,59,60,61} have been used to predict the solvation behavior of some of the structures to investigate the thermodynamics of binding, and predict equilibrium constants for the reactions of UO_2^{2+} with phosphate ligands.

5.2 Computational Methods

The geometries of anhydrous and hydrated uranyl phosphate complexes were optimized using gradient corrected density functional theory (DFT) with the hybrid B3LYP exchange-correlation functional.^{62,63} The DFT geometry optimizations and frequency calculations were performed with the 60 electron Stuttgart small core RECPs and the corresponding Stuttgart orbital basis sets for the U atom⁶⁴ and the TZVP orbital basis set for the P, O, and H atoms⁶⁵ following our prior work on uranyl complexes.⁴¹ We eliminated the most diffuse functions in the U basis set, those with an exponent of 0.005 due to difficulties in converging the wave function with such diffuse functions. These diffuse functions were replaced with diffuse s, p, d, and f functions with exponents of 0.013, 0.059, 0.026, and 0.067 respectively, obtained by geometric extrapolation following our previous work.⁴¹ We denote this basis set as TZVP-U(ECP). This approach is consistent with our prior work on uranyl complexes.^{39,41} The second derivatives were calculated to ensure that each structure was a minimum on the potential energy surface. Natural bond orbital (NBO) analyses,^{66,67,68,69,70} including natural population analyses (NPA), were performed at the optimized geometries at the B3LYP DFT level with the program Gaussian 09.

DFT-based approaches have been found to give reasonable structures and vibrational frequencies for actinide complexes,^{71,72} but for the hydration of uranyl, it was found that the MP2 results gave better agreement with experiment for the equilibrium between coordination number (CN) 4 and CN 5.^{39,73,74} Single point MP2 calculations were performed with the aug-cc-pVTZ^{75,76} basis set on H, P, and O and the above uranium basis set and associated ECP following our prior work on the hydration of UO_2^{2+} .³⁹

Solvation effects were included through the use of the conductor-like solvation model (CPCM)^{53,54} as implemented in Gaussian 09,⁷⁷ the polarizable continuum model (IEF-

PCM),^{55,56,60} and the isodensity polarizable continuum model (IPCM)⁵⁶ using a dielectric constant of 78.39 for water. Cavity size effects were studied using the IEF-PCM with the UA0,⁷⁸ UFF,⁷⁸ and Pauling⁷⁹ radii as implemented in Gaussian 03⁸⁰ and 09.⁷⁷ The continuous surface charge (CSC) approach for PCM in Gaussian 09 uses a formalism which ensures continuity of the reaction field, and builds from the original work of York and Karplus.⁸¹ A dielectric constant of 78.39 was used for water as the solvent. Single-point solvation calculations were done at the B3LYP/TZVP-U(ECP) level using the gas phase geometries obtained at this level. The aqueous Gibbs free energy (free energy in aqueous solution) (ΔG_{aq}) was calculated from Equation (1):

$$\Delta G_{\text{aq}} = \Delta G_{\text{gas}} + \Delta G_{\text{solv}} \quad (1)$$

where ΔG_{gas} is the gas phase free energy calculated in the double harmonic approximation using statistical mechanical approaches⁸² and ΔG_{solv} is the aqueous solvation free energy. $\Delta \Delta G_{\text{solv}}$ was calculated with the SCRF approaches given above. The pressure correction to the standard state for a water molecule is -4.3 kcal/mol and for the (H₂O)_n clusters is -4.3/n kcal/mol.

All calculations were performed with the Gaussian 03 or 09 suites of programs on the SGI Altix 350 and Cray XD1 at the Alabama Supercomputer Center and with the NWChem suite of programs,^{83,84} on the massively parallel 1980 processor HP Linux cluster in the Molecular Science Computing Facility in the William R. Wiley Environmental Molecular Sciences laboratory at the Pacific Northwest National Laboratory. All models were constructed using the AMPAC 9™ with Graphical User Interface (AGUI) package.⁸⁵

5.3 Results and Discussion

5.3.1 UO₂²⁺ and the Ligands. In order to understand the nature of the uranyl phosphate complexes, we first predicted the chemical properties of the uncomplexed ligands and UO₂²⁺.

Structural parameters, vibrational frequencies, and NPA charges are listed in Tables 1 and 2. As shown in previous studies, the U=O bond distance for the uncomplexed dication is calculated to be shorter than the bond distance in the complexed species by 0.070 to 0.09 Å. This is because there is no negative charge transfer from equatorial ligands and a large positive NPA charge of 3.26 e on the U center. Also consistent with very short oxo bonds are the high antisymmetric and symmetric U=O stretches, which are slightly higher than the best available values of 1113.0 and 1031.6 cm⁻¹ for free UO₂²⁺ calculated at the CCSD(T) level with a large basis set and including anharmonic and spin orbit corrections.⁴⁰ The small O=U=O bending mode of 151 cm⁻¹ (CCSD(T) value is 174.5 cm⁻¹) shows that the equatorial environment can readily influence this bond angles and lead to deviations from linearity.

The structural parameters for the phosphate ligands H₂PO₄⁻, HPO₄²⁻, and PO₄³⁻ are compared to that of the fully protonated acid H₃PO₄ in Table 1. From the neutral species to the highly anionic PO₄³⁻, the P=O bond distances increase by 0.13 Å; from the neutral to the dianion, the P-O(H) bond distance increases by 0.18 Å. Both trends are consistent with increased negative charge density (Table 2) on the terminal oxygen atoms from the neutral to the trianion. The NPA charge on the central phosphorus atom remains remarkably constant over all species at ~2.45 e. For species containing H atoms, the O-H bond distance remains constant, and the H charge decreases slightly from 0.50 to 0.44 e over the series.

The vibrational modes of the phosphate ligands, particularly the P=O and P-O(H) stretches, show the expected changes due to the changes in the bond distances. The symmetric P=O stretch decreases by ~500 cm⁻¹ from H₃PO₄ to PO₄³⁻, and the antisymmetric stretches decreases by ~400 cm⁻¹ from H₂PO₄⁻ to PO₄³⁻, both consistent with the increase in the P=O bond

distances with more negative charge. Similar decreases in vibrational frequencies are observed for the P-O(H) bonds from H_3PO_4 to HPO_4^{2-} .

The calculated frequencies are compared to those measured from the Raman spectrum of aqueous H_3PO_4 and H_2PO_4^- at concentrations ranging from 0.3 to 9.7 mol-dm⁻³ at 25°C.^{86,87} The fully protonated neutral H_3PO_4 ligand has predicted antisymmetric and symmetric stretches ranging from 1304 to 825 cm⁻¹, in good agreement with the experimental values. Our predicted antisymmetric and symmetric stretching vibrations for the tetra-hydrated H_2PO_4^- ligand range from 1312 to 742 cm⁻¹ and are also in good agreement with the experimental values. Pye and Rudolph⁸⁸ summarized the experimental data on PO_4^{3-} and HPO_4^{2-} in aqueous solution and noted the role of concentration and mis-assignments of the bands. For HPO_4^{2-} , our P=O stretches are consistent with the experimental results within ~ 30 cm⁻¹. For PO_4^{3-} , the calculated results are approximately 100 cm⁻¹ below the experimental values with a splitting between the t_2 and a_1 bands of 105 cm⁻¹ as compared to an experimental splitting of 73 cm⁻¹. The low calculated values for PO_4^{3-} are due to the calculations being done for an isolated gas phase ion with a high negative charge and the experiments being done in aqueous solution which stabilizes the anion and increases the P-O stretches.

5.3.2 Mono- and Di-ligand Anhydrous Uranyl Phosphate Complexes. Structural parameters and vibrational frequencies for the isolated gas-phase mono-ligand complexes, $[\text{UO}_2(\text{H}_2\text{PO}_4)]^+$, $\text{UO}_2(\text{HPO}_4)$, and $[\text{UO}_2(\text{PO}_4)]^-$ and the di-ligand complexes, $\text{UO}_2(\text{H}_2\text{PO}_4)_2$, $[\text{UO}_2(\text{HPO}_4)_2]^{2-}$, and $[\text{UO}_2(\text{PO}_4)_2]^{4-}$ are listed in Table 3 and structures are shown in Figures 1, 2 and 3. All of these structures show bidentate binding of the ligand to the uranium.

Charge transfer to the metal center is expected to be important due to the increase in the negative charge on the ligand from the -1 to -3 and will manifest itself in changes in the U=O

bond distances and the corresponding stretching frequencies. For the mono-ligand complexes due to increasing negative charge donation to the positive U center, the uranyl U=O distance increases by 0.07 Å with increasing negative charge on the ligand leading to a shift to lower frequencies for the symmetric and antisymmetric U=O stretches. The antisymmetric stretch decreases by 57 cm⁻¹ from [UO₂(H₂PO₄)]⁺ to UO₂(HPO₄), and the decrease almost doubles (103 cm⁻¹) from UO₂(HPO₄) to [UO₂(PO₄)]⁻. The symmetric stretch frequencies also decrease with smaller shifts of 48 cm⁻¹ and 51 cm⁻¹, respectively. Thus the splitting between the antisymmetric and symmetric U=O stretches decreases on ligand binding from that in the free uranyl. The actual values for the frequencies will be too high as compared to experiment predominantly due to neglect of other water molecules in the inner sphere and outer-sphere ligand influences.

As the U=O bond lengths increase with increasing negative charge on the ligand, the equatorial U-O bond lengths decrease as the overall charge changes from +1 to -1, due to enhanced electron donation to the electrophilic uranium center. The U-O bond length decreases by 0.16 Å, with the largest change of 0.09 Å occurring from [UO₂(H₂PO₄)]⁺ to UO₂(HPO₄). At the same time, the P-O_{bound} distances increase by 0.14 Å. The P-O_{terminal} and P-O_(-H) bond distance increase for the latter two complexes (neutral/anionic) by only 0.02 and 0.05 Å, respectively.

We have previously discussed the role of the bite angle in the interaction of anionic ligands with uranyl.⁴¹ The bite angle of the bound phosphate ligand (O-P-O) decreases by ~11° as the overall charge on the complex becomes more negative, and the O=U=O angle deviates from linearity by ~17°. This is due to the relatively small O=U=O bending force constant and the minimization of electrostatic repulsions of the negatively charged uranyl oxo oxygens with the negatively charged ligand oxygens.

The di-ligand complexes, $\text{UO}_2(\text{H}_2\text{PO}_4)_2$, $[\text{UO}_2(\text{HPO}_4)_2]^{2-}$, and $[\text{UO}_2(\text{PO}_4)_2]^{4-}$, have C_i , C_{2v} , and D_{2h} symmetry, respectively. Similar to the mono-ligand complexes, the U=O bond distance increases as the negative charge on the ligand increases due to a greater amount of charge donation to the uranium center. There is an increase of 0.06 Å from $\text{UO}_2(\text{H}_2\text{PO}_4)_2$ to $[\text{UO}_2(\text{PO}_4)_2]^{4-}$. For a particular ligand, the uranyl oxo bond distance is longer in the di-ligand complex than in the mono-ligand complex by ~0.01 to 0.02 Å consistent with more charge transfer in the di-ligand complex, although most of the increase is due to adding the first ligand. The increases in the U=O bond distance correlate directly with decreases in the vibrational frequencies. The UO_2 antisymmetric and symmetric stretches decrease, respectively, by 133 and 126 cm^{-1} from the neutral complex to the tetra-anion, indicative of longer, weaker U=O oxo bonds. For a particular ligand, the frequencies for the di-ligand complexes are lower than the mono-ligand complexes, consistent with the trends in the oxo bond distances.

The equatorial bond U-O bond distances in the di-ligand complexes are systematically longer than in corresponding monoligand complexes. These distances range decrease by 0.06 Å from the neutral to the -4 anion, and the decrease is significantly smaller than that observed across the mono-ligand series (0.16 Å). This smaller decrease can be attributed to the increased negative charge on the latter complexes (-2 and -4), resulting in more delocalization of charge. The $\text{P-O}_{\text{bound}}$ distances also increase for the di-ligand series by 0.10 Å as there is more negative charge, slightly smaller than that observed for the mono-ligand series (0.14 Å). Once again, the $\text{P-O}_{\text{terminal}}$ and $\text{P-O}_{(-\text{H})}$ increase by a smaller extent, 0.04 and 0.07 Å, respectively.

The O-P-O bite angle decreases down the di-ligand series by an amount comparable to that in the mono-ligand series (~10°). However, the actual O-P-O bite angles are 6 to 7° larger than the analogous angles in the mono-ligand series. Due to the symmetry of the di-ligand

complexes with the phosphate ligands trans to each other, the O=U=O angle does not deviate from linearity in all three di-ligand complexes.

Natural population analysis (NPA) atomic charges⁶⁶ for the mono-ligand and di-ligand complexes are given in Table 4. Particular emphasis is focused on the U and O (oxo) atomic charges. In both types of complexes, as the overall negative charge on the complex increases, the positive charge on the U center decreases. Significant charge transfer to the oxo oxygen atoms occurs, making them progressively less positive. The group charge on the uranyl decreases from +1.44 e to +0.99 e for the complexes $[\text{UO}_2(\text{H}_2\text{PO}_4)]^+$ to $[\text{UO}_2(\text{PO}_4)]^-$. Likewise, the group charge decreases from +1.22 e to +0.89 e from $\text{UO}_2(\text{H}_2\text{PO}_4)_2$ to $[\text{UO}_2(\text{PO}_4)_2]^{4-}$. As expected, significant charge transfer occurs in all cases (as the uncomplexed UO_2 group charge is +2.0 e), with more occurring for the di-ligand complexes due to greater overall negative charge on the complex. Due to a greater amount of negative charge localized on the U=O bonds, the uranyl bond distance increases and the uranyl vibrational frequencies decrease.

5.3.3 Tri- and Tetra-ligand Anhydrous Uranyl Phosphate Complexes. The anionic tri- and tetra-ligand complexes are shown in Figures 1, 2 and 3. Structural parameters are listed in Table 3 for the tri- and Tetra-ligand ligand complexes. All of the tri-ligand complexes exhibit some degree of monodentate phosphate binding rather than the bidentate binding predicted for the mono and di-ligand complexes. The lowest energy $[\text{UO}_2(\text{H}_2\text{PO}_4)_3]^-$ complex contains two bidentate phosphate ligands and one monodentate phosphate ligand stabilized by an equatorial hydrogen bond to the oxygen atom of a neighboring phosphate. The U=O bond distance increases as compared to the corresponding di-ligand complex by 0.01 Å. Two types of U- O_{eq} bonds are present due to the presence of both monodentate and bidentate coordination. The average bidentate U-O distance is 2.52 Å, which is 0.11 Å longer than in the analogous di-ligand

complex, likely due to steric crowding in the equatorial plane. The monodentate U-O distance is much shorter, as the ligand can approach closer without the restriction of bite angle, and because the negative charge is more localized on a single oxygen.

Both the $[\text{UO}_2(\text{HPO}_4)_3]^{4-}$ and $[\text{UO}_2(\text{PO}_4)_3]^{7-}$ complexes are characterized by only monodentate phosphate binding in contrast to the complexes with fewer ligands. A key structural feature present in the $[\text{UO}_2(\text{HPO}_4)_3]^{4-}$ that we believe has never been observed previously in a computational study of inner shell ligands⁸⁹ is intramolecular hydrogen-bonding that occurs between the hydrogen atoms of the phosphate ligands and the uranyl terminal oxygen atoms. It has been explained previously that the lack of Lewis base interaction at the oxygen atoms of the uranyl moiety is due to the low partial negative charges on these atoms.^{39,90,91} Thus, uranyl complexes tend to form extended sheets in the crystal.^{22,23,92,93,94} The oxo oxygen can act as a nucleophile as shown by the large partial negative charge of -0.95 e on the oxo ligands (Table 4) in $[\text{UO}_2(\text{HPO}_4)_3]^{4-}$. In $[\text{UO}_2(\text{HPO}_4)_3]^{4-}$, the U=O bond distance is 0.03 Å longer than in the analogous di-ligand complex due to increased charge donation to the U. As all of the phosphate ligands are bound in a monodentate fashion, the average U-O_{equatorial} distance is significantly shorter than that in the di-ligand complex by 0.15 Å. The average hydrogen bond distance between the phosphate hydrogen atoms and the uranyl oxygen atoms is 2.20 Å.

The $[\text{UO}_2(\text{H}_2\text{PO}_4)_4]^{2-}$ and $[\text{UO}_2(\text{HPO}_4)_4]^{6-}$ complexes are characterized by only monodentate phosphate binding. The $[\text{UO}_2(\text{H}_2\text{PO}_4)_4]^{2-}$ with only monodentate binding has CN 4 and two phosphate ligands are stabilized by an equatorial hydrogen bond to the oxygen atom of a neighboring phosphate. $[\text{UO}_2(\text{H}_2\text{PO}_4)_4]^{2-}$ has intramolecular hydrogen bonding between a hydrogen atom of each phosphate ligand and the uranyl terminal oxygen atoms as predicted in $[\text{UO}_2(\text{HPO}_4)_3]^{4-}$. The U=O bond distance increases as compared to the corresponding tri-ligand

complex by 0.05 Å and by 0.07 Å for the di-ligand complex. The monodentate U-O_{phos} distance of the tetra-ligand complex is longer than that of the tri-ligand complex by 0.03 Å and shorter than the bidentate U-O_{phos} distance of the tri-ligand complex by 0.25 Å. [UO₂(HPO₄)₄]⁶⁻ with only monodentate binding also has CN 4 and the phosphate ligands are stabilized by equatorial hydrogen bonds to the oxygen atoms of a neighboring phosphate. In [UO₂(HPO₄)₄]⁶⁻, the U=O bond distance is 0.03 Å shorter than in the analogous tri-ligand complex and is the same as the di-ligand complex. The monodentate U-O_{phos} distance of the tetra-ligand complex is longer than that of the tri-ligand complex by 0.18 Å, and 0.03 Å longer than the bidentate U-O_{phos} distance of the di-ligand complex.

5.3.4 Hydrated Phosphate Complexes. Under aqueous conditions, unoccupied coordination sites in the first shell of the anhydrous uranyl phosphates, particularly the mono-ligand and di-ligand species, will be filled by water molecules. Pure aquo ion complexes are believed to be the dominant species in the presence of weakly coordinating anions, such as ClO₄⁻.^{95,96} However, complexes with ligands and water are common when strongly coordinating ions are present, and water may even be excluded entirely from the first coordination sphere. The binding of explicit water molecules was investigated for the mono- and di-ligand phosphate complexes involving H₂PO₄⁻, HPO₄²⁻, and PO₄³⁻. In these complexes, adequate steric space is available in the equatorial region of the uranyl dication to accommodate multiple water molecules. Key geometry parameters and vibrational frequencies for the hydrated complexes [UO₂(H₂PO₄)(H₂O)_n]⁺, UO₂(HPO₄)(H₂O)_n and [UO₂(PO₄)(H₂O)_n]⁻ (*n* = 1 - 4) are given in Table 5 and the structures for *n* = 3 and 4 are shown in Figures 1, 2, and 3.

In the [UO₂(H₂PO₄)(H₂O)_n]⁺ complexes, up to three water molecules can readily be accommodated while the H₂PO₄⁻ ligands remains bidentate as in the anhydrous complex for a

total equatorial coordination number (CN) of 5. The value $r(\text{U}=\text{O})$ shows only a small dependence on the number of water molecules and increases by only 0.01 Å from $n = 1$ to $n = 3$. The equatorial $\text{U}-\text{O}_{\text{phos}}$ and $\text{U}-\text{OH}_2$ distances also increase by 0.08 Å and 0.06 Å, respectively. The longer $\text{U}-\text{OH}_2$ bond distances indicate that the water molecules are more weakly bound than the anionic phosphate ligands, consistent with the charge interactions. The $\text{O}=\text{U}=\text{O}$ angle is significantly non-linear for the $n = 1$ to $n = 3$ complexes at $\sim 170^\circ$. The symmetric and antisymmetric uranyl stretches in these three complexes follow expected trends in terms of electron donation. The antisymmetric uranyl stretch decreases by 33 cm^{-1} and the symmetric stretch decreases by 28 cm^{-1} from the anhydrous ion upon binding of three water molecules. These relatively small decreases are consistent with the relatively weak Lewis acid interactions of the water molecules.

The $n = 4$ complex $[\text{UO}_2(\text{H}_2\text{PO}_4)(\text{H}_2\text{O})_4]^+$ (Figure 1) exhibits the expected equatorial CN 5 so the phosphate ligand is now bound in a monodentate fashion. A hydrogen bond exists between one of the waters and the unbound terminal $\text{P}=\text{O}$ moiety of the phosphate ligand. As a result, the $\text{H}-\text{O}$ bond in this water molecule is elongated, creating a ‘hydroxide-like’ species which is bound to the uranyl center at a shortened $\text{U}-\text{O}$ distance, as compared to the other $\text{U}-\text{OH}_2$ distances. Due to the monodentate binding, the $\text{U}=\text{O}$ and $\text{U}-\text{O}_{\text{phos}}$ distances do not follow the previous trends.

Due to the increased negative charge on the HPO_4^{2-} ligand, the potential to abstract protons from bound water molecules in $\text{UO}_2(\text{HPO}_4)(\text{H}_2\text{O})_n$ complexes to form OH^- and H_2PO_4^- ligands to equalize the buildup of regions of negative charge exists. The $n = 1$ and $n = 2$ complexes contain equatorially bound, discrete water molecules. The $\text{U}=\text{O}$ and $\text{U}-\text{OH}_2$ distances are longer than in the analogous H_2PO_4^- complexes by $\sim 0.02 \text{ Å}$ and $\sim 0.07 \text{ Å}$, respectively.

However, the U-O_{phos} distances for bidentate binding are significantly shorter by 0.09 and 0.10 Å, respectively, due to tighter binding of the anion. The O=U=O angle is significantly bent in both cases at ~164°. The antisymmetric and symmetric uranyl stretches follow the expected decreasing trend from $n = 1$ to $n = 2$ and are substantially lower by ~50 cm⁻¹ as compared to the analogous H₂PO₄⁻ complexes.

The nominal UO₂(HPO₄)(H₂O)₃ complex displays a unique structure, as shown in Figure 2. The stable phosphate ligand in this complex is the H₂PO₄⁻ moiety, not HPO₄²⁻. In addition, the H₂PO₄⁻ ligand is bound in a monodentate fashion. The H₂PO₄⁻ ligand results from the abstraction of a proton from a water molecule to form a discrete hydroxide ligand bound to uranium at a short U-O bond distance. The monodentate mode is stabilized by a hydrogen bond from the terminal P=O group to a water molecule hydrogen, again resulting in an elongated H-OH water bond and a ‘hydroxide-like’ interaction with the uranyl center. The U-O_{phos} monodentate distance is long compared to the $n = 1$ and $n = 2$ structures as the ligand is H₂PO₄⁻, not HPO₄²⁻. The O=U=O is more nearly linear as compared to the other two structures by ~8 to 9°. The U-O stretches decrease as compared to the $n = 1$ and $n = 2$ complexes. Majumdar and Balasubramanian calculated the structure of UO₂(HPO₄)(H₂O)₃ (CN =5) and did not find a structure with abstraction of a proton from a water to form a hydroxide ligand.⁴⁶ We optimized their structure and found it to be ~ 15 kcal/mol higher in energy than our CN = 5 structure resulting from proton transfer.

The lowest energy structure predicted for UO₂(HPO₄)(H₂O)₄ is, on first glance, counterintuitive based on a comparison to the $n = 3$ complex. As shown in Figure 2, the ligands retain their identities. The HPO₄²⁻ ligand is bound in a bidentate fashion to the uranyl and three water molecules are bound in the remaining sites for an equatorial CN 5. The remaining water

molecule is displaced into the second coordination sphere. This is consistent with our discovery of another higher energy structure containing three bound waters, a bound hydroxide ligand, and a monodentate H_2PO_4^- ligand (proton abstraction occurred in this higher energy structure). This suggests that the inclusion of explicit second shell water molecules could lead to different amounts of proton transfer. The $\text{U}=\text{O}$, $\text{U}-\text{O}_{\text{phos}}$, and $\text{U}-\text{OH}_2$ distances follow the trends of the $n = 1$ and $n = 2$ series, and the $\text{O}=\text{U}=\text{O}$ is bent with an angle of 168° . The uranyl stretching frequencies are consistent with the values of other complexes.

Key geometry and vibrational parameters for the di-ligand $\text{UO}_2(\text{H}_2\text{PO}_4)_2(\text{H}_2\text{O})_n$ and $[\text{UO}_2(\text{HPO}_4)_2(\text{H}_2\text{O})_n]^{2-}$ hydrated complexes ($n = 1 - 3$) are given in Table 6. Fewer water molecules can be accommodated equatorially compared to the monoligand complexes due to the steric effect of the second phosphate. In these di-ligand complexes, bidentate coordination modes for the phosphate ligands are more common. The structure of $\text{UO}_2(\text{H}_2\text{PO}_4)_2(\text{H}_2\text{O})$ has bidentate H_2PO_4^- ligands and a discrete, bound water molecule, resulting in the expected CN 5 (Figure 1). Although it appears that a second water molecule may potentially fit *trans* to the water molecule in $\text{UO}_2(\text{H}_2\text{PO}_4)_2(\text{H}_2\text{O})$ resulting in CN 6, the structure of $\text{UO}_2(\text{H}_2\text{PO}_4)_2(\text{H}_2\text{O})_2$ reveals that this is not the case (Figure 1). The lowest energy structure contains one bidentate H_2PO_4^- ligand and a bound H_2O molecule. The second H_2PO_4^- ligand is bound in a monodentate fashion and is stabilized by a terminal $\text{P}=\text{O}$ hydrogen bond interaction with the second water molecule. The result of this interaction is an elongated $\text{H}-\text{OH}$ bond in the water and a ‘hydroxide-like’ $\text{U}-\text{O}$ interaction with the uranyl. Overall, the equatorial CN is 5. The normal $\text{U}-\text{OH}_2$ distance is 2.59 \AA whereas the ‘hydroxide-like’ $\text{U}-\text{O}$ distance is 2.50 \AA , which is longer than the $\text{U}-\text{OH}$ interaction distance of 2.13 \AA predicted for the proton transfer structure $\text{UO}_2(\text{HPO}_4)(\text{H}_2\text{O})_3$ as described above. The $\text{UO}_2(\text{H}_2\text{PO}_4)_2(\text{H}_2\text{O})_3$ complex is structurally

analogous to the $\text{UO}_2(\text{H}_2\text{PO}_4)_2(\text{H}_2\text{O})_2$ complex, with the exception that both H_2PO_4^- ligands are bound in a monodentate fashion. The elongated H-OH distances are due to interaction between the terminal P=O groups in both H_2PO_4^- . The typical U-OH₂ distance in $\text{UO}_2(\text{H}_2\text{PO}_4)_2(\text{H}_2\text{O})_3$ is 2.60 Å whereas the average ‘hydroxide-like’ U-O distance is 2.48 Å which is 0.01 Å shorter than that predicted for the ‘hydroxide-like’ U-O distance in $\text{UO}_2(\text{H}_2\text{PO}_4)_2(\text{H}_2\text{O})_2$. In both $n = 2$ and $n = 3$ complexes, equatorial CN 5 is maintained.

The $[\text{UO}_2(\text{HPO}_4)_2(\text{H}_2\text{O})_n]^{2-}$ ($n = 1 - 3$) complexes as a group all possess some degree of monodentate phosphate binding (Figure 2). The $[\text{UO}_2(\text{HPO}_4)_2(\text{H}_2\text{O})]^{2-}$ complex contains one bidentate phosphate and one monodentate phosphate. There is a substantial amount of localized negative charge, resulting in the abstraction of protons from the water ligand. The bidentate ligand is HPO_4^{2-} , whereas the monodentate ligand is H_2PO_4^- , formed by proton abstraction from a water molecule which formed an OH⁻ ligand. A hydroxide ligand is bound to uranium with a short U-O distance and is hydrogen bonded equatorially to H_2PO_4^- . Similar to the $n = 1$ structure, the $n = 2$ structure contains a bidentate HPO_4^{2-} , a monodentate H_2PO_4^- , and a bound hydroxide arising from proton abstraction to form the H_2PO_4^- . The remaining water molecule acts as a second sphere ligand, hydrogen bound to the hydroxide and HPO_4^{2-} ligands so the equatorial CN is 4. An H atom from monodentate H_2PO_4^- participates in a close interaction with a uranyl oxo ligand.

Both phosphate ligands exist as H_2PO_4^- moieties in the structure of $[\text{UO}_2(\text{HPO}_4)_2(\text{H}_2\text{O})_3]^{2-}$, and thus two hydroxide ligands are formed which are bound to the uranyl. The hydroxides are hydrogen bonded to H atoms from the phosphate ligands and the CN is 4. The remaining water molecule acts as a second sphere water molecule, and is hydrogen bonded to the hydroxide ligands. Thus, each hydroxide oxygen atoms acts as a hydrogen-bond

acceptor from two distinct sites. As in the $n = 2$ complex, one of phosphate hydrogen atoms participates in a close interaction with a uranyl oxo ligand. For the $[\text{UO}_2(\text{HPO}_4)_2(\text{H}_2\text{O})_n]^{2-}$ ($n = 1 - 3$) complexes, the equatorial CN is 4 rather than 5 as was primarily observed for the other complexes and as is typical in many uranyl structures.

Two other geometries were studied for the $[\text{UO}_2(\text{HPO}_4)_2(\text{H}_2\text{O})_3]^{2-}$ complex as shown in Figure 2. There is a structure 5.0 kcal/mol higher in energy than the lowest energy complex which contains two monodentate H_2PO_4^- ligands and results from the abstraction of a proton by each HPO_4^{2-} ligand from two of the water ligands. Both H_2PO_4^- moieties have a phosphate H atom participating in a close interaction to the same O atom of the uranyl oxo ligand. Similar to the lowest energy structure, two hydroxide ligands are bound to the uranyl and are also hydrogen bonded to H atoms from the phosphate ligands and the equatorial CN is 4. The remaining water molecule acts as a second sphere water molecule, and unlike the low energy structure, is positioned on the opposite side of the uranyl oxo ligand with its H atoms participating in a close interaction with O atoms of both phosphate ligands. The third structure is 31.0 kcal/mol higher in energy than the lowest energy complex. It contains a monodentate H_2PO_4^- ligand, a monodentate HPO_4^{2-} ligand, two water ligands and a hydroxide ligand resulting in an equatorial CN of 5. The H atom of the H_2PO_4^- moiety shares a hydrogen bond with the O atom of the hydroxide ligand bonded to the U. The H atom of one water is hydrogen bonded to the O_{phos} atom of HPO_4^{2-} that is bonded to U. The H atom of the second water is hydrogen bonded to the O atom of the hydroxide ligand of the HPO_4^{2-} moiety.

The $[\text{UO}_2(\text{PO}_4)(\text{H}_2\text{O})_n]^-$ ($n = 2, 4$) complexes each have an equatorial CN of 4 and bidentate phosphate binding. In contrast, the $n = 3$ complex has CN 5 with bidentate phosphate binding (Figure 3). The value of $r(\text{U}=\text{O})$ exhibits only a small dependence on the number of

water molecules, decreasing from $n = 1$ to 2, increasing to $n = 3$ complex, and decreasing in the $n = 4$ complex. The equatorial U-O_{phos} distances increase by 0.06 Å from $n = 1$ to $n = 4$, and the U-OH₂ distances increase by 0.17 Å from $n = 1$ to $n = 3$ and then decrease in the $n = 4$ structure. The O=U=O angle is significantly non-linear for the $n = 1$ to $n = 4$ complexes at $\sim 160^\circ$. The antisymmetric uranyl stretch increases by 40 cm⁻¹ from the anhydrous ion upon binding of four water molecules. The symmetric uranyl stretch has a range of 58 cm⁻¹ from one to four water molecules. For the $n = 1$ complex [UO₂(PO₄)(H₂O)]⁻, the water molecule participates in a hydrogen bond with an oxygen of the phosphate ligand complexed to UO₂²⁺. For the $n = 2$ complex [UO₂(PO₄)(H₂O)₂]⁻, the two water molecules each participate in a hydrogen bonds with an oxygen of the phosphate ligand complexed to UO₂²⁺. For the $n = 3$ complex [UO₂(PO₄)(H₂O)₃]⁻, one of the three water molecules in the inner coordination shell participates in a hydrogen bond with an oxygen of the phosphate ligand complexed to UO₂²⁺, and a second water participates in a hydrogen bond with an oxygen of the UO₂²⁺ complex. The two water molecule in the $n = 4$ complex [UO₂(PO₄)(H₂O)₄]⁻ remain in the first solvation shell and two are in an outer shell with hydrogen bonding as found in [UO₂(PO₄)(H₂O)₃]⁻.

The [UO₂(PO₄)₂(H₂O)_{*n*}]⁴⁻ ($n = 1, 2$) complexes both have a equatorial CN 4 (Figure 3). $r(\text{U}=\text{O})$ again shows essentially no small dependence on the number of water molecules from $n = 1$ to 2. The O=U=O angle is slightly non-linear for the $n = 2$ complex at 174° . The antisymmetric uranyl stretch increases by 22 cm⁻¹ and the symmetric uranyl stretch increases by 14 cm⁻¹ upon binding the second water molecule. In the $n = 1$ complex [UO₂(PO₄)₂(H₂O)]⁻, both phosphate ligands are bidentate bound to the uranyl dication so the water molecule in the second sphere is hydrogen bond to an oxygen of the phosphate ligand complexed to UO₂²⁺ as in

$[\text{UO}_2(\text{PO}_4)(\text{H}_2\text{O})_n]^-$. For $n = 2$, there is a proton transfer to a PO_4^{3-} group leading to the formation of an OH^- bonded to the UO_2^{2+} and one monodentate HPO_4^{2-} and one bidentate PO_4^{3-} .

5.3.5 Comparison to Experiment. We first compare our calculated distances to those from various crystal structures. The crystal structures of $[\text{UO}_2(\text{H}_2\text{PO}_4)_2(\text{H}_2\text{O})]_2 \cdot (18\text{-crown-6}) \cdot 5\text{H}_2\text{O}$ and $\text{UO}_2(\text{H}_2\text{PO}_4)_2(\text{H}_2\text{O}) \cdot (18\text{-crown-6}) \cdot 3\text{H}_2\text{O}$ ²¹ have monodentate phosphate ligand binding to the uranium atom and average $\text{U}=\text{O}$ bond distances of 1.76 and 1.77 Å respectively. The average experimental $\text{P}-\text{O}_{\text{bound}}$ bond lengths are 1.57 and 1.58 Å respectively, and the average $\text{P}-\text{O}_{\text{term}}$ bond lengths are 1.5 and 1.49 Å respectively. The UO_2^{2+} group is linear within 3° of 180°. Our predicted $\text{UO}_2(\text{H}_2\text{PO}_4)_2(\text{H}_2\text{O})_3$ structure is in good agreement with both crystal structures (Table 6).

We can compare our $[\text{UO}_2(\text{HPO}_4)_2(\text{H}_2\text{O})_2]^{2-}$ structure to the crystal structure of $[(\text{UO}_2)_3(\text{PO}_4)\text{O}(\text{OH})(\text{H}_2\text{O})_2](\text{H}_2\text{O})^{20}$ in which the phosphate ligands have bidentate binding to the uranium virtually identical to our predicted structure. Our predicted bond lengths are in good agreement with those reported in the crystal structure, with our predicted $\text{U}=\text{O}$ and $\text{P}-\text{O}_{\text{bound}}$ bond length being 0.033 and 0.036 Å longer than those of the crystal structure, and our predicted $\text{U}-\text{O}_{\text{phos}}$ and $\text{P}-\text{O}_{\text{term}}$ bond lengths being 0.132 and 0.030 Å shorter than those of the crystal structure.

The crystal structure²² of $(\text{UO}_2)_3(\text{PO}_4)_2(\text{H}_2\text{O})_4$ has an average $\text{U}-\text{O}$ bond distances of 1.77 Å. These $\text{U}=\text{O}$ bond distances are shorter than our values by ~0.04 Å for $[\text{UO}_2(\text{PO}_4)(\text{H}_2\text{O})_n]^-$ ($n = 1 - 4$), consistent with the fact that there is less negative charge donated to the UO_2^{2+} in the experimental structure because there is on average 2/3 of a PO_4^{3-} for each uranyl in the crystal as compare to 2 PO_4^{3-} for the uranyl in the calculated structure. The $\text{U}-(\text{OH}_2)$ distances of 2.49 Å in the crystal structure $(\text{UO}_2)_3(\text{PO}_4)_2(\text{H}_2\text{O})_4$ are shorter than our calculated values for

$[\text{UO}_2(\text{PO}_4)(\text{H}_2\text{O})_n]^-$ ($n = 1 - 4$) by 0.08 to 0.33 Å with our most solvated $[\text{UO}_2(\text{PO}_4)(\text{H}_2\text{O})_4]^-$ complex being in closest agreement with experiment.

Our predicted U=O distances in the complexes $[\text{UO}_2(\text{H}_2\text{PO}_4)(\text{H}_2\text{O})_n]^+$ ($n = 1 - 4$), $\text{UO}_2(\text{HPO}_4)(\text{H}_2\text{O})_n$ ($n = 1 - 3$), and $\text{UO}_2(\text{PO}_4)(\text{H}_2\text{O})_n^-$ ($n = 1 - 4$), are consistent with the values of 1.78, 1.80, and 1.80 Å calculated by Kubicki et al⁴⁷ for the complexes with more H₂O molecules forming at least a second solvation shell. Our predicted U-OH₂ distances (Table 5) are also in excellent agreement those predicted by Kubicki which range from 2.58 to 2.48 Å.

The UO_2^{2+} symmetric stretch in the experimental Raman spectrum of threadgoldite, $\text{Al}[(\text{UO}_2)_2(\text{PO}_4)_2](\text{OH})\cdot 8\text{H}_2\text{O}$ ⁹⁷ is not strongly dependent on the temperature and the peaks fall in a range of 12 cm⁻¹. The antisymmetric stretch bands in the Raman spectrum, on the other hand, fall in a much broader range of ~ 80 cm⁻¹. For $[\text{UO}_2(\text{PO}_4)(\text{H}_2\text{O})_n]^-$ ($n = 1 - 4$), the predicted antisymmetric and symmetric UO_2^{2+} stretches range from 907 to 880 cm⁻¹ and 862 to 804 cm⁻¹, respectively, in good agreement with the experimental values considering the differences in the environments. The antisymmetric and symmetric stretching vibrations for the PO_4^{3-} ligands of the hydrated complexes are also predicted to be in good agreement with those observed in threadgoldite. The calculated values for the vibrational frequencies of $\text{UO}_2(\text{HPO}_4)(\text{H}_2\text{O})_4$ are in good agreement with the experimental values (Table 5).⁹⁸

5.3.6 Gas-Phase Uranyl Phosphate Reaction Energies. In Table 7 the gas-phase binding energies, enthalpies, and free energies (in kcal/mol) are reported for phosphate and water binding, respectively. The absolute binding energies for complexation of up to four H_2PO_4^- and HPO_4^{2-} ligands and up to three PO_4^{3-} ligands with UO_2^{2+} . As expected for the addition of H_2PO_4^- to UO_2^{2+} , $\Delta G_{298}(0 \rightarrow 1) > \Delta G_{298}(1 \rightarrow 2) > \Delta G_{298}(2 \rightarrow 3) > \Delta G_{298}(3 \rightarrow 4)$. The final step is slightly endothermic so forming the tetra-ligand complex is unfavorable relative to the tri-ligand

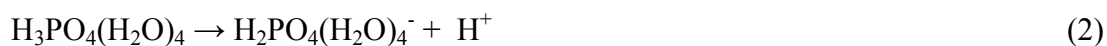
complex consistent with the substantial excess negative charge in the former. For the addition of HPO_4^{2-} to uranyl, $\Delta G_{298}(0 \rightarrow 1) > \Delta G_{298}(1 \rightarrow 2) > \Delta G_{298}(2 \rightarrow 3) > \Delta G_{298}(3 \rightarrow 4)$. The latter two reactions are highly endothermic so that formation of the free tri-ligand and tetra-ligand complexes in the gas phase is highly unfavorable, due to the buildup of substantial negative charge on the complexes. The reaction of PO_4^{3-} anion to uranyl is exothermic for the first two reactions but highly endothermic for the third so the the tri-ligand complex will not form. We were unable to find a stable tetraligand $[\text{UO}_2(\text{PO}_4)_4]^{10-}$ complex in the gas phase, due to the highly anionic nature of the species.

The binding free energy of adding water molecules to $[\text{UO}_2(\text{H}_2\text{PO}_4)]^+$, $\Delta G_{298}(0 \rightarrow 1)$ are exothermic for the first 3 additions but $\Delta G_{298}(3 \rightarrow 4) = 0.0$ kcal/mol. Thus there is no advantage in forming a complex with four water molecules relative to the three water complex (equatorial CN 5). (See Supporting Information). Table 8 reports the absolute energies for the binding of water molecules to the di-ligand complexes $\text{UO}_2(\text{H}_2\text{PO}_4)_2$ and $[\text{UO}_2(\text{HPO}_4)_2]^{2-}$. The free energies for the addition of one to four H_2O molecules to $\text{UO}_2(\text{H}_2\text{PO}_4)_2$, $\Delta G_{298}(0 \rightarrow 1)$, are all exothermic, and the second through fourth additions of water changes one of the ligands to monodentate binding to maintain CN 5. The binding free energy of up to two water molecules to $[\text{UO}_2(\text{HPO}_4)_2]^{2-}$, $\Delta G_{298}(0 \rightarrow 1)$ is exothermic. The addition of a third water is endothermic. The addition of a fourth water to $[\text{UO}_2(\text{HPO}_4)_2]^{2-}$, $\Delta G_{298}(3 \rightarrow 4) = -16.3$, is exothermic. Overall, the two water complex with the equatorial CN 5 is favored.

We also studied the energies for the addition of a water cluster rather than individual water molecules. (see Supporting Information). The reaction enthalpies are less negative for the water clusters and the reaction free energies are more negative due to the absence of free water molecules in the reactants.

5.3.7 Solution Phase Reaction Energies: Phosphoric Acid. Figure 5 and Table 9 shows the pK_a 's of the first, second, and third deprotonations of phosphoric acid using the gas phase geometries optimized at the B3LYP/DZVP2,⁶⁵ with single point energies at the MP2⁴⁸/aug-cc-pVnZ (n = D, T, and Q)⁷⁵ levels plus single point CPCM with COSMO-RS radii SCRF calculations as implemented in Gaussian 09. For the first deprotonation of H₃PO₄, all methods are within 2.4 pK_a unit of experiment with the exception of the MP2/aug-cc-pVDZ method which is within 4 pK_a units of experiment. For the second and third deprotonations of H₃PO₄, the B3LYP/DZVP2 method predicts the pK_a 's to increase linearly as found by experiment but the slope is too large and the pK_a 's are in error by ~ 5 and 10 pK_a units, respectively, as compared to experiment. The second pK_a units are within ~ 2 pK_a of experiment. The MP2/aug-cc-pVnZ (n = D, T, and Q) methods do not show a linear dependence for the pK_a 's with the third pK_a within ~ 6 pK_a units.

The errors in the phosphate acidities can be reduced by using explicit waters of solvation. Tang et al.⁹⁹ showed that microsolvation of phosphoric acid (following on previous work from other laboratories^{100,101}) with H_xPO₄^{x-3}(H₂O)_n, x = 0-3, and n = 0 - 5 plus a dielectric continuum model improved the ability to predict the pK_a 's. They calculated the solvation free energies using DFT as implemented in the DMol code¹⁰² at the COSMO^{103,104,105}/PBE¹⁰⁶/DNP level. We used a similar microsolvation approach as shown in Table 10 which gives the solution free energies involving reactions of phosphorus-based ligands combined with water molecules to create microsolvated solutes in our continuum solution model. Table 10 shows the dependence of the energies of reactions (2) – (4) on different solvation methods.

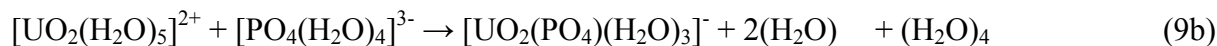
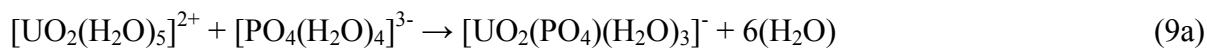




All of the solvation models predict the solution acidity (ΔG) for reaction (2) within ~ 3 kcal/mol or ~ 2 pK_a units. A similar result is found for reaction (3) with all of the models, except for the IEF-PCM with the UA0 and UFF radii models, giving reasonable results for the second pK_a for H₃PO₄. The two exceptions predict free energies that are too positive. For the third pK_a, CPCM with COSMO-RS radii and IEF-PCM and CSC-PCM, both with the Pauling radii give reasonable agreement with experiment. Our calculated free energies value for all three reactions are closer to experiment¹⁰⁷ than the Tang et al. values.⁹⁹ We note that they use an older value for the free energy of hydration of H⁺ in their calculations ($\Delta G(\text{H}^+) = -259.5$ kcal/mol) taken from Pearson's correlation of pK_a with gas phase acidity.¹⁰⁸ We used a value¹⁰⁹ of $\Delta G^{\text{solvation}}(\text{H}^+) = -265.9$ kcal/mol which is derived from experimental gas phase clustering energies^{110,111} and is consistent with high level calculations using a microsolvation/SCRF approach with appropriate thermodynamic corrections.¹¹² Tang et al. reported a pK_a of 8.4 for reaction (4) which is ~ 4 pK_a from experiment,¹⁰⁷ but we were only able to closely match this result using a PO₄(H₂O)₄ cluster in C₁ symmetry that was ~ 4 kcal/mol higher in energy than our lower energy D_{2d} geometry (Figure 4). This suggests that Tang et al. did not use the lowest energy structure. In summary, our best predictions of the pK_a's for the different protonation states of phosphoric acid were obtained with a microsolvation approach with 4 waters as shown in reactions (2) – (4), MP2/aug-cc-pVTZ for the gas phase values, and IEF-PCM with Pauling radii for the SCRF calculations. The first, second, and third acidities are now within -1.9, -0.8, and -1.2 pK_a units of experiment,¹⁰⁷ respectively.

5.3.8 Solution Phase Reaction Energies: Uranyl Phosphates. The reaction free energies in aqueous solution of reactions involving the uranyl dication and phosphate ligands are given in

Tables 11 and 12. In Table 11, we compare our calculated free energies in solution of reactions (5) – (9) from the microsolvation/SCRF approach to those from experiment,^{113,114} to examine the dependence on the solvation models. Mathur measured thermodynamic parameters for the aqueous reactions of $\text{UO}_2^{2+} + \text{H}_2\text{PO}_4^- \rightarrow [\text{UO}_2(\text{H}_2\text{PO}_4)]^+$ and $\text{UO}_2^{2+} + 2(\text{H}_2\text{PO}_4^-) \rightarrow \text{UO}_2(\text{H}_2\text{PO}_4)_2$ using a solvent extraction technique with NaClO_4 , corresponding to our reactions (7) and (8). Reaction type (a) has all of the displaced/released reactant waters as free waters



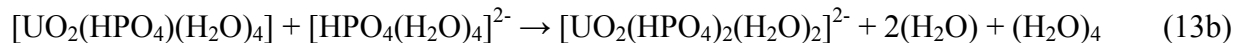
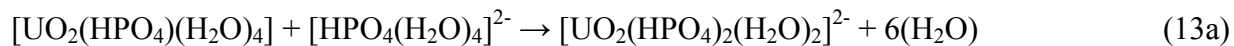
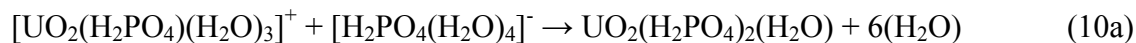
molecules and type (b) has the waters displaced from the uranyl as free water molecules and the waters from the phosphate released as a cluster. If all of the displaced/released reactant waters are treated as a cluster, the results are worse (Supporting Information), in part because of issues with treating the cluster properly as the clusters can have quite different dipole moments.

The cavity effects were studied using the same approaches and radii as used for phosphoric acid in Reactions (2) – (4). The data in Table 11 shows that the IPCM solvation model consistently agrees best with experiment in reactions in which the hydrated uranyl dication is involved. The best agreement between the calculated and experimental values for

reactions (5) – (9) is found when the waters displaced from hydrated UO_2^{2+} become free waters in the products (reaction type b). There is less of an effect if the waters about the $\text{H}_x\text{PO}_4^{y-}$ are treated as a cluster or as free waters.

We now provide a more detailed analysis of how the various methods perform. In reaction (5), CPCM using COSMO-RS radii, IEF-PCM using UFF and Pauling radii, IPCM, and CSC-PCM using Pauling radii all predict ΔG_{solv} values in good agreement with experiment; the IPCM method is the best coming within 0.4 kcal/mol of experiment. In reaction (6), the value of $\Delta G_{\text{solv}}(6b)$ differs from experiment by 1.9 kcal/mol at the IPCM level. The IEF-PCM with UFF radii, and CSC-PCM with Pauling radii methods show even better agreement with experiment, being within 0.5 kcal/mol. For reaction (6a), the IEF-PCM with UFF radii, and IPCM methods differ from experiment by 0.5, and -3.1 kcal/mol respectively. In reaction (7), only the IPCM method predicts reasonable values in terms of experiment. Reaction (7b) predicts ΔG_{solv} within 4.0 kcal/mol of experiment and Reaction (7a) is within 9 kcal/mol of experiment. For reaction (8) the IPCM method predicts a ΔG_{solv} differing by 2.9 kcal/mol from experiment for (8a) and by 7.2 kcal/mol for (8b). For reaction (9), the IPCM value is within 1.5 kcal/mol of experiment for (9b), and the IEF-PCM with Pauling radii and CSC-PCM with Pauling radii give values within 4.0 and 2.3 kcal/mol of experiment, respectively. The IPCM value for Reaction (9a) is within 3.6 kcal/mol of experiment. The most consistent set of results is found with the IPCM method and it is difficult to choose between whether reaction type (a) or (b) is best as the results are about evenly split. It is difficult to obtain better agreement with experiment as the solvation of the uranyl dication and the acidity of phosphoric acid are best predicted by different solvation models.

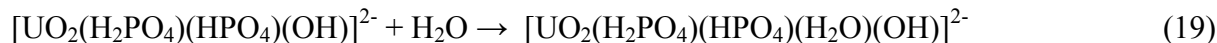
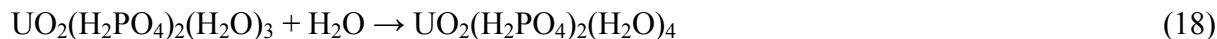
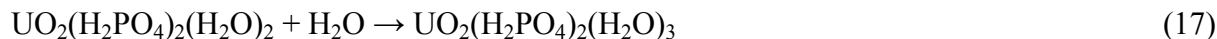
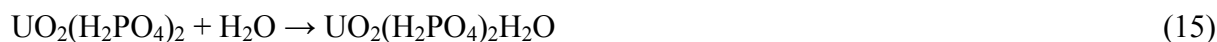
The benchmark results of reactions (5) – (9) suggest that the errors in the free energies for the ion/water displacement reactions (10) – (13) given in Table 12 are likely to be on the order of ± 4 kcal/mol using the IPCM model and reactions of type (a) as close to type (b) as possible.



The ΔG_{soln} for reaction type (a) where all of the displaced/released reactant waters are free water molecules are 5 kcal/mol more negative than type (b) where the waters are displaced from the uranyl as free water molecules and the waters from the phosphate are released as a cluster. Two waters are predicted to be displaced by $[\text{H}_2\text{PO}_4]^-$ in reaction (10) with a substantial negative ΔG_{soln} . A third $[\text{H}_2\text{PO}_4]^-$ will displace the final water from $[\text{UO}_2(\text{H}_2\text{PO}_4)_2(\text{H}_2\text{O})]$ producing $[\text{UO}_2(\text{H}_2\text{PO}_4)_3]^-$ exothermically in reaction (11). Similarly, in reaction (12) a third $[\text{H}_2\text{PO}_4]^-$ will displace the remaining three waters to form $[\text{UO}_2(\text{H}_2\text{PO}_4)_3]^-$ if the ligands are bonded monodentate in the reactant in contrast to the bidentate binding in reaction (11). In reaction (13) a second $[\text{HPO}_4]^{2-}$ is predicted to displace two additional waters to form $[\text{UO}_2(\text{HPO}_4)_2(\text{H}_2\text{O})_2]^{2-}$ where two phosphate ligands are both bonded to the uranyl moiety in a bidentate fashion. With

two waters also bonded to the uranyl, a CN 6 configuration with C_{2v} symmetry is formed, Figure 2. This provides the only CN 6 example of an exothermic process. Reaction (14) corresponds to displacement of H_2O by HPO_4^{2-} . Rather than forming $UO_2(HPO_4)(H_2O)_4$, a proton is transferred from a water to generate the $UO_2(H_2PO_4)(H_2O)_3OH$ isomer. This reaction is exothermic. The displacement reaction free energy for reaction (14) with $UO_2(HPO_4)(H_2O)_4$ being formed has been measured experimentally¹¹⁴ to be -8.2 kcal/mol, which is very similar to our values for the same reactants leading to proton transfer in the product.

Table 13 reports the absolute energies for the binding of water molecules to the di-ligand complexes $UO_2(H_2PO_4)_2(H_2O)_n$, and $[UO_2(HPO_4)_2(H_2O)_n]^{2-}$, $n = 1 - 4$ for reactions (15) to (21).



The best solvent model can be chosen from reaction (22) where there is good experimental⁷³ and computational data³⁹ which shows that the reaction has $\Delta G = -1.2$ kcal/mol from experiment and -2 kcal/mol from MP2/SCRF calculations with 2 solvent shells. We only used one solvent



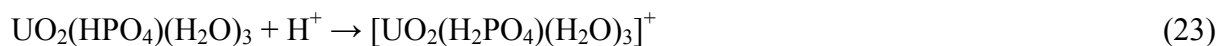
shell so we know that there will be some inherent error. The best results for reaction (22) are the COSMO and CSC-PCM Pauling ones with the CSC-PCM Pauling giving the best result, within 0.9 kcal/mol of experiment. These values allow us to estimate the H_2O addition reactions. The

IPCM solvent model which gives the best results for uranyl complexes involving negative ion displacement of H₂O fails for uranyl complexes involving water transfer reactions predicting reaction energies that are far too negative. The IEF-PCM-Pauling solvation model predicts a positive free energy for reaction (22) showing that it prefers CN 4 over CN 5.

In reaction (15), both H₂PO₄⁻ ligands in UO₂(H₂PO₄)₂(H₂O) maintain bidentate binding to the uranium atom giving CN 5 and the reaction is consistently predicted to be slightly exothermic, just as found for reaction (22). The addition of one water in reaction (16) yields a product which has mono and bidentate H₂PO₄⁻ ligand binding to the uranium atom in the product maintains the CN 5 structure with a slightly exothermic ΔG_{soln} . This means that addition of water can generate a structure potentially capable of cross-linking to other uranyl phosphates to form the types of structures found in the solid state.^{20,21,22,23} Each solvent model, with the exception of IPCM predicts the ΔG_{soln} for reactions (16) and (17) to be near thermoneutral. Addition of another water (Reaction (17)) forms two monodentate H₂PO₄⁻ ligands while maintaining CN 5 exothermically, which provides another potential bridging ligand. The addition of a water molecule to UO₂(H₂PO₄)₂(H₂O)₃ (reaction (18)) is endothermic and places two waters in the second solvation shell leaving an equatorial CN 5 structure. Thus CN 6 is not favored for this type of structure. Reaction (19) and (20) resulted in products having geometries which involve proton transfer from H₂O to the phosphate and are predicted to be essentially endothermic so this type of reaction is unlikely. Reaction (20) is more endothermic than reaction (19). Reaction (21) which is H₂O addition leading to proton transfer from 2 H₂PO₄⁻ ligands to OH⁻ ligands, in contrast, is exothermic.

[UO₂(HPO₄)(H₂O)₃] is predicted to be a strong base in the gas phase with $\Delta G = -238.2$ kcal/mol for reaction (23) (energetics for reactions (23) – (26) in Supporting Information). In

order to estimate the free energy in solution, we calculated the energy relative to that of the base NH_3 ($\text{pK}_a = 9.25$)¹¹⁵ as shown in reaction (24).



Reaction (23) is exothermic by -21.0, -17.9, -25.1, and -22.8 kcal/mol with the CPCM (COSMO radii), IEF-PCM(UA0), IPCM, and CSC-PCM Pauling SCRF approaches so it is a very strong base in aqueous solution. The corresponding value for NH_3 , for example, is -12.6 kcal/mol. $[\text{UO}_2(\text{HPO}_4)(\text{H}_2\text{O})_3]$ is predicted to be a moderate to weak acid in the gas phase with a ΔG of 343.1 kcal/mol for reaction (25)



We can use a similar approach by comparing its solution acidity to that of H_3PO_4 ($\text{pK}_a = 2.15$) as shown by reaction (26)



Reaction (25) is very endothermic, 22.0, 25.6, 19.0, and 29.3 kcal/mol with the CPCM (COSMO radii), IEF-PCM(UA0), IPCM, and CSC-PCM Pauling SCRF approaches so it is a very weak acid in aqueous solution. $\text{UO}_2(\text{HPO}_4)(\text{H}_2\text{O})_3$ has a large dipole moment of 13.5 D. This leads to a large interaction energy with the continuum, which partially cancels the solvation energy of the anion, making it an even weaker acid in solution.

5.4 Conclusions

The binding of water molecules for the mono- and di-ligand phosphate complexes of H_2PO_4^- , HPO_4^{2-} and PO_4^{3-} have been investigated at the DFT level. Adequate steric space is available in these complexes to accommodate multiple water molecules in the equatorial region

of the uranyl dication in addition to the phosphorus-based ligand(s). The $[\text{UO}_2(\text{H}_2\text{PO}_4)(\text{H}_2\text{O})_n]^+$ complexes can accommodate up to three water molecules with the H_2PO_4^- ligands remaining bidentate with a total equatorial CN of 5. $[\text{UO}_2(\text{H}_2\text{PO}_4)(\text{H}_2\text{O})_4]^+$ has an equatorial CN of 5 with the phosphate ligand bound in a monodentate fashion, and a strong hydrogen bond between the H atom on an equatorial water and the terminal P=O group of H_2PO_4^- . In the $\text{UO}_2(\text{HPO}_4)(\text{H}_2\text{O})_n$ complexes, protons can be abstracted from bound waters due to the increased negative charge on the HPO_4^{2-} ligand forming OH^- and H_2PO_4^- ligands which separates the buildup of regions of negative charge. In $\text{UO}_2(\text{HPO}_4)(\text{H}_2\text{O})_3$, the phosphate ligand is actually H_2PO_4^- moiety bound in a monodentate fashion and results from the abstraction of a proton from a water forming a hydroxide ligand bound to uranium leading to CN 4. A hydrogen bond from the terminal P=O group to the H atom of a water stabilizes the monodentate mode. This hydrogen bond results in an elongated H-OH water bond and a ‘hydroxide-like’ interaction of this water with the uranyl center. In $\text{UO}_2(\text{HPO}_4)(\text{H}_2\text{O})_4$, all of the ligands retain their identities. The HPO_4^{2-} ligand is bound in a bidentate fashion to the uranyl and three water molecules are bound in the remaining sites resulting in CN 5. The remaining water molecule is located in the second coordination sphere. Due to the steric effects of the second phosphate in the $\text{UO}_2(\text{H}_2\text{PO}_4)_2(\text{H}_2\text{O})_n$ and $[\text{UO}_2(\text{HPO}_4)_2(\text{H}_2\text{O})_n]^{2-}$ hydrated complexes ($n = 1 - 3$), fewer water molecules can be accommodated equatorially as compared to the monoligand complexes. Bidentate coordination modes for the phosphate ligands are more common. The structure of $\text{UO}_2(\text{H}_2\text{PO}_4)_2(\text{H}_2\text{O})$ has bidentate H_2PO_4^- ligands and a discrete bound water molecule resulting in the expected CN 5. The $\text{UO}_2(\text{H}_2\text{PO}_4)_2(\text{H}_2\text{O})_3$ complex is structurally similar to the $\text{UO}_2(\text{H}_2\text{PO}_4)_2(\text{H}_2\text{O})_2$ complex, with the exception both H_2PO_4^- ligands are bound in a monodentate fashion. For the $[\text{UO}_2(\text{HPO}_4)_2(\text{H}_2\text{O})_n]^{2-}$ ($n = 1$ and 3) complexes, the equatorial CN was found to be four rather

than five with both complexes having at least one phosphate with monodentate binding. The $[\text{UO}_2(\text{HPO}_4)_2(\text{H}_2\text{O})_2]^{2-}$ complex however, contains two bidentate HPO_4^{2-} with CN 6 and C_{2v} symmetry. In $[\text{UO}_2(\text{HPO}_4)_2(\text{H}_2\text{O})_3]^{2-}$, both phosphate ligands exist as H_2PO_4^- moieties with two hydroxide ligands bound to the uranyl. The hydroxides are hydrogen bonded to H atoms from the phosphate ligands and the remaining water acts as a second sphere water molecule hydrogen bonded to the hydroxide ligands. The $[\text{UO}_2(\text{PO}_4)(\text{H}_2\text{O})_n]^-$ ($n = 1, 2$ and 4) complexes each have CN 4 and some bidentate phosphate binding as do the $[\text{UO}_2(\text{PO}_4)_2(\text{H}_2\text{O})_n]^{4-}$ ($n = 1 - 2$) complexes. The ($n = 3$) complexes has CN 5 with the PO_4^{3-} ligand forming a bidentate bond to the uranyl dication. In $[\text{UO}_2(\text{PO}_4)_2(\text{H}_2\text{O})]^{4-}$ both phosphate ligands are bidentate bound to the uranyl dication. In $[\text{UO}_2(\text{PO}_4)_2(\text{H}_2\text{O})_2]^{4-}$, there is a proton transfer to a PO_4^{3-} ligand leading to the formation of an OH^- bonded to the UO_2^{2+} , a monodentate HPO_4^{2-} ligand and one bidentate PO_4^{3-} ligand.

Use of a hybrid microsolvation-continuum approach led to the prediction that $[\text{H}_2\text{PO}_4]^-$ will displace two H_2O molecule from $[\text{UO}_2(\text{H}_2\text{PO}_4)(\text{H}_2\text{O})_3]^+$ to exothermically form neutral $[\text{UO}_2(\text{H}_2\text{PO}_4)_2(\text{H}_2\text{O})]$. An additional $[\text{H}_2\text{PO}_4]^-$ will displace the remaining water to form the $[\text{UO}_2(\text{H}_2\text{PO}_4)_3]^-$ anion exothermically in solution. The addition of $[\text{H}_2\text{PO}_4]^-$ to $[\text{UO}_2(\text{H}_2\text{PO}_4)_2(\text{H}_2\text{O})_3]$ with all three waters displaced is even more exothermic. HPO_4^{2-} will displace two waters from $[\text{UO}_2(\text{HPO}_4)(\text{H}_2\text{O})_4]$ to form $[\text{UO}_2(\text{HPO}_4)_2(\text{H}_2\text{O})_2]^{2-}$ exothermically. The binding of water molecules to the di-ligand complexes $\text{UO}_2(\text{H}_2\text{PO}_4)_2(\text{H}_2\text{O})_n$, and $[\text{UO}_2(\text{HPO}_4)_2(\text{H}_2\text{O})_n]^{2-}$, $n = 1 - 4$, was studied. Additional water molecules can cause the bonding of H_2PO_4^- and HPO_4^{2-} to change from bidentate to monodentate exothermically while maintaining CN 5. This means that addition of water can generate a structure potentially capable of cross-linking to other uranyl phosphates to form the types of structures found in the solid

state. $[\text{UO}_2(\text{HPO}_4)(\text{H}_2\text{O})_3]$ is predicted to be a strong base in the gas phase and in aqueous solution and a moderate to weak acid in the gas phase and a very weak acid in solution. Our results show that one has to be careful in the type of solvent model that is used and also in the type of reaction to be used in the model. Different SCRF models perform differently for different types of reactions. Overall, the results show that it is possible to predict the energetic properties of aquo uranyl phosphate complexes using correlated molecular orbital theory in combination with SCRF approaches. The reaction energies derived from the DFT gas phase energies were not as reliable. The prediction of the solution energetics still requires the continued development of solvent modeling approaches as small changes in the models can lead to large changes in reaction energies in solution.

Acknowledgements. This work was supported by the U.S. Department of Energy, Office of Basic Energy Sciences, Geosciences Research Program. David A. Dixon is indebted to the Robert Ramsay Endowment of the University of Alabama. This research was performed in part using the Molecular Science Computing Facility (MSCF) in the William R. Wiley Environmental Molecular Sciences Laboratory, a national scientific user facility sponsored by the U. S. Department of Energy's Office of Biological and Environmental Research and located at the Pacific Northwest National Laboratory, operated for the Department of Energy by Battelle.

Supporting Information: Complete author lists for references 9, 58, 77, 80, 83, and 84. Total energies in a.u. at the B3LYP/TZVP(Stuttgart orbital basis sets for the U atom) level. Cartesian Coordinates (x, y, z) in Angstroms. Calculated reaction energetics for binding of water ligands to form hydrated uranyl phosphate complexes (kcal/mol). Reaction Energies of UO_2^{2+} /Phosphate/ H_2O Complexes in kcal/mol. This material is available free of charge via the Internet at <http://pubs.acs.org>.

References

-
- ¹ Choppin, G. R.; Morgenstern, A. Radionuclide Separations in Radioactive Waste Disposal. *J. Radio. Nucl. Chem.* **2000**, *243*, 45-51.
- ² Morss, L. R.; Edelstein, N. M.; Fuger, J.; Katz, J. J.; Eds, *Chemistry of the Actinide and Transactinide Elements*; 3rd Ed; Springer: 2006.
- ³ Gephart, R. E.; Lundgren, R.E. *Hanford Tank Cleanup: A Guide to Understanding the Technical Issues*, PNL-10773, Pacific Northwest National Laboratory (1995).
- ⁴ Riley, R. G.; Zachara, J. M. *Chemical Contaminants on DOE Lands and Selection of Contaminant Mixtures for Subsurface Science Research*, (U.S. Department of Energy, Office of Energy Research, Washington, D.C., 1992), DOE/ER-0547T.
- ⁵ *U.S. DOE Complex Cleanup. The Environmental Legacy of Nuclear Weapons Production*, (U.S. Department of Energy, Office of Technology Assessment, Washington, D.C., 1991), OTA-0-484.
- ⁶ Ewing, R. C. Nuclear Waste Forms For Actinides. *Proc. Natl. Acad. Sci. USA* **1999**, *96*, 3432-3439.
- ⁷ Felmy, A. R.; Xia, Y.; Wang, Z. The Solubility Product of $\text{NaUO}_2\text{PO}_4 \cdot x\text{H}_2\text{O}$ Determined in Phosphate and Carbonate Solutions. *Radiochim. Acta* **2005**, *93*, 401-408.
- ⁸ Barten, H.; Cordfunke, E. H. P. The Formation and Stability of Hydrated and Anhydrous Uranyl Phosphates. *Thermochim. Acta* **1980**, *40*, 357-365.
- ⁹ Brown, G. E. Jr.; Henrich, V. E.; Casey, W. H.; Clark, D. L.; Eggleston, C.; Felmy, A.; Goodman, D. W.; Grätzel, M.; Maciel, G.; McCarthy, M. I.; et al. Metal Oxide Surfaces and Their Interactions with Aqueous Solutions and Microbial Organisms. *Chem. Rev.* **1999**, *99*, 77-144.
- ¹⁰ Barnett, M. O.; Jardine, P. M.; Brooks, S. C.; Selim, H. M. Adsorption and Transport of U(VI) in Subsurface Media. *Soil Sci. Soc. Am. J.* **2000**, *64*, 908-917.
- ¹¹ Basnakova, G.; Stephens, E. R.; Thaller, M. C.; Rossolini, G. M.; Macaskie, L. E. The Use of *Escherichia Coli* Bearing A Phon Gene for the Removal of Uranium and Nickel from Aqueous Flows. *Appl. Microbiol. Biotechnol.* **1998**, *50*, 266-272.
- ¹² Nash, K. L.; Morss, L. R.; Jensen, M. P.; Appelman, E. H.; Schmidt, M. "Phosphate Mineralization of Actinides by Measured Addition of Precipitating Anions," Annual Report (FY1995) for the ESP Program (1995).

-
- ¹³ Wright, J.; Conca, J.; Moody, T.; Chen, X. "Immobilization of Metals Using Apatite Minerals: Precipitation or Sorption?" 211th ACS National Meeting, New Orleans, March 24-28, Division of Geochemistry Abstract #088 (1996).
- ¹⁴ Seaman, J. C.; Hutchinson, J. M.; Jackson, B. P.; Vulava, V. M. In Situ Treatment Of Metals in Contaminated Soils with Phytate. *J. Environ. Qual.* **2003**, *32*, 153-161.
- ¹⁵ Nash, K. L.; Jensen, M. P.; Schmidt, M. A. Actinide Immobilization in the Subsurface Environment By In-Situ Treatment with A Hydrolytically Unstable Organophosphorus Complexant: Uranyl Uptake By Calcium Phytate. *J. Alloys Comp.* **1998**, *271-273*, 257-261.
- ¹⁶ Nash K. L. *Organophosphorous Reagents in Actinide Separations: Unique Tools for Production, Cleanup and Disposal*; ANL/CHM/CP-100858; Argonne National Laboratory, Argonne, IL, 2000.
- ¹⁷ Wellman, D. M.; Pierce, E. M.; Oostrom, M.; Fruchter, J. S. *Experimental Plan: 300 Area Treatability Test: In Situ Treatment of the Vadose Zone and Smear Zone Uranium Contamination by Polyphosphate Infiltration*; PNNL-16823; NTIS: Springfield, VA, 2007.
- ¹⁸ Bostick, B. C.; Fendorf, S.; Barnett, M. O.; Jardine, P. M.; Brooks, S. C. Uranyl Surface Complexes Formed on Subsurface Media From DOE Facilities. *Soil Sci. Soc. Am. J.* **2002**, *66*, 99-108.
- ¹⁹ Romuald, D.; Simoni, E. Uranium(VI) and Europium(III) Speciation at the Phosphate Compounds-Solution Interface. *Langmuir*, **1999**, *15*, 4820-4827.
- ²⁰ Burns, P. C.; Alexopoulos, C. M.; Hotchkiss, P. J.; Locock, A. An Unprecedented Uranyl Phosphate Framework in the Structure of $[(\text{UO}_2)_3(\text{PO}_4)\text{O}(\text{OH})(\text{H}_2\text{O})_2](\text{H}_2\text{O})$. *J. Inorg. Chem.* **2004**, *43*, 1816-1818.
- ²¹ Danis, J. A.; Hawkins, H. T.; Scott, B. L.; Runde, W. H.; Scheetz, B. E.; Eichhorn, B. W. X-Ray Structure Determination of Two Related Uranyl Phosphate Crown Ether Compounds. *Polyhedron*, **2000**, *19*, 1551-1557.
- ²² Locock, A. J.; Burns, P. C. The Crystal Structure of Triuranyl Diphosphate Tetrahydrate. *J. Solid State Chem.* **2002**, *163*, 275-280.
- ²³ Locock, A. J.; Burns, P. C. Crystal Structures of Three Framework Alkali Metal Uranyl Phosphate Hydrates. *J. Solid State Chem.* **2002**, *167*, 226-236.
- ²⁴ Locock, A. J.; Burns, P. C. The Crystal Structure of Synthetic Autunite, $\text{Ca}[(\text{UO}_2)(\text{PO}_4)]_2(\text{H}_2\text{O})_{11}$. *Am. Mineral.* **2003**, *88*, 240-244.

-
- ²⁵ Mercier, R.; Thi, M. P.; Colombari, Ph. Structure, Vibrational Study and Conductivity of the Trihydrated Uranyl bis(dihydrogenophosphate): $\text{UO}_2(\text{H}_2\text{PO}_4)_2 \cdot 3\text{H}_2\text{O}$. *Solid State Ionics*, **1985**, *15*, 113-126.
- ²⁶ Burns, P. C. A New Uranyl Phosphate Chain In The Structure Of Parsonsite. *Am. Mineral.* **2000**, *85*, 801-805.
- ²⁷ Locock, A. J.; Kinman, W. S.; Burns, P. C. The structure and composition of uranospahtite, $\text{Al}_{1-x}[\text{Al}_x(\text{UO}_2)(\text{PO}_4)_2(\text{H}_2\text{O})_{20+3x}\text{F}_{1-3x}]$, $x = 0 - 0.33$, a Non-Centrosymmetric Flourine-Bearing Mineral of the Autunite Group, and of a Related Synthetic Lower Hydrate, $\text{Al}_{0.67}[\text{Al}_{0.33}(\text{UO}_2)(\text{PO}_4)_2(\text{H}_2\text{O})_{15.5}]$. *Can. Min.* **2005**, *43*, 989-1003.
- ²⁸ Locock, A. J. Crystal Chemistry of Uranyl Phosphates, Arsenates and Oxysalts of Chromium(V): Implications for Remediation. PhD. Dissertation, University of Notre Dame, Indiana, USA, 2004.
- ²⁹ Liu, C.; Jeon, B. H.; Zachara, J. M.; Wang, Z.; Biotech. Influence of Calcium on Microbial Reduction of Solid Phase Uranium (VI). *Bioeng.* **2007**, *97*, 1415-1422.
- ³⁰ Liu C.; Zachara, J. M.; Qafoku, O.; McKinley, P. J.; Heald, S. M.; Wang, Z. Dissolution of Uranyl Microprecipitates from Subsurface Sediments at Hanford Site, USA. *Geochim. Cosmochim. Acta* **2004**, *68*, 4519-4537.
- ³¹ Fredrickson, J. K.; Zachara, J. M.; Kennedy, D. W.; Duff, M. C.; Gorby, Y. A.; Li, S. M. W.; Krupka, K. M. Reduction of U(VI) in Goethite ($\alpha\text{-FeOOH}$) Suspensions by a Dissimilatory Metal-Reducing Bacterium. *Geochim. Cosmochim. Acta* **2000**, *64*, 3085-3098.
- ³² Renninger, N.; Knopp, R.; Nitsche, H.; Clark, D. S.; Keasling, J. D. Uranyl Precipitation by *Pseudomonas aeruginosa* via Controlled Polyphosphate Metabolism. *Appl. Environ. Microbio.* **2004**, *70*, 7404-7412.
- ³³ Hennig, C.; Panak, P. J.; Reich, T.; Roßberg, A.; Raff, J.; Selenska-Pobell, S.; Matz, W.; Bucher, J. J.; Bernhard, G.; Nitsche, H. EXAFS Investigation of Uranium(VI) Complexes Formed at *Bacillus Cereus* and *Bacillus Sphaericus* Surfaces. *Radiochim. Acta* **2001**, *89*, 625-631.
- ³⁴ Macaskie, L. E.; Bonthron, K. M.; Yong, P.; Goddard, D. T. Enzymically Mediated Bioprecipitation of Uranium by a *Citrobacter* sp.: A Concerted Role for Exocellular Lipopolysaccharide and Associated Phosphatase in Biomineral Formation. *Microbiol.* **2000**, *146*, 1855-1867.
- ³⁵ Valls, M.; de Lorenzo, V. Exploiting The Genetic and Biochemical Capacities of Bacteria for The Remediation of Heavy Metal Pollution. *FEMS Microbiol. Rev.* **2002**, *26*, 327-338.

-
- ³⁶ Wang, J.; Chen, C. Biosorbents for Heavy Metals Removal and Their Future. *Biotech. Adv.* **2009**, *27*, 195–226.
- ³⁷ Lumetta, G. J.; Felmy, A. R.; Braley, J. C.; Carter, J. C.; Edwards, M. K.; MacFarlan, P. J.; Qafoku, O. *Removing Phosphate from Hanford High-Phosphate Tank Wastes: FY 2010 Results*; PNNL-19778; NTIS: Springfield, VA, 2010.
- ³⁸ Koban, A.; Bernhard, G. Uranium(VI) Complexes with Phospholipid Model Compounds - A Laser Spectroscopic Study. *Journal of Inorganic Biochemistry. J. Inorg. Biochem.* **2007**, *101*, 750-757.
- ³⁹ Gutowski, K. E.; Dixon, D. A. Predicting the Energy of the Water Exchange Reaction and Free Energy of Solvation for the Uranyl Ion in Aqueous Solution. *J. Phys. Chem. A* **2006**, *110*, 8840-8856.
- ⁴⁰ Jackson, V. E.; Craciun, R.; Dixon, D. A.; Peterson, K. A.; de Jong, W. A. Prediction of Vibrational Frequencies of UO_2^{2+} at the CCSD(T) Level. *J. Phys. Chem. A* **2008**, *112*, 4095-4099.
- ⁴¹ de Jong, W. A.; Aprà, E.; Windus, T. L.; Nichols, J. A.; Harrison, R. J.; Gutowski, K. E.; Dixon, D. A. Complexation of the Carbonate, Nitrate, and Acetate Anions with the Uranyl Dication: Density Functional Studies with Relativistic Effective Core Potentials. *J. Phys. Chem. A* **2005**, *109*, 11568-11577.
- ⁴² Kaltsoyannis, N. Recent Developments in Computational Actinide Chemistry. *Chem. Soc. Rev.* **2003**, *32*, 9-16.
- ⁴³ Schreckenbach, G.; Hay, J. P.; Martin, R. L. Density Functional Calculations on Actinide Compounds: Survey of Recent Progress and Application to $[\text{UO}_2\text{X}_4]^{2-}$ (X = F, Cl, OH) and AnF_6 (An = U, Np, 6Pu). *J. Comp. Chem.* **1999**, *20*, 70-90.
- ⁴⁴ Hay, P. J.; Martin, R. L. Computational Studies of Actinide Chemistry. *Los Alamos Sci.* **2000**, *26*, 382-391.
- ⁴⁵ Schreckenbach, G.; Shamov, G. A. Theoretical Actinide Molecular Science. *Accts. Chem. Res.* **2010**, *43*, 19-29.
- ⁴⁶ Majumdar, D.; Balasubramanian, K. Theoretical Studies on The Nature of Uranyl–Silicate, Uranyl–Phosphate and Uranyl–Arsenate Interactions in the Model $\text{H}_2\text{UO}_2\text{SiO}_4 \cdot 3\text{H}_2\text{O}$, $\text{HUO}_2\text{PO}_4 \cdot 3\text{H}_2\text{O}$, and $\text{HUO}_2\text{AsO}_4 \cdot 3\text{H}_2\text{O}$ Molecules. *Chem. Phys. Lett.* **2004**, *397*, 26-33.
- ⁴⁷ Kubicki, J. D.; Halada, G. P.; Jha, P.; Phillips, B. L. Quantum Mechanical Calculation of Aqueous Uranium Complexes: Carbonate, Phosphate, Organic and Biomolecular Species. *Chem. Cent. J.* **2009**, *10*, 1186-1752.

-
- ⁴⁸ Pople J. A., Binkley J. S. and Seeger R. Theoretical Models Incorporating Electron Correlation. *Int. J. Quantum Chem. Symp.* **1976**, *10*, 1–19.
- ⁴⁹ Leavitt, C. M.; Bryantsev, V. S.; de Jong, W.A.; Diallo, M. S.; Goddard, W. A., III; Groenewold, G. S.; Van Stipdonk, M. J. Addition of H₂O and O₂ to Acetone and Dimethylsulfoxide Ligated Uranyl(V) Dioxocations. *J. Phys. Chem. A*, **2009**, *113*, 2350–2358.
- ⁵⁰ Rios, D.; Schoendorff, G.; Van Stipdonk, M. J.; Gordon, M. S.; Windus, T. L.; Gibson, J. K.; de Jong, W. A. Roles of Acetone and Diacetone Alcohol in Coordination and Dissociation Reactions of Uranyl Complexes *Inorg. Chem.*, **2012**, *51*, 12768–12775
- ⁵¹ Schoendorff, G.; de Jong, W. A.; Van Stipdonk, M. J.; Gibson, J. K.; Rios, D.; Gordon, M. S.; Windus, T. L. On the Formation of “Hypercoordinated” Uranyl Complexes. *Inorg. Chem.*, **2011**, *50*, 8490–8493.
- ⁵² Tomasi, J.; Mennucci, B.; Cammi, R. Quantum Mechanical Continuum Solvation Models. *Chem. Rev.* **2005**, *105*, 2999–3093.
- ⁵³ Barone, V.; Cossi, M. Quantum calculation of molecular energies and energy gradients in solution by a conductor solvent model. *J. Phys. Chem. A*. **1998**, *102*, 1995–2001.
- ⁵⁴ Cossi, M.; Rega, N.; Scalmani, G.; Barone, V. Energies, structures, and electronic properties of molecules in solution with the C-PCM solvation model. *J. Comp. Chem.* **2003**, *24*, 669–81.
- ⁵⁵ Miertus, S.; Scrocco, E.; Tomasi, J. Electrostatic Interaction of a Solute with a Continuum. A Direct Utilization of ab Initio Molecular Potentials for the Prevision of Solvent Effects. *Chem. Phys.* **1981**, *55*, 117–129.
- ⁵⁶ Pascual-Ahuir, J. L.; Silla, E.; Tuñón, I GEPOL: An Improved Description of Molecular-Surfaces. 3. A New Algorithm for The Computation of A Solvent-Excluding Surface. *J. Comp. Chem.* **1994**, *15*, 1127–1138.
- ⁵⁷ Cancès, M. T.; Mennucci, B.; Tomasi, J. A new integral equation formalism for the polarizable continuum model: Theoretical background and applications to isotropic and anisotropic dielectrics. *J. Chem. Phys.* **1997**, *107*, 3032–3041.
- ⁵⁸ Cossi, M.; Barone, V.; Mennucci, B.; Tomasi, J. Ab initio study of ionic solutions by a polarizable continuum dielectric model, *Chem. Phys. Lett.* **1998**, *286*, 253–260.
- ⁵⁹ Mennucci, B.; Tomasi, J. Continuum solvation models: A new approach to the problem of solute's charge distribution and cavity boundaries. *J. Chem. Phys.* **1997**, *106*, 5151–5158.
- ⁶⁰ Scalmani, G.; Frisch, M. J. Continuous Surface Charge Polarizable Continuum Models of Solvation. I. General Formalism. *J. Chem. Phys.* **2010**, *132*, 114110 (15 pages).

-
- ⁶¹ Foresman, J. B.; Keith, T. A.; Wiberg, K. B.; Snoonian, J.; Frisch, M. J. Solvent Effects. 5. Influence of Cavity Shape, Truncation of Electrostatics, and Electron Correlation on Ab Initio Reaction Field Calculations. *J. Phys. Chem.* **1996**, *100*, 16098-16104.
- ⁶² Becke, A. D. Density-Functional Thermochemistry. III. The Role of Exact Exchange. *J. Chem. Phys.* **1993**, *98*, 5648-5652.
- ⁶³ Lee, C.; Yang, W.; Parr, R. G. Development of the Colle-Salvetti Correlation-Energy Formula into a Functional of the Electron Density. *Phys. Rev. B* **1988**, *37*, 785-789.
- ⁶⁴ Cao, X.; Dolg, M.; Stoll, H. Valence Basis Sets For Relativistic Energy-Consistent Small-Core Actinide Pseudopotentials. *J. Chem. Phys.* **2003**, *118*, 487-496.
- ⁶⁵ Godbout, N.; Salahub, D. R.; Andzelm, J.; Wimmer, E. Optimization of Gaussian-Type Basis Sets for Local Spin Density Functional Calculations. Part I. Boron Through Neon, Optimization Technique and Validation. *Can. J. Chem.* **1992**, *70*, 560-571.
- ⁶⁶ Reed, A. E.; Curtiss, L. A.; Weinhold, F. Intermolecular Interactions from a Natural Bond Orbital, Donor-Acceptor Viewpoint. *Chem. Rev.* **1988**, *88*, 899-926.
- ⁶⁷ Foster, J. P.; Weinhold, F. Natural Hybrid Orbitals. *J. Am. Chem. Soc.* **1980**, *102*, 7211-7218.
- ⁶⁸ Reed, A. E.; Weinhold, F. Natural Atomic Orbitals and Natural Population Analysis. *J. Chem. Phys.* **1983**, *78*, 4066-4073.
- ⁶⁹ Reed, A. E.; Weinstock, R. B.; Weinhold, F. Natural Population Analysis. *J. Chem. Phys.* **1985**, *83*, 735-746.
- ⁷⁰ Reed, A. E.; Weinhold, F. Natural Localized Molecular Orbitals. *J. Chem. Phys.* **1985**, *83*, 1736-1740.
- ⁷¹ Hay, P. J.; Martin, R. L. Theoretical Studies of the Structures and Vibrational Frequencies of Actinide Compounds Using Relativistic Effective Core Potentials with Hartree-Fock and Density Functional Methods: UF₆ and PuF₆. *J. Chem. Phys.* **1998**, *109*, 3875-3881.
- ⁷² Hay, P. J.; Martin, R. L.; Schreckenbeck, G. Theoretical Studies of the Properties and Solution Chemistry of AnO₂²⁺ and AnO₂⁺ Aquo Complexes for An = U, Np, and Pu. *J. Chem. Phys.* **2000**, *104*, 6259-6270.
- ⁷³ Neuefeind, J.; Soderholm, L.; Skanthakumar, S. Experimental Coordination Environment of Uranyl(VI) in Aqueous Solution. *J. Phys. Chem. A* **2004**, *109*, 2733-2739.
- ⁷⁴ Soderholm, L.; Skanthakumar, S.; Neuefeind, J. Determination of Actinide Speciation in Solution Using High-Energy X-Ray Scattering. *Anal. Bioanal. Chem.* **2005**, *383*, 48-55.

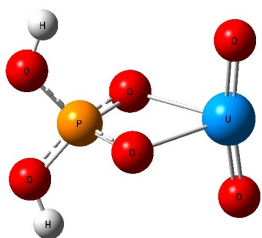
-
- ⁷⁵ Peterson, K. A. Systematically Convergent Basis Sets with Relativistic Pseudopotentials. I. Correlation Consistent Basis Sets for the Post-D Group 13–15 Elements. *J. Chem. Phys.* **2003**, *119*, 11099-11112.
- ⁷⁶ Peterson, K. A.; Figgen, D.; Goll, E.; Stoll, H.; Dolg, M. Systematically Convergent Basis Sets with Relativistic Pseudopotentials. II. Small-Core Pseudopotentials and Correlation Consistent Basis Sets for the Post-D Group 16–18 Elements. *J. Chem. Phys.* **2003**, *119*, 11113-11123.
- ⁷⁷ Frisch, M. J.; Trucks, G. W.; Schlegel, H. B.; Scuseria, G. E.; Robb, M. A.; Cheeseman, J. R.; Scalmani, G.; Barone, V.; Mennucci, B.; Petersson, G. A.; et al. *Gaussian 09*, revision B.01; Gaussian, Inc.: Wallingford, CT, 2009.
- ⁷⁸ Rappe, A. K.; Casewit, C. J.; Colwell, K. S.; Goddard III, W. A.; Skiff, W. M. UFF, a Full Periodic Table Force Field for Molecular Mechanics and Molecular Dynamics Simulations. *J. Am. Chem. Soc.* **1992**, *114*, 10024-10035.
- ⁷⁹ Pauling, L. *The Nature of the Chemical Bond*, 3rd Ed.; Cornell University Press: Ithaca, NY, 1960.
- ⁸⁰ Frisch, M. J.; Trucks, G. W.; Schlegel, H. B.; Scuseria, G. E.; Robb, M. A.; Cheeseman, J. R.; Montgomery, Jr., J. A.; Vreven, T.; Kudin, K. N.; Burant, J. C. et al. *Gaussian 03*, Revision E.01, Gaussian, Inc., Wallingford CT, 2004.
- ⁸¹ York, D.; Karplus, M. A Smooth Solvation Potential Based on the Conductor-Like Screening Model. *J. Phys. Chem. A* **1999** *103*, 11060-11079.
- ⁸² McQuarrie, D. A. *Statistical Mechanics*. University Science Books: Sausalito, CA, 2000.
- ⁸³ Valiev, M.; Bylaska, E.J.; Govind, N.; Kowalski, K.; Straatsma, T.P.; van Dam, H.J.J.; Wang, D.; Nieplocha, J.; Apra, E.; Windus, T.L.; et al. NWChem: A Comprehensive and Scalable Open-Source Solution for Large Scale Molecular Simulations. *Comput. Phys. Commun.* **2010**, *181*, 1477-1489.
- ⁸⁴ Kendall, R. A.; Aprà, E.; Bernholdt, D. E.; Bylaska, E. J.; Dupuis, M.; Fann, G. I.; Harrison, R. J.; Ju, J.; Nichols, J. A.; Nieplocha, J.; High Performance Computational Chemistry: An Overview of NWChem a Distributed Parallel Application. *Comp. Phys. Comm.* **2000**, *128*, 260-283.
- ⁸⁵ *AMPAC 9*; Semichem, Inc.: Shawnee, KS, 1992-2008.
- ⁸⁶ Cherif, M.; Mgaidi, A.; Ammar, G. V.; Furst, W. S. A New Investigation of Aqueous Orthophosphoric Acid Speciation Using Raman Spectroscopy. *Solution Chem.* **2000**, *29*, 255-269.

-
- ⁸⁷ Preston, C. M.; Adams, W. A. A Laser Raman Spectroscopic Study of Aqueous Phosphoric Acid. *Can. J. Spectrosc.* **1977**, *22*, 125-136.
- ⁸⁸ Pye, C. C.; Rudolph, An ab Initio, Infrared, and Raman Investigation of Phosphate Ion Hydration. *J. Phys. Chem. A*, **2003**, *107*, 8746-8755.
- ⁸⁹ Nichols, P.; Bylaska, E. J.; Schenter, G. K. and de Jong, W. Equatorial and Apical Solvent Shells of the UO_2^{2+} Ion. *J. Chem. Phys.* **2008**, *128*, 124507 (8 pages).
- ⁹⁰ Sullens, T. A.; Jensen, R. A.; Shvareva, T. Y.; Albrecht-Schmitt, T. E. Cation-Cation Interactions Between Uranyl Cations in a Polar Open-Framework Uranyl Periodate. *J. Am. Chem. Soc.* **2004**, *126*, 2676-2677.
- ⁹¹ Sarsfield, M. J.; Helliwell, M. Extending the Chemistry of the Uranyl Ion: Lewis Acid Coordination to a U=O Oxygen. *J. Am. Chem. Soc.* **2004**, *126*, 1036-1037.
- ⁹² Suzuki, Y.; Sato, T.; Isobe, H.; Kogure, T.; Murakami, T. Dehydration Processes in the Metaautunite Group Minerals, Meta-Autunite, Metasalecite and Metatorbernite. *Am. Mineral.* **2005**, *90*, 1308-1314.
- ⁹³ Sen, B. K.; Sen, S. Mechanism of Proton Transport in HUP ($\text{HUO}_2\cdot\text{PO}_4\cdot 4\text{H}_2\text{O}$). *Solid State Ionics*, **1986**, *18-19*, 1025-1030.
- ⁹⁴ Morosin, B. Hydrogen Uranyl Phosphate Tetrahydrate, A Hydrogen Ion Solid Electrolyte. *Acta Cryst. Sect B* **1978**, *34*, 3732-3734.
- ⁹⁵ Semon, L.; Boehme, C.; Billard, I.; Hennig, C.; Lutzenkirchen, K.; Reich, T.; Rossberg, A.; Rossini, I.; Wipff, G. Do Perchlorate and Triflate Anions Bind to the Uranyl Cation in an Acidic Aqueous Medium? A Combined EXAFS and Quantum Mechanical Investigation. *Chem. Phys. Chem.* **2001**, *2*, 591-598.
- ⁹⁶ Wahlgren, U.; Moll, H.; Grenthe, I.; Schimmelpfennig, B.; Maron, L.; Vallet, V.; Gropen, O. Structure of Uranium(VI) in Strong Alkaline Solutions. A Combined Theoretical and Experimental Investigation. *J. Phys. Chem. A* **1999**, *103*, 8257- 8264.
- ⁹⁷ Frost, R. L.; Cejka, J.; Weier, M. A Raman Spectroscopic Study Of The Uranyl Phosphate Mineral Threadgoldite. *Spectrochimica Acta Part A* **2006**, *65*, 797-801.
- ⁹⁸ Pekárek, V.; Veselý, V. A Study on Uranyl Phosphates-II Sorption Properties of Some 1- to 4- Valent Cations on Uranyl Hydrogen Phosphate Heated to Various Temperatures *J. Inorg. Nucl. Chem.* **1964**, *2*, 1151-1158.
- ⁹⁹ Tang, E.; Tommaso, D. D.; de Leeuw, N. H. Accuracy of the Microsolvation–Continuum Approach in Computing the pK_a and the Free Energies of Formation of Phosphate Species in Aqueous Solution. *Phys. Chem. Chem. Phys.* **2010**, *12*, 13804-13815.

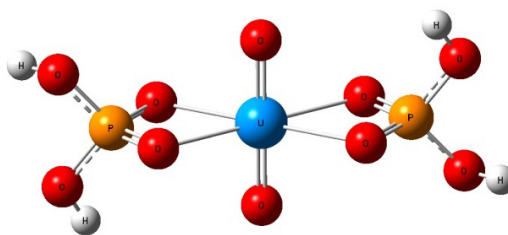
-
- ¹⁰⁰ Mora-Fonz, M. J.; Catlow, C. R. A.; Lewis, D. W. Modeling Aqueous Silica Chemistry in Alkali Media. *J. Phys. Chem. C*, **2007**, *111*, 18155-18158.
- ¹⁰¹ Zhang, L.; Xie, D.; Xu, D. Guo, H. Supermolecule Density Functional Calculations Suggest a Key Role for Solvent in Alkaline Hydrolysis of P-Nitrophenyl Phosphate. *Chem. Commun.*, **2007**, 1638-1640.
- ¹⁰² Stryer, L. *Biochemistry*, W. H. Freeman and Co., New York, 3rd Ed, 1988.
- ¹⁰³ Klamt, A.; Schüürmann, G. COSMO: A New Approach to Dielectric Screening in Solvents with Explicit Expressions for The Screening Energy and its Gradient *J. Chem. Soc. Perkin Trans. 2* **1993**, 799-805.
- ¹⁰⁴ Klamt, A.; Jonas, V.; Buerger, T.; Lohrenz, J. C. W. Refinement and Parametrization of COSMO-RS. *J. Phys. Chem.* **1998**, *102*, 5074-5085.
- ¹⁰⁵ Klamt, A. *COSMO-RS: from quantum chemistry to fluid phase thermodynamics and drug design, Volume I*; Elsevier, 2005.
- ¹⁰⁶ Perdew, J. P.; Burke, K.; Ernzerhof, M. Generalized Gradient Approximation Made Simple. *Phys. Rev. Lett.*, **1996**, *77*, 3865-3868.
- ¹⁰⁷ Lide, D. R., Ed.; *CRC Handbook of Chemistry and Physics*, 86th ed.; Taylor and Francis: Boca Raton, FL, 2005-2006; Chapter 7, p 14.
- ¹⁰⁸ Pearson, R. G. Ionization Potentials and Electron Affinities in Aqueous Solution. *J. Am. Chem. Soc.* **1986**, *108*, 6109-6114.
- ¹⁰⁹ Camaioni, D. M.; Schwerdtfeger, C. A. Comment on "Accurate Experimental Values for the Free Energies of Hydration of H⁺, OH⁻, and H₃O⁺." *J. Phys. Chem. A* **2005**, *109*, 10795-10797.
- ¹¹⁰ Tissandier, M. D.; Cowen, K. A.; Feng, W. Y.; Gundlach, E.; Cohen, M. H.; Earhart, A. D.; Coe, J. V. The Proton's Absolute Aqueous Enthalpy and Gibbs Free Energy of Solvation from Cluster-Ion Solvation Data. *J. Phys. Chem. A* **1998**, *102*, 7787-7794.
- ¹¹¹ Tuttle, T. R.; Malaxos, S.; Coe, J. V. A New Cluster Pair Method of Determining Absolute Single Ion Solvation Energies Demonstrated in Water and Applied to Ammonia. *J. Phys. Chem. A* **2002**, *106*, 925-932.
- ¹¹² Zhan, C.-G.; Dixon, D. A. Absolute Hydration Free Energy of the Proton from First-Principles Electronic Structure Calculations. *J. Phys. Chem. A* **2001**, *105*, 11534-11540.
- ¹¹³ Mathur, J. N. Complexation And Thermodynamics of The Uranyl Ion with Phosphate. *Polyhedron* **1991**, *10*, 47-53.

¹¹⁴ Grenthe, I.; Fuger, J.; Konings, R. J. M.; Lemire, R. J.; Muller, A. B.; Nguyen-Tsung Cregu, C.; Wanner, H. *Chemical Thermodynamics Of Uranium*. Eds.; Wanner, H.; Forest, I. Elsevier, Amsterdam, New York, 1992.

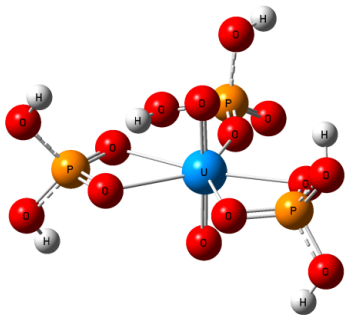
¹¹⁵ Goldberg, R. N.; Kishore, N.; Lennen, R. M. Thermodynamic Quantities for the Ionization Reactions of Buffers. *J. Phys. Chem. Ref. Data*, **2002**, *31*, 231-370.



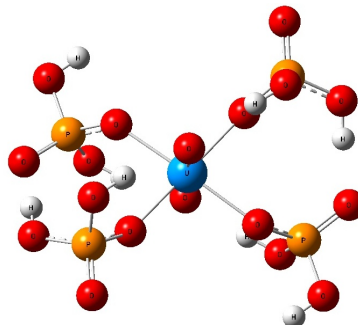
$[\text{UO}_2(\text{H}_2\text{PO}_4)]^+$



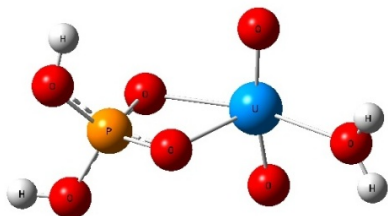
$\text{UO}_2(\text{H}_2\text{PO}_4)_2$



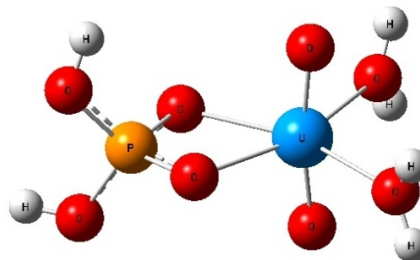
$[\text{UO}_2(\text{H}_2\text{PO}_4)_3]^-$



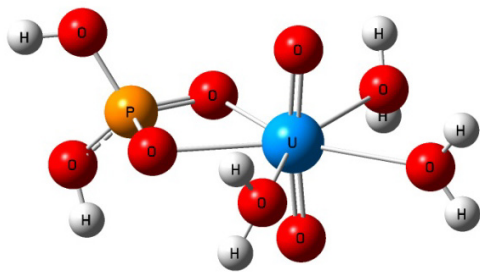
$[\text{UO}_2(\text{H}_2\text{PO}_4)_4]^{2-}$



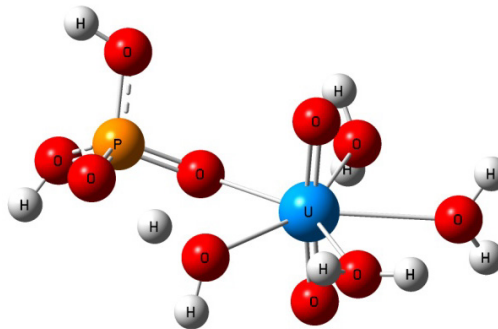
$[\text{UO}_2(\text{H}_2\text{PO}_4)(\text{H}_2\text{O})]^+$



$[\text{UO}_2(\text{H}_2\text{PO}_4)(\text{H}_2\text{O})_2]^+$



$[\text{UO}_2(\text{H}_2\text{PO}_4)(\text{H}_2\text{O})_3]^+$



$[\text{UO}_2(\text{H}_2\text{PO}_4)(\text{H}_2\text{O})_4]^+$

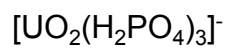
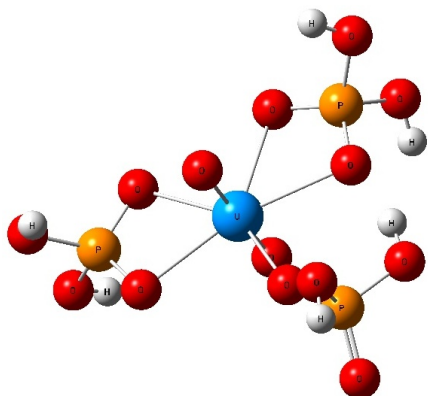
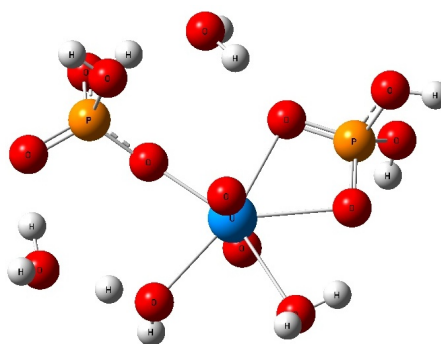
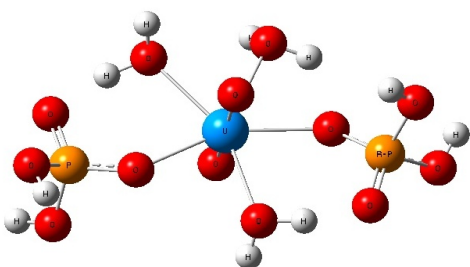
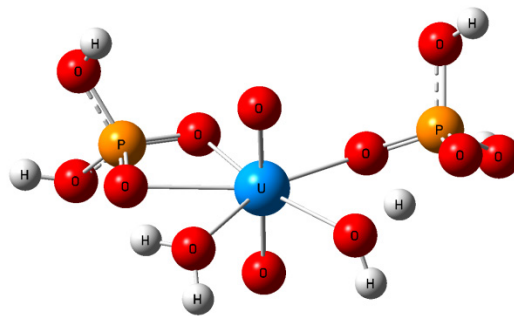
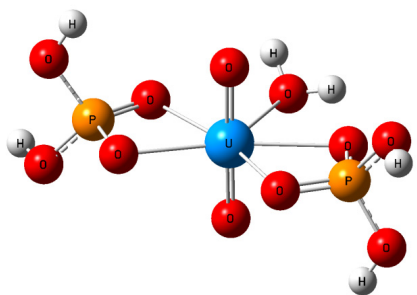
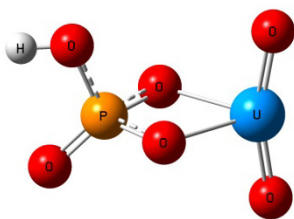
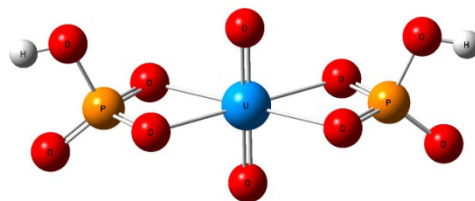


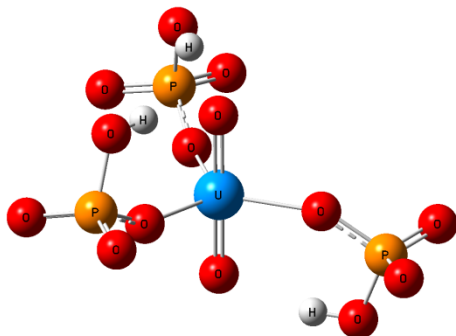
Figure 5.1. Optimized structures of $[\text{UO}_2(\text{H}_2\text{PO}_4)_n(\text{H}_2\text{O})_m]^{z\pm}$.



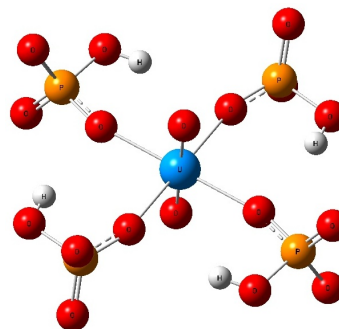
$\text{UO}_2(\text{HPO}_4)$



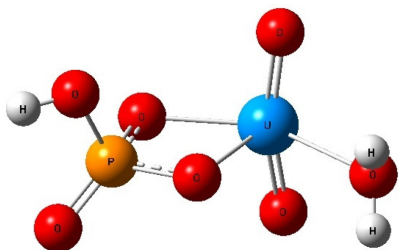
$[\text{UO}_2(\text{HPO}_4)_2]^{2-}$



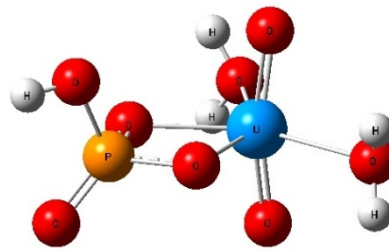
$[\text{UO}_2(\text{HPO}_4)_3]^{4-}$



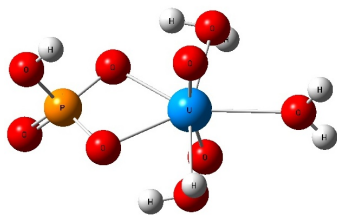
$[\text{UO}_2(\text{HPO}_4)_4]^{6-}$



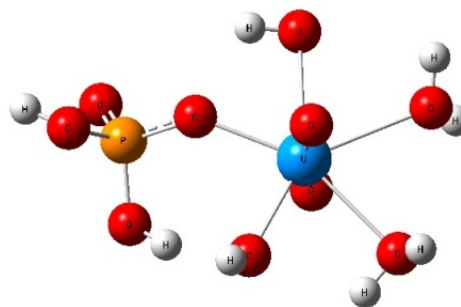
$\text{UO}_2(\text{HPO}_4)(\text{H}_2\text{O})$



$\text{UO}_2(\text{HPO}_4)(\text{H}_2\text{O})_2$



$\text{UO}_2(\text{HPO}_4)(\text{H}_2\text{O})_3$



$\text{UO}_2(\text{H}_2\text{PO}_4)(\text{H}_2\text{O})_3\text{OH}$
 $= \text{UO}_2(\text{HPO}_4)(\text{H}_2\text{O})_4$

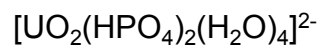
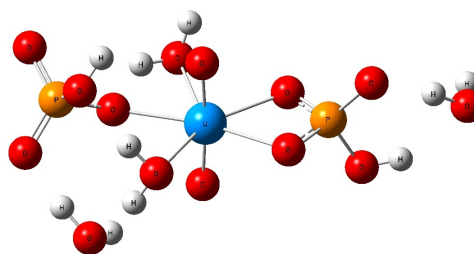
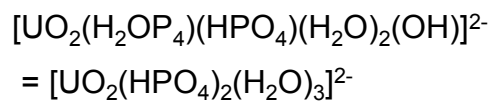
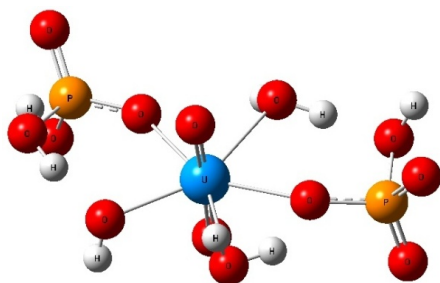
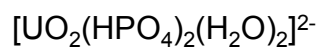
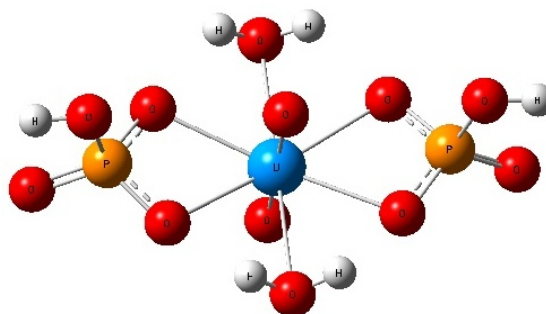
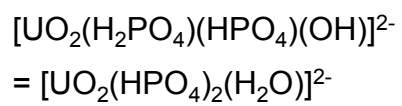
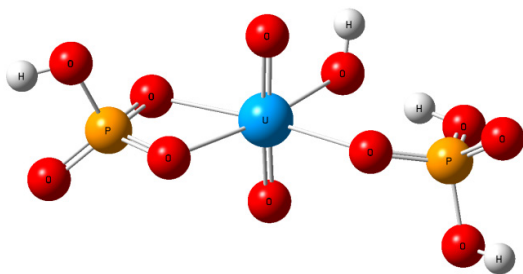
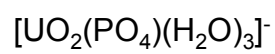
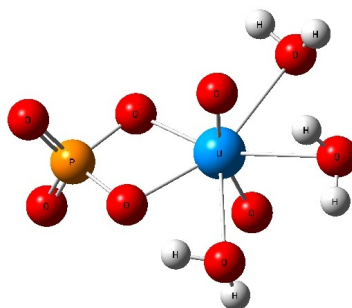
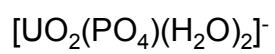
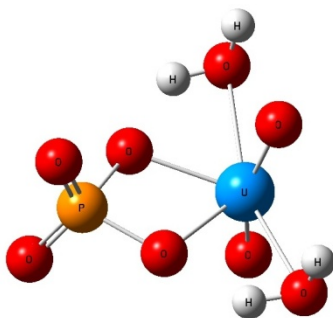
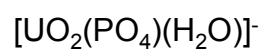
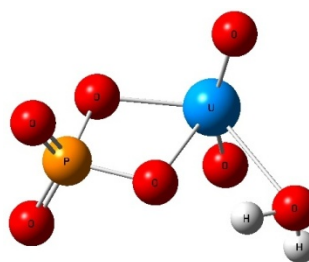
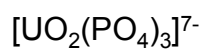
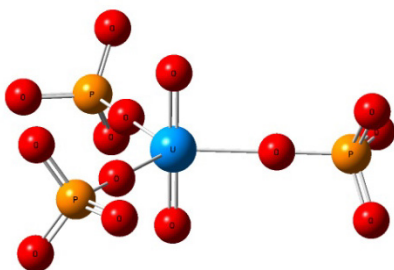
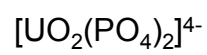
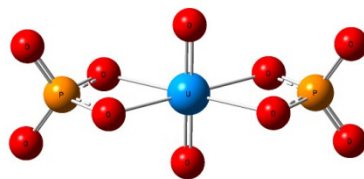
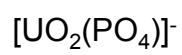
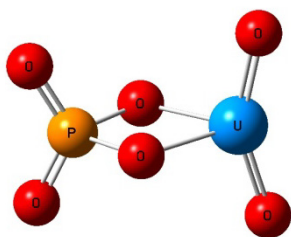


Figure 5.2. Optimized structures of $[\text{UO}_2(\text{HPO}_4)_n(\text{H}_2\text{O})_m]^{2-}$.



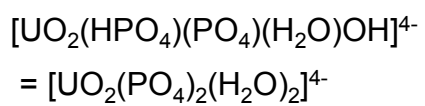
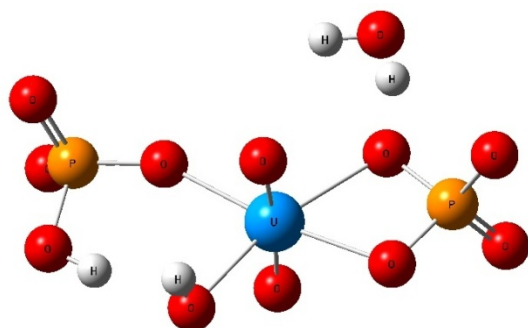
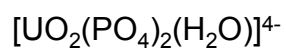
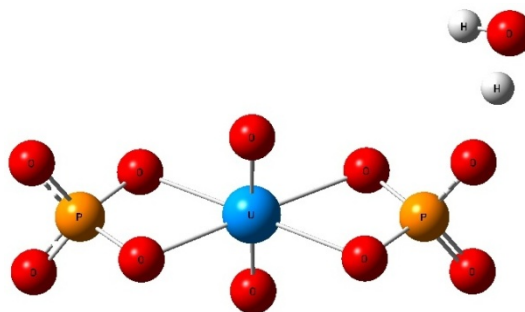
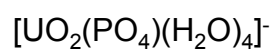
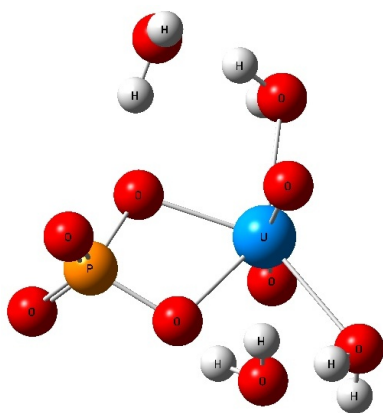


Figure 5.3. Optimized structures of $[\text{UO}_2(\text{PO}_4)_n(\text{H}_2\text{O})_m]^{z-}$.

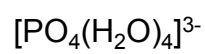
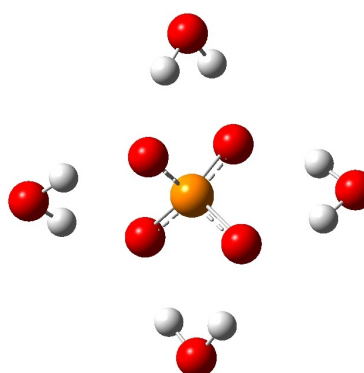
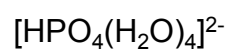
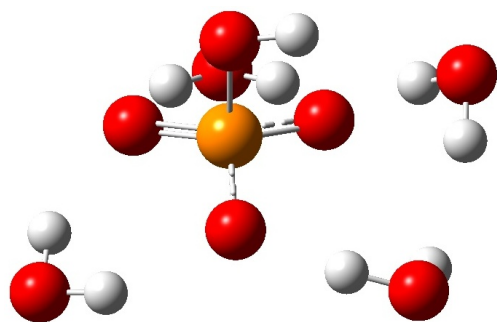
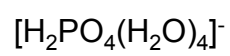
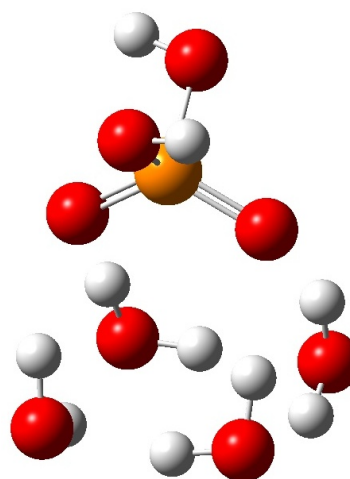
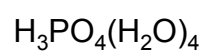
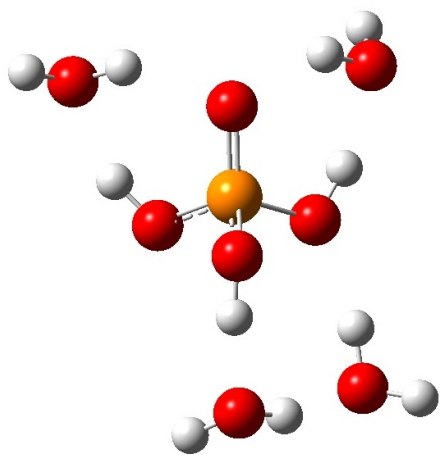


Figure 5.4. Optimized structures of $[\text{H}_n\text{PO}_4(\text{H}_2\text{O})_4]^z$.

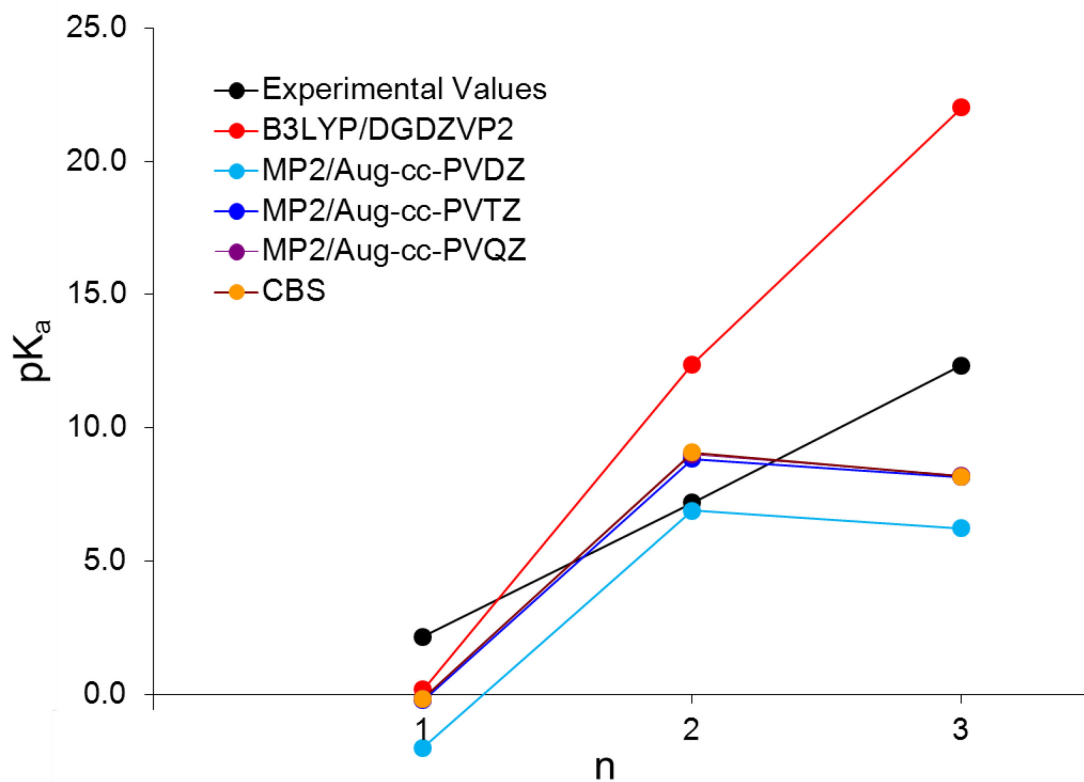


Figure 5.5. Phosphoric acid pK_a s for the 1st, 2nd, and 3rd ($n = 1, 2, 3$) deprotonations of H_3PO_4 geometries optimized at the B3LYP/DZVP2, with single point energies at the MP2/Aug-cc-pVnZ ($n = D, T, \text{ and } Q$) levels. pK_a 's calculated from the gas phase values at each level plus single point B3LYP/DZVP2 CPCM with COSMO-RS radii SCRF calculations. Experimental data from reference 107.

Table 5.1. Calculated Ligand and Uranyl Bond Distances (Å) and Vibrational Frequencies (ν in cm^{-1}).

Molecule	Sym	U=O	P=O	P-O(H)	O-H	$\nu_{\text{asym}}(\text{U=O})^{\text{a}}$	$\nu_{\text{sym}}(\text{U=O})^{\text{a}}$	$\nu(\text{P=O})$	$\nu(\text{P-O(H)})$
UO_2^{2+}	$D_{\infty h}$	1.701				1141 (σ_u)	1041 (σ_g)		
H_3PO_4	C_3		1.478	1.607	0.967			1304 (a)	915 (e), 825 (a)
H_3PO_4 Exp ^b								1170, 1010	892
H_2PO_4^-	C_2		1.503	1.679	0.965			1312 (b), 1079 (a)	766 (b), 742 (a)
H_2PO_4^- Exp ^b								1150, 1074	940, 874
H_2PO_4^- Exp ^b								1152, 1075	945, 877
HPO_4^{2-}	C_s		1.546	1.784	0.965			1114 (a''), 987 (a')	611 (a')
HPO_4^{2-} Exp ^c								1080 \pm 4, 990	
PO_4^{3-}	T_d		1.604					903 (t_2), 798 (a_1)	
PO_4^{3-} Exp ^c								1010 (t_2), 937 (a_1)	

^a asym = antisymmetric UO_2^{2+} stretch. sym = symmetric UO_2^{2+} stretch. UO_2^{2+} bend at 151 cm^{-1} (π). ^b Reference 86. ^c Reference 88.

Table 5.2. Average NPA Charges per Atom on Ligands and Uranyl.

Molecule/ion	U	P	O	O(H)	H
UO ₂ ²⁺	3.26		-0.63		
H ₃ PO ₄		2.46	-1.08	-0.96	0.50
H ₂ PO ₄ ⁻		2.42	-1.16	-1.02	0.47
HPO ₄ ²⁻		2.42	-1.26	-1.08	0.44
PO ₄ ³⁻		2.45	-1.36		

Table 5.3. Selected Bond Lengths (Å), Angles (degrees), and UO₂²⁺ Vibrational Frequencies (ν, cm⁻¹) for Anhydrous Uranyl Phosphates.

Complex	Sym	Bond Distances					Bond Angles		UO ₂ ²⁺ ν	
		U=O	U-O _{phos}	P-O _{bound}	P-O _{term}	P-O _(-H)	∠O-P-O _{bound}	∠O=U=O	asym ^a	sym ^a
[UO ₂ (H ₂ PO ₄)] ⁺	C ₁	1.750	2.256	1.557		1.570	99.8	168.4	1027	939
UO ₂ (HPO ₄)	C _s	1.776	2.167	1.611	1.476	1.616	94.4	162.3	970	891
[UO ₂ (PO ₄)] ⁻	C _{2v}	1.819	2.098	1.701	1.496		89.0	151.7	867	840
UO ₂ (H ₂ PO ₄) ₂	C _i	1.771	2.406	1.533		1.601	106.4	180.0	982	900
[UO ₂ (HPO ₄) ₂] ²⁻	C _{2v}	1.794	2.367	1.569	1.507	1.675	101.8	180.0	927	849
[UO ₂ (PO ₄) ₂] ⁴⁻	D _{2h}	1.826	2.351	1.630	1.547		96.7	180.0	849	774
[UO ₂ (H ₂ PO ₄) ₃] ⁻	C ₁	1.783	2.517 ^b 2.234	1.525 ^b 1.557	1.488 ^c	1.614 ^b 1.644	108.2	176.2	954	865
[UO ₂ (HPO ₄) ₃] ⁴⁻	C _s	1.824	2.213	1.626	1.519	1.696	111.3 ^d 111.4 (x2) ^d	179.6	866	760
[UO ₂ (PO ₄) ₃] ⁷⁻	C ₃	1.815	2.335	1.686	1.578		108.2 (x3) ^d	180.0	868	812
[UO ₂ (H ₂ PO ₄) ₄] ²⁻	C ₂	1.829	2.266	1.564	1.490	1.624	118.2(x2) ^d 117.2(x2) ^d	180.0	845	751
[UO ₂ (HPO ₄) ₄] ⁶⁻	C ₄	1.795	2.393	1.592	1.537	1.706	100.9(x4) ^d	180.0	919	815

^a asym = antisymmetric UO₂²⁺ stretch. sym = symmetric UO₂²⁺ stretch. ^b Average. ^c Due to one phosphate being monodentate, with equatorial hydrogen bonding. ^d Monodentate binding.

Table 5.4. Average NPA Charges (in electrons) for Anhydrous Uranyl Monophosphates.

Complex	U	O (oxo)	P	O (bound)	O (term)	O(H)	H
$[\text{UO}_2(\text{H}_2\text{PO}_4)]^+$	2.98	-0.77	2.51	-1.08		-0.94	0.54
$\text{UO}_2(\text{HPO}_4)$	2.88	-0.82	2.44	-1.08	-1.06	-0.97	0.51
$[\text{UO}_2(\text{PO}_4)]^-$	2.81	-0.91	2.42	-1.09	-1.12		
$\text{UO}_2(\text{H}_2\text{PO}_4)_2$	2.88	-0.83	2.49	-1.10		-0.96	0.51
$[\text{UO}_2(\text{HPO}_4)_2]^{2-}$	2.84	-0.88	2.46	-1.14	-1.17	-1.00	0.47
$[\text{UO}_2(\text{PO}_4)_2]^{4-}$	2.79	-0.95	2.46	-1.20	-1.26		
$[\text{UO}_2(\text{H}_2\text{PO}_4)_3]^-$	2.91	-0.88	2.49	-1.13	-1.12	-0.97	0.50
$[\text{UO}_2(\text{HPO}_4)_3]^{4-}$	3.00	-0.95	2.47	-1.21	-1.20	-1.05	0.49
$[\text{UO}_2(\text{PO}_4)_3]^{7-}$	2.98	-0.94	2.48	-1.24	-1.32		
$[\text{UO}_2(\text{H}_2\text{PO}_4)_4]^{2-}$	2.95	-0.96	2.51	-1.15	-1.12	-1.01	0.51
$[\text{UO}_2(\text{HPO}_4)_4]^{6-}$	3.00	-0.90	2.48	-1.23	-1.24	-1.07	0.50

Table 5.5. Selected Bond Lengths (Å), Angles (degrees), and UO_2^{2+} Vibrational Frequencies (ν , cm^{-1}) for Hydrated Uranyl Monophosphates.

Complex	n	Bond Distances					Bond Angles		UO_2^{2+} ν		
		U=O	U-O _{phos}	P-O _{bound}	P-O _{term}	P-O _(-H)	U-OH ₂	$\angle\text{O-P-O}$	$\angle\text{O=U=O}$	asym ^a	sym ^a
$[\text{UO}_2(\text{H}_2\text{PO}_4)(\text{H}_2\text{O})_n]^+$	1	1.758	2.288	1.552		1.576	2.467	101.2	169.4	1008	927
	2	1.766	2.318	1.547		1.582	2.488	102.2	170.3	998	916
	3	1.768	2.369	1.541		1.588	2.527	103.3	171.8	994	911
	4 ^b	1.765	2.230	1.559	1.508 ^c	1.599	2.566 2.447 ^c		172.8	1000	905
$\text{UO}_2(\text{HPO}_4)(\text{H}_2\text{O})_n$	1	1.782	2.194	1.605	1.479	1.622	2.531	95.2	163.6	958	879
	2	1.788	2.217	1.600	1.481	1.627	2.562	96.0	164.7	951	873
	3	1.791	2.286	1.546	1.512 ^c	1.610	2.566 2.495 ^c 2.130 ^c	114.2 ^d	172.6	946	862
	3 ^f	1.771 1.757	2.286	1.626	1.492	1.649	2.608 2.624(x2)		169.1		
	4	1.791	2.138	1.618	1.533	1.620	2.505 ^c 2.520 ^c 2.595 2.597	106.5 ^d	162.0	940	855
$\text{UO}_2(\text{HPO}_4)(\text{H}_2\text{O})_4$	Exp ^g									930	832
$[\text{UO}_2(\text{PO}_4)(\text{H}_2\text{O})_n]^-$	1	1.815	2.133	1.693	1.497		2.650	123.9	155.2	880	818

2	1.811	2.164	1.688	1.499	2.672(x2)	123.6	158.2	895	862
3	1.826	2.159	1.687	1.501	2.700	123.1	160.4	870	804
					2.824				
					2.711				
4	1.806	2.191	1.685	1.500	2.565	123.6	162.7	907	841

^a asym = antisymmetric UO_2^{2+} stretch. sym = symmetric UO_2^{2+} stretch. ^b Pentagonal bipyramidal (with monodentate phosphate ligand and 4 bound waters) is more stable by 2.5 kcal/mol (ΔE_{elec}) than hexagonal bipyramidal structure. ^c Hydrogen bonded; elongated H-OH bond. ^d Monodentate phosphate. ^e OH ligand, from proton transfer to phosphate. ^f B3LYP calculations. Reference 46. ^g Reference 98.

Table 6. Selected Bond Lengths (Å), Angles (degrees), and UO₂²⁺ Vibrational Frequencies (ν, cm⁻¹) for Hydrated Uranyl Diphosphates.

Complex	n	Bond Distances					Bond Angles		UO ₂ ²⁺ ν		
		U=O	U-O _{phos}	P-O _{bound}	P-O _{term}	P-O _(-H)	U-OH ₂	∠O-P-O	∠O=U=O	asym ^a	sym ^a
UO ₂ (H ₂ PO ₄) ₂ (H ₂ O) _n	1	1.773	2.491 ^b 2.404 ^c	1.530		1.604	2.535	107.1	178.6	979	896
	2	1.774	2.561 ^b 2.401 ^c 2.288 ^d	1.533	1.504	1.610	2.586 2.495 ^e	107.0	174.5	980	892
	3	1.773	2.305 ^d 2.386 ^d	1.543	1.503	1.615	2.600 2.510 ^e 2.451 ^e	108.0	177.1	982	890
[UO ₂ (H ₂ PO ₄) ₂ (H ₂ O)] ₂ · (18-crown-6)·5H ₂ O	Exp ^f	1.754(7)		1.569(8)	1.487(1)				178.9(3)		
		1.765(8)		1.569(7)	1.510(7)				177.7(3)		
		1.760(7)									
		1.765(6)									
UO ₂ (H ₂ PO ₄) ₂ (H ₂ O)·(1 8-crown-6)·3H ₂ O	Exp ^f	1.769		1.587(4)	1.485(5)				177.6		
				1.574(5)	1.490(5)						
[UO ₂ (HPO ₄) ₂ (H ₂ O) _n] ²⁻	1	1.798	2.363 2.370 ^d	1.560	1.504	1.650	2.290 ^g	101.5	176.0	925	844
	2	1.789	2.453 2.455	1.564	1.508	1.644	2.703 2.701	101.7	180.0	938	857

	3	1.820	2.346 ^d	1.558	1.487	1.631	2.264 ^g	105.7 ^c	179.4	902	772
							3.998 ^h				
$[(\text{UO}_2)_3(\text{PO}_4)\text{O}(\text{OH})(\text{H}_2\text{O})_2](\text{H}_2\text{O})$	Exp ⁱ	1.756	2.587	1.538	1.538						
$[\text{UO}_2(\text{PO}_4)_2(\text{H}_2\text{O})_n]^{4-}$	1	1.822	2.330	1.624	1.549			112.5	178.7	866	788
			2.328								
			2.371								
			2.392								
	2	1.821	2.350 ^c	1.623	1.536	1.705		114.9	174.1	871	786
			2.293 ^b								
			2.395 ^a								
$(\text{UO}_2)_3(\text{PO}_4)_2(\text{H}_2\text{O})_4$	Exp ^j	1.793	2.297	1.556	1.495	1.546	2.490		178.6		
		1.759					2.490				
$\text{Al}[(\text{UO}_2)_2(\text{PO}_4)_2](\text{OH})\cdot 8\text{H}_2\text{O}$	Exp ^k	1.748								953	
		1.749								952	
		1.766									845
		1.771									840
		1.783									828
		1.784									827
		1.794									817
		1.794									817

^a asym = antisymmetric UO_2^{2+} stretch. sym = symmetric UO_2^{2+} stretch. ^b Proximal to H_2O , bidentate phosphate. ^c Distal to H_2O , bidentate phosphate. ^d Monodentate phosphate. ^e Hydrogen bonded; elongated H-OH bond. ^f Reference 21. ^g OH ligand, from proton transfer to phosphate. ^h Second sphere water. ⁱ Reference 20. ^j Reference 22. ^k Reference 97.

Table 5.7. Calculated Reaction Energetics for Binding of Phosphate Ligands to Form Anhydrous Uranyl Phosphate Complexes (kcal/mol).

<i>N</i>	$\text{UO}_2^{2+} + n\text{H}_2\text{PO}_4^- \rightarrow [\text{UO}_2(\text{H}_2\text{PO}_4)_n]^{2-n}$		$\text{UO}_2^{2+} + n\text{HPO}_4^{2-} \rightarrow [\text{UO}_2(\text{HPO}_4)_n]^{2-2n}$		$\text{UO}_2^{2+} + n\text{PO}_4^{3-} \rightarrow [\text{UO}_2(\text{PO}_4)_n]^{2-3n}$	
	$\Delta\text{H}_{298}(\text{gas})$	$\Delta\text{G}_{298}(\text{gas})$	$\Delta\text{H}_{298}(\text{gas})$	$\Delta\text{G}_{298}(\text{gas})$	$\Delta\text{H}_{298}(\text{gas})$	$\Delta\text{G}_{298}(\text{gas})$
1	-353.4	-341.7	-597.6	-586.0	-861.2	-851.5
2	-524.3	-501.8	-754.9	-730.2	-895.9	-873.7
3	-580.2	-547.7	-621.0	-588.0	-399.5	-372.1
4	-589.0	-539.9	-282.2	-237.5		

Table 5.8. Calculated Gas Phase Reaction Energetics for the Reactions $\text{UO}_2(\text{H}_2\text{PO}_4)_2 + n\text{H}_2\text{O} \rightarrow [\text{UO}_2(\text{H}_2\text{O})_n(\text{H}_2\text{PO}_4)_2]$ and $[\text{UO}_2(\text{HPO}_4)_2]^{2-} + n\text{H}_2\text{O} \rightarrow [\text{UO}_2(\text{H}_2\text{O})_n(\text{HPO}_4)_2]^{2-}$ in kcal/mol.^a

<i>n</i>	$\text{UO}_2(\text{H}_2\text{PO}_4)_2$		$[\text{UO}_2(\text{HPO}_4)_2]^{2-}$	
	$\Delta\text{H}_{298}(\text{gas})$	$\Delta\text{G}_{298}(\text{gas})$	$\Delta\text{H}_{298}(\text{gas})$	$\Delta\text{G}_{298}(\text{gas})$
1	-21.7	-12.2	-19.5	-10.2
2	-34.4	-14.9	-41.7	-21.7
3	-45.7	-16.9	-35.0	-6.7
4	-58.5	-19.5	-62.7	-23.0

Table 5.9. Phosphoric Acid pK_as for the 1st, 2nd, and 3rd Deprotonation.^a

Method	1st	2nd	3^d
B3LYP/DZVP2	0.2	12.4	22.0
MP2/Aug-cc-pVDZ	-2.0	6.9	6.2
MP2/Aug-cc-pVTZ	-0.2	8.8	8.2
MP2/Aug-cc-pVQZ	-0.2	9.0	8.2
CBS	-0.2	9.1	8.2
Experiment ^b	2.15	7.20	12.35

^a Geometries optimized at the B3LYP/DZVP2 level. Single point energies at the MP2 level with the aug-cc-pVnZ (n = D, T, and Q) basis sets and extrapolated to the complete basis set limit (CBS). pK_a's calculated from the gas phase values at each level plus single point B3LYP/DZVP2 CPCM with COSMO-RS radii SCRF calculations.

^b Experimental data from reference 107.

Table 5.10. MP2/aug-cc-pVTZ Reaction Free Energies in Aqueous Solution ($\Delta G_{298}\text{Soln}$) of Solvated Phosphates/ H_2O

Complexes in kcal/mol.

Reaction	ΔH_{298}	ΔG_{298}	$\Delta G_{298}\text{Soln}$							
	gas	gas	CPCM-COSMO-RS Radii	IEF-PCM UA0	IEF-PCM UFF	IPCM	IEF-PCM Pauling^a	CSC-PCM Pauling^b	Tang et al.^c	Expt^d
2	312.6	307.4	-0.0	5.5	0.7	2.9	0.4	-0.4	8.6	2.9
3	407.6	398.7	8.9	19.8	14.2	13.8	8.8	9.2	12.7	9.8
4	512.2	507.6	13.4	23.7	26.5	29.9	15.2	16.7	11.7	16.9

^a IEF-PCM using Pauling Radii. ^b CSC-PCM with Pauling Radii. ^c Reference 99. ^d Reference 107.

Table 5.11. MP2 Calculated Free Energies in Aqueous Solution ($\Delta G_{298}\text{Soln}$) of UO_2^{2+} /Solvated Phosphates/ H_2O Complexes in kcal/mol.

Rxn	ΔH_{298}	ΔG_{298}	$\Delta G_{298}\text{Soln}$	$\Delta G_{298}\text{Soln}$	$\Delta G_{298}\text{Soln}$	$\Delta\Delta G(\text{Expt} - \text{IPCM})$				
	gas	gas	CPCM-COSMO-RS Radii	IEF-PCM UA0	IEF-PCM UFF	IPCM	IEF-PCM-Pauling ^a	CSC-PCM Pauling ^b	Expt.	
5	-77.8	-87.6	-2.2	-11.3	0.9	-0.6	-3.4	0.7	-1.0 ^c	-0.4
6a	12.7	-23.4	-11.2	-21.8	-0.5	-4.1	-15.6	-8.9	-1.0 ^c	3.1
6b	-10.3	-19.7	-3.4	-13.0	-1.4	0.9	-6.6	-1.5	-1.0 ^c	-1.9
7a	-141.1	-188.8	-30.2	-39.1	-21.6	-13.1	-32.8	-23.5	-3.99±0.03 ^d	9.1
7b	-164.0	-185.1	-22.4	-30.2	-22.5	-8.0	-23.8	-18.1	-3.99±0.03 ^d	4.0
8a	-221.4	-294.2	-51.9	-71.4	-44.0	0.5	-58.8	-41.6	-6.70±0.03 ^d	-7.2
8b	-267.3	-286.7	-36.4	-53.7	-45.8	-7.6	-40.9	-34.1	-6.70±0.03 ^d	-0.6
9a	-466.8	-513.7	-34.0	-48.6	-36.4	-19.0	-28.4	-23.2	-15.4 ^c	3.6
9b	-489.7	-510.0	-26.2	-39.8	-37.3	-13.9	-19.4	-17.7	-15.4 ^c	-1.5

^a IEF-PCM using Pauling Radii. ^b CSC-PCM with Pauling Radii. ^c Reference 114. Single point MP2/aug-cc-pVTZ basis set. ^d

Reference 113.

Table 5.12. MP2 Reaction Free Energies in Aqueous Solution ($\Delta G_{298}\text{Soln}$) of UO_2^{2+} /Solvated Phosphates/ H_2O Complexes Using the IPCM Approach in kcal/mol.

Rxn	$\Delta H_{298,\text{gas}}$	$\Delta G_{298,\text{gas}}$	$\Delta G_{298}\text{Soln}$
10a	-54.7	-99.5	-29.1
10b	-77.6	-95.8	-24.0
11a	13.7	-25.0	-13.3
11b	-9.2	-21.2	-8.3
12a	38.9	-19.1	-19.9
12b	16.0	-15.4	-14.9
13a	-15.3	-60.2	-28.4
13b	-38.2	-56.5	-23.4
14a	-311.7	-345.3	-7.6
14b	-334.7	-341.5	-2.6

Table 13. Calculated Reaction Free Energies in Aqueous Solution ($\Delta G_{298}\text{Soln}$, kcal/mol) for the Successive Binding of a 1st, 2nd, 3^d, and 4th Water Ligand to $\text{UO}_2(\text{H}_2\text{O})_n(\text{H}_2\text{PO}_4)_2$ to Form Hydrated Uranyl Phosphate Complexes.

Rxn	ΔH_{298}	ΔG_{298}	$\Delta G_{298}\text{Soln}$	$\Delta G_{298}\text{Soln}$				
	gas	gas	CPCM-COSMO-RS Radii	IEF-PCM UA0	IEF-PCM UFF	IPCM	IEF-PCM-Pauling ^a	CSC-PCM Pauling ^b
15	-21.7	-12.2	-11.2	-6.8	-4.6	-28.9	-5.5	-6.5
16	-12.7	-2.6	-2.4	-1.7	-2.0	-14.8	1.1	-2.4
17	-12.6	-3.2	-1.5	-1.3	-3.8	21.4	-0.1	-1.5
18	-11.5	-1.4	7.2	5.5	-1.9	1.1	3.5	1.9
19	-9.9	-0.4	0.0	3.6	2.4	22.4	5.6	3.3
20	-5.6	3.9	6.4	4.6	5.8	-11.4	6.2	5.0
21	-27.7	-16.3	0.6	7.2	-6.0	-15.3	1.2	-2.7
22	-26.6	-19.2	-5.7	-9.8	-7.4	-7.0	2.1	-2.1

^a IEF-PCM using Pauling Radii. ^b CSC-PCM with Pauling Radii.

CHAPTER 6

THERMOCHEMICAL PROPERTIES OF SELENIUM FLUORIDES, OXIDES AND OXOFLUORIDES

From Jackson, V. E.; Dixon, D. A.; Christe, K. O. Thermochemical Properties of Selenium Fluorides, Oxides and Oxofluorides *J. Phys. Chem. A* **2011**, *115*, 14407–14416.

6.1 Introduction

There is significant interest in the thermochemical properties including bond dissociation energies (BDEs) of compounds of the main group elements of the second- and higher-rows.^{1, 2} There have been a number of structural and spectroscopic studies of the binary selenium fluorides SeF_4 ,^{2,3,4,5,6,7} SeF_5^- ,^{2,8,9} and SeF_6^{2-} ^{10,11} and the selenium oxofluorides including SeOF_2 ,^{2,12,13,14,15,16} SeO_2F^- ,^{2,17,18,19,20,21} and SeOF_3^- .^{2,22,23,24} Octahedral SeF_6 has been studied extensively, and its geometry,²⁵ heat of formation,²⁶ vibrational frequencies,²⁷ and ^{77}Se NMR chemical shifts^{28,29,30} have been reported. The crystal structure of a compound of the form RSeF with R a phenyl ring with large bulky substituents was just reported.³¹ Schaefer and co-workers have reported the geometries and electron affinities of SeF_x ($x = 1-7$).³² Wang³³ predicted the heats of formation for $\text{SeF}_n^{0/\pm}$ for $n = 1-6$ using the G3 method.³⁴ In addition, Wang recommended a revised value of 57.90 ± 0.3 kcal/mol for $\Delta H_f(\text{Se})$ at 0 K based on the ionization chemistry of H_2Se .³⁵ This value differs substantially from the value given by Wagman *et al.*³⁶ of $\Delta H_f(\text{Se}) = 54.11$ kcal/mol at 0 K.

Because there is only a limited amount of information available on the above compounds as well as other selenium fluorides and oxofluorides, we have calculated the thermodynamic properties of a broad range of selenium fluorides, oxofluorides, and oxides using high level

correlated molecular orbital theory. In this paper, we report the ΔH_f 's, BDEs, fluoride affinities of SeF_n ($n = 1-6$), SeOF_n ($n = 1-4$), SeO_2F_n ($n = 1,2$), and SeO_n ($n = 1-3$), the fluorocation affinities of SeF_n ($n = 1-6$), SeOF_n ($n = 1-4$), SeO_2F_n ($n = 1,2$), and SeO_n ($n = 1-3$) and the electron affinities of SeF_n ($n = 1-6$), SeOF_n ($n = 1-4$) and SeO_2F_n ($n = 0-2$) predicted at the coupled cluster CCSD(T) theory level³⁷ extrapolated to the complete basis set limit³⁸ using the correlation-consistent basis sets.³⁹ In addition, we report the ionization potentials of many of these species.

6.2 Computational Methods

Geometries were initially optimized at the density functional theory level with the Becke's three-parameter exchange functional with the LYP correlation functional (B3LYP)^{40,41} and the standard augmented correlation consistent basis sets aug-cc-pVnZ, with $n = \text{D}$ and T , were used for O and F. A small core relativistic effective core potential (RECP) was used for Se, which subsumes the ($1s^2, 2s^2, 2p^6$) orbital space into the 10-electron core, and a 24 electron space ($3s^2, 3p^6, 4s^2, 3d^{10}$ and $4p^4$) where the electrons are treated explicitly together with the appropriate aug-cc-pVnZ basis set.⁴² We denote this combination of basis sets as aug-cc-pVnZ-PP. Only the spherical component subset (e.g., 5-term d functions, 7-term f functions, etc.) of the Cartesian polarization functions were used. The B3LYP/aug-cc-pVTZ-PP optimized geometries were then used as starting geometries for second-order Møller-Plesset perturbation theory (MP2)⁴³ optimizations which were in turn used as starting points for high accuracy CCSD(T) optimizations with the aug-cc-pVnZ-PP basis sets for $n = \text{D}$, T , and in some cases Q .

Frequencies including the IR and Raman intensities were calculated with the B3LYP and MPW1PW91 exchange-correlation functionals and at the CCSD(T)/aug-cc-pVDZ-PP level. The

unscaled vibrational frequencies from the CCSD(T)/aug-cc-pVDZ-PP calculations were used to calculate the vibrational zero point energies (ZPEs).

Only the 4s and 4p electrons on Se and the 2s and 2p electrons in O and F were correlated in the CCSD(T) valence electron correlation calculations. For the open shell atomic calculations, we used the R/UCCSD(T) (restricted method for the starting Hartree–Fock wavefunction and then relaxed the spin restriction in the coupled cluster portion of the calculation) approach.⁴⁴ The CCSD(T)/aug-cc-pVnZ-PP valence energies were extrapolated to the complete basis set (CBS) limit by using a mixed exponential/Gaussian function of the form:

$$E(n) = E_{\text{CBS}} + A \exp[-(n - 1)] + B \exp[-(n - 1)^2] \quad (1)$$

with $n = 2$ (aug-cc-pVDZ-PP), 3 (aug-cc-pVTZ-PP), and 4 (aug-cc-pVQZ-PP). We abbreviate these basis sets as AVDZ, AVTZ, and AVQZ. Core-valence corrections, ΔE_{CV} , were obtained as the difference between valence-only and all active electrons correlated calculations at the CCSD(T)/cc-pwCVTZ-PP level.⁴⁵ A scalar relativistic correction, ΔE_{SR} , due to the F and O atoms was evaluated from the expectation values for the two dominant terms in the Breit–Pauli Hamiltonian (the mass-velocity, and one-electron Darwin (MVD) corrections)⁴⁶ from configuration interaction singles and doubles (CISD) calculations with a cc-pVTZ basis set at the CCSD(T)/ aug-cc-pVTZ-PP geometry. Any “double counting” of the relativistic effect on the Se when applying a MVD correction to an energy, which already includes most of the relativistic effects via the RECP, is small. A second relativistic correction is due to the neglect of atomic spin orbit effects in our calculations, and spin orbit atomic corrections of 0.22 (O), 0.39 (F) and 2.70 (Se) kcal/mol were taken from the excitation energies compiled by Moore.⁴⁷ By combining our computed ΣD_0 values given by the following expression:⁴⁸

$$\Sigma D_0 = \Delta E_{\text{CBS}} + \Delta E_{\text{CV}} + \Delta E_{\text{SR}} + \Delta E_{\text{ZPE}} + \Delta E_{\text{SO}} \quad (2)$$

with the known atomic heats of formation^{33,49} at 0 K for the elements, $\Delta H_f(\text{O}) = 58.99$ kcal/mol, $\Delta H_f(\text{F}) = 18.47 \pm 0.07$ kcal/mol, and $\Delta H_f(\text{Se}) = 57.90 \pm 0.3$ kcal/mol,³³ we can derive ΔH_f values for the molecules under study. Heats of formation at 298 K were obtained by following the procedures outlined by Curtiss *et al.*⁵⁰

Calculations of the NMR chemical shifts were done using the gauge invariant atomic orbital (GIAO) approach to deal with the gauge invariance issue.⁵¹ All NMR calculations were done with the B3LYP/aVTZ-PP geometries. The NMR chemical shift calculations were done with the B3LYP functional and the Ahlrichs TZ2P⁵² Gaussian basis set on F and O and the aug-cc-pVTZ-PP on Se (labeled as TZ2P). Additional NMR chemical shift calculations were done with the BLYP^{41,53} functional with the TZP ADF basis set with and without using ZORA (zeroth-order regular approximation) for the relativistic effects^{54,55,56,57,58,59} with the ADF code.⁶⁰ The ⁷⁷Se chemical shifts were calculated relative to the reference standard $\text{Se}(\text{CH}_3)_2$ and the ¹⁹F shifts relative to CFCl_3 .

All of the CCSD(T) calculations were performed with the MOLPRO program system⁶¹ on the Dell Intel or Penguin AMD clusters at The University of Alabama. The DFT geometry optimizations and B3LYP NMR chemical shift calculations were done with the Gaussian program system.⁶² Molecular visualization was done using the AGUI graphics program from the AMPAC program package.⁶³

6.3 Results and Discussion

6.3.1 Geometries. The optimized geometry parameters for the selenium fluorides, oxides and oxofluorides are given in Table 1 together with the point group and ground-state symmetry labels. Drawings of all molecules and ions are given in Figure 1. We briefly discuss the $\text{SeF}_n^{0/\pm}$ geometries. The calculated CCSD(T)/AVQZ Se-F bond distance in SeF agrees well with the

experimental value within 0.002\AA .⁶⁴ As expected, SeF_2 has a C_{2v} geometry with a CCSD(T)/aVQZ calculated F-Se-F bond angle of 96.2° , which is much smaller than that of H_2O .⁶⁵ Our predicted geometry for SeF_3 at the CCSD(T)/aVQZ level is a planar, T-shaped molecule with C_{2v} symmetry. SeF_4 is a pseudotrigonal bipyramid, and SeF_5 is predicted to have C_{4v} symmetry, derived from a distorted octahedron. In octahedral SeF_6 , the Se-F bond length is in excellent agreement with experiment within 0.005\AA at the CCSD(T)/aVQZ level. The DFT BHLYP calculated geometries of Li *et al.*³² for the SeF_n compounds agree best with our higher level values. Starting from an initial structure with seven F atoms bonded to the Se, the SeF_7^+ cation dissociates to form SeF_5^+ plus difluorine (Figure 1) with a bond distance of 1.40\AA which suggests that it forms molecular fluorine which has an F-F bond length of $1.417 \pm 0.001\text{\AA}$.⁶⁶

Two selenium oxofluoride cations have interesting geometries. Starting from a structure with five F atoms and one O atom bonded to the Se, the SeOF_5^+ cation undergoes an isomerization (Figure 1) where an Se-F bond is transferred from the Se to the oxygen to form an O-F bond. A similar type of isomerization is predicted for the SeO_2F_3^+ cation starting from a structure with three F atoms and two O atoms bonded to the Se. On the basis of these results, we carefully investigated the structure of SeO_3F^+ . Starting from the pseudotetrahedral structure did not change the basic framework. We moved the F to bind to an O leading to a planar structure with C_s symmetry. The C_s structure is 17.0 kcal/mol higher in energy than the pseudotetrahedral structure with the 3 O and 1 F atoms bonded to the Se.

6.3.2 Vibrational Frequencies. Table 2 shows the comparison between theory and experiment for SeF_2 , SeF_2^+ , SeF_6 and SeO_2^- . For SeF_2 , the calculated symmetric and antisymmetric Se-F stretching modes at the CCSD(T)/aVTZ level are within 10 cm^{-1} of experiment,⁶⁷ which is excellent agreement considering that our calculated values do not include anharmonic

corrections. For SeF_2^+ , the symmetric Se-F stretching mode at the CCSD(T)/aVTZ level is within the 50 cm^{-1} of experiment.⁶⁸ For SeF_6 our CCSD(T)/aVDZ stretching modes are too small, for the a_g mode by $\sim 30 \text{ cm}^{-1}$ and for the e_g and t_{1u} modes by $\sim 10 \text{ cm}^{-1}$. This is consistent with the fact that, at this level, the bond distance is 0.045 \AA too long as compared to experiment. The t_{2g} bending mode is almost the same as experiment, but the other two bending modes are smaller than experiment with the largest difference found for the t_{1u} mode. The lower values of the calculated bending frequencies are also consistent with the longer predicted bond distance as the repulsion between fluorine ligands decreases with increasing bond length. For SeO_2^- , the symmetric Se-O stretching mode at the CCSD(T)/aVTZ level is within 10 cm^{-1} of the value of $810 \pm 80 \text{ cm}^{-1}$ derived from a photoelectron spectroscopy experiment.⁶⁹

Table 3 shows the vibrational stretching frequencies calculated at the CCSD(T)/aVDZ level for SeF_n ($n = 1,3,4,5$), SeF_n^- ($n = 1-4, 7$), SeF_3^+ , SeOF_n ($n = 0, 1-5$), SeOF_n^- ($n = 1,2,3,5$), SeO_2F_n ($n = 1,2$), SeO_2F_n^- ($n = 1-3$), and SeO_3 . These calculated values can be used to interpret new experimental results when they become available. Calculated frequencies for other molecules can be found in our previous report.²

6.3.3 NMR Chemical Shifts. The chemical shifts are given in Table 4 with different exchange-correlation functionals and basis sets: B3LYP/AhlrichsVTZP, BLYP/TZ2P, and at the ZORA-BLYP/TZ2P level. Our predicted ^{77}Se chemical shift for SeF_2 , using the B3LYP/AhlrichsVTZP method, differs by 45 ppm from Poleschner and Seppelt's⁷⁰ value of 3723.5 ppm, calculated at the MP2/6-311+G(d,p)//MP2/6-311+G(d,p) level. Their calculated ^{19}F chemical shift (-208.9 ppm) differs from our value by approximately 9 ppm. They also used B3LYP/6-311+G(d,p)//B3LYP/6-311+G(d,p) to predict a ^{77}Se chemical shift of 4368.0 ppm which differs significantly from our value by approximately 600 ppm due to their apparent neglect of

relativistic effects. Their DFT value of -204.2 for the ^{19}F chemical shift differs from our value by only 1.2 ppm. For SeF_6 , we predict ^{77}Se chemical shift values of 555 and 534 ppm at the BLYP/TZ2P and ZORA-BLYP/TZ2P levels, respectively. These values differ from the two reported experimental values of 600 and 610 ppm by 45 and 75 ppm. Our ^{19}F chemical shift values calculated at the same levels differ from the experimental value of 49.6⁷⁰ by 61 and 98 ppm, respectively.

6.3.4 Calculated Heats of Formation. Table 5 lists the calculated contributions to the total atomization energy (TAE). The core valence corrections have a range of 7.7 kcal/mol with SeF_7^- having the largest correction of -7.41 kcal/mol and SeO having the smallest correction of 0.11 kcal/mol. The scalar relativistic corrections are significantly smaller than both the core valence corrections with a range 1.8 kcal/mol.

The heats of formation at 0 and 298 K (Table 6) were calculated from the total atomization energies. Our predicted heat of formation for SeF_6 (O_h) of -267.7 kcal/mol is in excellent agreement with experiment when using Wang's recommended value of 57.9 kcal/mol for the heat of formation of the Se atom. Use of the Wagman *et al.* value³⁶ for $\Delta H_f(\text{Se})$ at 0 K leads to an error of almost 4 kcal/mol. The experimental heat of formation of SeF_6 was obtained from the reaction of solid Se with F_2 so it does not involve the heat of formation of the gaseous Se atom. Compared to the best experimental value for $\Delta H_f(\text{SeF}_6)$ of -267.18 kcal/mol at 298 K,⁷¹ our calculated value of -267.7 kcal/mol is in excellent agreement. Using our calculated total atomization energy, we predict a value of 58.43 kcal/mol for $\Delta H_f(\text{Se})$ at 0 K. To obtain another estimate of $\Delta H_f(\text{Se})$ at 0 K, we calculated the TAE of SeF_6 at the CCSD(T)/aug-cc-pVQZ-PP and CCSD(T)/aug-cc-pV5Z-PP levels and extrapolated these values to the complete basis set limit using the following expression.^{72,73}

$$E(l_{\max}) = E_{\text{CBS}} + B/l_{\max}^3 \quad (3)$$

This gives a TAE of 432.80 kcal/mol at 0K, resulting in a value of 57.54 kcal/mol for $\Delta H_f(\text{Se})$. We can average our two calculated values for $\Delta H_f(\text{Se})$ to give 58.0 ± 0.5 kcal/mol for $\Delta H_f(\text{Se})$ at 0 K, which is in excellent agreement with Wang's value³³ of 57.9 kcal/mol, derived from experiment. As a consequence, we used Wang's value³³ of 57.9 kcal/mol for all of the heats of formation predictions.

We can compare our calculated value for $\Delta H_f(\text{SeF}_4)$ at 298 K with that obtained from the experimental heat of formation of liquid SeF_4 at 298 K of -203 ± 6 kcal/mol and its estimated heat of vaporization⁷⁴ of 11 kcal/mol giving an estimated $\Delta H_f^{298}(\text{SeF}_4) = -192 \pm 6$ kcal/mol. Our value of -185.9 kcal/mol is in good agreement with this estimated value.

Our calculated value for the ΔH_f 's at 298 K of SeF_3^- and SeF_6^- are in excellent agreement with the respective experimentally derived values.^{75,76} In contrast, our calculated value for $\Delta H_f(\text{SeF}_4^-)$ at 298 K is 23 kcal more negative than that derived from experiment.⁷⁵

We can compare the predicted G3 values³⁴ for $\Delta H_f(\text{SeF}_n)$ for $n = 1-6$ with our higher level values which do not incorporate empirical corrections to the electronic energy (Table 6). The G3 value for $\Delta H_f(\text{SeF})$ is within 0.2 kcal/mol of our value. The G3 value for $\Delta H_f(\text{SeF}_2)$ differs from our value by 2.1 kcal/mol, the G3 value for $\Delta H_f(\text{SeF}_3)$ differs from our value by 4.7 kcal/mol, and the G3 value for $\Delta H_f(\text{SeF}_5)$ differs from ours by 4.7 kcal/mol. The G3 value for $\Delta H_f(\text{SeF}_4)$ differs from our value by 6.5 kcal/mol and is far outside the error bars of the estimated experimental value. Considering these differences, it is surprising that the G3 value for $\Delta H_f(\text{SeF}_6)$ differs from our value by only 0.3 kcal/mol.

6.3.5 Bond Dissociation Energies. There is little experimental information available for the BDEs for the range of selenium fluorides, selenium oxofluorides, and oxides, except for SeF_6 ,

SeF₅, SeF and SeO.⁷⁷ Table 7 shows the various Se-F and Se-O BDEs calculated from the heats of formation as well as those for the comparable sulfur compounds. We can define two types of BDEs:^{78,79} (a) adiabatic, dissociating to the ground states of the separated species and (b) diabatic, dissociating to electronic configurations appropriate for forming the bonds in the parent molecule. The adiabatic and diabatic BDEs can differ by varying amounts depending on the nature of the electronic states of the products. The diabatic BDE is always equal to or larger than the adiabatic BDE, and the difference between the adiabatic and diabatic BDEs corresponds to any reorganization energy of the product(s) and can be substantial. Considering these very large possible differences, it is important to use the appropriate values in thermodynamic calculations. For thermochemical calculations, such as Born-Haber cycles, the adiabatic values must be used, whereas for simple kinetic models, the diabatic values can be more appropriate. The inappropriate use of adiabatic and diabatic bond dissociation energies can lead to large errors and the wrong conclusions. In order to estimate the diabatic values, we calculated the singlet-triplet splittings of the appropriate products at the CCSD(T)/aVDZ level.

Our calculated SeF₆ adiabatic Se-F BDE is larger by 17.8 kcal/mol than the reported experimental value.^{77,76} Our calculated SeF₅ adiabatic Se-F BDE is smaller than the experimental value^{76,77} by 37.6 kcal/mol. This suggests that the experimental estimate for $\Delta H_f(\text{SeF}_5)$ used in the BDE calculations is far too negative. Our SeF adiabatic BDE is consistent with the experimental value.^{77,80}

The adiabatic and diabatic Se-F BDEs of SeF₆, SeF₄, SeF₂, and SeF are the same (see Table 7) and involve no reorganization energies. All of the values are substantial and range from 93.0 kcal/mol in SeF₄ to 76.1 kcal/mol in SeF. As noted above, the adiabatic BDEs can include possible reorganization energies and, therefore, are not always a measure for the bond strengths.

For the evaluation of bond strengths near the minimum, the diabatic values should be used as they describe the bonding when only small displacements of the atoms from their equilibrium positions are made. The adiabatic Se-F BDE of SeF₆ is 2.6 kcal/mol less than that in SeF₄ consistent with the lower steric interactions in the latter. The adiabatic Se-F BDE in SeF₂ is ~ 4 kcal/mol lower than that in SeF₆. The Se-F BDE in diatomic SeF is about 10 kcal/mol less than that in SeF₂. It is more appropriate to compare the diabatic Se-F BDEs in SeF₅, and SeF₃ with the above adiabatic values. The diabatic Se-F BDE in SeF₅ is between those of SeF₄ and SeF₂ and that for SeF₃ is ~ 2 kcal/mol less than that of SeF. The adiabatic Se-F BDE in SeF₅ is very low because of the stability of SeF₄. The adiabatic Se-F BDE in SeF₃ is surprisingly high suggesting that the SeF₃ radical is quite stable thermodynamically.

The SeF_n BDEs follow the same patterns previously found for the SF_n BDEs.¹ As would be expected from periodic trends, the Se-F adiabatic BDE in SeF₆ is 14.4 kcal/mol smaller than that of SF₆. We note that the calculated adiabatic S-F BDE in SF₆ is 12.6 kcal/mol larger than the experimental value⁴⁹ of 92.2 ± 3.8 kcal/mol, similar to what is found for SeF₆. The adiabatic Se-F BDE in SeF₅ is 10.7 kcal/mol smaller than that in SF₅. The Se-F BDEs of SeF₄ and SeF₂ are only 2.5 to 3 kcal/mol smaller than the corresponding S-F BDEs in SF₄ and SF₂. The adiabatic Se-F BDEs in SeF₃ and Se-F are 6 to 7 kcal/mol smaller than the S-F BDEs in SF₃ and SF.

We can compare the predicted G3 BDEs in SeF_n for n = 1–6 with our CCSD(T)/CBS adiabatic BDEs in kcal/mol at 298 K. The G3 value for SeF₆ (94.8 kcal/mol)³³ is 4.4 kcal/mol larger than our value. The G3 value for SeF₅ (28.8 kcal/mol)³³ differs by 1.8 kcal/mol. The G3 value for SeF₄ (91.2 kcal/mol)³³ is smaller than our value by 1.8 kcal/mol. The G3 value for SeF₃ (58.1 kcal/mol)³³ is smaller than ours by 2.7 kcal/mol. The G3 value for SeF₂ (83.7 kcal/mol)³³

is smaller than our value by 2.7 kcal/mol. The G3 value for SeF (76.7 kcal/mol)³³ is in excellent agreement with our value within 1.0 kcal/mol.

The adiabatic and diabatic Se-F BDEs in SeOF₄ and SeOF₂, SeOF, and SeO₂F₂ are the same. The Se-F BDE in SeF₄O is lower than that in Se-F, but the Se-F BDE in SeF₂O is comparable to that of SeF₆. The Se-F BDEs in SeOF and SeO₂F₂ are near 80 kcal/mol. The diabatic Se-F BDE in SeO₂F is similar to that in SeF₆. The highest diabatic Se-F BDE is found for SeOF₃ at 112 kcal/mol, although the adiabatic BDE is very low at 20 kcal/mol. The Mulliken atomic spin densities for the triplet state of SeOF₂ are mainly localized on the O (1.01e) and the Se atom (0.78e), with spin densities of only 0.11e on the two F atoms. In the doublet state of SeOF₃ the Mulliken atomic spin density is essentially localized on the O atom (0.95e).

The Se-O BDE in SeOF₂ (106.5 kcal/mol) is the largest adiabatic BDE of the SeO_xF_x and SeF_x compounds, and the Se-F BDE in SeOF₃ is the smallest at 19.9 kcal/mol. The adiabatic Se-F BDE in SeF₅ is small as expected because of the instability of SeF₅ and the stability of SeF₄. The Se-O BDE in SeO₂F has the largest diabatic BDE of the SeO_xF_x and SeF_x compounds.

The Se-F adiabatic BDE in SeOF₄ is 16.8 kcal/mol smaller than the S-F BDE in SF₄O. The Se-O BDE in SeOF₄ is 42.7 kcal/mol smaller than the S-F BDE in SF₄O. The Se-F adiabatic BDE in SeOF₃ is only 0.1 kcal/mol smaller than the S-F BDE in SF₃O, and the Se-O BDE in SeOF₃ is 28.3 kcal/mol smaller than the S-O BDE of SF₃O. The Se-F BDE in SeOF₂ is 5.5 kcal/mol smaller than the S-F BDE in SF₂O, whereas the Se-O BDE in SeOF₂ is 22.3 kcal/mol smaller than the S-O BDE in SF₂O. In SeOF, the same trend continues with the Se-F adiabatic BDE 5.7 kcal/mol which is smaller than the S-F BDE in SFO and the Se-O BDE of SeOF is 20.3 kcal/mol smaller than the S-O BDE in SFO. The adiabatic Se-O BDE of SeO is 21.8 kcal/mol smaller than that of SO. In SeO₂F₂ the Se-F adiabatic BDE is 26.1 kcal/mol smaller than the S-F

BDE in SF₂O₂ and the Se-O BDE is 46.7 kcal/mol smaller than the S-O BDE in SF₂O₂. The Se-F BDE in SeO₂F is only 0.7 kcal/mol smaller than the S-F BDE in SO₂F. The Se-O BDE in SeO₂F is 26.1 kcal/mol smaller than the S-O BDE in SO₂F. Overall, there is a much larger difference in the Se-O/S-O BDEs than in the Se-F/S-F BDEs.

The Se-O BDEs show the need to consider the diabatic values. As expected from comparing the bond lengths and vibrational frequencies, the diabatic Se-O BDE in SeOF₄ is greater than the Se-F BDE. The adiabatic Se-O BDE is quite low because of the stability of SeF₄. The diabatic Se-F BDE in SeOF₃ is essentially the same as the diabatic Se-O BDE. The diabatic Se-O BDEs increase from 96 kcal/mol in SeOF₄ to 111 kcal/mol in SeOF₃ to 126 kcal/mol in SeOF₂ to 138 kcal/mol in SeOF. The Se-O BDE for diatomic SeO is at the low end. In contrast, the diabatic Se-O BDE in SeO₂F₂ is in the upper range of Se-O BDEs, and that for SeO₂F is even higher. The diabatic Se-F BDE in SeO₂F is surprisingly low at 89 kcal/mol, about 10 kcal/mol lower than the diabatic value for SeO₃. The diabatic Se-O BDE for SeO₃ is comparable to the adiabatic (and diabatic) BDEs for SeO₂ and SeO. The adiabatic Se-O BDEs are comparable, 45 to 52 kcal/mol, and low in SeOF₄, SeO₂F₂, and SeO₃.

6.3.6 Fluoride Affinities. Table 8 gives the fluoride affinities predicted at the coupled cluster CCSD(T) theory level extrapolated to the complete basis set limit of selenium compared to those of the same reaction with sulfur when possible. An experimental value of $\Delta H_f^{298}(\text{F}^-) = -59.50$ kcal/mol was used.⁴⁹ The fluoride affinities for the SeF_x compounds span a range of 66 kcal/mol, with SeF₅ having the highest fluoride affinity of 80.7 kcal/mol and SeF₆ having the lowest one of 15.0 kcal/mol. The fluoride affinities for the SeO_x and SeO_xF_x compounds cover a range of 83 kcal/mol with SeO having the lowest fluoride affinity of 37.8 kcal/mol and SeO₃ having the highest one of 121.0 kcal/mol. A comparison of the fluoride affinities (FAs) of the Se

and S compounds shows that the selenium compounds are stronger Lewis acids than the corresponding sulfur compounds, in accord with the general trends in the periodic table.

6.3.7 Fluorocation Affinities. Table 9 gives our CCSD(T)/CBS fluorocation affinities obtained using the experimental value $\Delta H_f^{298}(F^+) = 420.75$ kcal/mol.⁴⁹ The fluorocation affinities for the SeF_x compounds differ by up to 162 kcal/mol, with SeF_2 having the largest fluorocation affinity of 263.1 kcal/mol and SeF_6 having the smallest of 101.2 kcal/mol. The small value for SeF_6 is consistent with the substantial steric hindrance in this compound for adding an additional fluorine, as well as the fact that the Se is in the +6 oxidation state leading to the formation of an SeF_5^+ complex with F_2 .

The fluorocation affinities for the SeO_x and SeO_xF_x compounds differ by up to 109 kcal/mol with SeO_2F_2 having the smallest fluorocation affinity of 147.7 kcal/mol and SeO having the largest of 256.3 kcal/mol. Again, the compound with the least steric hindrance and lowest formal positive charge on the Se has the highest fluorocation affinity. The two compounds with the lowest F^+ affinities are $SeOF_4$ and SeO_2F_2 which undergo a rearrangement so that the F is actually bonded to an O. The lowest F^+ affinity for the F bonded to Se is SeO_3 with the largest formal positive charge on the Se.

6.3.8 Electron Affinities and Ionization Potentials. The calculated electron affinities and ionization potentials are given in Tables 10 and 11. The electron affinity values predicted for Se, SeF_4 , SeF_5 , SeF_6 and SeO_2 are all in good agreement with the reported experimental values,^{25,67,69,81,82} as well as the ionization energies predicted for Se, SeF_2 and SeO_2 are also all in good agreement with the reported experimental values.^{68,81,83,69}

6.3.9 BDEs in the Cations and Anions. Table 12 gives the Se-F and Se-O anion BDEs of SeF_n^- ($n = 1-7$), $SeOF_n^-$ ($n = 1-4$) and $SeO_2F_n^-$ ($n = 1-2$) calculated from the heats of formation at

the CCSD(T)/CBS level. The SeF_n^- ($n = 1-7$) BDEs differ by up to 85 kcal/mol at 298 K with SeF_5^- having the largest BDE and SeF_7^- having the smallest BDE. The high BDE in SeF_5^- suggests the SeF_5^- anion is quite stable thermodynamically. The SeOF_n^- ($n = 1-4$) and SeO_2F_n^- ($n = 1-2$) Se-F BDEs differ by up to 59 kcal/mol at 298 K with SeOF_3^- having the largest Se-F BDE and SeOF_4^- having the smallest Se-F BDE. The SeOF_n^- ($n = 1-4$) and SeO_2F_n^- ($n = 1-2$) Se-O BDEs differ by up to 53 kcal/mol at 298 K with SeO_2F^- having the largest BDE and SeO_2F_2^- having the smallest BDE. The values of the BDEs in SeOF_2^- , SeOF_3^- and SeO_2F^- suggests that these anions are also quite stable thermodynamically in terms of loss of an $^2\text{F}\cdot$ or ^3O atomic radical.

Table 13 gives the Se-F and Se-O cation BDEs of SeF_n^+ ($n = 1-7$)⁺, SeOF_n^+ ($n = 1-4$) and SeO_2F_n^+ ($n = 1-2$), calculated from the heats of formation at the CCSD(T)/CBS level. The SeF_n^+ ($n = 1-7$) BDEs differ by up to 91 kcal/mol at 298 K with SeF_3^+ having the largest BDE. SeF_6^+ is predicted to be unstable with respect to loss of an F atom on ionization of SeF_6 , consistent with the fact that this ion has not been reported. The SeOF_n^+ ($n = 1-4$) and SeO_2F_n^+ ($n = 1-2$) Se-F BDEs differ by up to 39 kcal/mol at 298 K with SeOF_3^+ having the largest BDE and SeOF_4^+ having the smallest BDE. The SeOF_n^+ ($n = 1-4$) and SeO_2F_n^+ ($n = 1-2$) Se-O BDEs differ by up to 59 kcal/mol at 298 K with SeOF^+ having the largest and SeO_2F^+ having the smallest BDE.

Table 14 gives the $\text{Se}^+\text{-F}^-$ heterolytic bond cleavage of SeF_n ($n = 1-6$), SeOF_n ($n = 1-5$) and SeO_2F_n ($n = 1-2$) calculated from the heats of formation at the CCSD(T)/CBS level. The SeF_n ($n = 1-6$) heterolytic BDEs differ by up to 54 kcal/mol at 298 K with SeF_6 having the largest BDE and SeF_3 having the smallest. The SeOF_n ($n = 1-5$) and SeO_2F_n ($n = 1-2$) Se-F BDEs differ by up to 43 kcal/mol at 298 K with SeO_2F_2 having the largest BDE and SeOF_3 having the smallest.

Figure 2 give a summary of the calculated CCSD(T)/CBS heats of formation (kcal/mol) of SeOF_n at 298 K, the energy differences between the various species, the reaction enthalpies for the addition of either F^- , F and F^+ to the neutral parent. The SeOF^+ , SeOF_3^+ , SeOF_4^+ cations, the SeOF_2 molecule and the SeOF_3^- anion have the smallest enthalpies for addition of F in their series indicating that the addition of a F atom is less favored.

Figure 3 depicts the calculated CCSD(T)/CBS heats of formation (kcal/mol) of SeO_2F_n and SeO_3F_n at 298 K, the energy differences between the various species, the reaction enthalpies for the addition of either F^- , F and F^+ to the neutral parent. The reaction enthalpy for the addition of the first F atom to the neutral, cation, and anion are about the same, 40 to 45 kcal/mol. The exothermicity of the reaction to add F to SeO_2F_n increases for the neutral and the anion with the second addition almost double the value of the first. In contrast, the addition of the second F to the cation is essentially the same energy as the first. The addition of F to SeO_2F_2^+ to form SeO_2F_3^+ occurs by addition to an oxygen and not selenium (Figure 1).

In Figure 4 the reaction enthalpies for the addition of an F atom to $\text{SeF}_n^{0\pm 1}$ ($n = 1-7$) to form $\text{SeF}_{n+1}^{0\pm 1}$ range from -26.3 kcal/mol in SeF_6^- and -38.0 kcal/mol in SeF_5^- to -111.3 kcal/mol in SeF_4^- , suggesting that the addition of a fifth Se-F bond is strongly favored. The low values of -4.4 and -4.8 kcal/mol for the addition of F to SeF_3^+ and SeF_5^+ , respectively, suggest that the oxidation of these two cations may prove to be difficult. We have already noted that SeF_6^+ will dissociate. The energies to add an O or an F to a compound are summarized in Figure 5.

6.4 Conclusions.

The bond dissociation energies (BDEs) and fluoride affinities of SeF_n ($n = 1-6$), SeOF_n ($n = 0-4$), SeO_2F_n ($n = 0-2$), and SeO_3 and the electron affinities of SeF_n ($n = 1-6$) have been predicted with coupled cluster CCSD(T) theory and extrapolated to the complete basis set limit.

The calculated heats of formation are dependent on the correct value of $\Delta H_f^0(\text{Se})$. We used the value of 57.9 kcal/mol recommended by Wang,³³ and obtained excellent agreement with experiment for $\Delta H_f^{298}(\text{SeF}_6)$. Using the experimental heat of formation and our calculated TAEs, we predicted $\Delta H_f^0(\text{Se})$ 57.98 ± 0.5 kcal/mol in excellent agreement with Wang's value derived from experimental appearance potentials.

Acknowledgements. This research was supported, in part, by the U. S. Department of Energy, Office of Basis Energy Research, Chemical Sciences, in the geosciences program. D.A.D. thanks the Robert Ramsay Fund at the University of Alabama and Argonne National Laboratory for partial support. The work at USC was financially supported by the National Science Foundation, the Air Force Office of Scientific Research, the Office of Naval Research, and the Defense Threat Reduction Agency.

Supporting Information: Total valence electronic energies at the CCSD(T) level in a.u., optimized bond lengths (Å) and angles (degrees) for SeF_xO_y geometries, and optimized CCSD(T) Cartesian coordinates in Å. This material is available free of charge via the Internet at <http://pubs.acs.org>.

References

-
- ¹ Grant, D. J.; Matus, M. H.; Switzer, J. R.; Dixon, D. A.; Francisco, J. S.; and Christe, K.O. *J. Phys. Chem. A* **2008**, *112*, 3145-3156.
- ² Christe, K. O.; Dixon, D. A.; Haiges, R.; Hopinger, M.; Jackson, V. E.; Klapotke, T. M.; Krumm, B.; Scherr, M. *J. Fluor. Chem.* **2010**, *131*, 791.
- ³ Nakanishi, W.; Hayashi, S. *J. Phys. Chem. A* **1999**, *103*, 6074.
- ⁴ Kniep, R.; Korte, L.; Krysch, R.; Poll, W. *Angew. Chem., Int. Ed.* **1984**, *23*, 388.
- ⁵ Seppelt, K. *Z. Anorg. Allg. Chem.* **1975**, *415*, 12.
- ⁶ Bowater, I. C.; Brown, R. D.; Burden, F. R. *J. Mol. Spectrosc.* **1968**, *28*, 454.
- ⁷ Damerius, R.; Huppmann, P.; Lentz, D.; Seppelt, K. *J. Chem. Soc., Dalton Trans.* **1984**, 2821.
- ⁸ Mahjoub, A. R.; Leopold, D.; Seppelt, K. *Z. Anorg. Allg. Chem.* **1992**, *618*, 83.
- ⁹ Christe, K. O.; Curtis, E. C.; Schack, C. J.; Pilipovich, D. *Inorg. Chem.* **1972**, *11*, 1679.
- ¹⁰ Mahjoub, A. R.; Zhang, X.; Seppelt, K. *Chem.-Eur. J.* **1995**, *1*, 261.
- ¹¹ Moock, K. H.; Boere, R. T. *J. Fluorine Chem.* **1994**, *68*, 175.
- ¹² Bowater, I. C.; Brown, R. D.; Burden, F. R. *J. Mol. Spectrosc.* **1967**, *23*, 272.
- ¹³ Paetzold R.; Aurich, K. *Z. Anorg. Allg. Chem.* **1962**, *315*, 72.
- ¹⁴ Rolfe, J. A.; Woodward, L. A. *Trans. Faraday Soc.* **1955**, *51*, 778.
- ¹⁵ Prideaux, E. B. R.; Cox, C. B. *J. Chem. Soc.* **1928**, 739.
- ¹⁶ Prideaux, E. B. R.; Cox, C. B. *J. Chem. Soc.* **1927**, 928.
- ¹⁷ Feldmann, C.; Jansen, M. *Chem. Ber.* **1994**, *127*, 2173.
- ¹⁸ Gillespie, R. J.; Spekkens, P.; Milne, J. B.; Moffett, D. *J. Fluorine Chem.* **7** **1976**, *7*, 43.
- ¹⁹ Baran, E. J. *J. Fluorine Chem.* **1977**, *10*, 255.
- ²⁰ Milne, J. *Inorg. Chem.* **1978**, *17*, 3592.

-
- ²¹ Paetzold R.; Aurich, K. *Z. Anorg. Allg. Chem.* **1965**, 335, 281.
- ²² Milne, J.; Lahaie, P. *Inorg. Chem.* **1983**, 22, 2425.
- ²³ Paetzold, R.; Aurich, K. *Z. Anorg. Allg. Chem.* **1966**, 348, 94.
- ²⁴ Paetzold, R.; Aurich, K. *Z. Chem.* **1966**, 6, 152.
- ²⁵ Maggard, P.; Lobastov, V. A.; Schäfer, L.; Ewbank, J. D.; Ischenko, A. A. *J. Phys. Chem.* **1995**, 99, 13115.
- ²⁶ O'Hare, P. A. G.; Settle, J. L.; Hubbard, W. N. *Trans. Faraday Soc.*, **1966**, 62, 558.
- ²⁷ (a) Shimanouchi, T. *Tables of Molecular Vibrational Frequencies Consolidated*; National Bureau of Standards: Gaithersburg, MD, 1972; Vol. I, pp 1-160. (b) Huber, K. P.; Herzberg, G. *Molecular Spectra and Molecular Structure. IV. Constants of Diatomic Molecules*; Van Nostrand Reinhold Co.: New York, 1979.
- ²⁸ (a) Damerius, R.; Huppmann, P.; Lentz, D.; Seppelt, K. *J. Chem. Soc. Dalton Trans.* **1984**, 2821; (b) Seppelt, K. *Z. Anorg. Allg. Chem.* **1975**, 416, 12.
- ²⁹ (a) Mason, J., Ed. *Multinuclear NMR*; Plenum Press: New York, 1987. (b) Brevard, C.; Granger, P. *Handbook of High Resolution Multinuclear NMR*; Wiley: New York, 1981.
- ³⁰ Buhl, M.; Thiel, W.; Fleischer, U.; Kutzelnigg, W. *J. Phys. Chem.* **1995**, 99, 4000.
- ³¹ Poleschner, H.; Ellrodt, S.; Malischewski, M.; Nakatsuji, J-y.; Rohner, C.; Seppelt, K. *Angew. Chem., Int. Ed.* **2012**, 51, 419.
- ³² Xu, Q-s. Li, W.; Xie, Y.; Schaefer, H. F. III *J. Phys. Chem. A* **1999**, 103, 7496.
- ³³ Wang, L. *Int. J. Mass Spectrom.* **2007**, 264, 84.
- ³⁴ Curtiss, L. A.; Raghavachari, K.; Redfern, P. C.; Rassolov, V.; Kedziora, G.; Pople, J. A. *J. Chem. Phys.* **1998**, 109, 7764. Curtiss, L. A.; Redfern, P. C.; Rassolov, V.; Kedziora, G.; Pople, J. A. *J. Chem. Phys.* **2001**, 114, 9287.
- ³⁵ Gibson, S. T.; Greene, J. P.; Berkowitz, J. *J. Chem. Phys.* **1986**, 85, 4815. Gunn, S. R. *J. Phys. Chem.* **1964**, 68, 949.
- ³⁶ Wagman, D. D.; Evans, W. H.; Parker, V. B.; Schumm, R. H.; Halow, I.; Bailey, S. M.; Churney, K. L.; Nuttall, R. L. *J. Phys. Chem. Ref. Data* **1982**, Suppl. 2, 11.
- ³⁷ (a) Purvis, G. D. III; Bartlett, R. J. *J. Chem. Phys.* **1982**, 76, 1910. (b) Raghavachari, K.; Trucks, G. W.; Pople, J. A.; Head-Gordon, M. *Chem. Phys. Lett.* **1989**, 157, 479. (c) Watts, J.

D.; Gauss, J.; Bartlett, R. J. *J. Chem. Phys.* **1993**, *98*, 8718. (d) Bartlett, R. J.; Musial, M. *Rev. Mod. Phys.* **2007**, *79*, 291.

³⁸ Peterson, K. A., Woon, D. E.; Dunning, T. H. Jr. *J. Chem. Phys.* **1994**, *100*, 7410.

³⁹ (a) Dunning, T. H. Jr. *J. Chem. Phys.* **1989**, *90* (90), 1007. (b) Kendall, R. A.; Dunning, T. H. Jr.; Harrison, R. J. *J. Chem. Phys.* **1992**, *96*, 6796. (c) Woon, D. E.; Dunning, T. H. Jr. *J. Chem. Phys.* **1993**, *98*, 1358. (d) Dunning, T. H. Jr.; Peterson, K. A.; Wilson, A. K. *J. Chem. Phys.* **2001**, *114*, 9244. (e) Wilson, A. K.; Woon, D. E.; Peterson, K. A.; Dunning, T. H. Jr. *J. Chem. Phys.* **1999**, *110*, 7667.

⁴⁰ Becke, A. D. *J. Chem. Phys.* **1993**, *98*, 5648.

⁴¹ Lee, C.; Yang, C. W.; Parr, R. G. *Phys. Rev. B* **1988**, *37*, 785.

⁴² (a) Peterson, K. A. *J. Chem. Phys.* **2003**, *119*, 11099. (b) Peterson, K. A.; Figgien, D.; Goll, E.; Stoll, H.; Dolg, M. *J. Chem. Phys.* **2003**, *119*, 11113.

⁴³ Pople J. A., Binkley J. S. and Seeger R. *Int. J. Quantum Chem.* **1976**, Y- 10 (Suppl.), 1–19.

⁴⁴ (a) Knowles, P. J.; Hampel, C.; Werner, H. -J. *J. Chem. Phys.* **1993**, *99*, 5219. (b) Deegan, M. J. O.; Knowles, P. J. *J. Chem. Phys. Lett.* **1994**, *227*, 321.

⁴⁵ (a) Peterson, K. A.; Dunning, T. H. Jr. *J. Chem. Phys.* **2002**, *117*, 10548. (b) Woon, D. E.; Dunning, T. H. Jr. *J. Chem. Phys.* **1993**, *98*, 1358. (c) Peterson, K. A.; Yousaf, K. E. *J. Chem. Phys.* **2010**, *133*, 174116.

⁴⁶ Davidson, E. R.; Ishikawa, Y.; Malli, G. L. *Chem. Phys. Lett.* **1981**, *84*, 226.

⁴⁷ Moore, C. E. *Atomic energy levels as derived from the analysis of optical spectra*; U.S. Department of Commerce, National Technical Information Service, COM-72-50282: Washington, DC, 1949; Vol. 1, H to V, U. S. National Bureau of Standards Circular 467.

⁴⁸ (a) Feller D.; Dixon, D. A. *J. Phys. Chem. A* **2000** *104*, 3048. (b) Feller D.; Dixon, D. A. *J. Chem. Phys.* **2001**, *115*, 3484. (c) Dixon, D. A.; Feller, D.; Peterson, K. A. *J. Chem. Phys.* **2001**, *115*, 2576. (d) Feller D.; Dixon, D. A. *J. Phys. Chem. A* **2003**, *107*, 9641. (e) Dixon, D. A.; Feller, D.; Christe, K. O.; Wilson, W. W.; Vij, A.; Vij, V.; Jenkins, H. D. B.; Olson, R.M.; Gordon, M. S. *J. Am. Chem. Soc.* **2004**, *126*, 834. (f) Dixon, D. A.; Gutowski, M. *J. Phys. Chem. A* **2005**, *109*, 5129. (g) Pollack, L.; Windus, T. L.; de Jong, W. A.; Dixon, D. A. *J. Phys. Chem. A* **2005**, *109*, 6934. (h) Ruscic, B.; Wagner, A. F.; Harding, L. B.; Asher, R. L.; Feller, D.; Dixon, D. A.; Peterson, K. A. Song, Y.; Qian, X.; Ng, C.; Liu, J.; Chen, W.; Schwenke, D. W. *J. Phys. Chem. A* **2002**, *106*, 27277.

⁴⁹ Chase, M. W., Jr. *NIST-JANAF Tables, 4th ed. J. Phys. Chem. Ref. Data* **1998**, Mono. 9, Suppl. 1. See also: Linstrom, P. J.; Mallard, W. G., Eds.; *NIST Chemistry WebBook*, NIST

Standard Reference Database Number 69, June 2005, National Institute of Standards and Technology: Gaithersburg, MD, 2005 (<http://webbook.nist.gov/chemistry/>).

- ⁵⁰ Curtiss, L. A.; Raghavachari, K.; Redfern, P. C.; Pople, J. A. *J. Chem. Phys.* **1997**, *106*, 1063.
- ⁵¹ Wolinski, K.; Hinton, J. F.; Pulay, P. *J. Am. Chem. Soc.* **1990**, *112*, 8251.
- ⁵² Schäfer, A.; Horn, H.; Ahlrichs, R. *J. Chem. Phys.* **1992**, *97*, 2571.
- ⁵³ Becke, A. D. *Phys. Rev. A* **1988**, *38*, 3098.
- ⁵⁴ Schreckenbach, G.; Ziegler, T. *J. Phys. Chem.* **1995**, *99*, 606.
- ⁵⁵ Schreckenbach, G.; Ziegler, T. *Int. J. Quantum Chem.* **1997**, *61*, 899.
- ⁵⁶ Wolff, S. K.; Ziegler, T. *J. Chem. Phys.* **1998**, *109*, 895.
- ⁵⁷ Wolff, S. K.; Ziegler, T.; van Lenthe, E.; Baerends, E. J. *J. Chem. Phys.* **1999**, *110*, 7689.
- ⁵⁸ van Lenthe, E.; Baerends, E. J.; Snijders, J. G. *J. Chem. Phys.* **1993**, *99*, 4597.
- ⁵⁹ Autschbach, J.; Ziegler, T. In *Calculation of NMR and EPR Parameters: Theory and Application*; Kaupp, M., Buhl, M., Malkin, V. G., Eds.; Wiley-VCH & Co.: Weinheim, Germany, 2004; p 249.
- ⁶⁰ (a) ADF 2004.01, ADF Users Guide; SCM, Theoretical Chemistry, Vrije Universiteit: Amsterdam, The Netherlands, 2004; <http://www.scm.com>. (b) te Velde, G.; Bickelhaupt, F. M.; Baerends, E. J.; Fonseca Guerra, C.; van Gisbergen, J. A.; Snijders, J. G.; Ziegler, T. *J. Comput. Chem.* **2001**, *22*, 931.
- ⁶¹ Werner, H.-J.; Knowles, P. J.; Lindh, R.; Manby, F. R.; Schu

Austin, A. J.; Cammi, R.; Pomelli, C.; Ochterski, J. W.; Ayala, P. Y.; Morokuma, K.; Voth, G. A.; Salvador, P.; Dannenberg, J. J.; Zakrzewski, V. G.; Dapprich, S.; Daniels, A. D.; Strain, M. C.; Farkas, O.; Malick, D. K.; Rabuck, A. D.; Raghavachari, K.; Foresman, J. B.; Ortiz, J. V.; Cui, Q.; Baboul, A. G.; Clifford, S.; Cioslowski, J.; Stefanov, B. B.; Liu, G.; Liashenko, A.; Piskorz, P.; Komaromi, I.; Martin, R. L.; Fox, D. J.; Keith, T.; Al-Laham, M. A.; Peng, C. Y.; Nanayakkara, A.; Challacombe, M.; Gill, P. M. W.; Johnson, B.; Chen, W.; Wong, M. W.; Gonzalez, C.; Pople, J. A. *Gaussian03*, Revision C.02; Gaussian, Inc.: Wallingford, CT, 2004.

⁶³ *AMPAC 9*; Semichem, Inc.: Shawnee, KS, 1992-2008.

⁶⁴ Carrington, A.; Currie, G. N.; Miller, T. A.; Levy, D. H. *J. Chem. Phys.* **1969**, *50*, 2726.

⁶⁵ Feller, D.; Peterson, K. A.; Dixon, D. A. *J. Chem. Phys.* **2008**, *129*, 204105.

⁶⁶ Sutton, L. E., Ed.; *Tables of Interatomic Distances and Configuration in Molecules and Ions*; The Chemical Society: London, U.K. 1958.

⁶⁷ (a) Haas, A.; Willner, H. Z. *Anorg. Allg. Chem.* **1979**, *454*, 17. (b) Jacox, M. E. *J. Phys. Chem. Ref. Data*, **1998**, *27* (2), 115.

⁶⁸ de Leeuw, D. M.; Mooyman, R.; de Lange, C. A. *Chem. Phys.* **1979**, *38*, 21.

⁶⁹ (a) Snodgrass, J. T.; Coe, J. V.; McHugh, K. M.; Freidhoff, C. B.; Bowen, K. H. *J. Phys. Chem.* **1989**, *93*, 1249. (b) Coe, J. V.; Snodgrass, J. T.; Freidhoff, C. B.; McHugh, K. M.; Bowen, K. H. *J. Chem. Phys.* **1986**, *84*, 618. (c) Smoes, S.; Drowart, J. *J. Chem. Soc. Faraday Trans.* **1984**, *80*, 1171.

⁷⁰ Poleschner, H.; Seppelt, K. *Chem.-Eur. J.* **2004**, *10*, 6565.

⁷¹ O'Hare, P. A. G. *J. Chem. Thermodyn.* **1986**, *18*, 555-562.

⁷² (a) Helgaker, T.; Klopper, W.; Koch, H.; Noga, J. *J. Chem. Phys.* **1997**, *106*, 9639. (b) Halkier, A.; Helgaker, T.; Jørgensen, P.; Klopper, W.; Koch, H.; Olsen, J.; Wilson, A. K. *Chem Phys Lett* **1998**, *286*, 243.

⁷³ Martin, M. L. *Chem Phys Lett* **1996**, *259*, 699.

⁷⁴ Carre, J.; Claudy, P.; Letoffe, J. M.; Kolimannsberger, M.; Bousquet, E. *J. Fluorine Chem.* **1979**, *14*, 139. Carre, J.; Germain, P.; Kolimannsberger, M.; Perachon, G.; Thourey, J. *J. Fluorine Chem.* **1979**, *13*, 365.

⁷⁵ Brion, C. E. *Int. J. Mass Spectrom. Ion Phys.* **1969**, *3*, 197.

⁷⁶ Compton, R. N.; Reinhardt, P. W.; Cooper, C. D. *J. Chem. Phys.* **1978**, *68*, 2023.

⁷⁷ Luo, Y.-R. *Comprehensive Handbook of Chemical Bond Energies*, CRC Press: Boca Raton, FL, 2007.

⁷⁸ (a) Nicolaidis, A.; Borden, W. T. *J. Am. Chem. Soc.* **1991**, *113*, 6750. (b) Wang, S. Y.; Borden, W. T. *J. Am. Chem. Soc.* **1989**, *111*, 7282. (c) Carter, E. A.; Goddard, W. A. III *J. Am. Chem. Soc.* **1988**, *110*, 4077. (d) Carter, E. A.; Goddard, W. A. III *J. Phys. Chem.* **1986**, *90*, 998.

⁷⁹ (a) Grant, D. J.; Dixon, D. A. *J. Phys. Chem. A* **2006**, *110*, 12955. (b) Grant, D. J.; Matus, M. H.; Switzer, J. K.; Dixon, D. A.; Francisco, J. S.; Christe, K. O. *J. Phys. Chem. A* **2008**, *112*, 3145.

⁸⁰ (a) O'Hare, P. A. G.; Wahl, A. C. *J. Chem. Phys.* **1970**, *53*, 2834. (b) O'Hare, P. A. G.; Hubbard, W. N.; Feder, H. M. IUPAC Thermodynamik Symposium, Heidelberg, Germany, September 1967; Paper No. II-5.

⁸¹ Lide, D. R., Ed.; *CRC Handbook of Chemistry and Physics*, 86th ed.; Taylor and Francis: Boca Raton, FL, 2005; pp (10-202)-(10-222).

⁸² Harland, P. W.; Thynne, J. C. *J. Inorg. Nucl. Chem. Lett.* **1973**, *9*, 265.

⁸³ Ficalora, P. J.; Thompson, J. C.; Margrave, J. L. *J. Inorg. Nucl. Chem.* **1969**, *31*, 3771.

Table 6.1. Optimized Bond Lengths (Å) and Angles (degrees) for SeF_xO_y Geometries^a.

Molecule	Basis set	R _{SeF}	R _{SeO}	∠FSeF	∠FSeO	∠OSeO	∠FSeF
SeF(² Π, C _{∞v})	aVQZ	1.744					
	Exp ^{b,c}	1.742					
SeF ₂ (² B ₁ , C _{2v})	aVTZ	1.665					
SeF ₂ (¹ A ₁ , C _{2v})	aVQZ	1.738		96.2			
SeF ₃ (¹ A ₁ , C _{3v})	aVQZ	1.648		97.3			
SeF ₃ (² B ₁ , C _{2v})	aVQZ	1.699eq		86.0			
		1.795ax					
SeF ₃ (¹ A ₁ , C _{2v})	aVQZ	1.769eq		86.3			
		1.916ax					
SeF ₄ (¹ A ₁ , C _{2v})	aVTZ	1.691eq		100.4eq			
		1.777ax		168.6ax			
SeF ₄ (² A ₁ , C _{2v})	aVTZ	1.645eq		100.8eq			
		1.723ax		161.5ax			
SeF ₅ (¹ A ₁ , C _{2v})	aVTZ	1.643eq		120.0			
		1.663ax		180.0			
SeF ₅ (² A ₁ , C _{4v})	aVTZ	1.741eq		91.0			90.0
		1.674ax					
SeF ₅ (¹ A ₁ , C _{4v})	aVTZ	1.721eq		84.3			89.4
		1.841ax					
SeF ₆ (¹ A _{1g} , O _h)	aVQZ	1.683		90.0			90.0
	Exp ^d	1.678					
SeF ₆ (² A _{1g} , O _h)	aVTZ	1.819		90.0			90.0
SeF ₆ (²⁻ 1A _{1g} , O _h)	aVQZ	1.948		90.0			90.0
SeF ₇ (¹ A ₁ , D _{5h})	aVTZ	1.817eq		72.0			90.0
		1.704ax		180.0			
SeO(² Σ ⁻ , C _{∞v})	aVTZ		1.597				
SeO(³ Σ ⁻ , C _{∞v})	aVQZ		1.644				
SeOF(¹ A', C _s)	aVTZ	1.679	1.576		106.7		
SeOF(² A'', C _s)	aVQZ	1.753	1.607		105.6		

SeOF ⁻ (¹ A',C _s)	aVQZ	1.868	1.680		104.3
SeOF ₂ (¹ A',C _s)	aVTZ	1.738	1.585	92.6	104.9
SeOF ₂ ⁺ (² A',C _s)	aVTZ	1.667	1.720	95.5	99.8
SeOF ₂ ⁻ (¹ A ₁ ,C _{2v})	aVTZ	1.953	1.640	167.7	96.2
SeOF ₂ ²⁻ (¹ A ₁ ,C _{2v})	aVTZ	2.202	1.703	158.0	101.0
SeOF ₃ ⁺ (¹ A ₁ ,C _{3v})	aVTZ	1.643	1.561	99.5	118.2
SeOF ₃ (² A''C _s)	aVTZ	1.701	1.733		103.9
		1.789			
SeOF ₃ ⁻ (¹ A ₁ ,C _s)	aVTZ	1.771eq	1.606		104.5
		1.903ax			
SeOF ₄ ⁺ (² B ₂ ,C _{2v})	aVTZ	1.642eq	1.713	110.8	124.6
		1.675ax		174.2	87.1
SeOF ₄ (¹ A ₁ ,C _{2v})	aVQZ	1.682eq	1.575	111.6	124.2
		1.714ax		162.8	98.6
SeOF ₄ ⁻ (¹ A ₁ ,C _{4v})	aVTZ	1.839	1.597	158.4	100.8
				88.0	
SeOF ₅ ⁻ (¹ A ₁ ,C _{4v})	aVTZ	1.753eq	1.614		96.9
		1.757ax			
SeO ₂ F ⁺ (¹ A',C _s)	aVTZ	1.666	1.581		111.4
					137.2
SeO ₂ F (² A',C _s)	aVQZ	1.734	1.617		104.0
					120.2
SeO ₂ F ⁻ (A',C _s)	aVQZ	1.850	1.632		100.3
					110.9
SeO ₂ F ₂ (¹ A ₁ ,C _{2v})	aVTZ	1.696	1.582	90.5	107.8
					126.9
SeO ₂ F ₂ ⁻ (² A ₁ ,C _{2v})	aVTZ	1.902	1.624	141.7	100.0
					116.3
SeO ₂ F ₃ ⁻ (¹ A ₁ ,C _{2v})	aVTZ	1.740eq	1.609	82.1	114.9
		1.802ax			130.1
SeO ₂ ⁺ (² A',C _s)	aVTZ		1.592		104.2
			1.732		
SeO ₂ (¹ A ₁ ,C _{2v})	aVTZ		1.618		114.3
SeO ₂ ⁻ (² B ₁ ,C _{2v})	aVTZ		1.682		111.9
SeO ₃ (¹ A',D _{3h})	aVQZ		1.597		120.0
SeO ₃ F (¹ A',C _s)	aVTZ	1.657	1.573,	106.3,	58.6,

1.718

114.1

129.7

^a CCSD(T) optimizations on SeF, SeO, and SeF_xO_y compounds; ax = axial and eq = equatorial. ^b

Reference 26. ^c Reference 54. ^d Reference 55.

Table 6.2. Calculated CCSD(T)/aug-cc-pVDZ (-PP on Se) Vibrational Frequencies, for SeF₂, SeF₂⁺, SeF₆ and SeO₂⁻.

Molecule	CCSD(T)	Experiment
SeF ₂	689.9 (a ₁)	699 (a ₁) ^a
	245.8 (a ₁)	
	669.3 (b ₂)	672 (b ₂) ^a
SeF ₂ ⁺	811.1(a ₁)	780 ± 50(a ₁) ^b
	297.1(a ₁)	
	803.5(b ₂)	
SeF ₆	676.5(a _g)	707(a _g) ^{c, d}
	648.9(e _g)	659(e _g) ^c
	410.7(t _{2g})	405(t _{2g}) ^e
	769.8(t _{1u})	780(t _{1u}) ^e
	372.6(t _{1u})	437(t _{1u}) ^e
	247.7(t _{2u})	264(t _{2u}) ^f
SeO ₂ ⁻	836.2(b ₂)	810 ± 80(a ₁) ^g
	820.8(a ₁)	
	326.2(a ₁)	

^a Reference 67. ^b Reference 68. ^c 1~3 cm⁻¹ uncertainty, ^d Reference 27. ^e 3~6 cm⁻¹ uncertainty, ^f 15 ~30 cm⁻¹ uncertainty, ^g Reference 69.

Table 6.3. Calculated CCSD(T)/aug-cc-pVDZ-PP Se-F and Se-O Vibrational Stretching**Frequencies.**

Molecule	Symmetric and Antisymmetric Stretches, cm^{-1}			
SeF ⁺	808.1(σ)			
SeF	670.2(σ)			
SeF ⁻	534.9(σ)			
SeF ₂ ⁺	811.12(a ₁)(Se-F)	803.5(b ₂)(Se-F)		
SeF ₂ ⁻	443.9(a ₁)	405.0(b ₂)		
SeF ₃ ⁺	785.6(a')	782.5(a'')	782.5(a')	
SeF ₃	709.4(a ₁)	611.4(b ₂)	569.7(a ₁)	
SeF ₃ ⁻	619.5(a ₁)	455.0(a ₁)	440.8(b ₂)	
SeF ₄ ⁺	883.8(b ₂)(Se-F)	865.4(a ₁)(Se-F)	657.74(b ₁)(Se-F)	651.2(a ₁)(Se-F)
SeF ₄	710.8(a ₁) (Se-F)	705.8(b ₂) (Se-F)	615.5(b ₁) (Se-F)	572.6(a ₁) (Se-F)
SeF ₄ ⁻	580.0(a ₁)	504.0(b ₂)	477.0(a ₁)	
SeF ₅ ⁺	909.8(b ₂)(Se-F)	909.8(a ₁)(Se-F)	898.7(b ₁)(Se-F)	787.5(a ₁)(Se-F)
	765.0(a ₁)(Se-F)			
SeF ₅	739.7(a ₁)	639.3(b ₂)	639.3(b ₁)	592.2(a ₁)
	585.4(a ₁)			
SeF ₅ ⁻	673.8(a ₁) (Se-F)	526.8(a ₁) (Se-F)	525.8(e) (Se-F)	474.8(b ₁) (Se-F)
SeF ₆ ⁺	870.6(a ₁)	847.2(b ₂)	846.1(b ₁)	754.5(a ₁)
	718.0(a ₁)			
SeF ₆ ⁻	585.2(a _g)	538.7(b _u)	538.7(b _u)	538.6(a _u)
	502.5(a _u)	502.0(a _g)		
SeF ₆ ²⁻	514.2 (a _{1g}) (Se-F)	424.3 (t _{1u}) (Se-F)	424.3(t _{1u}) (Se-F)	380.9 (e _g) (Se-F)
SeF ₇ ⁻	725.5(b ₁)	615.227(a ₁)	577.1(a ₁)	577.1(b ₂)
	575.9(b ₂)	575.9(a ₁)	563.1(a ₁)	
SeO ⁺	868.9(σ) (Se-O)			
SeO	868.9(σ)			
SeOF ⁺	1051.8(a')(Se-O)	771.7(a')(Se-F)		
SeOF	985.3(a') (Se-O)	745.0(a') (Se-F)		

SeOF ⁻	780.4(a') (Se-O)	467.7(a') (Se-F)		
SeOF ₂ ⁺	841.6(a'')(Se-F)	841.5(a')(Se-F)	740.4(a')(Se-O)	
SeOF ₂	1000.4 (a') (Se-O)	652.3(a') (Se-F)	625.3(a'') (Se-F)	
SeOF ₂ ⁻	886.1(a ₁) (Se-O)	427.5(a ₁) (Se-F)	409.1(b ₂) (Se-F)	
SeOF ₂ ²⁻	775.6(a ₁)(Se-O)	250.4(b ₂)(Se-F)	235.9(a ₁)(Se-F)	
SeOF ₃ ⁺	1098.1(a ₁)(Se-O)	833.0(e)(Se-F)	775.9(a ₁)(Se-F)	
SeOF ₃	711.9(a') (Se-O)	698.3(a') (Se-F)	617.2(a'') (Se-F)	561.2(a') (Se-F)
SeOF ₃ ⁻	933.5(a')(Se-O)	580.9(a')(Se-F)	455.3(a'')(Se-F)	439.9(a')(Se-F)
SeOF ₄ ⁺	869.0(a ₁)(Se-O)	865.4(b ₁) (Se-F)	832.1(b ₂) (Se-F)	761.8(a ₁) (Se-F)
	717.6(a ₁) (Se-F)			
SeOF ₄	974.2(a ₁) (Se-O)	728.5(b ₁) (Se-F)	703.5(b ₂) (Se-F)	677.2(a ₁) (Se-F)
	603.2(a ₁) (Se-F)			
SeOF ₅ ⁺	984.2(a) (O-F)	856.6(a) (Se-F)	823.9(a)(Se-F)	816.1(a)(Se-F)
	718.1(a)(Se-F)	685.9(a) (Se-O)		
SeOF ₅	784.8(a ₁)(Se-F)(Se-O)	778.4(b ₂) (Se-F)	769.9(b ₁)(Se-F)	710.1(a ₁)(Se-F)
	667.4(a ₁) (Se-F)	653.3(a ₁) (Se-F)		
SeOF ₅ ⁻	877.4(a ₁) (Se-O)	637.9(b ₁) (Se-F)	637.9(b ₂) (Se-F)	620.3(a ₁) (Se-F)
	539.8(a ₁) (Se-F)	539.5(a ₁) (Se-F)		
SeO ₂ ⁺	999.0(a') (Se-O)	684.3(a') (Se-O)		
SeO ₂	922.1(b ₂) (Se-O)	874.9(a ₁) (Se-O)		
SeO ₂ ⁻	836.2(a ₁) (Se-O)	820.8(a ₁) (Se-O)		
SeO ₂ F ⁺	1080.0(b ₂) (Se-O)	958.8(a ₁) (Se-O)	760.51(a ₁) (Se-F)	
SeO ₂ F	815.9(a') (Se-O)	769.5(a'') (Se-O)	620.6(a') (Se-F)	
SeO ₂ F ⁻	868.6(a'')(Se-O)	856.5(a')(Se-O)	464.0(a')(Se-F)	
SeO ₂ F ₂ ⁺	1190.2(a') (Se-O)	821.6(a'') (Se-F)	816.4(a') (Se-F) (Se-O)	756.7(a') (Se-O)
SeO ₂ F ₂	1011.7(b ₁) (Se-O)	927.4(a ₁) (Se-O)	684.6(b ₂) (Se-F)	681.7(a ₁) (Se-F)
SeO ₂ F ₂ ⁻	859.7(b ₂) (Se-O)	838.7(a ₁) (Se-O)	442.6(b ₁) (Se-F)	438.5(a ₁) (Se-F)
SeO ₂ F ₃ ⁻	932.8(b ₁) (Se-O)	853.4(a ₁) (Se-O)	618.6(a ₁) (Se-F)	561.5(b ₁) (Se-F)
	493.4(a ₁) (Se-F)			
SeO ₃	1017.5(e)	893.2(a ₁)		

SeO_3F^+ (C_s)	1074.6(a') (Se-O)	957.7(a') (O-F)	900.0(a'') (Se-O)	625.2(a') (Se-F)
SeO_3F^+ (“ T_d ”)	1201.0(a') (Se-O)	859.5(a') (Se-O)	812.3(a'') (Se-O)	780.2(a') (Se-F)
SeO_3F	1904.0(a'') (Se-O)	1127.1(a') (Se-O)	982.7(a') (Se-O)	706.1(a') (Se-F)
SeO_3F^-	912.1(a') (Se-O)	912.0(a'') (Se-O)	829.3(a') (Se-O)	559.5(a') (Se-F)

Table 6.4. Calculated $\delta(^{19}\text{F})/\text{ppm}^{\text{a}}$ and $\delta(^{77}\text{Se})/\text{ppm}^{\text{b}}$ NMR chemical shifts.

Molecule	Atom	Chem Shift	Chem Shift	Chem Shift
		B3LYP/TZVP	BLYP/TZ2P	ZORA-BLYP/TZVP
SeF ⁻	Se	3751.7	3760.3	3605.8
	F	-841.6	-832.4	-839.5
SeF ₂	Se	3768.5	3844.3	3667.0
	F (2)	-217.5	-203.0	-197.9
SeF ₃ ⁺	Se	1295.4	1277.8	1203.0
	F(3)	79.7	60.2	69.5
SeF ₃ ⁻	Se	2957.4	3219.2	3098.3
	F(2) ax	-74.3	-38.5	-36.7
	F eq	-303.9	-280.2	-279.4
SeF ₅ ⁺	Se	898.5	734.9	696.4
	F eq	166.2	140.5	175.7
	F(2) eq	167.3	141.5	167.8
	F(2) ax	195.8	200.0	245.9
SeF ₆	Se	694.0	554.9	534.4
	F	104.6	110.4	147.8
SeF ₇ ⁻	Se	675.4	582.2	559.8
	F (5) eq	431.1	531.2	667.3
	F (2) ax	155.6	177.9	225.6
SeOF ⁻	Se	3940.7	4024.6	3862.9
	F	-403.2	-373.1	-378.6
SeOF ₂ ²⁻	Se	3629.4	3826.1	3642.2
	F	-264.8	-233.6	-240.0
SeO ₂ F ₂	Se	943.7	784.7	739.3
	F	93.6	68.8	87.6
SeOF ₃ ⁺	Se	872.6	703.4	654.3
	F	144.1	110.1	138.1
SeOF ₄	Se	793.3	633.7	593.1
	F (2) ax	154.3	157.1	191.2

SeOF ₅ ⁻	F (2) eq	133.6	121.9	152.4
	Se	662.6	504.9	471.7
SeO ₂ F ⁺	F (4) eq	116.5	123.1	154.2
	F ax	173.0	203.9	248.7
	Se	1119.1	943.2	886.9
SeO ₂ F ₃ ⁻	F	325.6	285.1	314.1
	Se	862.1	718.2	680.9
	F (2) ax	98.2	98.3	118.6
SeO ₃ F ⁻	F eq	94.3	89.3	111.3
	Se	1060.2	892.6	846.9
	F	51.7	44.9	57.8

^a ¹⁹F chemical shifts relative to CFC₃. Absolute ¹⁹F chemical shift = 156.1 ppm at the GIAO B3LYP/AhlrichsVTZP level. Absolute ¹⁹F chemical shift = 135.3 ppm at the GIAO BLYP/TZ2P level, Absolute ¹⁹F chemical shift = 134.5 ppm at the GIAO BLYP-ZORA/TZ2P level.

^b ⁷⁷Se chemical shifts relative to Se(CH₃)₂. Absolute ⁷⁷Se chemical shift = 1698.8 ppm at the GIAO B3LYP/AhlrichsVTZP level. Absolute ⁷⁷Se chemical shift = 1616.2 ppm at the GIAO BLYP/TZ2P level. Absolute ⁷⁷Se chemical shift = 1747.9 ppm at the GIAO BLYP-ZORA/TZ2P level.

Table 6.5. Components for Calculating the Atomization Energies in kcal/mol^a.

Molecule	(CBS) ^b	$\Delta E_{\text{ZPE}}^{\text{c}}$	$\Delta E_{\text{CV}}^{\text{d}}$	$\Delta E_{\text{SR}}^{\text{e}}$	$\Delta E_{\text{SO}}^{\text{f}}$	$\Sigma D_0(0\text{K})^{\text{g}}$
SeF ⁺	-143.53	1.18	-1.10	0.10	-3.09	-148.81
SeF	80.49	0.96	-0.26	-0.08	-3.09	76.10
SeF ⁻	135.95	0.76	-0.01	-0.19	-3.09	131.89
SeF ₂ ⁺	-59.01	2.73	-1.67	0.12	-3.84	-66.78
SeF ₂	169.03	2.29	-0.71	-0.08	-3.48	162.47
SeF ₂ ⁻	212.70	1.33	-0.15	-0.35	-3.48	207.40
SeF ₃ ⁺	33.78	4.60	-2.72	0.16	-3.87	22.74
SeF ₃	232.28	3.53	-1.48	-0.12	-3.87	223.29
SeF ₃ ⁻	306.41	3.12	-0.76	-0.46	-3.87	298.20
SeF ₄ ⁺	40.55	6.07	-4.10	0.28	-4.26	26.40
SeF ₄	328.77	5.38	-2.73	-0.14	-4.26	316.26
SeF ₄ ⁻	364.79	4.30	-1.89	-0.42	-4.26	353.93
SeF ₅ ⁺	110.62	9.08	-7.00	0.46	-4.65	90.36
SeF ₅	359.89	7.38	-4.51	-0.02	-4.65	343.32
SeF ₅ ⁻	478.85	6.56	-2.37	-0.55	-4.65	464.76
SeF ₆ ⁺	115.29	9.72	-7.15	0.23	-5.04	93.62
SeF ₆	456.41	10.54	-7.22	0.08	-5.04	433.70
SeF ₆ ⁻	517.54	7.40	-2.22	-0.60	-5.04	502.28
SeF ₆ ²⁻	492.40	5.45	0.33	-1.10	-5.04	481.15
SeF ₇ ⁺	156.45	11.08	-7.15	0.01	-5.43	132.81
SeF ₇ ⁻	551.17	11.00	-7.41	-0.40	-5.43	526.92
SeO ⁺	-125.10	1.46	-0.56	0.21	-2.92	-129.84
SeO	105.29	1.24	0.11	0.03	-2.92	101.27
SeO ⁻	50.37	0.75	0.10	0.06	-2.92	46.85
SeOF ⁺	-37.55	3.07	-1.46	0.29	-3.31	-45.10
SeOF	187.54	2.90	-0.38	0.00	-3.31	180.95
SeOF ⁻	222.77	2.10	-0.38	-0.19	-3.31	216.79
SeOF ₂ ⁺	1.19	4.49	-2.36	0.18	-3.70	-9.18
SeOF ₂	278.86	4.48	-1.72	0.06	-3.70	269.02
SeOF ₂ ⁻	318.58	3.34	-0.50	-0.30	-3.70	310.74

SeOF ₂ ²⁻	240.22	2.35	-0.26	-0.54	-3.70	233.37
SeOF ₃ ⁺	69.04	7.19	-5.31	0.58	-4.09	53.03
SeOF ₃	301.04	5.58	-2.33	-0.09	-4.09	288.95
SeOF ₃ ⁻	418.35	5.30	-1.72	-0.31	-4.09	406.93
SeOF ₄ ⁺	94.96	8.95	-6.42	0.50	-4.48	75.61
SeOF ₄	380.11	8.45	-5.60	0.22	-4.48	361.80
SeOF ₄ ⁻	457.81	6.47	-2.93	-0.30	-4.48	443.62
SeOF ₅ ⁺	135.87	10.86	-6.20	0.20	-4.87	114.15
SeOF ₅	420.37	10.78	-6.72	0.14	-4.87	398.13
SeOF ₅ ⁻	545.95	9.88	-6.01	-0.18	-4.87	525.00
SeO ₂ ⁺	-65.37	2.72	-1.06	0.31	-3.14	-71.98
SeO ₂	207.33	3.05	-0.86	0.28	-3.14	200.56
SeO ₂ ⁻	249.04	2.84	-0.60	0.02	-3.14	242.49
SeO ₂ F ⁺	-8.24	5.14	-3.30	0.61	-3.53	-19.60
SeO ₂ F	249.81	4.34	-1.98	0.25	-3.53	240.21
SeO ₂ F ⁻	352.29	4.38	-1.51	0.00	-3.53	342.88
SeO ₂ F ₂ ⁺	39.58	7.08	-4.77	0.59	-3.92	24.40
SeO ₂ F ₂	335.60	6.88	-4.20	0.40	-3.92	321.01
SeO ₂ F ₂ ⁻	395.31	5.37	-2.26	-0.05	-3.92	383.71
SeO ₂ F ₃ ⁺	83.49	8.88	-4.54	0.34	-4.31	66.10
SeO ₂ F ₃ ⁻	485.44	8.23	-4.66	0.00	-4.31	468.24
SeO ₃	259.57	5.55	-2.59	0.53	-3.36	248.59
SeO ₃ F ⁺ (C _s)	11.96	6.72	-2.71	0.38	-3.75	-0.85
SeO ₃ F ⁺ ("T _d ")	28.04	7.55	-4.04	0.65	-3.75	13.35
SeO ₃ F	302.97	9.14	-3.80	0.50	-3.75	286.78
SeO ₃ F ⁻	435.76	6.90	-3.70	0.26	-3.75	421.67

^a $\sum D_0 = \Delta E_{\text{elec}}(\text{CBS}) - \Delta E_{\text{ZPE}} + \Delta E_{\text{CV}} + \Delta E_{\text{SR}} + \Delta E_{\text{SO}}$. ^b Valence electron dissociation energy extrapolated to the CBS limit by using eq 1 with $n = \text{D,T,Q}$. ^c ΔE_{ZPE} calculated at the CCSD(T)/aug-cc-pVDZ-PP level. ^d Core/valence corrections were obtained with the cc-pwCVTZ basis sets at the optimized geometries. ^e The scalar relativistic correction is based on a

CISD(FC)/cc-pVTZ MVD calculation. ^f Correction due to the incorrect treatment of the atomic asymptotes as an average of spin multiplets. Values are based on Moore's tables.⁴⁷ ^g The theoretical value of the dissociation energy to atoms $\sum D_0(0K)$.

Table 6.6. Calculated CCSD(T)/CBS Heats of Formation (kcal/mol) at 0 and 298 K.

Molecule	$\Delta H_f(0K)$	$\Delta H_f(298K)$	$\Delta H_f(298K)$	$\Delta H_f(0 K)$	$\Delta H_f(298K)$
	CCSD(T)/CBS	CCSD(T)/CBS	Expt	G3 ^f	G3 ^f
Se ⁺	281.1	281.2			
Se			58.1 (57.9@0 K)		
Se ⁻	13.1	13.3			
SeF ⁺	225.2	225.0			
SeF	-0.5	-0.8		-0.4	-0.6
SeF ⁻	-55.5	-55.7			
SeF ₂ ⁺	161.6	161.0			
SeF ₂	-67.6	-68.2		-65.6	-66.1
SeF ₂ ⁻	-112.6	-112.7			
SeF ₃ ⁺	90.6	89.4			
SeF ₃	-110.0	-110.7			
SeF ₃ ⁻	-184.9	-185.5	-185.0 ^a		
SeF ₄ ⁺	105.4	104.0			
SeF ₄	-184.5 ^b	-185.9 ^b	-203 ± 6 ^d	-178.0	-179.4
SeF ₄ ⁻	-222.1	-223.5	-190 ± 10 ^a		
SeF ₅ ⁺	59.9	58.2			
SeF ₅	-193.1	-194.8		-188.3	-190.1
SeF ₅ ⁻	-314.5 ^b	-315.9 ^b	-331.1 ± 9.6 ^c		
SeF ₆ ⁺	75.1	72.4			
SeF ₆	-265.0	-267.7	-267.18 ^e	-264.6	-267.4
SeF ₆ ⁻	-333.6	-334.9	-333.9 ± 6.8 ^c		
SeF ₆ ²⁻	-312.4 ^b	-313.8 ^b			
SeF ₇ ⁺	54.4	51.9			
SeF ₇ ⁻	-339.7	-342.3			
SeO ⁺	246.7	246.5			
SeO	15.6	15.4			
SeO ⁻	70.0	69.8			
SeOF ⁺	180.5	179.8			

SeOF	-45.6	-46.2
SeOF ⁻	-81.4	-81.9
SeOF ₂ ⁺	163.0	161.9
SeOF ₂	-115.2 ^b	-116.3 ^b
SeOF ₂ ⁻	-156.9	-157.5
SeOF ₂ ²⁻	-79.5	-79.8
SeOF ₃ ⁺	119.3	118.0
SeOF ₃	-116.6	-117.9
SeOF ₃ ⁻	-234.6	-235.7
SeOF ₄	-171.0	-173.1
SeOF ₄ ⁻	-252.9	-254.9
SeOF ₅ ⁺	95.1	92.6
SeOF ₅	-188.9	-191.4
SeOF ₅ ⁻	-315.8	-318.3
SeO ₂ ⁺	247.9	247.1
SeO ₂	-24.7 ^b	-25.4 ^b
SeO ₂ ⁻	-66.6	-67.4
SeO ₂ F ⁺	214.0	212.9
SeO ₂ F	-45.9	-46.9
SeO ₂ F ⁻	-148.5 ^b	-149.6 ^b
SeO ₂ F ₂ ⁺	188.4	186.8
SeO ₂ F ₂	-108.2	-109.2
SeO ₂ F ₂ ⁻	-170.9	-171.9
SeO ₂ F ₃ ⁺	165.2	163.2
SeO ₂ F ₃ ⁻	-236.9	-239.6
SeO ₃	-13.7	-15.0
SeO ₃ F ⁺ (T _d)	240.0	238.3
SeO ₃ F	-33.4	-35.1
SeO ₃ F ⁻	-168.3	-170.0

^a Reference 75. ^b Reference 2. ^c Reference 76. ^d Reference 74. ^e Reference 71. ^f Reference 33.

Table 6.7. Calculated CCSD(T)/CBS Adiabatic and Diabatic BDEs in kcal/mol.

Reactions	Adiabat Se	Diabat Se	Adiabat S
	0K	0K	0K ^a
${}^1\text{SeF}_6 \rightarrow {}^2\text{SeF}_5 + {}^2\text{F}$	90.4	90.4	104.8
${}^2\text{SeF}_5 \rightarrow {}^1\text{SeF}_4 + {}^2\text{F}$	27.0	88.1 (${}^3\text{SeF}_4$)	37.7
${}^1\text{SeF}_4 \rightarrow {}^2\text{SeF}_3 + {}^2\text{F}$	93.0	93.0	95.5
${}^2\text{SeF}_3 \rightarrow {}^1\text{SeF}_2 + {}^2\text{F}$	60.8	74.4 (${}^3\text{SeF}_2$)	54.8
${}^1\text{SeF}_2 \rightarrow {}^2\text{SeF} + {}^2\text{F}$	86.4	86.4	89.1
${}^2\text{SeF} \rightarrow {}^3\text{Se} + {}^2\text{F}$	76.1	76.1	83.2
${}^1\text{SeOF}_4 \rightarrow {}^2\text{SeOF}_3 + {}^2\text{F}$	72.9	72.9	89.7
${}^1\text{SeOF}_4 \rightarrow {}^1\text{SeF}_4 + {}^3\text{O}$	45.5	96.3 (${}^3\text{SeF}_4$)	88.2
${}^2\text{SeOF}_3 \rightarrow {}^1\text{SeOF}_2 + {}^2\text{F}$	19.9	112.2 (${}^3\text{SeOF}_2$)	20.0
${}^2\text{SeOF}_3 \rightarrow {}^2\text{SeF}_3 + {}^3\text{O}$	65.7	111 (${}^1\text{O}$)	94.0
${}^1\text{SeOF}_2 \rightarrow {}^2\text{SeOF} + {}^2\text{F}$	88.1	88.1	93.6
${}^1\text{SeOF}_2 \rightarrow {}^1\text{SeF}_2 + {}^3\text{O}$	106.5	125.9 (${}^3\text{SeF}_2$)	128.8
${}^2\text{SeOF} \rightarrow {}^3\text{SeO} + {}^2\text{F}$	79.7	79.7	85.4
${}^2\text{SeOF} \rightarrow {}^2\text{SeF} + {}^3\text{O}$	104.0	138.4 (${}^4\text{SeF}$)	124.3
${}^3\text{SeO} \rightarrow {}^3\text{Se} + {}^3\text{O}$	101.3	101.3	123.1
${}^1\text{SeO}_2\text{F}_2 \rightarrow {}^1\text{SeOF}_2 + {}^3\text{O}$	52.0	129.7 (${}^3\text{SeOF}_2$)	98.7
${}^1\text{SeO}_2\text{F}_2 \rightarrow {}^2\text{SeO}_2\text{F} + {}^2\text{F}$	80.8	80.8	106.9
${}^2\text{SeO}_2\text{F} \rightarrow {}^2\text{SeOF} + {}^3\text{O}$	59.3	154.4 (${}^4\text{SeOF}$)	85.4
${}^2\text{SeO}_2\text{F} \rightarrow {}^1\text{SeO}_2 + {}^2\text{F}$	39.7	88.9 (${}^3\text{SeO}_2$)	40.4
${}^1\text{SeO}_3 \rightarrow {}^1\text{SeO}_2 + {}^3\text{O}$	48.0	97.2 (${}^3\text{SeO}_2$)	
${}^2\text{SeO}_3\text{F} \rightarrow {}^1\text{SeO}_3 + {}^2\text{F}$	38.2		
${}^1\text{SeO}_2 \rightarrow {}^3\text{SeO} + {}^3\text{O}$	99.3		131.1

^a Reference 1.

Table 6.8. CCSD(T)/CBS Fluoride Affinities in kcal/mol at 298 K.

Reactions	CCSD(T) ^a
$\text{Se} + \text{F}^- \rightarrow \text{SeF}^-$	56.9
$\text{SeF} + \text{F}^- \rightarrow \text{SeF}_2^-$	52.5
$\text{SeF}_2 + \text{F}^- \rightarrow \text{SeF}_3^-$	57.8 (47.2)
$\text{SeF}_3 + \text{F}^- \rightarrow \text{SeF}_4^-$	53.3
$\text{SeF}_4 + \text{F}^- \rightarrow \text{SeF}_5^-$	70.5
$\text{SeF}_5 + \text{F}^- \rightarrow \text{SeF}_6^-$	80.7
$\text{SeF}_6 + \text{F}^- \rightarrow \text{SeF}_7^-$	15.0
$\text{SeO} + \text{F}^- \rightarrow \text{SeOF}^-$	37.8
$\text{SeOF} + \text{F}^- \rightarrow \text{SeOF}_2^-$	51.8
$\text{SeOF}_2 + \text{F}^- \rightarrow \text{SeOF}_3^-$	60.0 (43.5)
$\text{SeOF}_3 + \text{F}^- \rightarrow \text{SeOF}_4^-$	77.5
$\text{SeOF}_4 + \text{F}^- \rightarrow \text{SeOF}_5^-$	85.7 (62.3)
$\text{SeO}_2 + \text{F}^- \rightarrow \text{SeO}_2\text{F}^-$	64.6
$\text{SeO}_2\text{F} + \text{F}^- \rightarrow \text{SeO}_2\text{F}_2^-$	65.5
$\text{SeO}_2\text{F}_2 + \text{F}^- \rightarrow \text{SeO}_2\text{F}_3^-$	69.6 (39.8)
$\text{SeO}_3 + \text{F}^- \rightarrow \text{SeO}_3\text{F}^-$	95.5

^a Fluoride affinities for corresponding sulfur compound.

Table 6.9. CCSD(T)/CBS Fluorocation Affinities (FCA) in kcal/mol at 298 K.

Reactions	FCA
$\text{Se} + \text{F}^+ \rightarrow \text{SeF}^+$	256.6
$\text{SeF} + \text{F}^+ \rightarrow \text{SeF}_2^+$	259.0
$\text{SeF}_2 + \text{F}^+ \rightarrow \text{SeF}_3^+$	263.1
$\text{SeF}_3 + \text{F}^+ \rightarrow \text{SeF}_4^+$	206.1
$\text{SeF}_4 + \text{F}^+ \rightarrow \text{SeF}_5^+$	176.7
$\text{SeF}_5 + \text{F}^+ \rightarrow \text{SeF}_6^+$	122.0
$\text{SeF}_6 + \text{F}^+ \rightarrow \text{SeF}_7^+$	101.2
$\text{SeO} + \text{F}^+ \rightarrow \text{SeOF}^+$	256.3
$\text{SeOF} + \text{F}^+ \rightarrow \text{SeOF}_2^+$	212.6
$\text{SeOF}_2 + \text{F}^+ \rightarrow \text{SeOF}_3^+$	186.5
$\text{SeOF}_3 + \text{F}^+ \rightarrow \text{SeOF}_4^+$	189.7
$\text{SeOF}_4 + \text{F}^+ \rightarrow \text{SeOF}_5^+$	155.1
$\text{SeO}_2 + \text{F}^+ \rightarrow \text{SeO}_2\text{F}^+$	182.4
$\text{SeO}_2\text{F} + \text{F}^+ \rightarrow \text{SeO}_2\text{F}_2^+$	187.0
$\text{SeO}_2\text{F}_2 + \text{F}^+ \rightarrow \text{SeO}_2\text{F}_3^+$	147.7
$\text{SeO}_3 + \text{F}^+ \rightarrow \text{SeO}_3\text{F}^+$	167.4

Table 10. CCSD(T)/CBS Electron Affinities at 0 K in eV.

Molecule	CCSD(T)	Expt	G3 ^a
Se	2.05	2.020682 ± 0.000044^b	2.125
SeF	2.40		2.442
SeF ₂	1.93		2.032
SeF ₃	3.24		3.385
SeF ₄	1.63	$1.7 \pm 0.10^{c,d,e}$	2.247
SeF ₅	5.25	$3.3 \pm 0.2^{d,e}, \geq 5.1 \pm 0.4^{d,f}$	5.236
SeF ₆	2.92	$2.9 \pm 0.2^{d,f}, 3.0 \pm 0.2^{d,g}$	2.815
SeOF	1.55		
SeOF ₂	1.79		
SeOF ₃	5.11		
SeOF ₄	3.55		
SeO ₂	1.82	1.823 ± 0.050^h	
SeO ₂ F	4.45		
SeO ₂ F ₂	2.69		

^a Reference 33. ^b Reference 81. ^c Reference 82. ^d Reference 25. ^e Reference 80. ^f Reference 67.

^g Reference 49. ^h Reference 69.

Table 6.11. CCSD(T)/CBS Ionization energies at 0 K in eV.

Molecule	CCSD(T)	Expt	G3 ^f
Se	9.67 (9.69)	9.75238 ^a	9.727
SeF	9.79		9.813
SeF ₂	9.94	10.20 ^b	10.006
SeF ₃	8.68		8.744
SeF ₄	12.57		12.499
SeF ₅	10.97		10.576
SeF ₆	14.75		14.504
SeO	10.02	11.5 ± 0.5 ^c	
SeOF	9.80		
SeOF ₂	12.06		
SeOF ₃	10.23		
SeOF ₄	12.41		
SeOF ₅	12.31		
SeO ₂	11.82	11.5±0.5 ^d , 11.76 ^e	
SeO ₂ F	11.27		
SeO ₂ F ₂	12.86		
SeO ₃ F	11.86		

^a Reference 81. ^b Reference 68. ^c Reference 33. ^d Reference 83. ^e Reference 69. Total (TAE) of Value in parentheses represents Se calculated at the CCSD(T)/aug-cc-pVQZ-PP and CCSD(T)/aug-cc-pV5Z-PP levels extrapolated to complete basis set limit using the expression in equation 3.

Table 6.12. CCSD(T)/CBS Adiabatic Anion BDEs in kcal/mol at 0 and 298 K.

Reactions	0 K	298K	(298 K) G3 ^a
$\text{SeF}_7^- \rightarrow \text{SeF}_6^- + \text{F}$	24.6	26.3	
$\text{SeF}_6^- \rightarrow \text{SeF}_5^- + \text{F}$	37.6	38.0	38.9
$\text{SeF}_5^- \rightarrow \text{SeF}_4^- + \text{F}$	110.8	111.3	97.7
$\text{SeF}_4^- \rightarrow \text{SeF}_3^- + \text{F}$	55.7	57.0	65.0
$\text{SeF}_3^- \rightarrow \text{SeF}_2^- + \text{F}$	90.8	91.8	89.3
$\text{SeF}_2^- \rightarrow \text{SeF}^- + \text{F}$	75.5	76.0	74.2
$\text{SeF}^- \rightarrow \text{Se}^- + \text{F}$	86.9	90.0	84.0
$\text{SeOF}_4^- \rightarrow \text{SeOF}_3^- + \text{F}$	36.7	38.1	
$\text{SeOF}_4^- \rightarrow \text{SeF}_4^- + \text{O}$	89.7	90.9	
$\text{SeOF}_3^- \rightarrow \text{SeOF}_2^- + \text{F}$	96.2	97.2	
$\text{SeOF}_3^- \rightarrow \text{SeF}_3^- + \text{O}$	108.7	109.8	
$\text{SeOF}_2^- \rightarrow \text{SeOF}^- + \text{F}$	94.0	94.6	
$\text{SeOF}_2^- \rightarrow \text{SeF}_2^- + \text{O}$	103.6	104.3	
$\text{SeOF}^- \rightarrow \text{SeF}^- + \text{O}$	83.3	81.9	
$\text{SeO}_2\text{F}_2^- \rightarrow \text{SeO}_2\text{F}^- + \text{F}$	40.8	41.3	
$\text{SeO}_2\text{F}_2^- \rightarrow \text{SeOF}_2^- + \text{O}$	73.0	73.9	
$\text{SeO}_2\text{F}^- \rightarrow \text{SeO}_2^- + \text{F}$	96.2	97.2	
$\text{SeO}_2\text{F}^- \rightarrow \text{SeOF}^- + \text{O}$	126.1	127.2	

^a Reference 33.

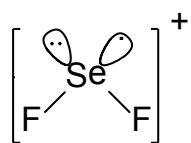
Table 13. CCSD(T)/CBS Adiabatic Cation BDEs in kcal/mol at 0 and 298 K.

Reactions	0 K	298K	298K G3 ^a
$\text{SeF}_7^+ \rightarrow \text{SeF}_6^+ + \text{F}$	39.2	39.5	
$\text{SeF}_6^+ \rightarrow \text{SeF}_5^+ + \text{F}$	3.3	4.8	4.2
$\text{SeF}_5^+ \rightarrow \text{SeF}_4^+ + \text{F}$	64.0	64.8	73.1
$\text{SeF}_4^+ \rightarrow \text{SeF}_3^+ + \text{F}$	3.7	4.4	4.6
$\text{SeF}_3^+ \rightarrow \text{SeF}_2^+ + \text{F}$	89.5	90.6	87.3
$\text{SeF}_2^+ \rightarrow \text{SeF}^+ + \text{F}$	76.1	77.0	79.2
$\text{SeF}^+ \rightarrow \text{Se}^+ + \text{F}$	72.2	73.1	74.8
$\text{SeOF}_4^+ \rightarrow \text{SeOF}_3^+ + \text{F}$	22.6	23.9	
$\text{SeOF}_4^+ \rightarrow \text{SeF}_4^+ + \text{O}$	49.2	50.4	
$\text{SeOF}_3^+ \rightarrow \text{SeOF}_2^+ + \text{F}$	62.2	62.9	
$\text{SeOF}_3^+ \rightarrow \text{SeF}_3^+ + \text{O}$	30.3	31.0	
$\text{SeOF}_2^+ \rightarrow \text{SeOF}^+ + \text{F}$	35.9	36.9	
$\text{SeOF}_2^+ \rightarrow \text{SeF}_2^+ + \text{O}$	57.6	58.7	
$\text{SeOF}^+ \rightarrow \text{SeF}^+ + \text{O}$	84.7	85.6	
$\text{SeO}_2\text{F}_2^+ \rightarrow \text{SeO}_2\text{F}^+ + \text{F}$	44.0	45.0	
$\text{SeO}_2\text{F}_2^+ \rightarrow \text{SeOF}_2^+ + \text{O}$	33.6	34.7	
$\text{SeO}_2\text{F}^+ \rightarrow \text{SeO}_2^+ + \text{F}$	62.2	62.9	
$\text{SeO}_2\text{F}^+ \rightarrow \text{SeOF}^+ + \text{O}$	25.5	26.5	

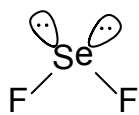
^a Reference 33.

Table 6.14. CCSD(T)/CBS Adiabatic Heterolytic Se-F BDEs in kcal/mol at 0 and 298 K to Form a Cation and F⁻.

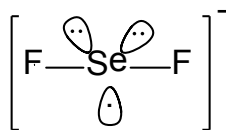
Reactions	0 K	298K
$\text{SeF} \rightarrow \text{Se}^+ + \text{F}^-$	219.9	220.3
$\text{SeF}_2 \rightarrow \text{SeF}^+ + \text{F}^-$	233.3	233.7
$\text{SeF}_3 \rightarrow \text{SeF}_2^+ + \text{F}^-$	212.1	212.3
$\text{SeF}_4 \rightarrow \text{SeF}_3^+ + \text{F}^-$	215.5	215.8
$\text{SeF}_5 \rightarrow \text{SeF}_4^+ + \text{F}^-$	238.9	239.3
$\text{SeF}_6 \rightarrow \text{SeF}_5^+ + \text{F}^-$	265.4	266.4
$\text{SeOF} \rightarrow \text{SeO}^+ + \text{F}^-$	232.8	233.2
$\text{SeOF}_2 \rightarrow \text{SeOF}^+ + \text{F}^-$	236.1	236.6
$\text{SeOF}_3 \rightarrow \text{SeOF}_2^+ + \text{F}^-$	220.2	220.3
$\text{SeOF}_4 \rightarrow \text{SeOF}_3^+ + \text{F}^-$	230.8	231.6
$\text{SeOF}_5 \rightarrow \text{SeOF}_4^+ + \text{F}^-$	244.5	245.0
$\text{SeO}_2\text{F} \rightarrow \text{SeO}_2^+ + \text{F}^-$	234.2	234.5
$\text{SeO}_2\text{F}_2 \rightarrow \text{SeO}_2\text{F}^+ + \text{F}^-$	262.6	263.2



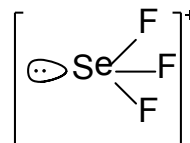
[SeF₂]⁺



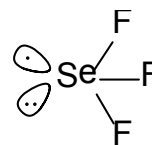
SeF₂



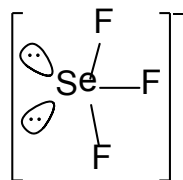
[SeF₂]⁻



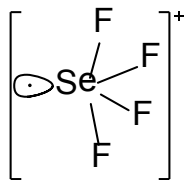
[SeF₃]⁺



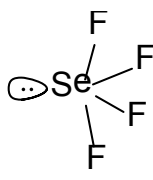
SeF₃



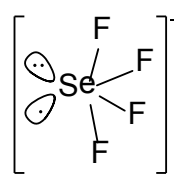
[SeF₃]⁻



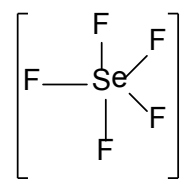
[SeF₄]⁺



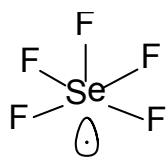
SeF₄



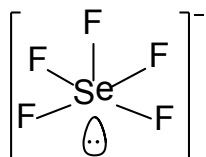
[SeF₄]⁻



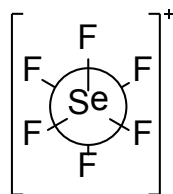
[SeF₅]⁺



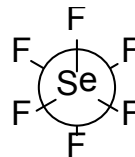
SeF₅



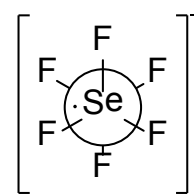
[SeF₅]⁻



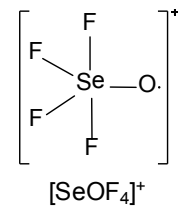
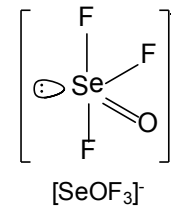
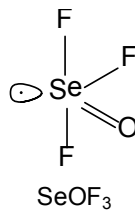
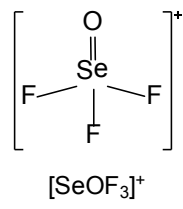
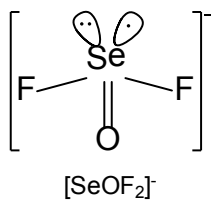
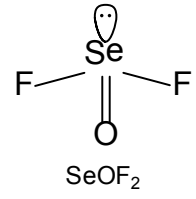
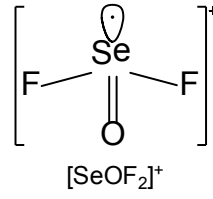
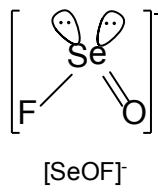
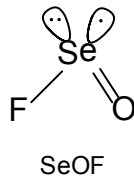
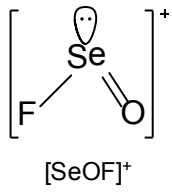
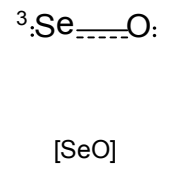
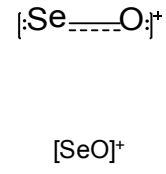
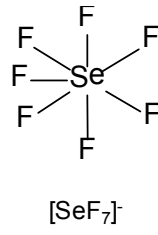
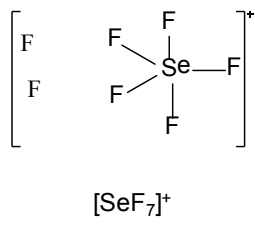
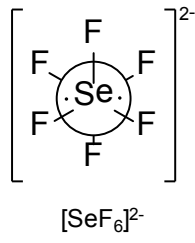
[SeF₆]⁺



SeF₆



[SeF₆]⁻



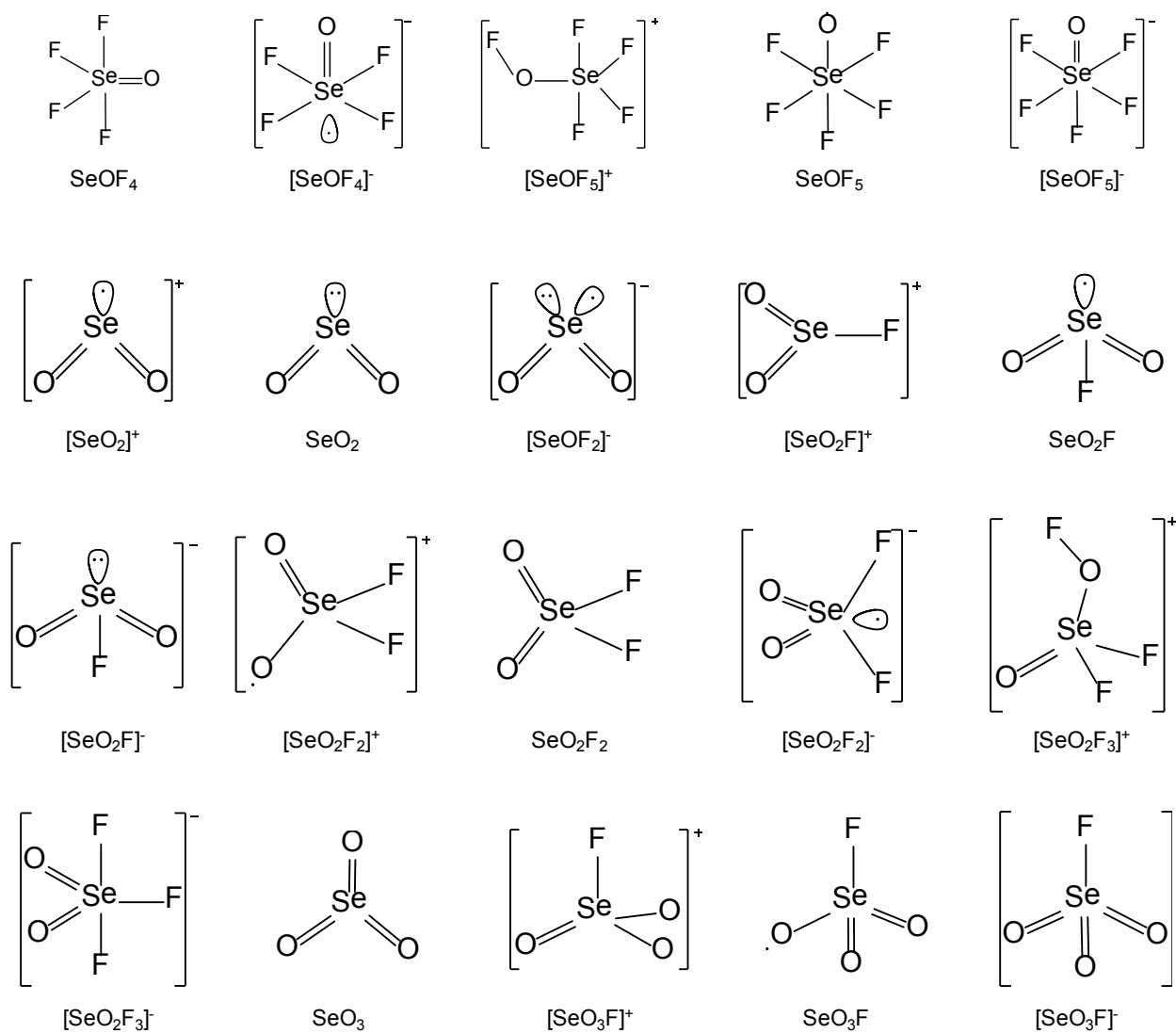


Figure 6.1. Lewis dot structures for the selenium fluorides, oxides and oxofluorides of SeF_n ($n=2-6$)^{+,0,-}, SeOF_n ($n=0-4$)^{+,0,-}, and SeO_2F_n ($n=0-2$)^{+,0,-} molecules.

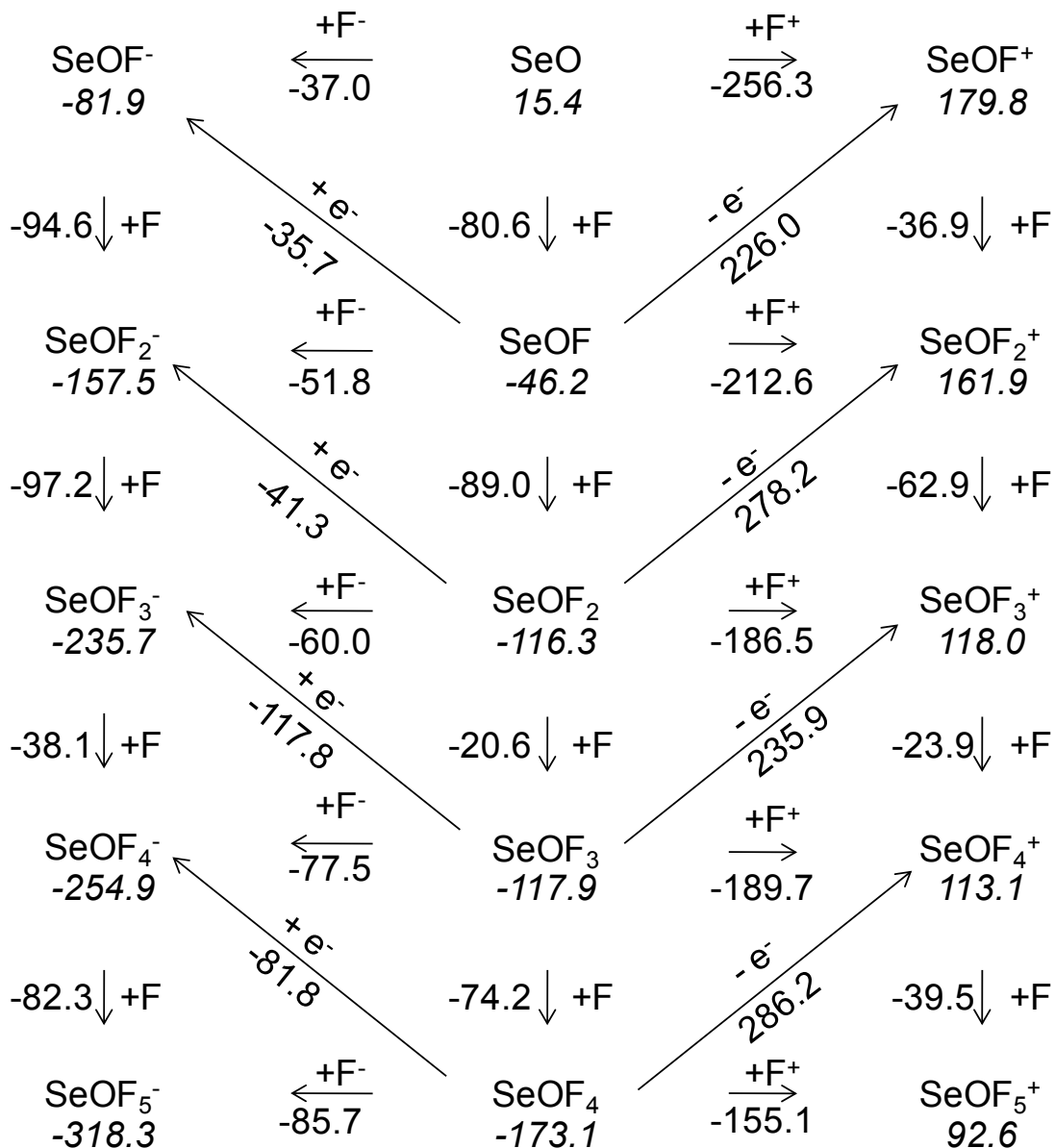


Figure 6.2. Heats of formation and the reaction enthalpies for the addition of F^+ , F , and F^- at 298 K as well as ionization potentials ($-e^-$) and electron affinities ($+e^-$) of SeOF_n . All values in kcal/mol. Heats of formation are given below each species *in italics*. Vertical arrows correspond to the addition of F to SeOF_n to form SeOF_{n+1} for the cation, neutral, and anion. Horizontal arrows to the left correspond to fluoride anion affinities. Horizontal arrows to the right correspond to fluorocation affinities. Diagonal arrows to the left correspond to the ionization potential ($-e^-$). Diagonal arrows to the right correspond to the electron affinity ($+e^-$). The heat of formation of F^- at 298 K is -59.5 kcal/mol using the electron affinity of F .⁴⁹

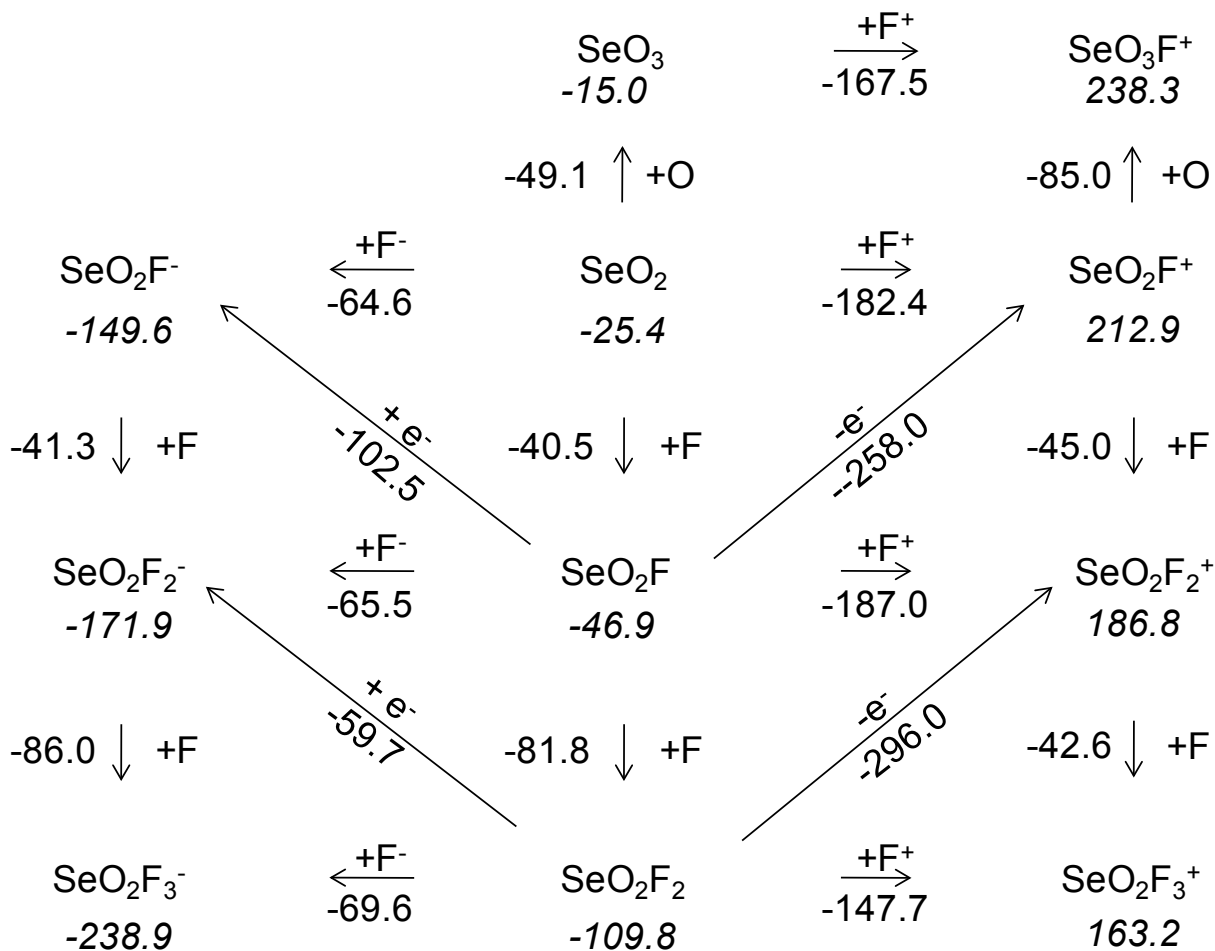


Figure 6.3. Heats of formation and the reaction enthalpies for the addition of F^+ , F , and F^- at 298 K as well as ionization potentials ($-e^-$) and electron affinities ($+e^-$) of SeO_2F_n . All values in kcal/mol. Heats of formation are indicated below each species *in italics*. Vertical arrows correspond to the addition of F to SeO_2F_n to form $\text{SeO}_2\text{F}_{n+1}$ in terms of the cation, neutral, and anion. Horizontal arrows to the left correspond to the fluorocation affinities. Horizontal arrows to the right correspond to fluoride anion affinities. Diagonal arrows to the left correspond to the ionization potential ($-e^-$). Diagonal arrows to the right correspond to the electron affinity ($+e^-$).

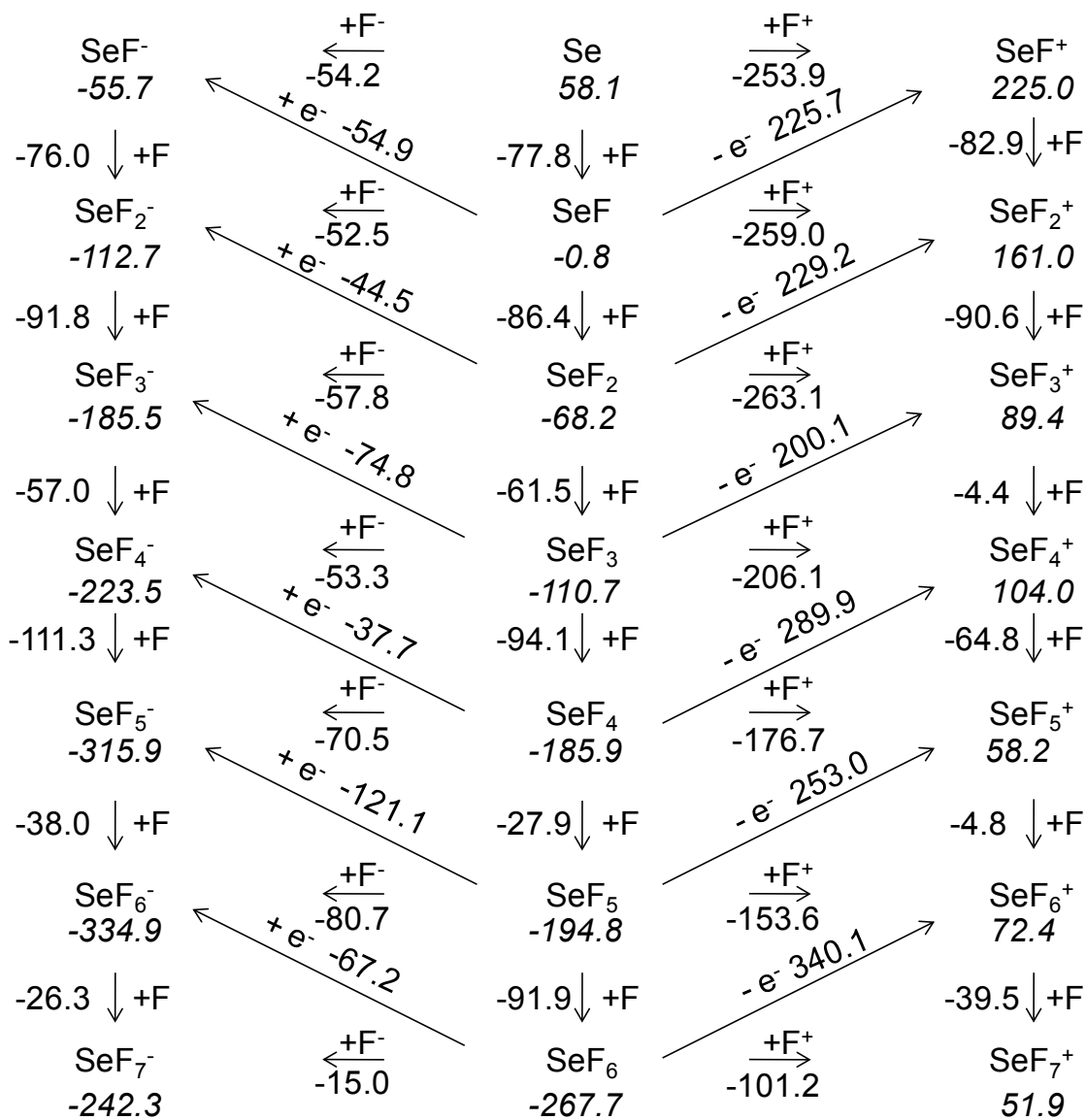


Figure 6.4. Heats of formation and the reaction enthalpies for the addition of F^+ , F , and F^- at 298 K as well as ionization potentials ($-e^-$) and electron affinities ($+e^-$) of SeF_n . All values in kcal/mol. Heats of formation are indicated below each species *in italics*. Vertical arrows correspond to the addition of F to SeF_n to form SeF_{n+1} in terms of the cation, neutral, and anion. Horizontal arrows to the left correspond to fluoride anion affinities. Horizontal arrows to the right correspond to fluorocation affinities. Diagonal arrows to the left correspond to the ionization potential ($-e^-$). Diagonal arrows to the right correspond to the electron affinity ($+e^-$).

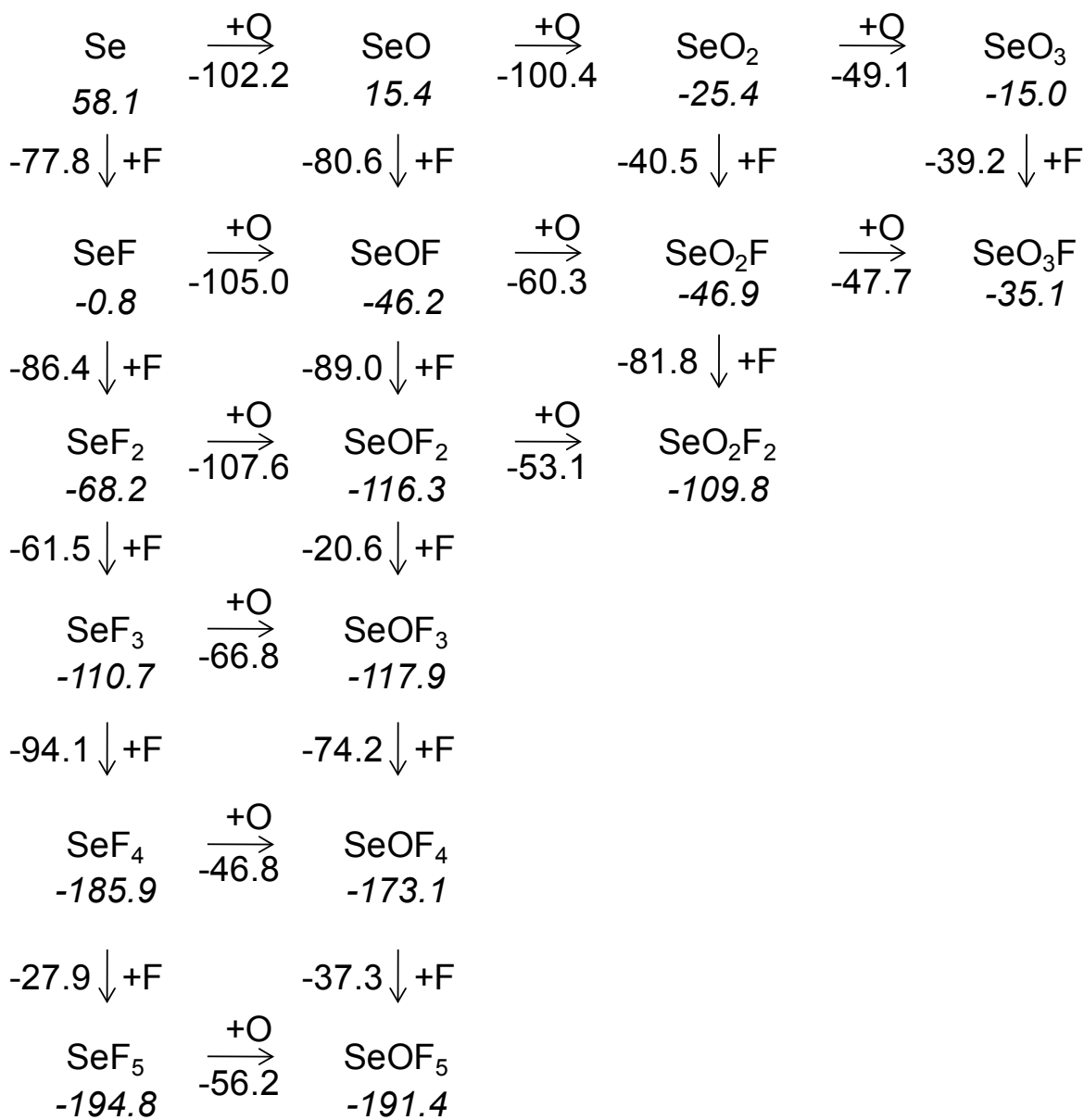


Figure 6.5. Heats of formation and reaction enthalpies for the addition of an F to SeF_n to form SeF_{n+1} , O to SeF_n to form SeOF_n , F to SeOF_n to form SeOF_{n+1} and O to SeO_2F_n to form SeO_3F_n at 298 K in kcal/mol. Heats of formation are indicated below each molecule *in italics*. Vertical arrows correspond to the addition of F to SeF_n or SeOF_n to form SeF_{n+1} or SeOF_{n+1} . Horizontal arrows to the right correspond to the addition of O to SeF_n , SeOF_n or SeO_2F_n to form SeOF_n , SeO_2F_n and SeO_3F_n respectively.

CHAPTER 7

CONCLUSIONS

Chapter 2 describes the prediction of the vibrational frequencies of UO_2^{2+} at the CCSD(T) Level. The harmonic stretching frequencies for UO_2^{2+} are found to be sensitive to the correlation treatment, the basis set, and the treatment of relativistic effects. The CCSD method overestimates the values by a considerable amount as shown by a comparison of the results at the CCSD(T)/aVTZ(1) level. The CCSD(T) values for the asymmetric stretch are within 20 cm^{-1} and do not show much dependence on whether an ECP is used or if the relativistic effects are included at the Dirac-Hartree-Fock (DHF) level. Once a reasonable size basis set is reached (aVTZ(1)), the frequencies are not strongly dependent on the quality of the basis set. The CASPT2 values show that there can be a substantial underlying basis set dependence for the asymmetric stretch. The CASPT2 method appears to underestimate the harmonic stretching frequencies, however the DFT B3LYP values, show little dependence on the basis set for this stretch and are about 20 cm^{-1} above the CCSD(T)/aVQZ(2) value. The difference between the asymmetric and symmetric stretch is very dependent on the method. All of the calculations with an ECP predict a fundamental separation of 80 to 100 cm^{-1} . The CASPT2 calculations predict a value of around 110 cm^{-1} whereas the DHF+CCSD(T) results predict a separation of close to 150 cm^{-1} . This latter value seems to be too high and may be due to the somewhat smaller basis set that was used in those calculations. Experimental results for mono-, di- and tri-acetate binding to uranyl in solution and the solid state show a decrease in the band origin separation from 93 to 87

to 75-78 cm^{-1} as the charge changes from +1 to 0 to -1.^{1,2,3,4,5} The splitting for UO_2^{2+} in aqueous solution with 4 to 5 bound waters is $\sim 90\text{-}95 \text{ cm}^{-1}$.^{6,7,8,9} Calculations at the B3LYP/ECP level on UO_2^{2+} embedded in up to 15 waters predict a value of approximately 95 cm^{-1} , which is consistent with the experimental results. Our best results (CCSD(T)/SO/aVQZ(2)) predict a splitting of 81 cm^{-1} . Therefore we suggest that the splitting for the symmetric and asymmetric stretches in the bare ion UO_2^{2+} should be 80 to 85 cm^{-1} . The bending frequency is sensitive to the method and to the actual criteria used in the calculations. The quality of the grid, the level of convergence of the wavefunction, and the integral accuracy can cause variations in the bending frequency of up to 30 cm^{-1} in DFT calculations. This can lead to issues when looking at the deviation of uranyl from linearity in the presence of different ligands, so care should be taken in calculations to ensure that there are no artifacts being introduced by the grid or the convergence criteria. The anharmonic effects are larger than the spin orbit corrections but both are small. The anharmonic effects decrease all the frequencies whereas the spin orbit corrections increase the stretches and decrease the bend. Overall, these two corrections decrease the harmonic asymmetric stretch frequency by 6 cm^{-1} , the symmetric stretch by 3 cm^{-1} and the bend by 3 cm^{-1} . The best calculated values for UO_2^{2+} for the asymmetric stretch, symmetric stretch, and bend are 1113 , 1032 , and 174 cm^{-1} , respectively. The separation between the asymmetric and symmetric stretch band origins is predicted to be 81 cm^{-1} , which is consistent with experimental trends for substituted uranyls in solution and in the solid state.

Chapter 3 discusses the study of reactions of laser-ablated thorium atoms and O_2 using matrix isolation infrared spectroscopy. Electronic structure calculations were used to interpret the infrared spectra of three new thorium oxide species, ThO_2^- , Th_2O_2 , and Th_2O_4 obtained in argon and neon matrixes. The ThO_2^- anion is predicted to have a ${}^2\text{A}_1$ ground state with C_{2v} symmetry

just as found for MO_2 for $M = \text{Ti}, \text{Zr},$ and Hf . Upon electron attachment the bond length and angle of the ThO_2^- anion are only slightly different from those of the neutral ThO_2 molecule. The antisymmetric and symmetric Th-O stretches for the anion is predicted to be 692.9 and 756.4 cm^{-1} at the CCSD(T) level of theory with relative intensities of about 2.2:1 at the B3LYP level. The experimental 653.2 cm^{-1} absorption is in qualitative agreement with the frequency of the antisymmetric stretching mode of the free anion and the observed isotopic $^{16}\text{O}:^{18}\text{O}$ ratio for the band of 1.0542 is nearly the same as the calculated value of 1.0547. The antisymmetric Th-O stretch for the $^{16}\text{OTh}^{18}\text{O}^-$ isotopmer is predicted to be 12 cm^{-1} higher than that of the $\text{Th}^{18}\text{O}_2^-$ isotopmer, which is in good agreement with the experimental observations. The matrix shift for ThO_2^- is 13.6 cm^{-1} from Ar to Ne so the calculated harmonic value is 24 cm^{-1} higher than the neon matrix value suggesting that the anharmonicity correction is larger in the anion or that there is a red neon matrix shift.

The ground state of the rhombus-shaped Th_2O_2 molecule is predicted to have D_{2h} symmetry and is a singlet with the triplet is 22.3 kcal/mol higher in energy at the B3LYP level. The Th-O bond length of the Th_2O_2 molecule is approximately the same as that of the rhombic ring in the Th_2O_4 molecule and the calculated Th-Th distance, 3.358 \AA , is slightly shorter than that in the Th_2O_4 molecule. The b_{1u} mode is calculated to be 621.4 cm^{-1} with an $^{16}\text{O}/^{18}\text{O}$ ratio of 1.0565, both in excellent agreement with experimental values at the CCSD(T) level. The small predicted infrared intensity for the b_{2u} mode at 520.3 cm^{-1} as compared with the b_{1u} mode may make it impossible for the b_{2u} mode to be observed in the matrix experiment. The a_g mode at 630.4 cm^{-1} is IR-inactive so it cannot be observed. The recently characterized M_2O_2 ($M=\text{Zr}, \text{Hf}$) molecules also have D_{2h} symmetry, and only one rhombic M-O stretching mode was observed in the matrix IR experiments.¹⁰

The lowest energy structure of the Th₂O₄ is predicted to have nonplanar C_{2h} symmetry for its closed shell singlet ground state. Only three vibrational modes, 806.9, 611.7, and 481.1 cm⁻¹, are predicted to be infrared active above 400 cm⁻¹ with the latter two IR active Th-O stretches having respective ¹⁶O/¹⁸O isotopic ratios (DFT) of 1.0555 and 1.0562, which are close to the experimental ¹⁶O/¹⁸O ratios of 1.0546 and 1.0559; the corresponding experimental frequencies are 581.4 and 478.0 cm⁻¹ for comparison. The antisymmetric Th=O terminal stretching frequency is predicted to be 806.9 cm⁻¹, approximately 30 cm⁻¹ higher than band observed in the experiment, which is consistent with the type of matrix shift expected from the CCSD(T) calculations on ThO₂.¹¹ The infrared inactive symmetric stretching mode of 805.8 cm⁻¹ is predicted to be essentially the same as the antisymmetric stretching mode, and the inactive rhombus Th-O stretch is predicted to be 565.9 cm⁻¹.

Chapter 4 describes the potential energy surface for the reaction of matrix isolated ThO with CH₄ to give the CH₃Th(O)H intermediate. Calculations at the B3LYP level reveal that the CH₃Th(O)H molecule possesses a pyramidal structure with a closed shell singlet ground state. From the calculated potential energy surface, formation of the CH₃Th(O)H molecule from the reaction of ThO and methane has an energy barrier of 30 kcal/mol, which is consistent with the appearance of the ¹CH₃Th(O)H absorptions under broad band mercury arc UV irradiation, and the CH₃Th(O)H product is 11 kcal/mol more stable than the asymptotic reactants. The ³Th + ¹CH₃OH asymptote is predicted to be 128 kcal/mol above the reactant asymptote ¹ThO + CH₄. Utilizing the experimental spin orbit splittings^{12,13,14} for the Th atom to apply a spin orbit correction to the ³Th atom gives a predicted reaction energy of 119 kcal/mol, which is in excellent agreement with the value of 118.7 ± 3.8 kcal/mol calculated from the experimental heats of formation.^{15,16,17,18} Further decomposition of the ¹CH₃Th(O)H complex is forbidden by

energy barriers of 47 and 77 kcal/mol separating it from $^1\text{CH}_3\text{ThOH}$ and $^1\text{CH}_3\text{OThH}$ with $^1\text{CH}_3\text{ThOH}$ being 24 kcal/mol more stable than $^1\text{CH}_3\text{OThH}$. Both of the additional intermediates are predicted to be less stable than the reactant asymptote of $\text{ThO} + \text{CH}_4$, and each have singlet ground states as observed in other divalent thorium species.^{19,20,21} The $^3\text{CH}_3\text{ThOH}$ complex is predicted to be 14 kcal/mol higher in energy than $^1\text{CH}_3\text{ThOH}$, and the $^3\text{CH}_3\text{OThH}$ complex is predicted to be 12 kcal/mol above that of $^1\text{CH}_3\text{OThH}$. The presence of small singlet-triplet splittings for the heavy Th element should enable spin orbit coupling in this region permitting a crossing from the singlet to the triplet thereby allowing access to the lowest energy $^3\text{Th} + ^1\text{CH}_3\text{OH}$ product asymptote. The molecular singlet-triplet splitting is smaller than the 20.8 kcal/mol $^3\text{F}-^1\text{D}$ splitting in the thorium atom, which is consistent with this premise.¹² The reactions of thorium oxide and methane suggests that actinide oxides such as ThO might be used to oxidize methane to methanol under photochemical conditions, analogous to transition metal oxide molecules.^{22,23}

Chapter 5 discusses the modeled behavior of uranyl phosphate complexes in the environment; the predicted structures have shown a great deal of diversity in the binding modes between the uranyl cation and phosphate anions. The energetics of anhydrous and hydrated complexes of UO_2^{2+} with the phosphate anions H_2PO_4^- , HPO_4^{2-} , and PO_4^{3-} for up to three phosphorus ligands were studied at the density functional theory (DFT) and MP2 molecular orbital theory levels as isolated gas phase species and in aqueous solution by using self-consistent reaction field (SCRF) calculations with different solvation models. The geometries, and vibrational frequencies of the major binding modes for these complexes are compared to experiment where possible and good agreement is found. Adequate steric space is available in these complexes to accommodate multiple water molecules in the equatorial region of the uranyl

dication with up to two phosphorus ligands. The uranyl moiety is nonlinear in many of the complexes and coordination number (CN) 5 in the equatorial plane is the predominant binding motif. The phosphates are found to bind in both monodentate and bidentate binding modes depending on the charge and the number of water molecules. The $[\text{UO}_2(\text{H}_2\text{PO}_4)(\text{H}_2\text{O})_n]^+$ complexes can accommodate up to three water molecules with the H_2PO_4^- ligands remaining bidentate with a total equatorial CN of 5. $[\text{UO}_2(\text{H}_2\text{PO}_4)(\text{H}_2\text{O})_4]^+$ has an equatorial CN of 5 with the phosphate ligand bound in a monodentate fashion, and a strong hydrogen bond between the H atom on an equatorial water and the terminal P=O group of H_2PO_4^- . In the $\text{UO}_2(\text{HPO}_4)(\text{H}_2\text{O})_n$ complexes, protons can be abstracted from bound waters due to the increased negative charge on the HPO_4^{2-} ligand forming OH^- and H_2PO_4^- ligands which equalizes the buildup of regions of negative charge. In $\text{UO}_2(\text{HPO}_4)(\text{H}_2\text{O})_3$, the phosphate ligand is actually the H_2PO_4^- moiety bound in a monodentate fashion and results from the abstraction of a proton from a water forming a hydroxide ligand bound to uranium leading to CN 4. A hydrogen bond from the terminal P=O group to the H atom of a water stabilizes the monodentate mode. This hydrogen bond results in an elongated H-OH water bond and a ‘hydroxide-like’ interaction of this water with the uranyl center. In $\text{UO}_2(\text{HPO}_4)(\text{H}_2\text{O})_4$, all of the ligands retain their identities. The HPO_4^{2-} ligand is bound in a bidentate fashion to the uranyl and three water molecules are bound in the remaining sites resulting in CN 5. The remaining water molecule is located in the second coordination sphere. Due to the steric effects of the second phosphate in the $\text{UO}_2(\text{H}_2\text{PO}_4)_2(\text{H}_2\text{O})_n$ and $[\text{UO}_2(\text{HPO}_4)_2(\text{H}_2\text{O})_n]^{2-}$ hydrated complexes ($n = 1 - 3$), fewer water molecules can be accommodated equatorially as compared to the monoligand complexes. Bidentate coordination modes for the phosphate ligands are more common. The structure of $\text{UO}_2(\text{H}_2\text{PO}_4)_2(\text{H}_2\text{O})$ has bidentate H_2PO_4^- ligands and a discrete bound water molecule resulting in the expected CN 5.

The $\text{UO}_2(\text{H}_2\text{PO}_4)_2(\text{H}_2\text{O})_3$ complex is structurally similar to the $\text{UO}_2(\text{H}_2\text{PO}_4)_2(\text{H}_2\text{O})_2$ complex, with the exception both H_2PO_4^- ligands are bound in a monodentate fashion. For the $[\text{UO}_2(\text{HPO}_4)_2(\text{H}_2\text{O})_n]^{2-}$ ($n = 1$ and 3) complexes, the equatorial CN was found to be four rather than five with both complexes having at least one phosphate with monodentate binding. The $[\text{UO}_2(\text{HPO}_4)_2(\text{H}_2\text{O})_2]^{2-}$ complex however, contains two bidentate HPO_4^{2-} with CN 6 and C_{2v} symmetry. In $[\text{UO}_2(\text{HPO}_4)_2(\text{H}_2\text{O})_3]^{2-}$, both phosphate ligands exist as H_2PO_4^- moieties with two hydroxide ligands bound to the uranyl. The hydroxides are hydrogen bonded to H atoms from the phosphate ligands and the remaining water acts as a second sphere water molecule hydrogen bonded to the hydroxide ligands. The $[\text{UO}_2(\text{PO}_4)(\text{H}_2\text{O})_n]^-$ ($n = 1, 2$ and 4) complexes each have CN 4 and some bidentate phosphate binding as do the $[\text{UO}_2(\text{PO}_4)_2(\text{H}_2\text{O})_n]^{4-}$ ($n = 1 - 2$) complexes. The ($n = 3$) complexes has CN 5 with the PO_4^{3-} ligand forming a bidentate bond to the uranyl dication. In $[\text{UO}_2(\text{PO}_4)_2(\text{H}_2\text{O})]^{4-}$ both phosphate ligands are bidentate bound to the uranyl dication. In $[\text{UO}_2(\text{PO}_4)_2(\text{H}_2\text{O})_2]^{4-}$, there is a proton transfer to a PO_4^{3-} ligand leading to the formation of an OH^- bonded to the UO_2^{2+} , a monodentate HPO_4^{2-} ligand and one bidentate PO_4^{3-} ligand.

A detailed benchmark study of the three pK_a 's for phosphoric acid was performed to better understand the reactions of UO_2^{2+} with phosphates. pK_a 's of the first, second, and third deprotonations of phosphoric acid using the gas phase geometries optimized at the B3LYP/DZVP2 level, with single point energies at the MP2/aug-cc-pVnZ ($n = \text{D, T, and Q}$) levels plus single point self-consistent reaction field (SCRF) CPCM with COSMO-RS radii SCRF calculations as implemented in Gaussian 09. For the first deprotonation of H_3PO_4 , all methods are within 2.4 pK_a unit of experiment with the exception of the MP2/aug-cc-pVDZ method which is within 4 pK_a units of experiment. For the second and third deprotonations of

H₃PO₄, the B3LYP/DZVP2 method predicts the pK_a's to increase linearly as found by experiment but the slope is too large and the pK_a's are in error by ~ 5 and 10 pK_a units, respectively, as compared to experiment. The second pK_a is within ~ 2 pK_a of experiment. The MP2/aug-cc-pVnZ (n = D, T, and Q) methods do not show a linear dependence for the pK_a's with the third pK_a within ~ 6 pK_a units.

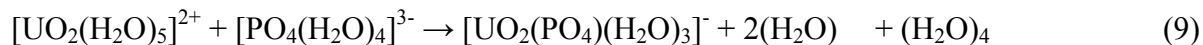
The errors in the phosphate acidities can be reduced by using explicit waters of solvation. We used a microsolvation approach which gives the solution free energies involving reactions of phosphorus-based ligands combined with water molecules to create microsolvated solutes in our continuum solution model. The dependence of the energies of reactions (1) – (3) on different solvation methods.



All of the solvation models predict the solution acidity (ΔG) for reaction (1) within ~ 3 kcal/mol or ~ 2 pK_a units. A similar result is found for reaction (2) with all of the models, except for the IEF-PCM with the UA0 and UFF radii models, giving reasonable results for the second pK_a for H₃PO₄. The two exceptions predict free energies that are too positive. For the third pK_a, CPCM with COSMO-RS radii and IEF-PCM and CSC-PCM, both with the Pauling radii give reasonable agreement with experiment. Our calculated free energies value for all three reactions are closer to experiment than the previously calculated values²⁴ due in part to their use of an incorrect value for the free energy of hydration of H⁺. We used a value of $\Delta G_{\text{solvation}}(\text{H}^+) = -265.9$ kcal/mol which is derived from experimental gas phase clustering energies and is consistent with our high level calculations using a microsolvation/SCRF approach with appropriate

thermodynamic corrections. Tang et al. reported a pK_a of 8.4 for reaction (3) which is ~ 4 pK_a from experiment, but we were only able to closely match this result using a $PO_4(H_2O)_4$ cluster in C_1 symmetry that was ~ 4 kcal/mol higher in energy than our lower energy D_{2d} geometry, suggesting that Tang et al. did not use the lowest energy structure. In summary, our best predictions of the pK_a 's for the different protonation states of phosphoric acid were obtained with a microsolvation approach with 4 waters as shown in reactions (1) – (3), MP2/aug-cc-pVTZ for the gas phase values, and IEF-PCM with Pauling radii for the SCRF calculations. The first, second, and third acidities are now within -1.9, -0.8, and -1.2 pK_a units of experiment, respectively.

The SCRF calculations with the CPCM, IEF-PCM and IPCM models/parameterizations have been used to predict the behavior of these complexes in solution to investigate the thermodynamics of binding, and the equilibrium constants for the reactions of UO_2^{2+} with phosphate and water ligands. These approaches were first tested on known reactions ((4)-(9)).



The cavity effects were studied using the same approaches and radii as used for the phosphoric acidities. The IPCM solvation model consistently agrees best with experiment in reactions in which the hydrated uranyl dication is involved. The best agreement between the calculated and experimental values for reactions (4) – (9) is found when the waters displaced from hydrated

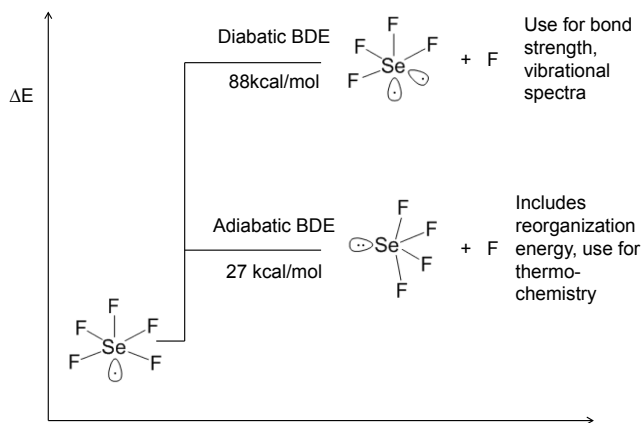
UO_2^{2+} become free waters in the products. There is less of an effect if the waters about the $\text{H}_x\text{PO}_4^{y-}$ are treated as a cluster or as free waters.

Use of our carefully benchmarked hybrid microsolvation-continuum approach led to the prediction that $[\text{H}_2\text{PO}_4]^-$ will displace two H_2O molecule from $[\text{UO}_2(\text{H}_2\text{PO}_4)(\text{H}_2\text{O})_3]^+$ to exothermically form neutral $[\text{UO}_2(\text{H}_2\text{PO}_4)_2(\text{H}_2\text{O})]$. An additional $[\text{H}_2\text{PO}_4]^-$ will displace the remaining water to form the $[\text{UO}_2(\text{H}_2\text{PO}_4)_3]^-$ anion exothermically in solution. The addition of $[\text{H}_2\text{PO}_4]^-$ to $[\text{UO}_2(\text{H}_2\text{PO}_4)_2(\text{H}_2\text{O})_3]$ with all three waters displaced is even more exothermic. HPO_4^{2-} will displace two waters from $[\text{UO}_2(\text{HPO}_4)(\text{H}_2\text{O})_4]$ to form $[\text{UO}_2(\text{HPO}_4)_2(\text{H}_2\text{O})_2]^{2-}$ exothermically. $[\text{UO}_2(\text{HPO}_4)(\text{H}_2\text{O})_3]$ is predicted to be a strong base in the gas phase and in aqueous solution and a moderate to weak acid in the gas phase and a weak acid in solution. Our results show that one has to be careful in the type of solvent model that is used and also in the type of reaction to be used in the model. Overall, the results show that it is possible to predict the energetic properties of aquo uranyl phosphate complexes using correlated molecular orbital theory in combination with SCRF approaches. The prediction of the solution energetics still requires the continued development of solvent modeling approaches as small changes in the models can lead to large changes in reaction energies in solution.

Chapter 6 describes the calculation of the thermodynamic properties of selenumoxyfluorides. Many of these molecules possess both a Se free valence electron pair and a free unpaired valence electron, and questions about their preferred location and their influence on the Se-F and Se=O bond strengths can be addressed by high level calculations. As an example, the pair-wise substitution of two fluorine atoms in SeF_5^- by a doubly bonded oxygen atom to make SeF_3O^- reduces the CN of Se from 6 to 4, and the presence of a sterically active free valence electron pair on Se could have a strong influence on the bonding of the fluorine

ligands. The SeF_5 molecule has an unpaired electron and an F atom on Se in its axial region forming a CN 6 with four F atoms in its equatorial region. Its adiabatic Se-F BDE is low (27.0 kcal/mol) due to the stability of the CN 5 SeF_4 molecule which has a free valence electron pair and two F atoms on Se in the equatorial region and two axial F atoms. The Se-F BDE of the CN 5 SeF_3 molecule, having both a free valence electron pair and a free unpaired valence electron on Se, is 60.8 kcal/mol, resulting in the CN 4 SeF_2 molecule which has two free valence electron pairs on Se. SeF resulting from the Se-F bond dissociation of SeF_2 is CN 4 with two free valence electron pairs and one free unpaired electron on Se. The CN 5 SeOF_3 molecule has a doubly bonded oxygen atom, a fluorine atom, and an unpaired electron on Se in the equatorial region, its Se-F BDE (19.9 kcal/mol) is the smallest adiabatic BDE of the SeO_xF_x and SeF_x compounds. The resulting Se-F bond dissociation of SeOF_3 produces the CN 4 SeOF_2 molecule which retains its doubly bonded oxygen atom and has a free valence electron pair, and two remaining F atoms on Se, the Se-O BDE of SeOF_2 (106.5 kcal/mol) is the largest BDE of the SeO_xF_x and SeF_x compounds. The bond dissociation energies (BDEs), fluoride and fluorocation affinities, and electron affinities of SeF_n ($n = 1 - 6$), SeOF_n ($n = 0 - 4$), and SeO_2F_n ($n = 0 - 2$) have been predicted with coupled cluster CCSD(T) theory extrapolated to the complete basis set limit. To achieve near chemical accuracy, additional corrections were added to the complete basis set binding energies based on frozen core coupled cluster theory energies. The adiabatic BDEs contain contributions from product reorganization energies and, therefore, can be much smaller than the diabatic BDEs and can vary over a wide range. An example of the difference in the adiabatic and diabatic bond energies is shown to the right. The adiabatic Se-F BDEs of SeF_n ($n = 1 - 6$) are: $\text{SeF}_6 = 90$, $\text{SeF}_5 = 27$, $\text{SeF}_4 = 93$, $\text{SeF}_3 = 61$, $\text{SeF}_2 = 86$, and $\text{SeF} = 76$ kcal/mol, and the corresponding diabatic values are: $\text{SeF}_6 = 90$, $\text{SeF}_5 = 88$, $\text{SeF}_4 = 93$, $\text{SeF}_3 = 74$, $\text{SeF}_2 = 86$, and

SeF = 76 kcal/mol. The adiabatic Se-O BDEs of SeO_n ($n = 1 - 3$), SeOF_n ($n = 1 - 4$), and SeO_2F_n ($n = 1, 2$) range from 23 to 107 kcal/mol, and the diabatic ones range from 62 to 154 kcal/mol. The adiabatic Se-F BDEs of SeOF_n ($n = 1 - 4$) and



SeO_2F_n ($n = 1, 2$) range from 20 to 88 kcal/mol, and the diabatic ones range from 73 to 112 kcal/mol. The fluoride affinities of SeF_n , ($n=1 - 6$), SeO_n , ($n = 1 - 3$), SeOF_n , ($n = 1 - 4$), and SeO_2F_n ($n = 1, 2$) range from 15 to 121 kcal/mol, demonstrating that the Lewis acidity of these species covers the spectrum from very weak (SeF_6) to very strong (SeO_3) acids. The electron affinities which are a measure of the oxidizing power of a species, span a wide range from 1.56 eV in SeF_4 to 5.16 eV in SeF_5 and for the free radicals are much higher than for the neutral molecules. The calculations led to the re-examination of the NMR and vibrational spectra of a number of these compounds. For example, the assignments for SeF_5^- , SeOF_3^- and SeO_2F^- , were corrected by using the theoretical calculations. Whereas the previously published normal coordinate analysis of SeF_5^- is correct, that for SeOF_3^- needed major revision.

The SeOF^+ , SeOF_3^+ , SeOF_4^+ cations, the SeOF_2 molecule and the SeOF_3^- anion have the smallest enthalpies for addition of F in their series indicating that the addition of a F atom is less favored. The reaction enthalpy for the addition of the first F atom to the neutral, cation, and anion are about the same, 40 to 45 kcal/mol. The exothermicity of the reaction to add F to SeO_2F_n increases for the neutral and the anion with the second addition almost double the value of the first. In contrast, the addition of the second F to the cation is essentially the same energy as the first. The addition of F to SeO_2F_2^+ to form SeO_2F_3^+ occurs by addition to an oxygen and

not selenium. Reaction enthalpies for the addition of an F atom to $\text{SeF}_n^{0\pm 1}$ ($n = 1 - 7$) to form $\text{SeF}_{n+1}^{0\pm 1}$ range from -26.3 kcal/mol in SeF_6^- and -38.0 kcal/mol in SeF_5^- to -111.3 kcal/mol in SeF_4^- , suggesting that the addition of a fifth Se-F bond is strongly favored. The low values of -4.4 and -4.8 kcal/mol for the addition of F to SeF_3^+ and SeF_5^+ , respectively, suggest that the oxidation of these two cations may prove to be difficult, and SeF_6^+ will dissociate.

References

- ¹ Nguyen-Trung, C.; Begun, G. M.; Palmer, D. A. Aqueous Uranium Complexes. 2. Raman Spectroscopic Study of the Complex Formation of the Dioxouranium(VI) ion with a Variety of Inorganic and Organic Ligands. *Inorg. Chem.* **1992**, *31*, 5280-5287.
- ² Quilès, F.; Burneau, A. Infrared and Raman Spectroscopic Study of Uranyl Complexes: Hydroxide and Acetate Derivatives in Aqueous Solution. *Vib. Spectrosc.* **1998**, *18*, 61-75.
- ³ McGlynn, S. P.; Smith, J. K.; Neely, W. C. Electronic Structure, Spectra, and Magnetic Properties of Oxycations. III. Ligation Effects on the Infrared Spectrum of the Uranyl Ion. *J. Chem. Phys.* **1961**, *35*, 105-116.
- ⁴ Ga'1, M.; Goggin, P. L.; Mink, J. Vibrational Spectroscopic Studies of Uranyl Complexes in Aqueous and Non-Aqueous Solutions. *Spectrochim Acta* **1992**, *48A*, 121-132.
- ⁵ Kline, R. J.; Kershner, C. J. , C. J. The Oxidation of Uranium(IV) Acetate by Silver Acetate in Liquid Ammonia. *Inorg. Chem.* **1966**, *5*, 932-934.
- ⁶ Toth, L. M.; Begun, G. M. Raman Spectra of Uranyl Ion and its Hydrolysis Products in Aqueous Nitric Acid. *J. Phys. Chem.* **1981**, *85*, 547-549.
- ⁷ Basile, L. J.; Sullivan, J. C.; Ferraro J. R.; LaBonville, P. The Raman Scattering of Uranyl and Transuranium V, VI, and VII Ions. *Appl. Spectrosc.* **1974**, *28*, 142-145.
- ⁸ Jones, L. H.; Penneman, R. A. Infrared Spectra and Structure of Uranyl and Transuranium (V) and (VI) Ions in Aqueous Perchloric Acid Solution. *J. Chem. Phys.* **1952**, *21*, 542-544.
- ⁹ Quilès, F.; Burneau, A. Infrared and Raman Spectra of Uranyl(VI) oxo-Hydroxo Complexes in Acid Aqueous Solutions: A Chemometric Study. *Vibrational Spect.* **2000**, *23*, 231-241.
- ¹⁰ Gong, Y.; Zhang, Q. Q.; Zhou, M. F. Matrix Isolation Infrared Spectroscopic and Theoretical Study of Group IV Metal Oxide Clusters: M_2O_2 and M_2O_4 . *J. Phys. Chem. A* **2007**, *111*, 3534-3539.
- ¹¹ Jackson, V. E.; Craciun, R.; Dixon, D. A.; Peterson, K. A.; de Jong, W. A. Prediction of Vibrational Frequencies of UO_2^{2+} at the CCSD(T) Level. *J. Phys. Chem. A* **2008**, *112*, 4095-4099.
- ¹² Blaise, J.; Wyart, J. F. Energy Levels and Atomic Spectra of Actinides, Int'l Tables of Selected Constants **20**, Tables de Constantes, Paris (1992).
- ¹³ Handbook of Basic Atomic Spectroscopic Data
<http://www.nist.gov/pml/data/handbook/index.cfm> (accessed Aug 03, 2013)

-
- ¹⁴ Sansonetti, J. E.; Martin, W. C. Handbook of Basic Atomic Spectroscopic Data. *J. Phys. Chem. Ref. Data.* **2005**, *34*, 1559-2259.
- ¹⁵ Konigs, R. J. M.; Benes, O. J. The Thermodynamic Properties of the f-Elements and Their Compounds. I. The Lanthanide and Actinide Metals. *J. Phys. Chem. Ref. Data* 2010, *39*, No. 043102 (47pages).
- ¹⁶ Konigs, R. J. M.; Morss, L. R.; Fuger, J. *In The Chemistry of the Actinide and Transactinide Elements*, 3rd Ed.; Springer: Dordrecht, the Netherlands, 2006; Vol. 4, Chapter 19, pp 2113–2224.
- ¹⁷ Cox, J. D.; Wagman, D. D.; Medvedev, V. A. *CODATA Key Values for Thermodynamics*, Hemisphere: New York, 1989.
- ¹⁸ Chase, M. W. Jr. *NIST-JANAF Thermochemical Tables*, 4th ed.; *J. Phys. Chem. Ref. Data*, Mono. 9; American Institute of Physics: Woodbury, NY, 1998; Suppl. 1.
- ¹⁹ Liang, B. Y.; Andrews, L.; Li, J.; Bursten, B. E. Experimental and Theoretical Studies of the Products of Laser-Ablated Thorium Atom Reactions with H₂O in Excess Argon. *J. Am. Chem. Soc.* **2002**, *124*, 6723-6733.
- ²⁰ Gong, Y.; Andrews, L. Matrix Infrared Spectroscopic and Density Functional Theoretical Investigations on Thorium and Uranium Atom Reactions with Dimethyl Ether. *Dalton Trans.* **2011**, *40*, 11106-11114.
- ²¹ Wang, X. F.; Andrews, L. Infrared Spectra and Structures of the Th(OH)₂ and Th(OH)₄ Molecules. *Phys. Chem. Chem. Phys.* **2005**, *7*, 3834-3838.
- ²² Wang, G. J.; Zhou, M. F. Probing the Intermediates in the MO + CH₄ ↔ M + CH₃OH Reactions by Matrix Isolation Infrared Spectroscopy. *Int. Rev. Phys. Chem.* **2008**, *27*, 1–25.
- ²³ Wang, G. J.; Gong, Y.; Chen, M. H.; Zhou, M. F. Methane Activation by Titanium Monoxide Molecules: A Matrix Isolation Infrared Spectroscopic and Theoretical Study. *J. Am. Chem. Soc.* **2006**, *128*, 5974–5980.
- ²⁴ Tang, E.; Tommaso, D. D.; de Leeuw, N. H. Accuracy of the Microsolvation–Continuum Approach in Computing the pK_a and the Free Energies of Formation of Phosphate Species in Aqueous Solution. *Phys. Chem. Chem. Phys.* **2010**, *12*, 13804-13815.